AUG 6 1987

Y 3. N 88: 25/3228/v. 5

NUREG/CR-3228
MEA-2207
Vol. 5

Structural Integrity of Water Reactor Pressure Boundary Components

Annual Report for 1986

Edited by F. J. Loss

Materials Engineering Associates, Inc.

**Prepared for
U.S. Nuclear Regulatory
Commission**

ORIGINAL

CDV

BEST COPY AVAILABLE

COMPLETED

NOTICE

This report was prepared as an account of work sponsored by an agency of the United States Government. Neither the United States Government nor any agency thereof, or any of their employees, makes any warranty, expressed or implied, or assumes any legal liability of responsibility for any third party's use, or the results of such use, of any information, apparatus, product or process disclosed in this report, or represents that its use by such third party would not infringe privately owned rights.

NOTICE

Availability of Reference Materials Cited in NRC Publications

Most documents cited in NRC publications will be available from one of the following sources:

1. The NRC Public Document Room, 1717 H Street, N.W.
   Washington, DC 20555
2. The Superintendent of Documents, U.S. Government Printing Office, Post Office Box 37082,
   Washington, DC 20013-7082
3. The National Technical Information Service, Springfield, VA 22161

Although the listing that follows represents the majority of documents cited in NRC publications, it is not intended to be exhaustive.

Referenced documents available for inspection and copying for a fee from the NRC Public Document Room include NRC correspondence and internal NRC memoranda; NRC Office of Inspection and Enforcement bulletins, circulars, information notices, inspection and investigation notices; Licensee Event Reports; vendor reports and correspondence; Commission papers; and applicant and licensee documents and correspondence.

The following documents in the NUREG series are available for purchase from the GPO Sales Program: formal NRC staff and contractor reports, NRC-sponsored conference proceedings, and NRC booklets and brochures. Also available are Regulatory Guides, NRC regulations in the *Code of Federal Regulations*, and *Nuclear Regulatory Commission Issuances*.

Documents available from the National Technical Information Service include NUREG-series reports and technical reports prepared by other federal agencies and reports prepared by the Atomic Energy Commission, forerunner agency to the Nuclear Regulatory Commission.

Documents available from public and special technical libraries include all open literature items, such as books, journal and periodical articles, and transactions. *Federal Register* notices, federal and state legislation, and congressional reports can usually be obtained from these libraries.

Documents such as theses, dissertations, foreign reports and translations, and non-NRC conference proceedings are available for purchase from the organization sponsoring the publication cited.

Single copies of NRC draft reports are available free, to the extent of supply, upon written request to the Division of Information Support Services, Distribution Section, U.S. Nuclear Regulatory Commission, Washington, DC 20555.

Copies of industry codes and standards used in a substantive manner in the NRC regulatory process are maintained at the NRC Library, 7920 Norfolk Avenue, Bethesda, Maryland, and are available there for reference use by the public. Codes and standards are usually copyrighted and may be purchased from the originating organization or, if they are American National Standards, from the American National Standards Institute, 1430 Broadway, New York, NY 10018.

BEST COPY AVAILABLE

NUREG/CR-3228
MEA-2207
Vol. 5
RF, R5

Structural Integrity of Water Reactor Pressure Boundary Components

Annual Report for 1986

Manuscript Completed: June 1987
Date Published: July 1987

Edited by
F. J. Loss

Materials Engineering Associates, Inc.
9700-B Martin Luther King, Jr. Highway
Lanham, MD 20706-1837

Prepared for
Division of Engineering
Office of Nuclear Regulatory Research
U.S. Nuclear Regulatory Commission
Washington, DC 20555
NRC FIN B8900

ABSTRACT

This program is being conducted for the NRC to provide analytical and experimental methods and data that are necessary to ensure the structural safety and reliability of pressure boundary components in commercial, light water reactor power systems. Emphasis is placed on characterization of material properties performance in a nuclear environment for the application to plant-life extension and mitigation of the consequences of postulated accident scenarios. Current work is organized into three major tasks: (1) fracture mechanics investigations, (2) environmentally-assisted crack growth in high temperature, primary reactor water, and (3) radiation sensitivity and postirradiation properties recovery. Research progress in these three tasks for 1986 is summarized in this report.

Fracture tests of stainless steel clad RPV steel in the unirradiated condition showed that the cladding process improved the toughness of local region over that of the ferritic base metal. It appears that the HAZ dominates the crack initiation behavior of the clad zone. Correlation studies of the irradiation embrittlement trends between Charpy (C_v) tests and fracture mechanics tests have shown that for base metals a fracture mechanics test indicates the temperature elevation of the transition region with irradiations to be higher than the temperature elevation predicted by C_v tests, but the opposite is true for weld metals. The warm prestress phenomenon is being modeled to provide a predictive capability to possibly mitigate the consequences of a PTS scenario. Studies have shown that the full benefit of warm prestress is retained for reloading (during PTS) if the initial unloading is less than one-third of the warm prestress level. Fracture mechanics tests of irradiated weld metal (HSST 5th Irradiation Series) suggests a temperature elevation of the K_{Ic} curve whose magnitude is predicted well by C_v tests. A Piping Fracture Mechanics Data Base has been established and placed "on-line." A joint USA-FRG program is underway to evaluate material from the decommissioned Gundremmingen reactor vessel for a critical assessment of power reactor vs. test reactor environment effects. Trepans from the vessel showed more embrittlement than archive material irradiated to the same fluence in a test reactor.

Fatigue-life testing of A 106-B piping steel to validate the ASME Code, Section III curves has been completed in air for both smooth and notched specimens and testing in a PWR environment was initiated. A program to understand the mechanisms responsible for environmentally-assisted cracking in high-temperature water has produced a report describing a time-based, two-mechanism calculational model; another report was issued that examines the contaminent elements in the fracture surface oxides. Studies of load interactions during fatigue crack growth in a water environment have shown that significant accelerations can occur and that ASME code-based calculations may be nonconservative in some cases. Fatigue crack growth of specimens containing part-through surface flaws is being conducted to more closely simulate the structural case than does the CT specimen. Testing on plate and clad specimens is underway in a water environment.

Studies of irradiation-anneal-reirradiation (IAR) behavior of RPV weld metal showed that the benefit of IAR appears to be greatest with a 454°C instead of a 399°C annealing temperature. It is suggested that IAR procedures may provide a means to avoid concerns of vessel embrittlement during a PTS scenario in operation during plant-life extension. Research studies to uncover the effect of steel composition on annealing have shown that copper but not phosphorus has a detrimental effect on notch ductility recovery by the annealing method. A composition including of 0.68% Ni, with a high copper content has been shown to exert a detrimental effect on notch ductility recovery. Consequently, steel composition must be treated as a potentially critical variable influencing both recovery and the degree of residual embrittlement after annealing. A coordinated program of study on radiation effects mechanisms was developed by MEA at the University of Florida, GKSS (Germany), and VTT (Finland). The program emphasizes sophisticated techniques such as FIM, SANS, and PA to uncover the embrittlement mechanisms. This program has shown that phosphorus does not enhance yield strength elevation by irradiation and that the phosphorus mechanism is not due to radiation-enhanced diffusion to prior austenite grain boundaries in the manner of temper embrittlement. A program to evaluate the relative embrittlement of steels in a test reactor vs. power reactor scenario (e.g., dose-rate effect) has uncovered phenomena which may extend to power reactor surveillance as well as test reactors. Observed dose-rate effects, while not large, could influence data interpretation within the framework of NRC Regulatory Guide 1.99.

CONTENTS

	Page
ABSTRACT	iii
LIST OF FIGURES	vii
LIST OF TABLES	xvi
PREFACE	xix
FOREWORD	xxi
ACKNOWLEDGMENT	xxv
SUMMARY	1
1. FRACTURE MECHANICS INVESTIGATIONS	11
1.1 Fracture Resistance of Irradiated Stainless Steel Clad Vessels	11
1.2 Correlation of Dynamic C_v and Static K_{Ic}/K_{Jc} Tests	17
1.3 Warm Prestress Modeling	20
1.4 Irradiation-Induced K_{Ic} Curve Shift	26
1.5 Piping Fracture Mechanics Data Base	33
1.6 Gundremmingen RPV Material Characterization	36
2. ENVIRONMENTALLY-ASSISTED CRACK GROWTH IN LWR MATERIALS	54
2.1 Environmental Degradation of Fatigue Life	54
2.2 Mechanisms and Models for Environmentally-Assisted Fatigue Crack Growth	62
2.3 Cumulative Damage Factor in Environmentally-Assisted Fatigue Crack Growth	64
2.4 Evaluation of the Effects of Environment and Cladding on the Growth of Surface Flaws	118
2.5 Environmentally-Assisted Fatigue Crack Growth	141
3. RADIATION SENSITIVITY AND POSTIRRADIATION PROPERTIES RECOVERY	144
3.1 Effect of Temperature on Annealing for Alleviating Radiation-Induced Embrittlement	144
3.2 Influence of Steel Composition on Embrittlement Relief by Postirradiation Heat Treatment	170
3.3 Mechanisms of Irradiation Damage for Reactor Vessel Steels	183
3.4 Investigation of Long- vs. Short-Term Irradiation Embrittlement of RPV Steels	190
REFERENCES	206

BLANK PAGE

LIST OF FIGURES

Figure		Page
1-1	Schematic representation of the specimen sampling for baseline material characterization	13
1-2	Transition temperature characteristics of base metal, heat-affected zone, and clad metal as determined from compact specimens	13
1-3	Four-point loaded bend beam	14
1-4	K_{Jc} data on clad bend beam specimens with surface cracks	14
1-5	K_{Jc} data on base metal bend beam specimens with surface cracks	16
1-6	Crack growth in base metal at upper shelf temperature	16
1-7	Schematic of LUCF loading from point O to A, and then path A-O-B-C to failure	22
1-8	Effect of warm prestress load level, K_{wps}, on K_f trend in a LUCF cycle predicted by the Chell Model	23
1-9	Effect of partial unload on the K_f trend predicted by the Chell model	24
1-10	K_{Jc} data for unirradiated and irradiated compact specimens of 72W	28
1-11	K_{Jc} data for unirradiated and irradiated compact specimens of 73W	29
1-12	Weibull predicted median K_{Jc} values for 4T-, 6T-, and 8T-compact specimens from 2T-CT data of 72W	30
1-13	Weibull predicted median K_{Jc} values for 4T-, 6T-, and 8T-compact specimens from 2T-CT data of 73W	31
1-14	Through-thickness fracture toughness of archive ring forging, GEB (side 2), before irradiation	38
1-15	J-R curve determinations for 1/8T- and 1/4T-thickness locations in code GEB material (upper shelf test condition)	39
1-16	Charpy-V notch ductility of archive ring forging, GEB (side 2) before and after irradiation at 288°C (550°F) to 8.8×10^{18} n/cm^2, E > 1 MeV	41

LIST OF FIGURES

Figure		Page
1-17	Charpy-V notch ductility of archive ring forging, GEB (side 2) before and after irradiation at 288°C (550°F) and after postirradiation annealing at 399°C (750°F) for 168 h	42
1-18	Charpy-V notch ductility of archive ring forging, GEB (side 2) before and after irradiation at 288°C (550°F) and after postirradiation annealing at 454°C (850°F) for 168 h	43
1-19	Fracture toughness of archive ring forging, GEB (side 2) before and after irradiation at 288°C (550°F) to 8.6 x 10^{18} n/cm^2, E > 1 MeV	47
1-20	Postirradiation annealing at 399°C for 168 h results in no recovery or up to 80% recovery	48
1-21	Postirradiation annealing at 454°C for 168 h provides at least partial recovery in every case, although the amount of recovery indicated by individual specimens is not the same	49
1-22	Through-thickness determinations by MEA/EG&G Idaho, Inc. for vessel trepan material	51
1-23	Comparison of as-irradiated condition Charpy-V test results for MEA archive material (test reactor irradiation) and MPA trepan material (KRB-A vessel service)	53
2-1	S-N miniautoclave system	56
2-2	Stress-life plot of notched and unnotched SA 106-B specimens tested in 288°C (550°F) air	57
2-3	Stress-life plot of unnotched SA 106-B specimens tested in 288°C (550°F) air and PWR environments	58
2-4	Stress-life plot of notched (K_t = 6) SA 106-B specimens tested in 288°C (550°F) air and PWR environments	59
2-5	Schematic of the three-component model for environmentally-assisted crack growth	66
2-6	CISE ductile baseline for fatigue crack growth, compared with the ASME code dry line and with air data from ICCGR	67

LIST OF FIGURES

Figure		Page
2-7	Schematic representation of stress corrosion crack growth rates as a function of applied stress intensity factor, showing three regions which can be visibly and mechanistically differentiated	69
2-8	Stress corrosion component of fatigue crack growth rate as a function of crack-tip strain rate, for tests of a pressure vessel steel in oxygenated, high-temperature water	71
2-9	Calculated limit curves for the maximum expected crack growth rate (empirical approach)	72
2-10	Plot of time-based, total crack growth rate vs. crack-tip strain rate for MEA data at 288°C	75
2-11	Plot of the arbitrarily chosen true corrosion fatigue part of data shown in Fig. 2-10	77
2-12	Plot showing only the stress corrosion component of crack growth rate, as calculated by using the analytical baseline, for MEA data at 288°C	78
2-13	Family of baselines obtained analytically from MEA data at 288°C	80
2-14	Correction factor for R ratio, based on a synthesis of data by Eason	81
2-15	Fe 2p spectra of specimen CQ2-3 from the fracture surface (II)	84
2-16	Potential-pH diagram for Fe-S-H_2O at 300°C	85
2-17	Carbon concentration in fatigue fracture surface oxides as a function of depth as determined by AES	86
2-18	XPS spectra of Cl 2p and B 1s of V82-3 specimen	88
2-19	Specimen used to cyclically prestrain A 516 Gr. 70 carbon steel before converting material to CERT specimens	90
2-20	Constant extension rate specimen to be used in this study	91
2-21	Schematic of the autoclave used in the CERT program	93
2-22	Crack extension vs. cyclic count for tests of A 533-B using the ICCGR spectrum	96

LIST OF FIGURES

Figure		Page
2-23	Fatigue crack growth rate vs. applied cyclic stress intensity factor for the test of W8R-6 at R = 0.1 together with the linear best-fit results to a Paris equation	97
2-24	Regeneration of the crack extension vs. cyclic count for the test of W8R-6, together with the original test data	98
2-25	Regeneration of the crack extension vs. cyclic count for all the constant amplitude tests conducted in 288°C helium gas, together with the original test data	100
2-26	Cumulative plot of fatigue crack growth rate vs. applied maximum stress intensity factor for all the tests conducted in 288°C helium gas, together with the results of fitting the Walker equation	102
2-27	Regeneration of the crack extension vs. cyclic count for all the constant amplitude tests conducted in 288°C helium gas using the Walker equation, together with the original test data	103
2-28	Schematic of the stress-strain excursion of previously unstrained material near the crack tip during one and one-half fatigue cycles	105
2-29	Schematic and nomenclature of the plastic zones which are necessary to characterize a crack tip in materials subject to overloads and underloads	106
2-30	Analytical results using linear analysis for the crack extension vs. cyclic count for the test of W8R-13	110
2-31	Fatigue crack growth rate vs. applied cyclic stress intensity factor for the tests of W8R-4 and W8R-16 conducted at R = 0.9	112
2-32	Regeneration of the crack extension vs. cyclic count for tests at R = 0.9 of W8R-4 (helium gas) and W8R-16 (PWR water)	113
2-33	Analytical results using linear analysis for the crack extension vs. cyclic count for the PWR environment tests of W8R-17 and W8R-18	114
2-34	Analytical results for the tests of W8R-13 and 1BH-Y2, both conducted with the ICCGR round robin spectrum	116

LIST OF FIGURES

Figure		Page
2-35	Analytical results for the tests of W8R-17 and W8R-18, both conducted in PWR water with the ICCGR round robin spectrum	117
2-36	Photograph of the fatigue surface from the test of specimen code W7-24-10	120
2-37	Crack length vs. cyclic count for the "a" and "c" directions for the test of specimen W7-24-10	121
2-38	Fatigue crack growth rate vs. applied cyclic stress intensity factor for the test of specimen W7-24-10	122
2-39	Fatigue crack growth rate vs. applied cyclic stress intensity factor for the tests of A 533-B steel	123
2-40	Photograph of the fatigue fracture surface from the tests of specimen code XE4S-5	125
2-41	Crack length vs. cylic count for the "a" and "c" directions for the test of specimen XE4S-5	126
2-42	Fatigue crack growth rate vs. applied cyclic stress intensity factor for the test of specimen XE4S-5	127
2-43	Photograph of the fatigue fracture surface from the test of specimen code A 106-R2-B	128
2-44	Crack length vs. cyclic count for the "a" and "c" directions for the test of specimen A 106-R2-B	129
2-45	Fatigue crack growth rate vs. applied cyclic stress intensity factor for the test of specimen A 106-R2-B	130
2-46	Fatigue crack growth rate vs. applied cyclic stress intensity factor for the tests of A 533-B steel from the same plate as specimen A 106-R2-B	131
2-47	Photograph and accompanying schematic of the fatigue fracture surface from the clad specimen test at room temperature	132
2-48	Photograph and accompanying schematic of the fatigue fracture surface from the clad specimen test at 288°C (550°F)	133
2-49	Crack length vs. cyclic count for the "a" and "c" directions for the test of clad specimen XE2-SC4	134

LIST OF FIGURES

Figure		Page
2-50	Crack length vs. cyclic count for the "a" and "c" directions for the test of clad specimen XE2-SC1	135
2-51	Fatigue crack growth rate vs. applied cyclic stress intensity factor for the test of clad specimen XE2-SC4	136
2-52	Fatigue crack growth rate vs. applied cyclic stress intensity for the test of clad specimen XE2-SC1	137
3-1	Plan for Phase 1 investigations (I and IA conditions)	146
3-2	Plan for Phase 2 investigations (two IAR fluence conditions)	146
3-3	Charpy-V notch ductility of submerged-arc welds, code W8A and code W9A before and after irradiation in assembly HTA-1	147
3-4	Charpy-V notch ductility of submerged-arc weld, code WW4, before and after irradiation in assembly HTA-1	148
3-5	Charpy-V notch ductility of submerged-arc weld, code WW7, before and after irradiation in assembly HTA-1	149
3-6	Charpy-V notch ductility of submerged-arc weld, code W8A, before and after irradiation and after postirradiation annealing at 454°C and at 399°C	150
3-7	Charpy-V notch ductility of submerged-arc weld, code W9A, before and after irradiation and after postirradiation annealing at 454°C and at 399°C	151
3-8	Charpy-V notch ductility of submerged-arc weld, code WW4, before and after irradiation and after postirradiation annealing at 454°C and at 399°C	152
3-9	Charpy-V notch ductility of submerged-arc weld, code WW7, before and after irradiation and after postirradiation annealing at 454°C and at 399°C	153
3-10	Charpy-V notch ductility of submerged-arc weld, code W8A and code W9A before and after irradiation to ~ 8 x 10^{19} n/cm^2	154
3-11	Charpy-V notch ductility of submerged-arc weld, code WW4, before and after irradiation to ~ 8 x 10^{18} n/cm^2	155

LIST OF FIGURES

Figure		Page
3-12	Charpy-V notch ductility of submerged-arc weld, code WW7, before and after irradiation to ~ 8 x 10^{18} n/cm^2	156
3-13	Charpy-V notch ductility of submerged-arc weld, code W8A, after reirradiation following a 454°C intermediate anneal and after reirradiation following a 399°C intermediate anneal	157
3-14	Charpy-V notch ductility of submerged-arc weld, code W9A, after reirradiation following a 454°C intermediate anneal and after reirradiation following a 399°C intermediate anneal	158
3-15	Charpy-V notch ductility of submerged-arc weld, code WW4, after reirradiation following a 454°C intermediate anneal and after reirradiation following a 399°C intermediate anneal	159
3-16	Charpy-V notch ductility of submerged-arc weld, code WW7, after reirradiation following a 454°C intermediate anneal and after reirradiation following a 399°C intermediate anneal	160
3-17	Summary of notch ductility changes observed for weld codes W8A, W9A, WW4, and WW7 after irradiation and after postirradiation annealing at 454°C and 399°C	167
3-18	Summary of notch ductility change by second exposure cycle only for weld codes W8A, W9A, WW4, and WW7 with IAR treatment	168
3-19	Summary of total notch ductility change observed for weld codes W8A, W9A, WW4, and WW7 after reirradiation following a 454°C or 399°C anneal	169
3-20	Comparison of transition temperature increases observed for five materials from two separate reactor irradiation experiments	172
3-21	Comparison of transition temperature recovery by postirradiation annealing (399°C-168 h)	173
3-22	Irradiation and postirradiation annealing data for plate 5C obtained from two separate reactor irradiation experiments	174
3-23	Irradiation and postirradiation annealing data for plate 5D obtained from two separate reactor irradiation experiments	175

LIST OF FIGURES

Figure		Page
3-24	Irradiation and postirradiation annealing data for plate 6A obtained from two separate reactor irradiation experiments	176
3-25	Irradiation and postirradiation annealing data for plate 6B obtained from two separate reactor irradiation experiments	177
3-26	Irradiation and postirradiation annealing data for plate 6C obtained from two separate reactor irradiation experiments	178
3-27	Strength properties of plates from a 4-way split laboratory melt of iron with sequential additions of nickel, phosphorus, and copper in unirradiated and irradiated conditions	187
3-28	Strength properties of plates from a 4-way split laboratory melt of iron with sequential additions of copper and nickel in unirradiated and irradiated conditions	188
3-29	Schematic illustration showing the locations of the irradiation facilities used for fluence rate effects qualitication experiments	192
3-30	C_v notch ductility of ASTM A 302-B reference plate after 288°C irradiation at intermediate fluence rate	194
3-31	C_v notch ductility of MEA reference weld (Linde 80 flux) after 288°C irradiation at intermediate fluence rate	195
3-32	C_v notch ductility of ASTM A 302-B reference plate after 288°C irradiation at the high fluence rate	197
3-33	C_v notch ductility of MEA reference weld (Linde 80 flux) after 288°C irradiation at high fluence rate	198
3-34	Comparison of C_v 41-J transition temperature elevations produced by intermediate vs. high fluence rate irradiations of A 302-B plate and Linde 80 weld	199
3-35	Fracture toughness data for the Linde 80 weld code W8A after irradiation in the core-edge facilities	200
3-36	Fracture toughness data for the A 302-B reference plate code 23F after irradiation in the core-edge facilities	201

LIST OF FIGURES

Figure		Page
3-37	Fracture toughness data for the Linde 80 weld code W8A irradiated in the in-core facility	202
3-38	Fracture toughness data for the A 302-B reference plate code 23F irradiated in the in-core facility	203

LIST OF TABLES

Table		Page
1-1	Tensile Properties -- Base Metal	12
1-2	Preliminary ΔT Shift Comparisons of A 302-B and A 533-B Laboratory Melts	19
1-3	Preliminary Comparison of Irradiation-Induced ΔT's From C_v and K_{Jc}	19
1-4	Predictions via Chell Model of k_f at -140°C After Partial Unload	25
1-5	Piping Materials Which Have Been Characterized	35
1-6	Postirradiation Test Matrix	40
1-7	Postirradiation Charpy-V Test Results for KRB-A Vessel Archive Material	44
1-8	Postirradiation 24°C Tensile Test Results for Archive Material GEB (Side 2)	50
2-1	Summary of Completed Testing	60
2-2	Chemical Composition of the Tested Steels	82
2-3	Evaluation of Best-Fit Crack Growth Rate Curves	99
2-4	Conditions for Interaction Effects	108
2-5	Loads for One Block as Applied	109
2-6	da/dN ΔK Table for Water Environment	111
3-1	Submerged-Arc Weld Deposit Materials	145
3-2	Postirradiation 24°C Tensile Test Results for Submerged-Arc Welds	161
3-3	Compositions of Submerged-Arc Weld Deposits	166
3-4	Chemical Compositions of Plates From Laboratory Melts of Steel	171
3-5	Preirradiation Tensile Properties of Test Plates From Melts 5 and 6	179
3-6	Notch Ductility Determinations for A 302-B and A 533-B Plates in Irradiation Assemblies CNI-1, CNI-2, and CEA-2	180
3-7	Matrix For Melting Iron-Binary and Iron-Ternary Alloys	183

LIST OF TABLES

Table		Page
3-8	Chemical Compositions and Heat Treatment of Laboratory-Melted Plates	184
3-9	Composition Type and Ambient Temperature Tensile Strengths of Laboratory-Melted Plates Before and After 550°F Irradiation	186
3-10	Reference Plates and Submerged-Arc Weld Deposits	191
3-11	Irradiation Matrix	193
3-12	Postirradiation Tensile Strengths of A 302-B Plate and Linde 80 Submerged-Arc Weld	204

BLANK PAGE

PREFACE

This program consists of research relating to fracture, fatigue, and radiation sensitivity of nuclear structural steels and weldments and addresses many of the key uncertainties related to life extension of operating nuclear plants. All tasks are integrated to focus on structural integrity of LWR pressure boundary components. The approach centers on an experimental characterization of nuclear-grade steels and an assessment of fracture and environmentally-assisted cracking under conditions of a nuclear environment, so investigation of irradiated materials is a key element of each task. Emphasis is placed on identifying metallurgical factors responsible for radiation embrittlement of steels and on developing procedures for embrittlement relief, including guidelines for radiation-resistant steels. Experimental studies are supported by analytical models and investigations of the mechanisms responsible for the observed behavior. The underlying goal is the interpretation of material properties performance to help establish engineering criteria for structural reliability and long-term operation. Data developed in the program will provide the basis for recommendations for the ASME Boiler and Pressure Vessel Code and ASTM test methods, and revisions to NRC Guides.

The work is being performed by Materials Engineering Associates, Inc. under the direction of F. J. Loss. NRC funding is provided by the Office of Nuclear Regulatory Research, Materials Engineering Branch, A. Taboada, project manager.

Prior progress reports on this program are NUREG/CR-3228, Vols. 1-4.

BLANK PAGE

FOREWORD

The work reported here was performed at Materials Engineering Associates (MEA) under the program Structural Integrity of Water Reactor Pressure Boundary Components, F. J. Loss, Program Manager. The program is sponsored by the Office of Nuclear Regulatory Research of the U. S. Nuclear Regulatory Commission (NRC). The technical monitor for the NRC is Alfred Taboada.

Prior reports under the current contract are listed below:

1. J. R. Hawthorne, "Significance of Nickel and Copper to Radiation Sensitivity and Postirradiation Heat Treatment Recovery of Reactor Vessel Steels," USNRC Report NUREG/CR-2948, Nov. 1982.

2. "Structural Integrity of Water Reactor Pressure Boundary Components, Annual Report for 1982," F. J. Loss, Ed., USNRC Report NUREG/CR-3228, Vol. 1, Apr. 1983.

3. J. R. Hawthorne, "Exploratory Assessment of Postirradiation Heat Treatment Variables in Notch Ductility Recovery of A 533-B Steel," USNRC Report NUREG/CR-3229, Apr. 1983.

4. W. H. Cullen, K. Torronen, and M. Kemppainen, "Effects of Temperature on Fatigue Crack Growth of A 508-2 Steel in LWR Environment," USNRC Report NUREG/CR-3230, Apr. 1983.

5. "Proceedings of the International Atomic Energy Agency Specialists' Meeting on Subcritical Crack Growth," Vols. 1 and 2, W. H. Cullen, Ed., USNRC Conference Proceeding NUREG/CP-0044, May 1983.

6. W. H. Cullen, "Fatigue Crack Growth Rates of A 508-2 Steel in Pressurized, High-Temperature Water," USNRC Report NUREG/CR-3294, June 1983.

7. J. R. Hawthorne, B. H. Menke, and A. L. Hiser, "Notch Ductility and Fracture Toughness Degradation of A 302-B and A 533-B Reference Plates from PSF Simulated Surveillance and Through-Wall Irradiation Capsules," USNRC Report NUREG/CR-3295, Vol. 1, Apr. 1984.

8. J. R. Hawthorne and B. H. Menke, "Postirradiation Notch Ductility and Tensile Strength Determinations for PSF Simulated Surveillance and Through-Wall Specimen Capsules," USNRC Report NUREG/CR-3295, Vol. 2, Apr. 1984.

9. A. L. Hiser and F. J. Loss, "Alternative Procedures for J-R Curve Determination," USNRC Report NUREG/CR-3402, July 1983.

10. A. L. Hiser, F. J. Loss, and B. H. Menke, "J-R Curve Characterization of Irradiated Low Upper Shelf Welds," USNRC Report NUREG/CR-3506, Apr. 1984.

11. W. H. Cullen, R. E. Taylor, K. Torronen, and M. Kemppainen, "The Temperature Dependence of Fatigue Crack Growth Rates of A 351 CF8A Cast Stainless Steel in LWR Environment," USNRC Report NUREG/CR-3546, Apr. 1984.

12. "Structural Integrity of Light Water Reactor Pressure Boundary Components -- Four-Year Plan 1984-1988," F. J. Loss, Ed., USNRC Report NUREG/CR-3788, Sep. 1984.

13. W. H. Cullen and A. L. Hiser, "Behavior of Subcritical and Slow-Stable Crack Growth Following a Postirradiation Thermal Anneal Cycle," USNRC Report NUREG/CR-3833, Aug. 1984.

14. "Structural Integrity of Water Reactor Pressure Boundary Components: Annual Report for 1983," F. J. Loss, Ed., USNRC Report NUREG/CR-3228, Vol. 2, Sept. 1984.

15. W. H. Cullen, "Fatigue Crack Growth Rates of Low-Carbon and Stainless Piping Steels in PWR Environment," USNRC Report NUREG/CR-3945, Feb. 1985.

16. W. H. Cullen, M. Kemppainen, H. Hanninen, and K. Torronen, "The Effects of Sulfur Chemistry and Flow Rate on Fatigue Crack Growth Rates in LWR Environments," USNRC Report NUREG/CR-4121, Feb. 1985.

17. "Structural Integrity of Water Reactor Pressure Boundary Components: Annual Report for 1984," F. J. Loss, Ed., USNRC Report NUREG/CR-3228, Vol. 3, June 1985.

18. A. L. Hiser, "Correlation of C_v and K_{Ic}/K_{Jc} Transition Temperature Increases Due to Irradiation," USNRC Report NUREG/CR-4395, Nov. 1985.

19. W. H. Cullen, G. Gabetta, and H. Hanninen, "A Review of the Models and Mechanisms For Environmentally-Assisted Crack Growth of Pressure Vessel and Piping Steels in PWR Environments," USNRC Report NUREG/CR-4422, Dec. 1985.

20. "Proceedings of the Second International Atomic Energy Agency Specialists' Meeting on Subcritical Crack Growth," W. H. Cullen, Ed., USNRC Conference Proceeding NUREG/CP-0067, Vols. 1 and 2, Apr. 1986.

21. J. R. Hawthorne, "Exploratory Studies of Element Interactions and Composition Dependencies in Radiation Sensitivity Development," USNRC Report NUREG/CR-4437, Nov. 1985.

22. R. B. Stonesifer and E. F. Rybicki, "Development of Models for Warm Prestressing," USNRC Report NUREG/CR-4491, Jan. 1987.

23. E. F. Rybicki and R. B. Stonesifer, "Computational Model for Residual Stresses in a Clad Plate and Clad Fracture Specimens," USNRC Report NUREG/CR-4635, Oct. 1986.

24. D. E. McCabe, "Plan for Experimental Characterization of Vessel Steel After Irradiation," USNRC Report NUREG/CR-4636, Oct. 1986.

25. E. F. Rybicki, J. R. Shadley, and A. S. Sandhu, "Experimental Evaluation of Residual Stresses in a Weld Clad Plate and Clad Test Specimens," USNRC Report NUREG/CR-4646, Oct. 1986.

26. "Structural Integrity of Water Reactor Pressure Boundary Components: Annual Report for 1985," F. J. Loss, Ed., USNRC Report NUREG/CR-3228, Vol. 4, June 1986.

27. G. Gabetta and W. H. Cullen, "Application of a Two-Mechanism Model for Environmentally-Assisted Crack Growth," USNRC Report NUREG/CR-4723, Oct. 1986.

28. W. H. Cullen, "Fatigue Crack Growth Rates in Pressure Vessel and Piping Steels in LWR Environments," USNRC Report NUREG/CR-4724, Mar. 1987.

29. W. H. Cullen, M. E. Mayfield, and M. R. Jolles, "Fatigue Crack Growth of Part-Through Cracks in Pressure Vessel and Piping Steels: Air Environment Results, USNRC Report NUREG/CR-4828 (in publication).

30. D. E. McCabe, "Evaluation of Surface Cracks Embedded in Reactor Vessel Cladding Unirradiated Bend Specimens," USNRC Report NUREG/CR-4841, May 1987.

31. H. Hanninen, M. Vulli, and W. H. Cullen, "Surface Spectroscopy of Pressure Vessel Steel Fatigue Fracture Surface Films Formed in PWR Environments," USNRC Report NUREG/CR-4863 (in publication).

32. A. L. Hiser and G. M. Callahan, "A User's Guide to the NRC's Piping Fracture Mechanics Data Base (PIFRAC)," USNRC Report NUREG/CR-4894, May 1987.

33. "Proceedings of the Second CSNI Workshop on Ductile Fracture Test Methods (Paris, France, April 17-19, 1985)," F. J. Loss, Ed., USNRC Conference Proceeding NUREG/CP-0064, (in publication).

34. W. H. Cullen and D. Broek, "The Effects of Variable Amplitude Loading on A 533-B Steel in High-Temperature Air and Reactor Water Environments," USNRC Report NUREG/CR-4929 (in publication).

BLANK PAGE

ACKNOWLEDGMENT

The continuing support and guidance of A. Taboada and M. Vagins as the NRC project managers for this effort is gratefully acknowledged. The authors acknowledge with appreciation the personal assistance given by J. W. Rogers (EG&G Idaho, Inc.) on matters of neutron dosimetry and spectrum evaluations. We would like to acknowledge June Phillips' efforts in the coordination and preparation of this report.

SUMMARY

1. FRACTURE MECHANICS INVESTIGATIONS

1.1 Fracture Resistance of Irradiated Stainless Steel Clad Vessels

The purpose of this project is to evaluate the severity of surface flaws embedded in the clad layer of reactor pressure vessels during a pressurized thermal shock scenario. The work involves the development of data that is relevant to both unirradiated and irradiated conditions.

The baseline material toughness of the various materials in the region of the clad layer was determined for the unirradiated and irradiated conditions. Tests made on A 533-B base metal and clad-layered bend beam specimens have shown that the cladding process improved the overall toughness performance of the local region over that of the base metal. The principal mechanism was through improved heat-affected zone (HAZ) toughness. The baseline material property tests showed that the HAZ material toughness is strongly reduced by irradiation damage. This means that the irradiated bend beam specimens are expected to be pivotal with respect to the overall safety issue addressed in this study.

1.2 Correlation of Dynamic C_v and Static K_{Ic}/K_{Jc} Tests

Since transition temperature shifts (ΔT) from Charpy-V tests are used to index the critical (K_{Ic}) and reference (K_{IR}) stress intensity factor curves, an assessment of the conservatism, or lack thereof, of such a procedure is required to ensure that adequate safety margins are preserved. This assessment is most important when use of ΔT data from surveillance Charpy-V tests are made to approximate ΔT shifts from fracture toughness tests.

This project has shown that for base metals the fracture toughness transition temperature shift, i.e., $\Delta T(K)$ exceeds $\Delta T(C_v)$ on average, while for weld metals $\Delta T(C_v)$ tends to exceed $\Delta T(K)$. A NUREG report detailing postirradiation characterization results for four plates will be available in 1987.

1.3 Warm Prestress Modeling

The advantage of warm prestress, WPS, is an apparent increase of fracture toughness in the transition region and lower shelf region for ferritic steels after warm preloading in the upper shelf region. The phenomenon can be utilized in safety assessment issues if it can be demonstrated that the effect is both quantifiable and reliable as a

physical property of materials. Analytical models for WPS are being evaluated and refined to suit the conditions relevant to the pressurized thermal shock scenario.

A five-step program with integrated analysis and experimental interaction was started to evaluate WPS effects at K_{wps} levels typical of the pressurized thermal shock scenario. The available analytical models have been used to predict WPS effects on thermomechanical cycles that include both complete unloading and partial unloading during cool down to the instability condition. The analytical models have been shown to predict significant differences. The experimental/analytical refinement work is currently in progress. The experiments have shown strong WPS effects.

1.4 Irradiation-Induced K_{Ic} Curve Shift (HSST 5th Irradiation)

The K_{Ic} fracture toughness transition curve characterization for irradiated RPV steels is based on a temperature transposition of the K_{Ic} curve for unirradiated steel. The magnitude of this transposition is obtained from Charpy-V tests of irradiated vs. unirradiated steel. Hence, it is assumed that the K_{Ic} curve shape given in Section XI of the ASME Boiler and Pressure Vessel Code is unchanged after irradiation and that the magnitude of shift is the same as Charpy-V despite the significant geometry and strain-rate differences between the two test methods. The purpose of this 5th Irradiation Program in the Heavy Section Steel Technology Series has been to evaluate the appropriateness of the above assumption. The test material is A 533-B weld metal having two copper impurity levels (0.2% and 0.3%).

This is a cooperative program between ORNL and MEA. Both laboratories have completed the testing of unirradiated compact specimens for K_{Ic}/K_{Jc} (1T-, 2T-, 4T-, 6T-, and 8T-CT sizes), Charpy-V, and drop weight-NDT tests. Irradiated Charpy-V and NDT tests have also been completed at both laboratories. MEA has completed the testing of irradiated 1T- and 2T-compact specimens. The current evidence suggests that the irradiated curve shift of K_{Ic} at the 100 MPa$\sqrt{m}$ level is almost identical to the 41-J Charpy-V shift. The NDT shift is also reasonably consistent with this, but this was less clear cut because of some difficulty in interlaboratory reproducibility. Irradiated 4T-CT tests and more unirradiated 8T-CT tests remain for MEA. ORNL has additional irradiated 1T- and 2T-compact specimens to test.

1.5 Piping Fracture Mechanics Data Base

The Piping Fracture Mechanics Data Base task has been established to develop a comprehensive, computerized data base of fracture toughness (J-R curve) and other support data from nuclear piping steels. In 1986, the data base was placed "on-line." A "user's guide" to the system has just been completed and should be available soon.

The payoff from this task will be easy access for the NRC and others to the available piping data, as they need the data in analyses of known or postulated flaw and loading conditions.

Thus far, 14 piping lots have been characterized, including some aged cast stainless, several A 106 B melts, wrought stainless, and a heat of Inconel. Materials to be characterized in 1987 include A 516 Gr. 70 base and welds, two melts of Type 347 stainless and welds, and several carbon-stainless welds. Several reports summarizing the characterization results will be prepared in NUREG form in 1987.

1.6 Gundremmingen RPV Material Characterization

The 250-MW boiling water Gundremmingen reactor, KRB-A, has been decommissioned by the Federal Republic of Germany. The reactor vessel operated at ~ 288°C; the inner wall fluence estimate at the time of decommissioning was about 1×10^{19} n/cm^2, E > 1 MeV. A joint USA-FRG study, conceived by the NRC, is underway to evaluate material removed from the vessel for a critical assessment of power vs. test reactor environment effects. MEA and Staatliche Materialpruefungsanstalt (MPA) are responsible for experimental phases of the joint USA-FRG program.

MEA's responsibilities include determination of fracture resistance properties' changes produced by a test reactor irradiation environment at a fluence matching that of the material trepanned from the vessel. Additionally, determinations of embrittlement relief by post-irradiation heat treatment (annealing) are included in the workscope. MEA has acquired a welded forging segment believed to be leftover (archive) material from the KRB-A vessel fabrication. Forging characterization tests conducted in 1985 (program phase 1) included composition, microstructure, and mechanical properties tests. The results indicate a high probability that the archive material and the vessel material were from the same steel melt and that the archive material is representative of the vessel belt-line forging, no. 7.1, as first placed in service.

In 1986, MEA completed the characterization of the through-thickness properties of one of the base metals of the welded forging segment and proceeded to the irradiation phase of the studies. Charpy-V (C_v), tensile, and 0.5T-CT specimens of this archive material were exposed in the light-water-cooled UBR reactor at 288°C to about 8×10^{18} n/cm^2, E > 1 MeV (0.014 dpa). Samples were tested in the as-irradiated condition, the 399°C-168 h annealing condition, and in the 454°C-168 h annealed condition. A postirradiation 44°C elevation in 41-J temperature and a 16% elevation in yield strength were observed. The elevation in 100 MPa$\sqrt{m}$ temperature found with 0.5T-CT specimen tests matched well the elevation in 41-J temperature. Furthermore, the latter was predicted well by Regulatory Guide 1.99 Rev. 2.

A technical surprise was found on comparing the cited UBR data against the MPA data for the trepans. The trepans showed more embrittlement than the archive material irradiated to a higher fluence in the UBR (CL test orientation). Also, MPA observed a major difference in radiation sensitivity between CL (high) and LC (low) test orientations. If confirmed, the difference will have major impact on the application of R.G. 1.99 which has made extensive use of strong test orientation data, especially in its method of upper shelf analysis.

MEA also performed dosimetry tests on a through-thickness slice of trepan material. The results show the vessel fluence to be much lower than FRG projections made at the time of vessel decommissioning. As a result, NRC and MEA are considering additional UBR irradiations for more precise dose rate effect assessments.

2. ENVIRONMENTALLY-ASSISTED CRACK GROWTH IN LWR MATERIALS

2.1 Environmental Degradation of Fatigue Life

This research effort is aimed at defining the effect of a simulated PWR environment on the fatigue life of typical LWR materials and weldments. If a detrimental effect of the water environment is established, this task will provide the basis for recommended modification to stress-life curves in Section III of the ASME Boiler and Pressure Vessel Code. The approach involves testing of round bar specimens obtained from A 106-B pipe; specimens are also taken across a girth-butt weld between two sections of the same material. Welded pipe specimens fabricated by welding together two sections of 102-mm (4-in.) Schedule 80 A 106-B pipe will also be tested.

The fatigue-life testing of both smooth and notched (K_t = 2, 3, and 6) bar base metal specimens in 288°C air were completed. The presence of a notch produced a detrimental effect on fatigue life as expected. The testing of smooth and notched (K_t = 6) bar specimens in a PWR environment was initiated. The frequency sensitivity study is still in progress at this time, but it appears that a frequency of 1 Hz may prove to be the most detrimental frequency in a PWR environment with respect to crack initiation. All 24 of the girth-butt welded 102-mm (4-in.) pipe specimens have been fabricated and should be tested in 1987. Improvements in the S-N fatigue testing system have broadened the possible range of testing.

2.2 Mechanisms and Models for Environmentally-Assisted Fatigue Crack Growth

Understanding the mechanisms which are responsible for environmentally-assisted cracking in high-temperature water would greatly assist researchers interpret test results and plan critical tests. Development of a calculational model based on this mechanism would provide a way of calculating environmentally-assisted crack extension rates which could be plant specific and account for the long-term effects which cannot be measured in real-time within the laboratory situation. Strides in both directions were made during 1986. A NUREG describing a time-based, two-mechanism calculational model which reconciled a significant portion of the MEA constant amplitude fatigue crack growth rate data was published. Data sets for tests with various load ratios, test temperatures, and cyclic frequencies can be included within the framework of the model. In order to help clarify the mechanisms which are involved in the fatigue crack growth process, a NUREG report on the examination of contaminent elements in the fracture surface oxides was issued. Auger Electron Spectroscopy and X-ray Photoelectron Spectroscopy were used in this examination. This report showed that a connection between crack growth rate and sulfur species included in the oxide layer did not always exist, even though crack growth rates increase with sulfur content in the steel. Spectroscopic evidence of chlorine, boron, and carbon content in the oxide layer was also evaluated. In order to

evaluate the cracking modes of the cyclically plasticized material at the tip of an environmentally-assisted fatigue crack, constant extension rate experiments have been planned using prefatigued carbon piping steel in simulated crack-tip environments which are high in dissolved manganese sulfide content. A test facility has been constructed, and specimen testing will be conducted during 1987.

2.3 Cumulative Damage Factor for Environmentally-Assisted Fatigue Crack Growth

Appendix A of Section XI of the ASME Boiler and Pressure Vessel Code contains fatigue crack growth rate reference lines which are based on constant amplitude test data and a linear summation rule for growth rate calculations based on the applied cyclic stress intensity factor, ΔK, for each cycle. Therefore, load interactions which may cause accelerations in the overall crack extension are not accounted for by the Code rules. Research completed in 1986 shows that significant accelerations can occur, and the ASME-code based calculations may be nonconservative, at least for the subsurface flaw case. While cycling about a high mean load, the accelerations are caused principally by downloading to a relatively small load and then reloading to the mean load and resuming the cycling again. Data sets for tests with simple and complex underloads and overloads have been used to refine and calibrate a calculational model which allows evaluation of crack growth rates for (at present) simplified reactor-typical load-time histories. Test results and modeling evaluations have been completed for both high-temperature air and water environments. For the waveforms, frequencies, test loads, and A 533-B steel investigated to date, there is little difference between air and water environment results, and little frequency sensitivity in water environments. Additional tests are to be conducted throughout 1987.

2.4 Evaluation of the Effects of Environment and Cladding on the Growth of Surface Flaws

The fatigue crack growth rate testing on pressure vessel and piping steels has been carried out largely with the use of compact fracture (CT) specimens. The ASME Code Section XI Appendix A reference lines are based exclusively on CT specimen results. However, naturally occurring surface flaws are more closely approximated by a laboratory specimen which is a relatively large panel with a semi-elliptical, part-through crack (PTC). Tests have been conducted on similar materials in high-temperature air environments using both types of specimens, and a report has been written comparing the results. Testing in high-temperature water environments is underway currently. The report describes the development and calibration of a direct current potential drop system to monitor the crack extension. The results show that growth rates for the PTC specimen in an air environment are nearly identical to growth rates from CT specimens. Some of the tests are conducted using panel specimens clad with stainless steel. For

these specimens, crack extension along the surface, at room temperature, is higher than at 288°C by about a factor of two. The crack growth was not rigorously self-similar, but a linear correction was used which seems to be sufficiently accurate for the amounts of crack extension allowed by this specimen.

3. RADIATION SENSITIVITY AND POSTIRRADIATION PROPERTIES RECOVERY

3.1 Effect of Temperature on Annealing for Alleviating Radiation-Induced Embrittlement

The study of irradiation-annealing and irradiation-annealing-reirradiation behavior of four radiation-sensitive weld metals was initiated to resolve three issues: firstly, the difference between (and the variability of) 454°C vs. 399°C annealing recovery in submerged-arc weld metals typical of early vessel fabrication; secondly, reembrittlement trends and rates following 454°C vs. 399°C annealing; and lastly, the significance of material type and fabrication history to the recovery obtainable and to reirradiation behavior. Progress in 1985 included the fabrication of a high copper, low nickel, thick-section weld required to complete the material matrix consisting of four generic types of welds found in early vessels. Each of the welds now in hand has a high copper content or an intermediate copper content synonomous with high radiation sensitivity. Nickel content and welding flux types depict the range of these variables found in early weld fabrication.

In 1986, Irradiation (I), Irradiation-Anneal (IA) and initial Reirradiation (IAR) tests of the four welds were completed. The first cycle fluence was about 1.2×10^{19} n/cm^2; the reirradiation fluence was about 0.3×10^{19} n/cm^2. All irradiations were at 288°C. A key determination from the 454°C vs. 399°C postirradiation annealing studies is that C_v 41-J transition temperature recovery may or may not be significantly greater with a 454°C anneal. However, reembrittlement of the welds was significantly less after a 454°C anneal compared to a 399°C anneal. In turn, the benefit of IAR procedures appears to be greatest with the higher temperature anneal.

The findings indicate that, properly applied, IAR procedures may be a means of avoiding PTS concerns and for overall plant-life extension. MEA experiment assemblies now irradiated but untested are designed to explore radiation embrittlement saturation tendencies by IAR-treated welds at high fluences.

3.2 Influence of Steel Composition on Embrittlement Relief by Post-irradiation Heat Treatment

Metallurgical influences on the annealing process have not been investigated in detail but obviously form a prerequisite to NRC's weighing of annealing as a means for plant-life extension. In 1984, MEA initiated investigations to systematically explore composition effects on notch ductility recovery and the extent of residual embrittlement after an anneal. Test materials include ten plates from laboratory melts having statistical variations in copper, nickel, and phosphorus content. The plates were irradiated at 288°C to $\sim 2 \times 10^{19}$ n/cm^2, E > 1 MeV and then annealed at 399°C for 168 h. Annealing recovery was to be judged from both transition temperature behavior and upper shelf energy behavior.

In 1985, evaluations were completed on the materials group depicting high vs. low copper contents and high vs. intermediate vs. low phosphorus contents. The data clearly revealed that copper but not phosphorus has a detrimental effect on notch ductility recovery by the annealing method. Full recovery was observed in plates having a low copper content, irrespective of the phosphorus content. The results confirmed initial NRC/MEA suspicions that composition must be treated as a potentially critical variable influencing both recovery and the degree of residual embrittlement after the anneal.

The second group of materials in the experiment matrix was evaluated after postirradiation annealing in 1986. A composition including 0.68% Ni (with a high copper content) is shown to exert a detrimental effect on notch ductility recovery. On the other hand, no significant effect of nickel content on recovery was found for the range of 0.005% to 0.27% Ni. Accordingly, nickel content has a capability for influencing the annealing response of A 533-B steel (> 0.4% Ni) but not A 302-B steel (< 0.4% Ni). Additionally, the results for the current group of materials support the 1985 determination on the influence of copper on annealing recovery.

3.3 Mechanisms of Irradiation Damage for Reactor Vessel Steels

The study on irradiation effects mechanisms in reactor pressure vessel materials was initiated by MEA in FY 85, with the aims of confirming the basic mechanism for the copper content contribution to radiation sensitivity, defining the mechanism by which nickel alloy reinforces the copper content contribution, and isolating the mechanism for the independent contribution of phosphorus to radiation sensitivity development. Since then, the study has been expanded to include a fourth objective: the development of a mechanisms explanation for the inverse dependence of the phosphorus contribution on copper content revealed by recent MEA investigations.

Primary research materials are low alloy steels from split laboratory-melts previously irradiated by MEA for composition effects determinations. In 1985, MEA produced two special (4-way split) melts of iron binary and iron ternary alloys for inclusion in the program. The alloys represent statistical combinations of copper, phosphorus, and nickel.

In 1986, an experiment assembly containing mechanical and microscopy test samples of the plates from the new melts were irradiated to about 4.5×10^{19} n/cm^2, E > 1 MeV at 288°C. Postirradiation tensile tests by MEA proved highly significant: the results refute earlier reports that phosphorus does not enhance the yield strength elevation by irradiation. Specifically, high phosphorus (0.025% P) material compared to low (0.001% P) material from the same split melt exhibited a major yield strength sensitivity to irradiation. The increase in strength was about 75% of the increase in strength of a 0.3% copper content material from the companion melt.

One MEA subcontractor (University of Florida) obtained evidence that the phosphorus mechanism is not due to radiation-enhanced diffusion to prior austenite grain boundaries in the manner of temper embrittlement. This and other determinations by the University of Florida make phosphorus precipitation in the matrix highly suspect. FIM examinations to verify this projection were undertaken by late 1986.

Another MEA subcontractor (GKSS at Geesthacht, FRG) is performing small angle neutron scattering analysis (SANS) on the same MEA materials. With increasing phosphorus content, the high copper materials show an increase in the number density of defects consistent with MEA findings on tensile strength change by irradiation in high vs. low phosphorus materials.

Further examination of the steel and iron alloys, using positron annihilation (PA) techniques, is underway at VTT (Helsinki, Finland) as part of a cooperative VTT-MEA program. Initial results will be reported in early 1987.

3.4 Investigation of Long-Term vs. Short-Term Irradiation Effects on Reactor Vessel Steels

The significance of high vs. low neutron exposure rates to the magnitude of mechanical properties changes by a given fluence at 288°C is being investigated experimentally. The tests are designed to resolve the base issue of the level of representation afforded by test reactor irradiation assessment of materials to the power reactor service case.

Radiation exposures were undertaken in 1983 in facilities of a water-cooled test reactor (UBR) where irradiation temperature conditions can be closely controlled and monitored. Notch ductility, fracture toughness, and tensile tests of four reference materials (two plates, two weld deposits) are being exposed to fluxes of 7-8 x 10^{10}, 4-5 x 10^{11}, and 7-8 x 10^{12} n/cm^2-s^{-1} and to fluences as high as 2 x 10^{19} n/cm^2.

In 1986, reactor exposures to all but 4 of the 18 capsules forming the irradiation matrix were completed. Further, postirradiation tests were completed for all capsules irradiated at 5-6 x 10^{11} n/cm^2-s^{-1} (intermediate flux) and two of the six capsules irradiated at 8-9 x 10^{12} n/cm^2-s^{-1} (high flux). The materials in the cited capsules are the ASTM A 302-B reference plate and a high copper content, Linde 80 submerged-arc weld.

The data on relative notch ductility and tensile strength change describe a dose rate effect which may extend to power reactor surveillance as well as test reactor facilities now in use. A different embrittlement sensitivity vs. exposure rate relationship was observed for plate compared to weld deposit. Observed differences in property change attributable to an intermediate vs. high fluence rate are not considered large but could influence data interpretation within the framework of NRC Regulatory Guide 1.99.

STRUCTURAL INTEGRITY OF WATER REACTOR PRESSURE BOUNDARY COMPONENTS ANNUAL REPORT FOR 1986

1. FRACTURE MECHANICS INVESTIGATIONS

1.1 Fracture Resistance of Irradiated Stainless Steel Clad Vessels

D. E. McCabe

1.1.1 Background

Operating experience with nuclear power plants has led to the recognition that repressurization during a postulated thermal shock event is a possibility (Ref. 1). This has led to a reassessment by the NRC of the various conceivable accident scenarios. One of the outcomes was the recognition that a small flaw embedded in the stainless steel clad layer in the reactor pressure vessel could become critical at some point during a minor mishap such as a steamline break or control malfunction. It has not been clearly established at this point, however, if the material toughness vs. the stress and temperature conditions within this local region would be critical. The bimetal interfacial region is a complex combination of material toughness variations plus primary stress with superimposed residual stress that requires detailed study.

This research task is designed to evaluate quantitatively the severity of crack initiation from a surface flaw in a clad layer of RPV steel in the irradiated condition. The task will develop data that can be used in assessing the role played by cladding in either enhancing or mitigating crack initiation in a postulated PTS scenario. The complete background information on the steel was reported in the 1984 annual report (Ref. 2). Baseline behavior for similar flaws in irradiated base metal will be used for comparison. Clad material was prepared for this study using a three-wire process typical of older vessel construction.

1.1.2 Summary of Results

Tensile tests were made on the A 533-B base metal in unirradiated and irradiated conditions and the results are given in Table 1-1.

Table 1-1 Tensile Properties -- A 533-B Base Metal

Condition	Temp. (°C)	Yield Strength (MPa)	Tensile Strength (MPa)	Elongation (%)	Reduction in Area (%)
Unirradiated	24	398	584	35.9	70
Irradiated	29	586	738	13.5	--

The fracture toughness of the materials local to the clad layer had been determined using subthickness 0.5T-compact specimens. All were nominally 5-mm thick. Their location and orientation is indicated in Fig. 1-1. The clad metal had ductile tearing characteristics at test temperatures between +100°C and -150°C. However, the R-curve growth resistance slope was extremely low for an austenitic stainless steel. Base metal and HAZ material showed the usual transition temperature characteristics with K_{Jc} crack instability behavior between -100°C and +100°C. This is shown in Fig. 1-2 along with the onset of stable growth K values for stainless clad specimens. Of interest is the evidence that the transition temperature of HAZ material is lower than that of the virgin base metal. Some 20% side-grooved 1T-compact specimens of base metal had been tested previously, giving the solid line shown. K_{Jc} data obtained from the 0.5T-compact specimens seem to indicate the same transition temperature, viz., no specimen size effect is evident.

Beams loaded in four-point bending were used to evaluate surface cracks in clad layered material (Fig. 1-3). There were two levels of surface crack size: 5-mm deep (0.2 in.), where the crack was entirely embedded in clad metal, and 10-mm deep (0.4 in.), where the flaw penetrates into the heat-affected zone. The testing was performed over a transition temperature range and K_{Jc} values were defined for the onset of crack instability. Because there always was extensive plastic deformation in the beam prior to crack instability, elastic-plastic computational practices were applied. Figure 1-4 summarizes all of the clad specimen results. A general observation about the effect of cladding is that the fracture toughness performance is improved over that of base metal. Note, however, that in this particular case the HAZ material had low transition temperature and that the clad K_{Jc} data tended toward the HAZ transition curve, as if it were the controlling metallurgical zone. This has led to the working hypothesis that the HAZ fracture toughness is the dominant property affecting the overall performance of the composite with respect to crack initiation. Specimens with 5-mm flaws were shown to develop slow-stable crack growth that propagated to the HAZ material where K_{Jc}-type crack instability occurred. Applied K_I during crack propagation and at instability is derived from total crack dimensions, essentially independent of the variability in properties of the

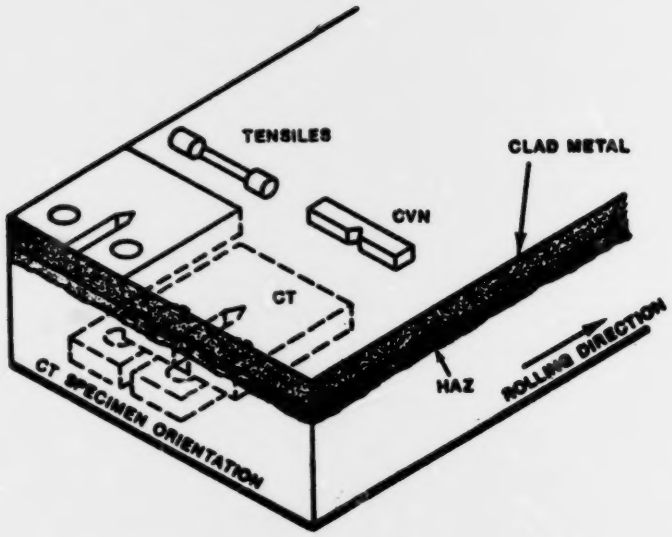

Fig. 1-1 Schematic representation of the specimen sampling for baseline material characterization.

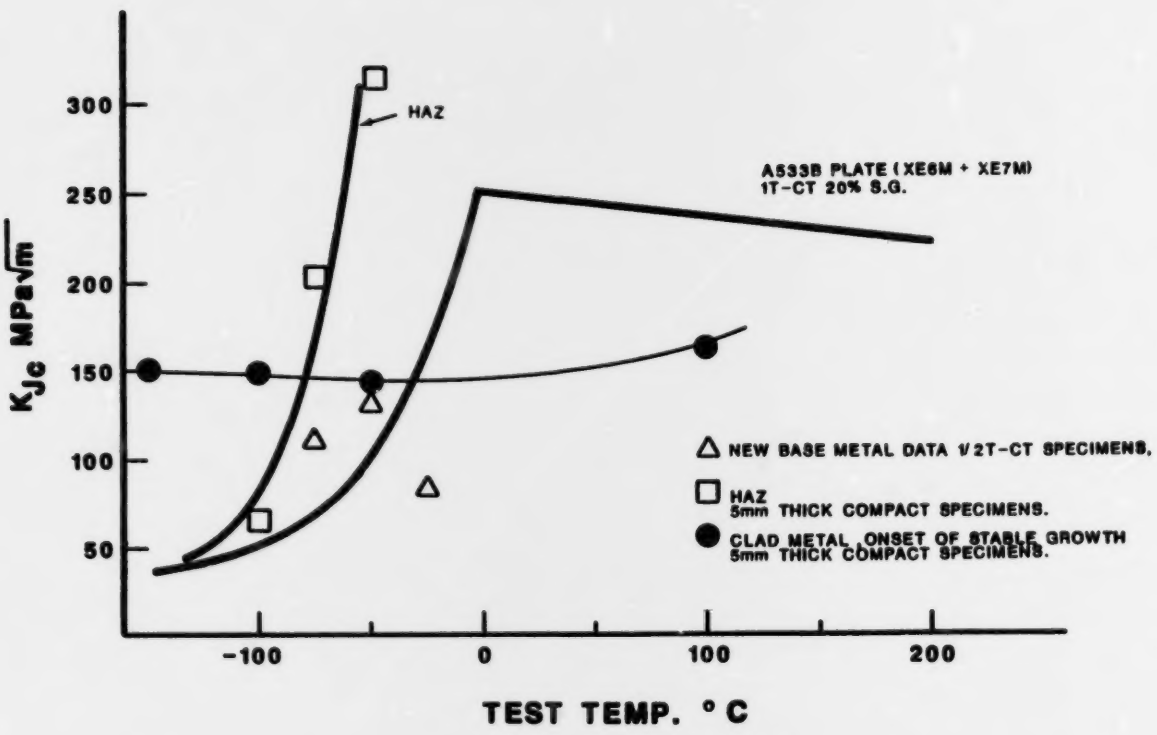

Fig. 1-2 Transition temperature characteristics of base metal, heat-affected zone, and clad metal as determined from compact specimens.

BEST COPY AVAILABLE

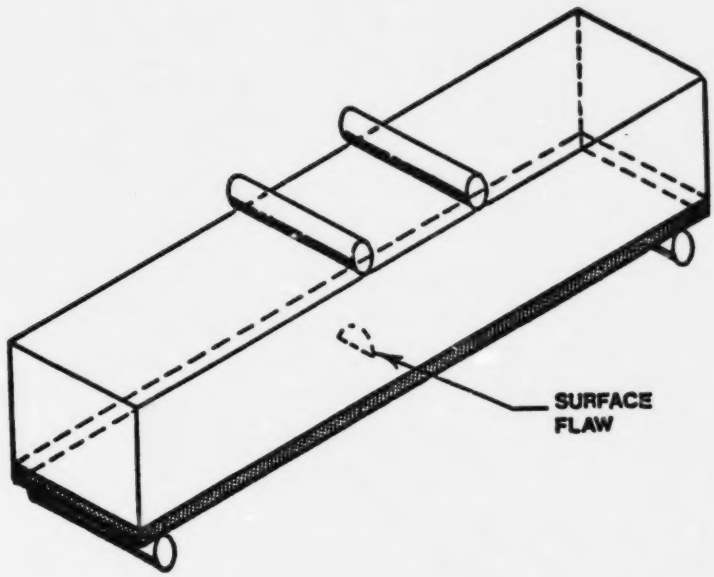

Fig. 1-3 Four-point loaded bend beam.

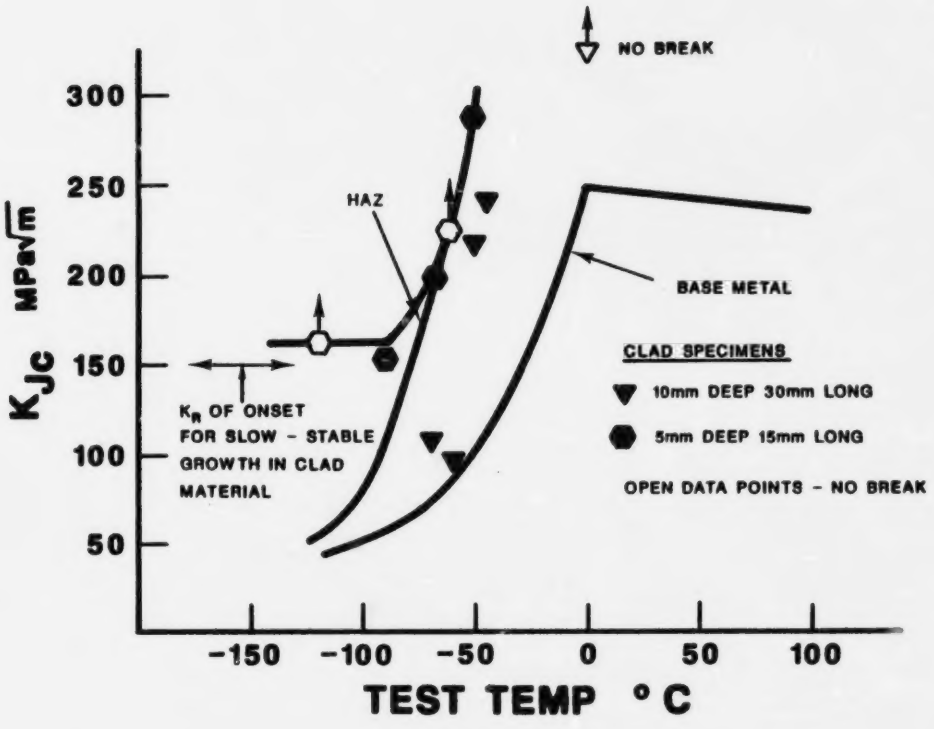

Fig. 1-4 K_{Jc} data on clad bend beam specimens with surface cracks. Solid lines are from compact specimen tests.

BEST COPY AVAILABLE

different materials involved. The low slow-stable crack growth resistance of clad material is the more serious damaging feature of clad layering of pressure vessel walls.

The A 533-B base metal was also tested with 5-mm and 10-mm deep flaws to provide baseline information for comparison or evaluation of the cladding data and to evaluate the various surface crack analysis schemes. Figure 1-5 shows the K_{Jc} transition temperature data. The elastic-plastic analysis schemes applied to bend beams with 10-mm deep flaws produced the same transition temperature trend as the 1T- and 0.5T-compact specimen data. The specimens with 5-mm deep flaws had considerably reduced transition temperature, presumably from signficantly reduced constraint. These same small flaws also created problems in the elastic-plastic analysis schemes which could not be resolved in this particular project because the needed calibration work was not within the scope. One base metal specimen with a 10-mm deep flaw had been tested at an upper shelf temperature, and there had been some slow-stable growth up to the point where the test had been stopped (Fig. 1-6). The amount of growth seen was consistent with that seen in compact specimens at the same K_R level.

The testing of unirradiated specimens is complete, and the test temperatures used to develop K_{Jc} transition behavior, -50°C to -100°C, indicate that unstable running cracks will not be initiated in the clad layer of unirradiated reactor pressure vessels during a pressurized thermal shock scenario. Baseline data that are presently being acquired on irradiated materials suggest a strong transition temperature shift that should make the tests on irradiated bend beam specimens have greater relevance to the pressurized thermal shock licensing issue.

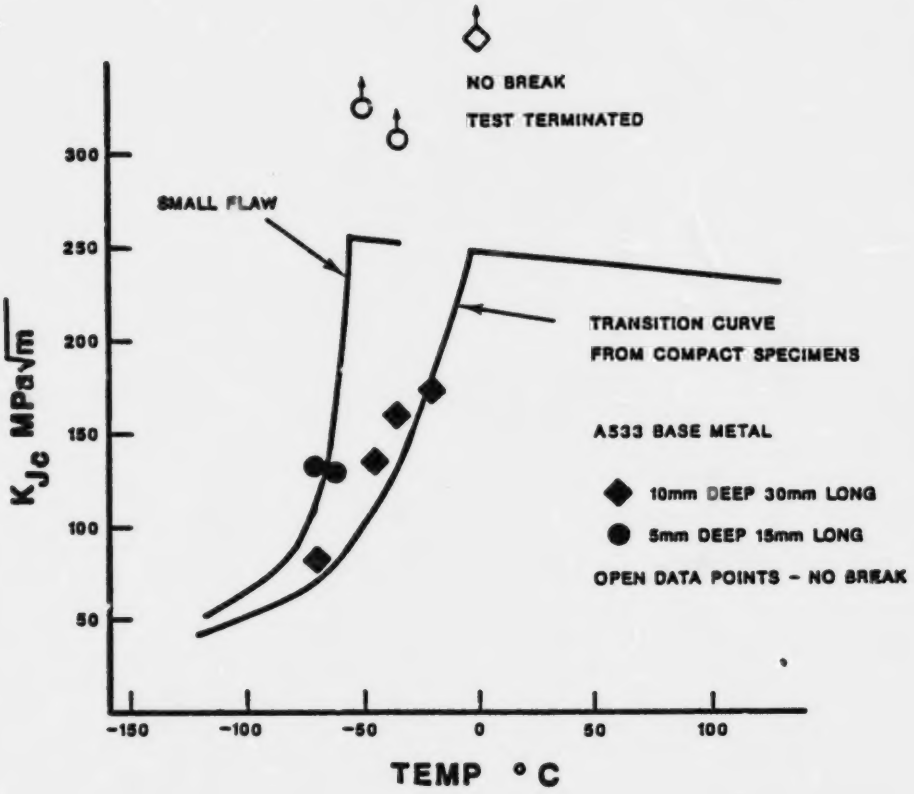

Fig. 1-5 K_{Jc} data on base metal bend beam specimens with surface cracks. Solid lines are from compact specimens.

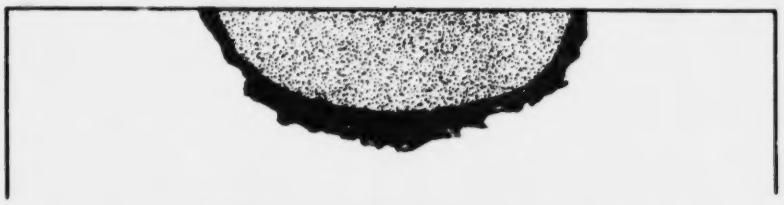

Fig. 1-6 Crack growth in base metal at upper shelf temperature.

BEST COPY AVAILABLE

1.2 Correlation of Dynamic C_v and Static K_{Ic}/K_{Jc} Tests

A. L. Hiser

1.2.1 Background

Appendix G of 10CFR50 (Title 10, Part 50 of the Code of Federal Regulations) places lower limits on the temperature at which the reactor pressure vessel (RPV) can be pressurized to certain levels. To guard against LEFM failure of the RPV materials, the temperature limits are stated as a function of the reference temperature, RT_{NDT}, as defined in the ASME code. RT_{NDT} is also used in an analytical sense to index the K_{IR} (reference stress intensity factor curve). Prior to operation of the RPV, determination of RT_{NDT} is a relatively simple task, involving tests of Drop Weight-NDT and Charpy-V notch (C_v) specimens. RT_{NDT} is defined in the ASME code as the greater of T_{NDT} ("at or above the nil-ductility transition temperature by Drop Weight tests") and T_{Cv}-60°F, where T_{Cv} is the index at which each C_v test "shall exhibit at least 35 mils lateral expansion and not less than 50 ft-lb absorbed energy." During operation, the toughness is reduced by neutron irradiation. One manifestation of the toughness degradation is an increase in the temperature at which C_v specimens will exhibit certain energy levels within the brittle-to-ductile transition region. This increase in temperature must be accounted for in determining the reference temperature of the irradiated RPV material. Indeed, Appendix G of 10CFR50 states that "'Adjusted reference temperature' means the reference temperature as adjusted for irradiation effects by adding to RT_{NDT} the temperature shift, measured at the 41 J (30 ft-lb) level, in the average Charpy curve for the irradiated material relative to that for the unirradiated material." Since the stress intensity curve (K_I) is then indexed at this adjusted reference temperature, one must know that the C_v shift at 41 J is an accurate or conservative estimation of the shift in the critical stress intensity factor curve (K_{Ic} curve) to ensure that overestimation of the material toughness does not occur.

Obviously, estimation of the material fracture toughness (K) behavior using an indexed curve plus an estimated temperature shift does not provide accurate information in every case. The best circumstances would be to have actual irradiated and unirradiated fracture toughness data to use in any analyses. Since actual data generally are not available, assurance that the actual behavior is conservatively predicted by the estimated curve (i.e., indexed curve with a conservative estimation of the temperature shift) is sufficient justification for use of the estimated curves.

The objective of this subtask is to investigate the transition temperature shifts (ΔT) provided by C_v (ΔT_{Cv}) and fracture toughness (ΔT_K) testing. This investigation will provide assurance that $\Delta T_{Cv} > \Delta T_K$, or if that condition does not hold, will provide recommendations on ways to convert ΔT_{Cv} to a value consistent with ΔT_K.

1.2.2 Summary of Results

To assess this behavior, comparison of ΔT values defined by elastic-plastic fracture toughness and C_v tests have been made using data from RPV weld and base metal in which irradiations were made under test reactor conditions (Ref. 3). These comparisons represent the first systematic consideration of the ΔT from C_v and ΔT from fracture toughness relationship. Using "as-measured" fracture toughness values (K_{Jc}), $\Delta T(K_{Jc}$ @ 100 MPa$\sqrt{m})$ tends to be less than $\Delta T(C_v$ @ 41 J) for weld metals but greater than $\Delta T(C_v$ @ 41 J) for base metals. This trend is also followed when the fracture toughness data are adjusted using the β_{Ic}-correction suggested by Merkle (Ref. 4).

To assess chemical composition effects on transition temperature response, four plates have been characterized in the pre- and post-irradiation conditions using Charpy-V, tensile, and compact tension (for fracture toughness) specimens. The fracture toughness tests were performed at quasi-static and rapid-loading conditions using unirradiated material, while irradiated specimens were tested using only quasi-static loading conditions. All of the fracture toughness test data were evaluated using the K_{Jc} approach outlined in Reference 3.

As given in Table 1-2, the four plates used represent significant variations in copper, nickel, and phosphorus contents, with moderate to high irradiation sensitivity expected. Table 1-2 also gives preliminary evaluations of ΔT's for the fracture toughness data, as evaluated at the 100 MPa$\sqrt{m}$ level. As expected, the greatest irradiation-induced shift ("U → I" in the table) is for the high Cu, high Ni, high P heat, followed by the high Cu, high Ni, low P heat, and the high Cu, low Ni, and low P heat. The "copper" effect is clearly demonstrated, as the low copper heat requires elevations in Ni and P to attain the same embrittlement as the high Cu, low Ni, and low P heat. The effect of rapid loading on the 100 MPa$\sqrt{m}$ level temperature ("Static → Dynamic" in the table) is consistent despite the chemical composition differences, although increased levels of Cu, Ni, and P all appear to successively decrease the ΔT for the rapid loading condition. However, neither element tends to be dominant in terms of its effect on the dynamic-loading-induced ΔT.

Preliminary comparison of irradiation-induced ΔT's from C_v and K_{Jc} are listed in Table 1-3. In each case, $\Delta T(K_{Jc})$ exceeds $\Delta T(C_v)$, with the relative level of $\Delta T(C_v)$ for each heat consistent with the K_{Jc} results. For these heats, the average underestimate of $\Delta T(K_{Jc})$ by $\Delta T(C_v)$ is 9°C, much less than the average of 22°C found previously in Reference 3.

A NUREG report summarizing these results will be available in 1987.

Table 1-2 Preliminary ΔT Shift Comparisons of A 302-B and A 533-B Laboratory Melts (ΔT (K_{Jc}) @ 100 MPa$\sqrt{m}$)

Code	Static → Dynamic	U → I	Composition		
			Cu	Ni	P
	(°C)	(°C)			
6A2	44	83	0.28	0.045	0.002
67C	35	81	0.002	0.70	0.025
68C	29	159	0.30	0.70	0.028
68A	36	140	0.30	0.70	0.003

Table 1-3 Preliminary Comparison of Irradiation-Induced ΔT's from C_v and K_{Jc}

Code	$\Delta T(C_v)$ (°C)	$\Delta T(K_{Jc})$ (°C)	$\Delta T(K_{Jc})/\Delta T(C_v)$
6A2	74	83	1.12
67C	69	81	1.17
68C	146	159	1.09
68A	137	140	1.02

1.3 Warm Prestress Modeling

D. E. McCabe

1.3.1 Background

The phenomenon of warm prestress (WPS) and its effect on the apparent fracture toughness enhancement of steel has been known and demonstrated experimentally for more than 20 years. If this phenomenon could be utilized for analysis of loss-of-coolant situations in PWR reactors, it would represent a clear advance in efficient and safe use of current operating units.

The WPS enhancement results from an apparent increase in fracture toughness at low temperature after a preload of the crack at upper shelf temperature where the material is ductile. The mechanism has been attributed to material work hardening, residual stresses, and/or crack-tip blunting from a prior plastic-zone development. The effectiveness of the mechanism has been found to depend upon the load-temperature path between the warm prestress load and the low temperature condition. A model of the WPS phenomenon is required before credit can be taken for improved low temperature toughness in plant-specific accident scenarios. A specific objective of this task is to model the crack tip under reloading after WPS to simulate a pressurized thermal shock (PTS) event.

The initial objective of this project was to evaluate some features of the available mathematical models used to predict WPS effects. Finite-element analysis was used to study the characteristics of each. A further objective was to arrive at a representative finite-element based model to predict WPS results. This could then be incorporated into computer codes for LOCA and PTS scenarios. A recommendation for a future course of action could then be developed.

The available models to be evaluated were Chell (J_e) (Ref. 5), Curry (Critical Stress) (Ref. 6), Atluri (T_p^*) (Ref. 7), conventional crack-tip opening displacement (CTOD), and differential CTOD (dCTOD), a proposal introduced in the present program. The Chell criterion is based on plastic-zone estimates (Dugdale type); the Curry model is for critical-cleavage stress at a fixed distance within the plastic zone. The Atluri T_p^* parameter is a line-integral calculation determined in a similar manner to J integral except that it is made in a region local to the crack tip. The tip-opening displacement model (CTOD) is self-explanatory, and dCTOD is a measure of the change of CTOD from the point of the last load reversal.

1.3.2 Summary of Results

The phase of study related to analytical model evaluation has been completed and reported in Reference 8. A second phase recently initiated involves a combined analytical/experimental study to develop the usefulness of the analytical models for the pressurized thermal shock scenario. A six-task program was set up for model development,

progressing from the simple "load-unload-cool-fracture" (LUCF) cycle into partial unloadings such as might be involved in pressurized thermal shock scenarios. The following lists the objectives and progress made within each task.

Task 1: Analytical Model Comparisons, LUCF

The more promising analytical models found in the phase 1 study were used to predict the shift of K_{Ic} transition temperature from LUCF loading (Fig. 1-7). The feature of significance here is that K_{wps} levels were much higher than normally performed for experiments reported in the literature. The K_{wps} values were more like that associated with the pressurized thermal shock scenario. An example calculation of the load level effect predicted by the Chell model is shown in Fig. 1-8. High K_{wps} generally develops the greater transition curve shift but with LUCF cycles the efficiency diminishes. Compare the relative improvement between K_{wps} increment of 60 to 100 MPa$\sqrt{m}$ vs. 100 to 195 MPa$\sqrt{m}$. Other analytical models of dCTOD and Curry indicate about the same effects, and these differ only in the magnitudes of the trends.

Task 2: Experimental Data

The LUCF loading predictions from Task 1 are to be proved with experimental data. This also involves the development of the raw data that would be needed to refine the analytical models. This includes multiple K_{Ic} tests to firmly fix the virgin material K_{Ic} values and tensile stress-strain curves on the subject material. The transposition of the K_{Ic} curve due to the K_{wps} will be checked experimentally for one level of K_{wps} 192 MPa$\sqrt{m}$ loading. There will be two fracture temperatures: one at a high position in the transition curve where K_{Ic} is in the 120-140 MPa$\sqrt{m}$ range, and one at low temperature for K_{Ic} at approximately 50 MPa$\sqrt{m}$ toughness. All specimens have been made and precracked for testing. Fifteen 1T-CT specimens are to be used for virgin material K_{Ic} characterization and twenty 4T-CT (50-mm thick) specimens are ready for K_{wps} testing.

Task 3: Model Refinement

This task involves evaluating the differences between Task 1 and Task 2 outcomes. Refinements can be made to the analytical models based on the experimental outcome. The models are to be fine-tuned in preparation for Tasks 4-6.

Task 4: Analytical Model Predictions, Partial Unloading

This task is aimed at evaluation of partial unloading after K_{wps} loading and cooling. Previous experiments and the analytical models predict improved benefit with smaller unloads. The Chell model was again employed for the illustrative example (Fig. 1-9). When K_{wps} is 180 MPa$\sqrt{m}$ and partial unloading does not go below 2/3 of the K_{wps} level, almost the full benefit from warm prestress load is retained. If the warm preload, K_{wps}, is lower, then unloading down to
can be tolerated without loss of benefit

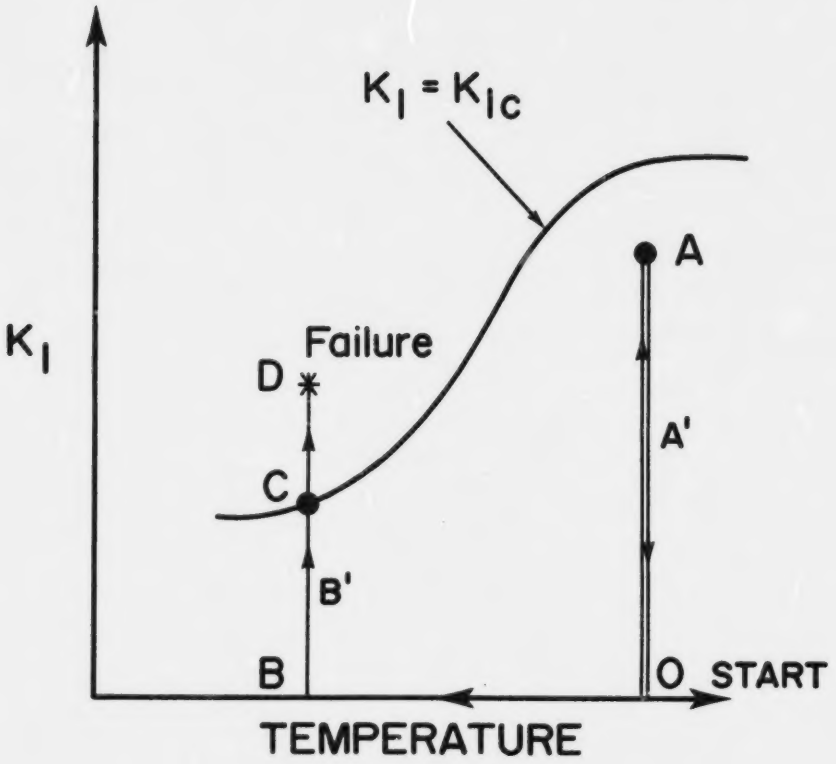

Fig. 1-7 Schematic of LUCF loading from point O to A, and then path A-O-B-C to failure, $K_{If} > K_{Ic}$.

BEST COPY AVAILABLE

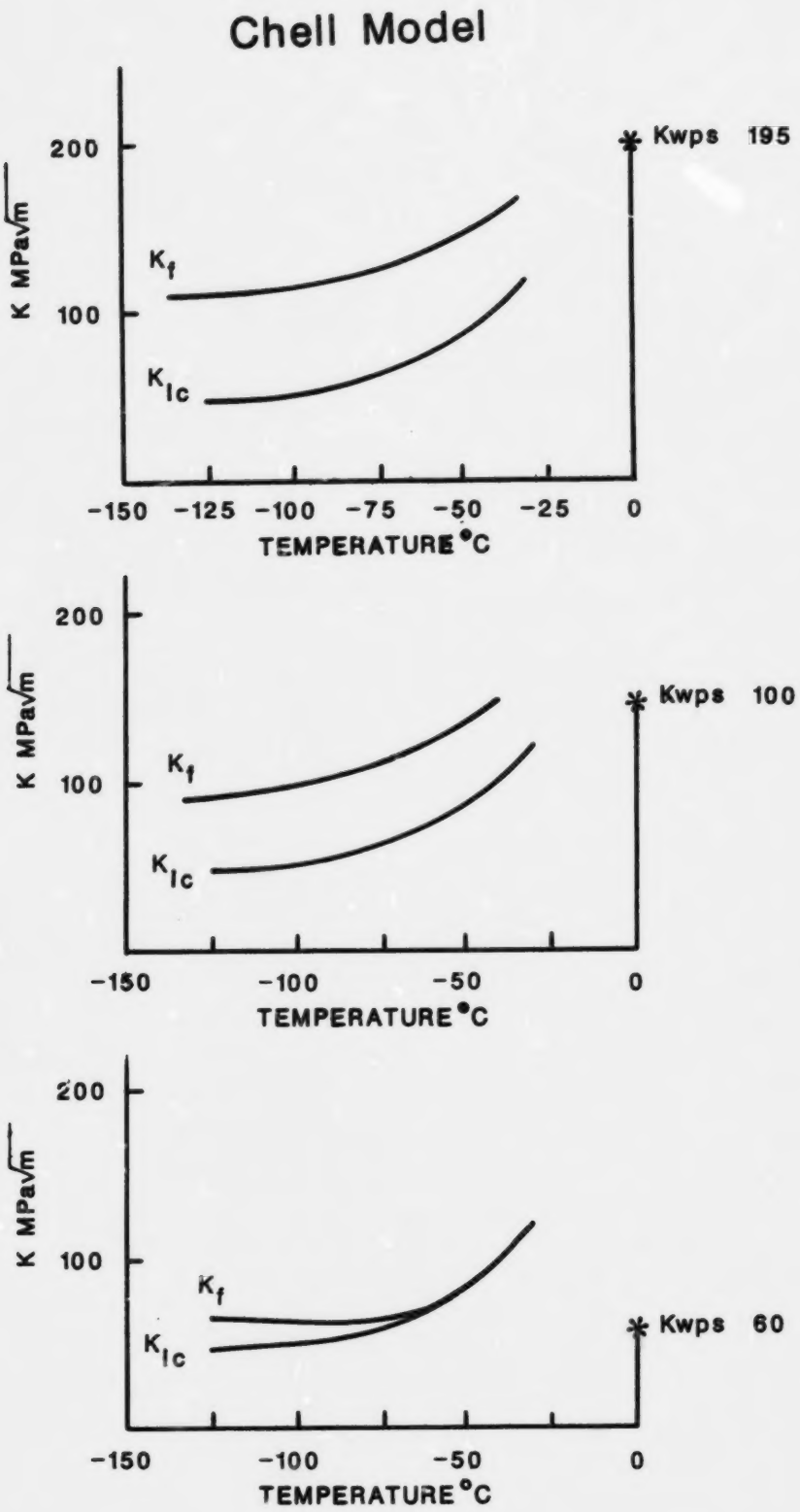

Fig. 1-8 Effect of warm prestress load level, K_{wps}, on K_f (fracture) trend in a LUCF cycle predicted by the Chell model.

BEST COPY AVAILABLE

Chell Model

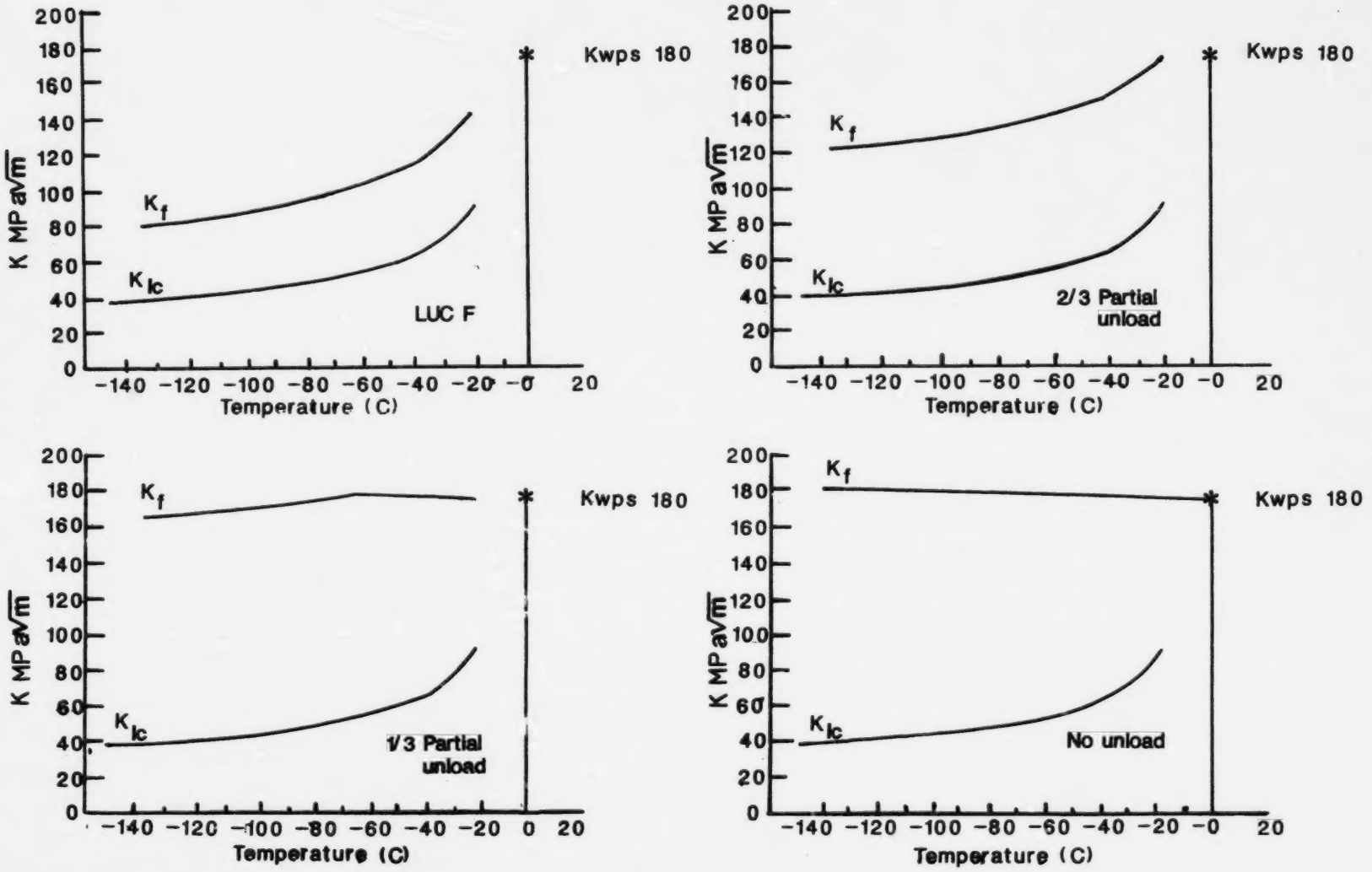

Fig. 1-9 Effect of partial unload on the K_f (fracture) trend predicted by the Chell model. A high initial K_{wps} is used.

BEST COPY AVAILABLE

24

defined in Table 1-4, where the dashed line indicates the breakdown point.

Table 1-4 Predictions via Chell Model of K_f at -140°C After Partial Unload

Initial Conditions (MPa$\sqrt{m}$)		K_f After % Unloading and Cooling (MPa$\sqrt{m}$)			
K_{wps}[a]	K_{Ic}[b]	100%	67%	33%	0%
175	38	80	120	165	180
100	38	65	90	105	105
50	38	50	60	60	60

[a] WPS at 177°C [b] K_{Ic} at -140°C

If PTS reloading can be shown to follow a K_{wps} unloading of less than 1/3, near full benefit can be expected.

Task 5: Partial Unload Experimental Data

As before with Task 3, this task is intended to verify and refine the analytical models. The experiments will have one level of K_{wps}, nominally 190 MPa$\sqrt{m}$, and two levels of partial unloading. Only one temperature will be used for K_f loading, and there will be two levels of unloading. Replication of tests will be ten times to determine statistical variability.

Task 6: Application to PTS

The final step will be to predict the warm prestress history for a chosen presssurized thermal shock accident scenario. The objective is to provide a demonstration of the use of principles established from the previously performed research.

The present status is that the preliminary analytical work has produced a good starting point for this work. All specimens are ready for testing.

1.4 Irradiation-Induced K_{Ic} Curve Shift

D. E. McCabe and B. H. Menke

1.4.1 Background

In order to assess the margin of safety against catastrophic brittle fracture initiation in nuclear reactor pressure vessel material, the plane strain fracture toughness, K_{Ic}, of the material in the irradiated condition must be known. Unfortunately, insufficient data of K_{Ic} vs. temperature exist to permit a quantitative assessment. This situation results from the difficulty and expense of irradiating the large specimens required to measure K_{Ic} by ASTM E 399 criteria. For example, 100-mm thick compact toughness specimens can measure valid K_{Ic} only up to 100-135 MPa$\sqrt{m}$. While higher toughness measurements with larger specimens are desirable, it is not practical since gamma heating and self-shielding during irradiation prevents achievement of uniform fluence and temperature distribution throughout the test specimen.

In the absence of these critical data, the fracture toughness for irradiated steels in the transition region has been based upon the behavior of unirradiated steels coupled with Charpy (C_v) tests of irradiated material. Currently, the unirradiated fracture toughness properties are either measured with the appropriately sized specimens or they are assumed to be the K_{Ic} curve given in Sec. XI of the ASME Boiler and Pressure Vessel Code. It is then assumed that the toughness trend of irradiated material can be approximated by elevating the K_{Ic} vs. temperature curve for the unirradiated material by the temperature shift (ΔT) of the C_v energy vs. temperature curve, where ΔT is determined at the C_v 41-J level.

It is well known that the C_v curve changes shape with irradiation, and it can be argued that a shape change could also occur in the irradiated K_{Ic} curve. For this reason, it is necessary to determine the shape of the irradiated curve by direct measurement for at least a few materials. Consequently, the Heavy Section Steel Technology (HSST) 5th Irradiation Program has been formulated to resolve this question.

The HSST 5th Irradiation includes Charpy, tensile, and compact specimens both in the irradiated and unirradiated condition. Compact specimen sizes are 1T-CT up to 4T-CT (irradiated) and 1T-CT up to 8T-CT (unirradiated).

Specimen preparation and irradiation has been conducted by ORNL. Specimen testing was conducted jointly by ORNL and MEA with each laboratory testing approximately half of the specimens. However, ORNL tested all tensiles, and MEA was responsible for testing 4T-CT and larger compact specimens. The specimens have been machined from two weld deposits, each containing a high copper impurity level [0.2-0.25% (weld 72W) and 0.3-0.35% (weld 73W)]. This copper level will produce a relatively large elevation in the brittle-ductile transition region with irradiation.

1.4.2 Summary of Results

Progress in 1986 included the testing of 6T- and 8T-size compact specimens of unirradiated material and the testing of all irradiated 1T- and 2T-size compact specimens. Weibull statistics and the Merkle method of estimating lower bound K_{Ic} were used to select the most productive test temperature for the 6T- and 8T-CT specimens. Also, there was some cooperative interlaboratory testing between ORNL and MEA to resolve a discrepancy in drop-weight NDT temperatures on 72W and 73W materials.

To select optimum test temperature for 6T- and 8T-CT specimens, an estimate was made (+10°C for 72W and -5°C for 73W), and the choice was defended by establishing K_{Jc} statistical distributions with smaller specimens. Four 2T-size compact specimens of each material were tested and although the sampling was mediocre by usual statistical standards, a K_{Jc} distribution was fitted by three-parameter Weibull. Median K_{Jc} values were predicted as a function of specimen size using the theory of extremal statistics. At the aforementioned temperatures, the median K_{Jc} for 8T-size specimens would yield valid K_{Ic} by satisfying the minimum thickness requirement $[B > 2.5 (K_Q/\sigma_y)^2]$. The median K_{Jc} predictions are compared to test data subsequently developed from 4T-, 6T-, and 8T-CT specimens in Figs. 1-10 and 1-11. The size effect projections seemed reasonable, and in general the 4T- and 6T-CT specimens confirmed the predictions. The K_{Jc} values of 8T-CT specimens did not fit the trend, and they instead appeared to belong amongst the 2T-CT data scatter band. This variance from the usual size effect phenomenon suggests that at the chosen temperatures, the metallurgical effects of inclusion-cleavage fracture interactions become unregimented and hence less amenable to extremal statistics.

Lower bound K_{Ic} values obtained by the Merkle β_{Ic} procedure yield distinctly conservative estimates of K_{Ic} (Figs. 1-10 and 1-11). K_{Jc} test data seldom ever fall below the projected $K_{\beta Ic}$ scatter band. The two approaches of Weibull analysis and $K_{\beta Ic}$ involve median K_{Jc} and lower bound K_{Jc} predictions, respectively, and as such these concepts are complementary as opposed to being competitive in interpretation of transition temperature effects.

MEA has completed its K_{Jc} testing of irradiated 1T- and 2T-CT specimens. The data are compared to unirradiated tests in Figs. 1-12 and 1-13. It is premature at this point to conclude that the irradiated K_{Ic} curve shape will be either the same or different because considerable additional data input is due, and the largest irradiated specimens, 4T-CT specimens, have not been tested. However, the data presently available suggest that there may be no shape change and that the extent of the transition temperature shift at the 100 MPa$\sqrt{m}$ level will be about the same as the 41-J Charpy-V transition temperature shift.

Some discrepancy had been noted in the previous report between ORNL and MEA NDT test results. MEA reported -18°C on both 72W and 73W materials. ORNL reported -46°C on 73W and -29°C on 72W. The cause of

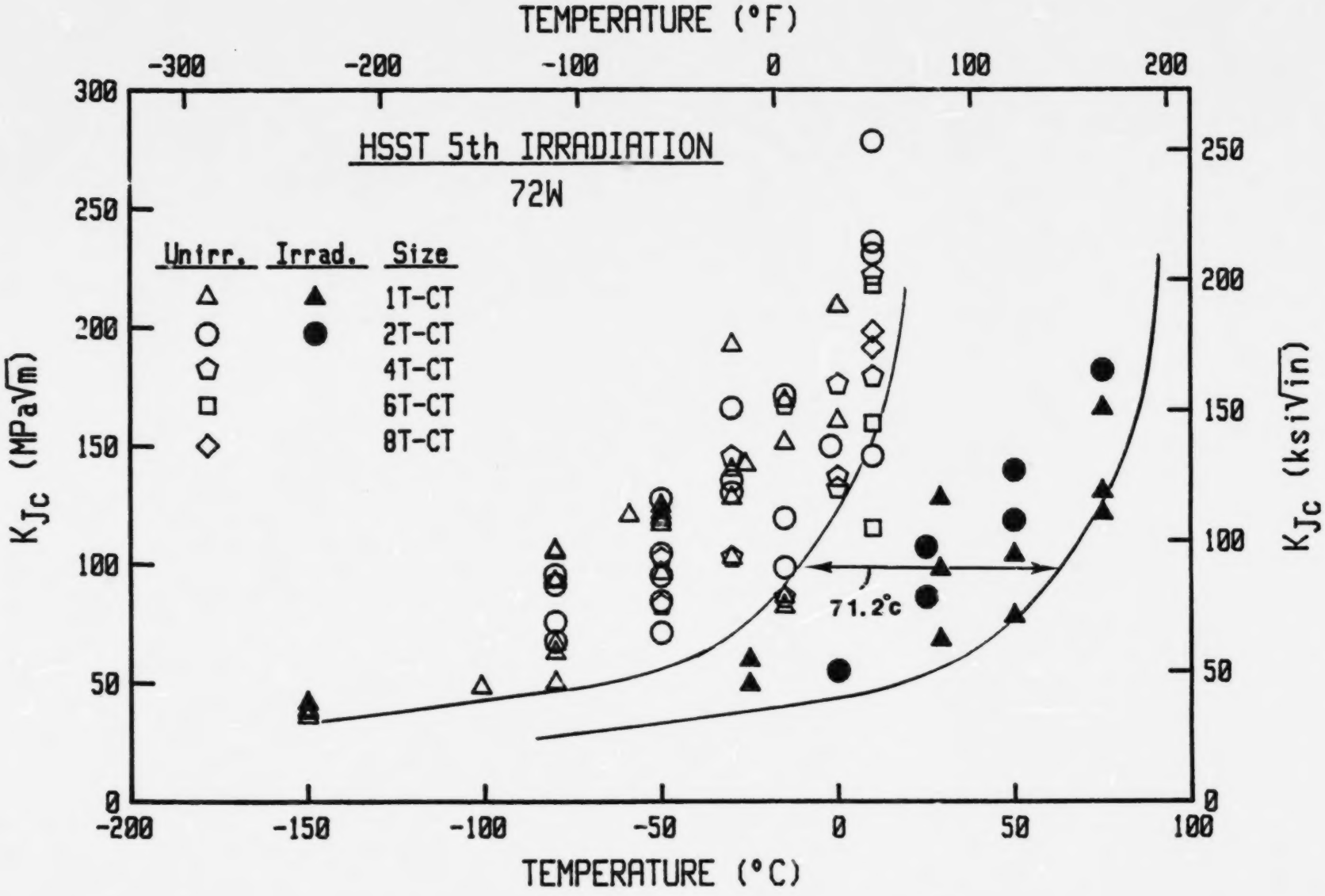

Fig. 1-10 K_{Jc} data for unirradiated and irradiated compact specimens of 72W. The temperature shift is from the C_v curve.

BEST COPY AVAILABLE

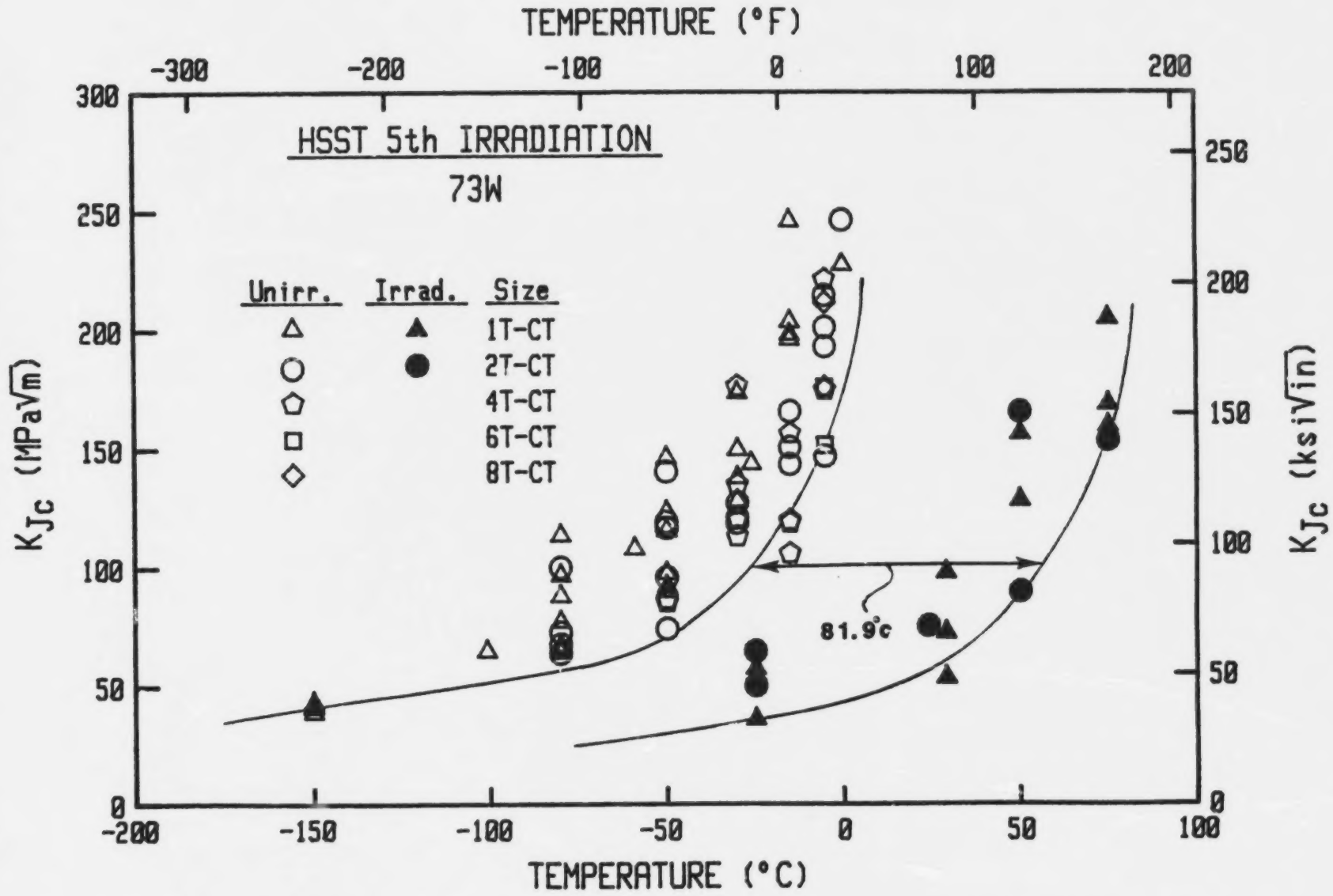

Fig. 1-11 K_{Jc} data for unirradiated and irradiated compact specimens of 73W. The temperature shift is from the C_v curve.

BEST COPY AVAILABLE

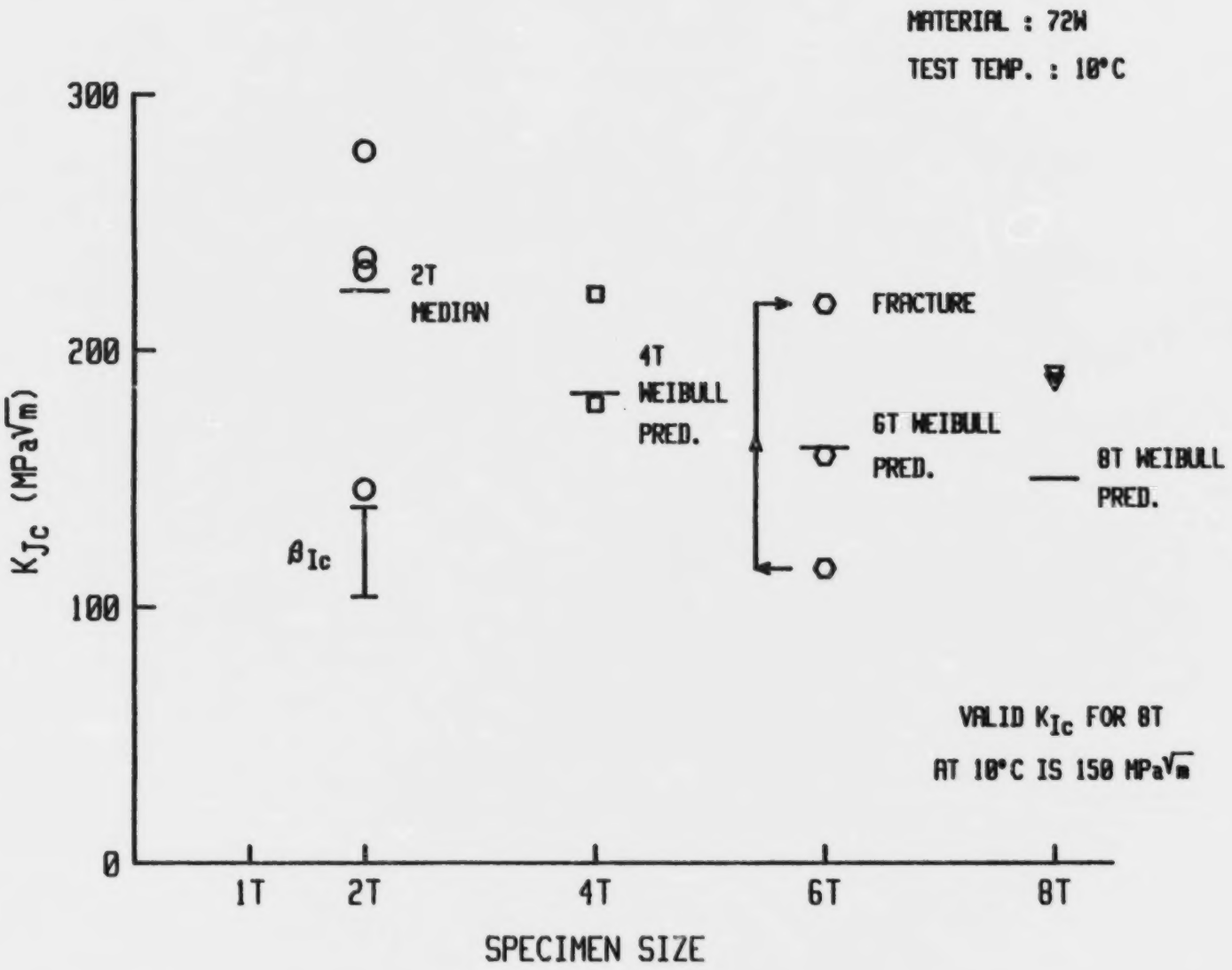

Fig. 1-12 Weibull predicted median K_{Jc} values for 4T-, 6T-, and 8T-compact specimens from 2T-CT data of 72W. Also included are subsequently developed test data.

BEST COPY AVAILABLE

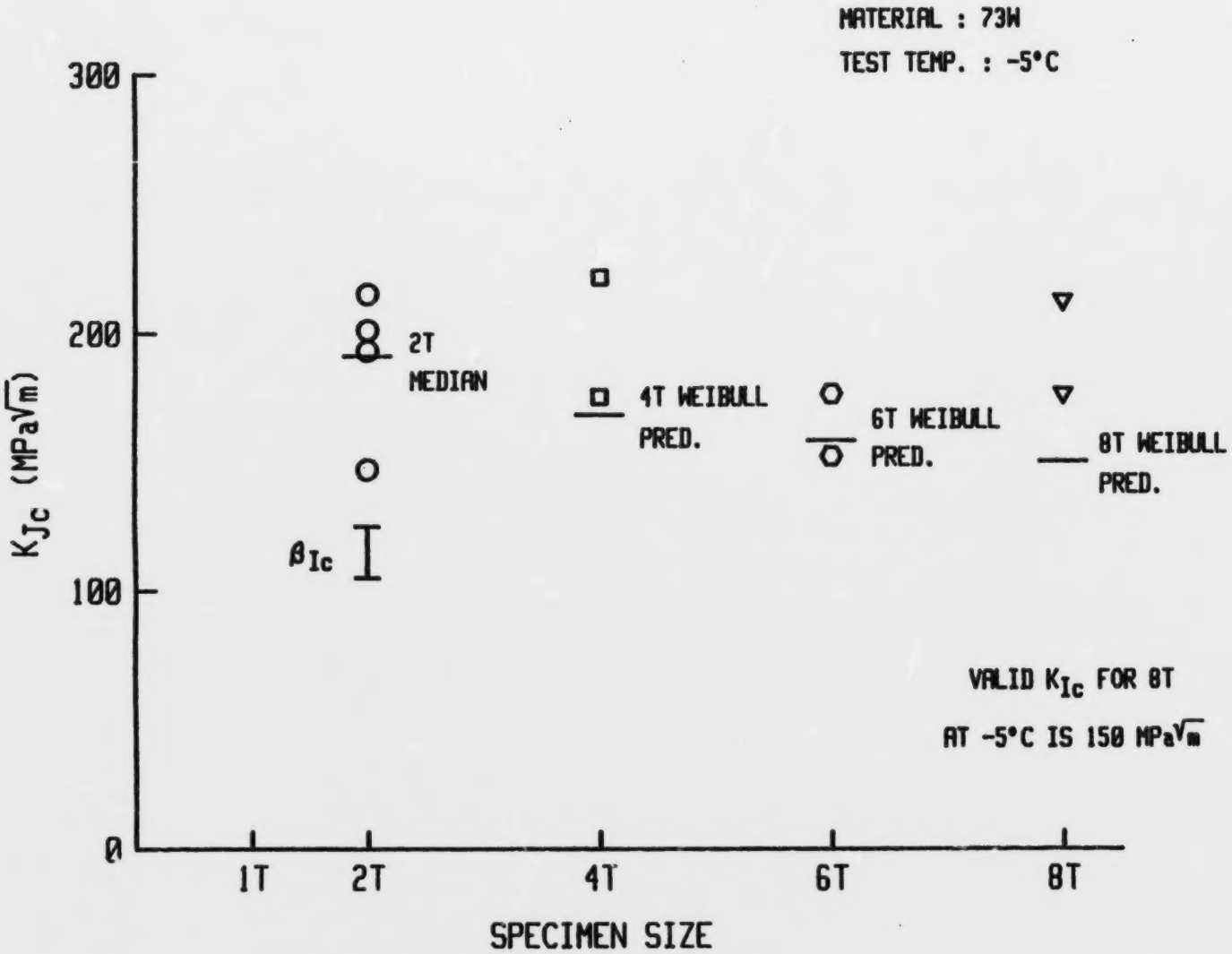

Fig. 1-13 Weibull predicted median K_{Jc} values for 4T-, 6T-, and 8T-compact specimens from 2T-CT data of 73W. Also included are subsequently developed test data.

BEST COPY AVAILABLE

the NDT discrepancy was investigated with additional cooperative tests using A 533-B Drop-Weight specimens. Both laboratories obtained the same result: -18°C (0°F), thereby demonstrating that the testing practices were consistent. ORNL then supplied MEA with additional specimens of 72W and 73W. This time, the NDT temperature of 72W was -23°C (-10°F), essentially the same; that of 73W was -34°C (-30°F) which approached the ORNL result. The conclusion was a material inhomogeneity effect. Irradiated NDT specimens were subsequently tested, and the transition shift was 56°C/78°C (72W/73W) which appears to be about the same as that of the 41-J Charpy index: about 71°C/82°C (72W/73W).

The balance of the testing to be performed by MEA is 16 irradiated 4T-CT specimens and 4 more 8T-CT unirradiated specimens (2 of 72W and 2 of 73W). This program will be completed in 1987.

1.5 Piping Fracture Mechanics Data Base

A. L. Hiser

1.5.1 Background

An important consideration in assessing nuclear power plant safety is a determination of the structural integrity of the coolant water piping systems. Besides system-dependent concerns such as loading and flaw distributions, properties of the constituent materials such as tensile strength, fatigue crack growth rates, and fracture toughness values are also required. The fracture toughness takes on special significance since it is used to determine whether or not a crack will propagate through thickness under specified loading scenarios, and additionally, whether or not a through-thickness crack will be stable or will result in a large break.

The development of fracture analysis procedures for LWR piping systems has passed through several stages. Currently, J-integral concepts are receiving considerable attention as a suitable technique. Initially, the idea of a critical J value (J_{Ic}) for the initiation of fracture was being applied to many structures, including piping. In general, J_{Ic} was seen as conservative, but perhaps overly conservative, for piping applications. J_{Ic} analyses did not account for the appreciable tearing resistance of very tough materials. In 1979, Paris and coworkers (Refs. 9 and 10) introduced the tearing instability analysis and applied it to a number of structures, including circumferential cracks in pipe. This analysis is considered by many to provide the best measure of the fracture resistance of a structure.

The essence of the tearing instability analysis is that a material has a tearing (resistance) modulus (T_m), which can be determined from the J resistance, or J-R, curve. For instability of a given crack to occur, T applied to the structure must be greater than T_m and J applied must be greater than J_{Ic}. Both T_m and J_{Ic} come from the J-R curve, which is the primary data for the tearing instability analysis.

To facilitate analysis of piping systems, a computerized data base of J-R curves and other pertinent information on steels used in nuclear piping is being developed. This data base will provide easy access for the NRC and others to available piping data as needed for the analysis of flawed piping systems.

1.5.2 Summary of Results

Reference 11 outlines the multiphased effort used to establish the Piping Fracture Mechanics Data Base. In 1986, the basic search system of the data base was established, with a substantial number of fracture toughness data, J-R curves, available for use. A "user's guide" to the data base has been prepared and will be available soon.

Data Base Characteristics

The Piping Fracture Data Base contains the following information on nuclear piping steels:

- Fracture toughness data, J-R curves
- Tensile data, engineering and true stress-strain curves
- Charpy-V data
- Chemical composition
- Other descriptive information

Besides test data, specimen dimensional information and limited test set-up information are available. For nonstandard test specimens besides the compact tension and bend bars used, allowance for documenting validation of such nonstandard specimens has been made. This aspect is a look to the future when specimen development may result in improved test specimens.

The actual data stored consist of raw (measured) and calculated values. Coefficients to commonly used equations describing the data are given for C_v curves, true stress-strain tensile curves, and J-R curves. The equations used are the hyperbolic tangent, Ramberg-Osgood, and power-law relations, respectively. Prefitting to these equations helps for cases in which an analyst prefers not to use discrete data.

The data base is in a computerized format, accessible via remote terminals. The system is menu-driven for ease of use, with each menu keyed in a manner to simplify use of the data base user's guide. Output from the data base is via screen output to the user's equipment or file down-loading if the user has the necessary hardware.

Reference 12 provides sample output from the data base.

Characterization Results

Fourteen heats of piping steel have been characterized thus far. A list of these heats is given in Table 1-5. The thermal aging of MEA designations ZP19, ZP20, and ZP22 was performed by Argonne National Laboratories under their program with the USNRC (see Ref. 13 for details). While tensile test results for many of these heats have been summarized in Reference 14 previously, reports summarizing all of the characterization results will be prepared in FY 1987.

Materials scheduled for characterization in FY 1987 include weld and base material from A 516 Gr. 70 pipe, Type 347 and Type 304, base metals, a Type 304-Type 347 weld, a Type 347 weld, and a bimetallic (carbon-stainless) weld.

While the data base currently contains ~ 200 J-R curves, the expected acquisition of data from Battelle's Columbus Division, Babcock & Wilcox (Alliance), Ontario Hydro, and David Taylor Naval Ship Research & Development Center (Annapolis) should add significantly to this number. The acquisition of these data should be complete by the end of FY 1987.

Table 1-5 Piping Materials Which Have Been Characterized

Material	MEA Code	Pipe Diam. (mm)	Pipe Sch.	Wall Thickness (mm)	Comments
SA 376 (304)	ZP17	152	120	14.3	Safe end material
SA 376 (304)	ZP1	168	80	11.0	Flattened and Stress-reliefed tests also
SA 376 (304)	ZP12	152	40	7.1	
SA 182 (F304)	ZP6	508	100	31.0	
Inconel 600	ZP16	152	80	11.0	
A 106-B	ZP14	152	XXS	21.9	
A 106-B	ZP15	152	120	14.3	
A 106-B	ZP2	152	80	11.0	Flattened and stress-reliefed tests also
A 106-B	ZP13	152	40	7.1	
A 106-C	ZP21	813	—	82.6	
SA 351-CF8A	ZP18	813	—	57.0	
A 451-CF8	ZP19	890	—	63.5	Centrifugal cast stainless, thermally aged also
A 451-CF3	ZP20	930	—	73.0	Centrifugal cast stainless, thermally aged also
A 351-CF3	ZP22	—	—	—	Static cast pump impeller, thermally aged also

1.6 Gundremmingen RPV Materials Characterization

J. R. Hawthorne

1.6.1 Background

The 250-MW boiling water Gundremmingen Reactor, KRB-A, has been decommissioned by the Federal Republic of Germany (FRG). Prior to decommissioning, the reactor vessel operated at a nominal 288°C and had an estimated inner wall fluence of $\sim 1 \times 10^{19}$ n/cm^2 (E > 1 MeV). As such, the reactor vessel presented a unique opportunity for a critical correlation test of power vs. test reactor environment effects. A joint USA-FRG study, conceived by the NRC, was initiated in 1985 to evaluate material removed from the vessel by remote cutting (trepanning). MEA and Staatliche Materialpruefungsanstalt (MPA), its counterpart in the FRG, are responsible for the experimental phases of the joint program.

MEA objectives in this task were to characterize, irradiate in a test reactor, and evaluate Gundremmingen reactor vessel material and thereby reveal long-term, in-service irradiation effects. Initial MEA goals were the development of mechanical properties for the unirradiated (preservice) vessel condition using archival material and the determination of fracture resistance at a test reactor fluence matching that of trepans cut from the vessel. The test reactor irradiation was to include sufficient specimen numbers for supplemental studies of properties recovery by postirradiation annealing. Qualification of exposure rate effects will be made jointly by MEA and MPA. Rate effects are to be judged from radiation-induced changes in Charpy-V (C_v) notch ductility, fracture toughness (J-R curve), and tensile properties produced by the test reactor environment vs. vessel service.

In 1985, MEA located and acquired two welded ring segments, believed to be residual (archive) material from the KRB-A vessel fabrication. One piece, approximately 119-mm thick and weighing about 1450 kg, was given the identification code GEB. The base metals on either side of the weld deposit (GEB-1 and GEB-2) were subsequently tested to determine if one (or both) of the base metals is representative of the vessel as first placed in service. The verification test findings are documented in Reference 15. The results indicate a high probability that the base metals were from the same steel melt. Moreover, the compositions of the GEB archive base metals, the composition of surveillance specimen base metal, and the composition of drillings taken from the vessel itself by MPA are in good agreement. These findings, coupled with intercomparisons of notch ductility, tensile strength, and microstructure, led to a conclusion by MPA, NRC, and MEA that the GEB archive base material is representative of that KRB-A belt-line material identified as ring forging 7.1. The program subsequently moved on to the next phase of investigation.

1.6.2 Summary of Results

In 1986, two major efforts were completed. One was the performance of fracture toughness tests of the forging GEB (base metal side 2) through its thickness. The second was the completion of the planned postirradiation tests of GEB-2 material involving Charpy-V (C_v), tensile, and 0.5T-CT fracture toughness specimens. The specimens were evaluated in as-irradiated (I) and postirradiation annealed (IA) conditions and represented the 1/8T-thickness position of the GEB material. This decision to irradiate 1/8T-location specimens stemmed from the equivalence found in C_v upper shelf energy levels of the 1/8T vs. 1/4T positions (103 J) and the near-equivalence in C_v 41-J transition temperatures (-29°C vs. -18°C) of these two positions. An additional consideration was that the 1/8T layer would receive a greater service-induced fluence than the 1/4T layer and furthermore would better represent the small flaw case in PTS.

Fracture toughness tests of the 1/8T vs. 1/4T vs. 1/2T vs. 3/4T layers produced the results shown in Fig. 1-14. For those specimens which did not fail in the K_{Ic} mode, that is, those which showed indications of elastic-plastic fracture capability, the test procedure was switched on-line to obtain the J-R curve via unloading compliance method after the limits on ASTM E 399 validity criteria were exceeded. Reference 16 describes the method used for J-R curve development by the single-specimen compliance technique. J-R curve trends are illustrated in Fig. 1-15. Referring to Fig. 1-14, the data in the transition region describe good correspondence between the 1/8T- vs. the 1/4-thickness positions. Equally important, the difference between the 1/8T and the 1/4T positions in terms of transition temperature indexed to the 100 MPa$\sqrt{m}$ level is small (about 14°C). The magnitude of difference is about the same as that found in C_v testing. (NOTE: the axial orientation, defined as ASTM orientation C-L, is the weak orientation of the forging and was purposely chosen for the continuing program for consistency with current surveillance program practice.)

Plans for the irradiation test called for an exposure temperature of 288°C and a target fluence of 8×10^{18} n/cm^2, E > 1 MeV. These parameters reflected best estimates of the vessel operating conditions and end-of-life (EOL) exposure by the Federal Republic of Germany (FRG) at the time of program initiation. As discussed below, both parameters were revised downward in late 1986 based on new information obtained by MEA and MPA. The specimen complement for irradiation included 47 C_v, 8 tensile, and 24 0.5T-CT specimens. The division of specimens by postirradiation test condition is given in Table 1-6. At present, one set of C_v specimens for anneal condition studies is in reserve at NRC direction.

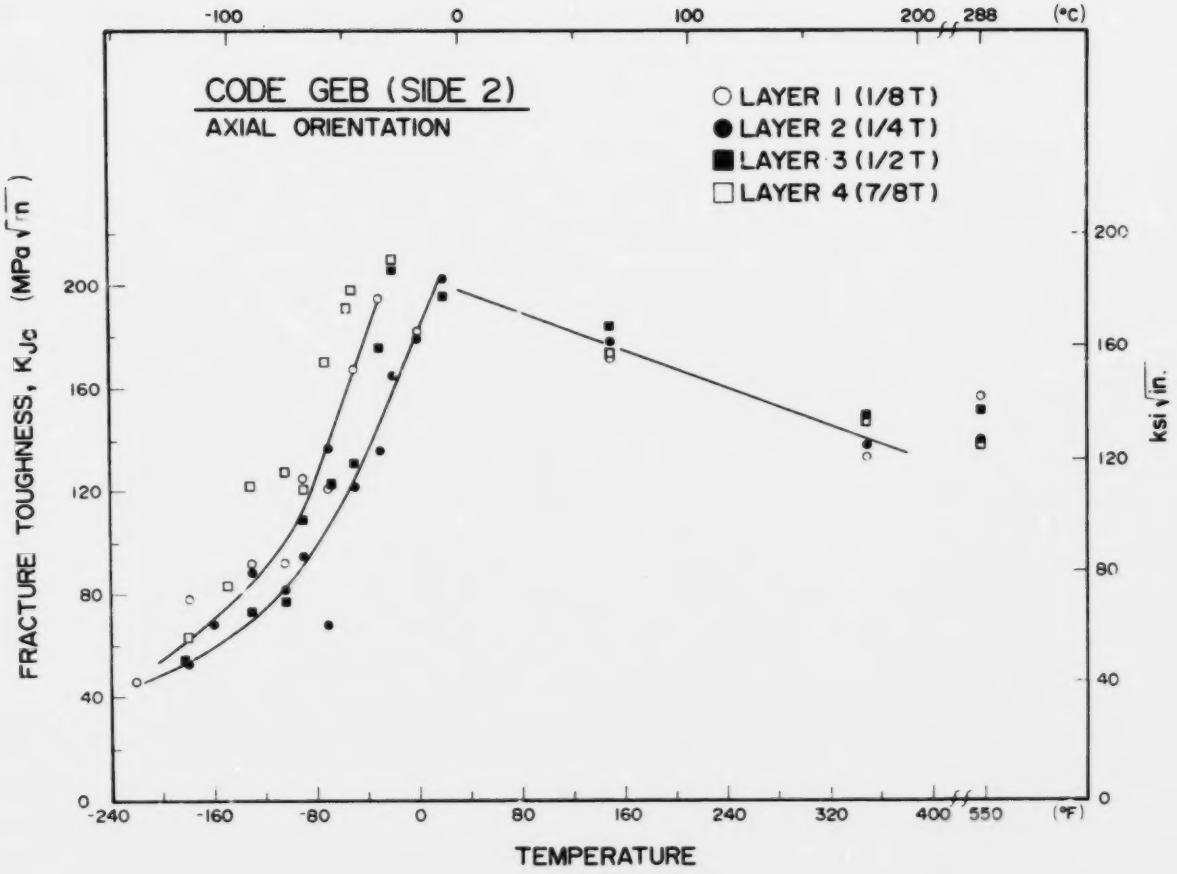

Fig. 1-14 Through-thickness fracture toughness of archive ring forging, GEB (side 2), before irradiation.

BEST COPY AVAILABLE

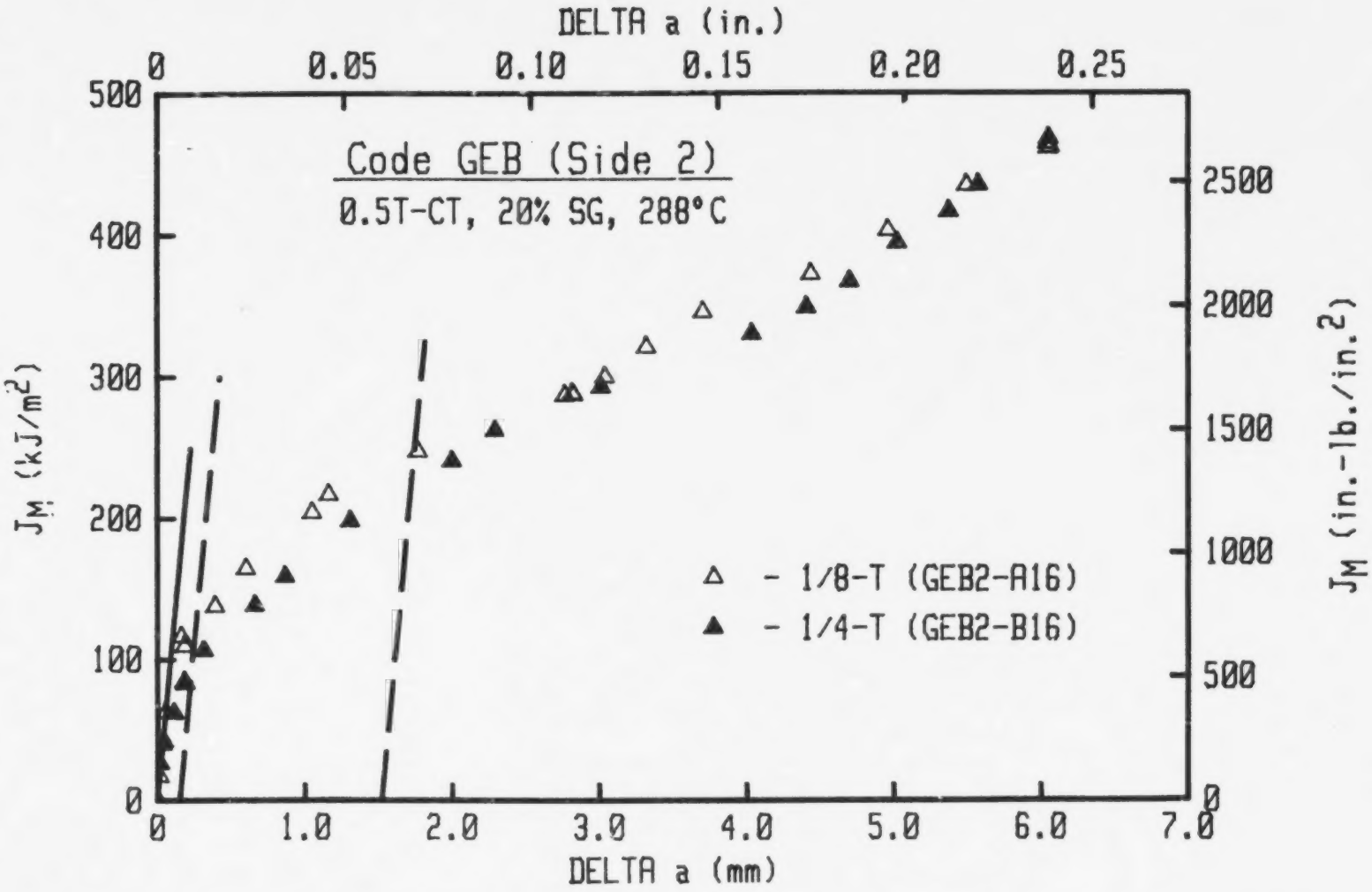

Fig. 1-15 J-R curve determinations for 1/8T- and 1/4T-thickness locations in code GEB material (upper shelf test condition).

BEST COPY AVAILABLE

Table 1-6 Postirradiation Test Matrix

Condition	Specimen Complement		
	C_v	Tensile	CT
As-irradiated	12	2	12
399°C-168 h annealed	12	2	8
454°C-168 h annealed	12	2	6
Spare annealing set	11	2	0

The irradiation assembly, designated UBR-68, was exposed in the 2-MW light water cooled and moderated test reactor (UBR) located in the Buffalo Materials Research Center (BMRC). The irradiation time was 249 h at 2 MW. The average fluence received by the C_v and tensile specimens was 8.76×10^{18} n/cm^2; that received by the CT specimens was 8.6×10^{18} n/cm^2, E > 1 MeV. (Fluence values given here and elsewhere in this report are calculated spectrum values unless noted otherwise.) Fluences were determined from iron wire and nickel wire neutron dosimeters placed within the specimen arrays. The uncertainty in fluence rate (neutron flux) determinations assigned to values from the respective dosimeters by the counting laboratory, EG&G Idaho, Inc., was ± 8% and ± 7% for the 1 σ confidence level. A ^{238}U dosimeter capsule was included in the C_v specimen array and in the CT specimen array. Fluences determined from the two capsules were 8.34×10^{18} n/cm^2 and 8.29×10^{18} n/cm^2, respectively. The uncertainty in the fluence rates is 5% in this case. The cited uncertainties do not include any uncertainties that would be associated with actual spectrum averaged cross-sections of the irradiation fields or with burnout of the reaction products of interest.

Charpy-V results are illustrated in Fig. 1-16 (irradiated condition) and Figs. 1-17 and 1-18 (postirradiation annealed conditions). Data are listed in Table 1-7. A transition temperature elevation of 44°C was produced by the irradiation. The data show NRC Regulatory Guide 1.99 Rev. 1 and Rev. 2 to be conservative in projecting the radiation embrittlement sensitivity of the material which contained 0.15% Cu, 0.015% P, and 0.79% Ni. Specifically, Rev. 1 and Rev. 2 project elevations of about 67°C and 59°C, respectively, vs. the measured value of 44°C. In Fig. 1-17, the 399°C-168 h anneal obtained full C_v upper shelf recovery but only partial 41-J transition temperature recovery. The 454°C-168 h anneal, in contrast, produced full upper shelf recovery and essentially full 41-J recovery. Notice that the C_v upper shelf energy level of the annealed material is significantly higher than that of unirradiated condition material (114 J vs. 103 J, respectively). MEA has proposed that the effect of

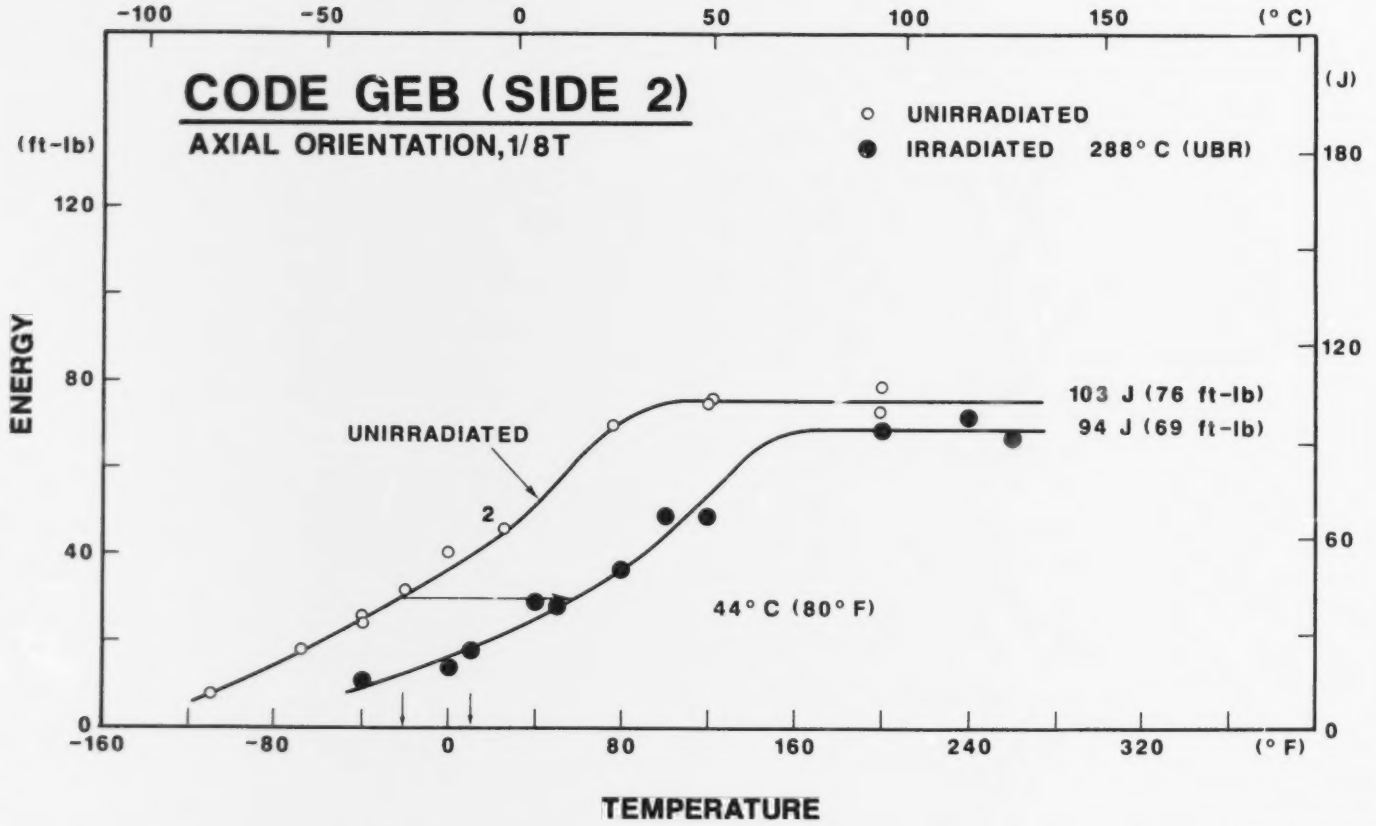

Fig. 1-16 Charpy-V notch ductility of archive ring forging, GEB (side 2) before and after irradiation at 288°C (550°F) to 8.8×10^{18} n/cm^2, E > 1 MeV. Specimens were irradiated in the light-water-cooled and moderated UBR.

BEST COPY AVAILABLE

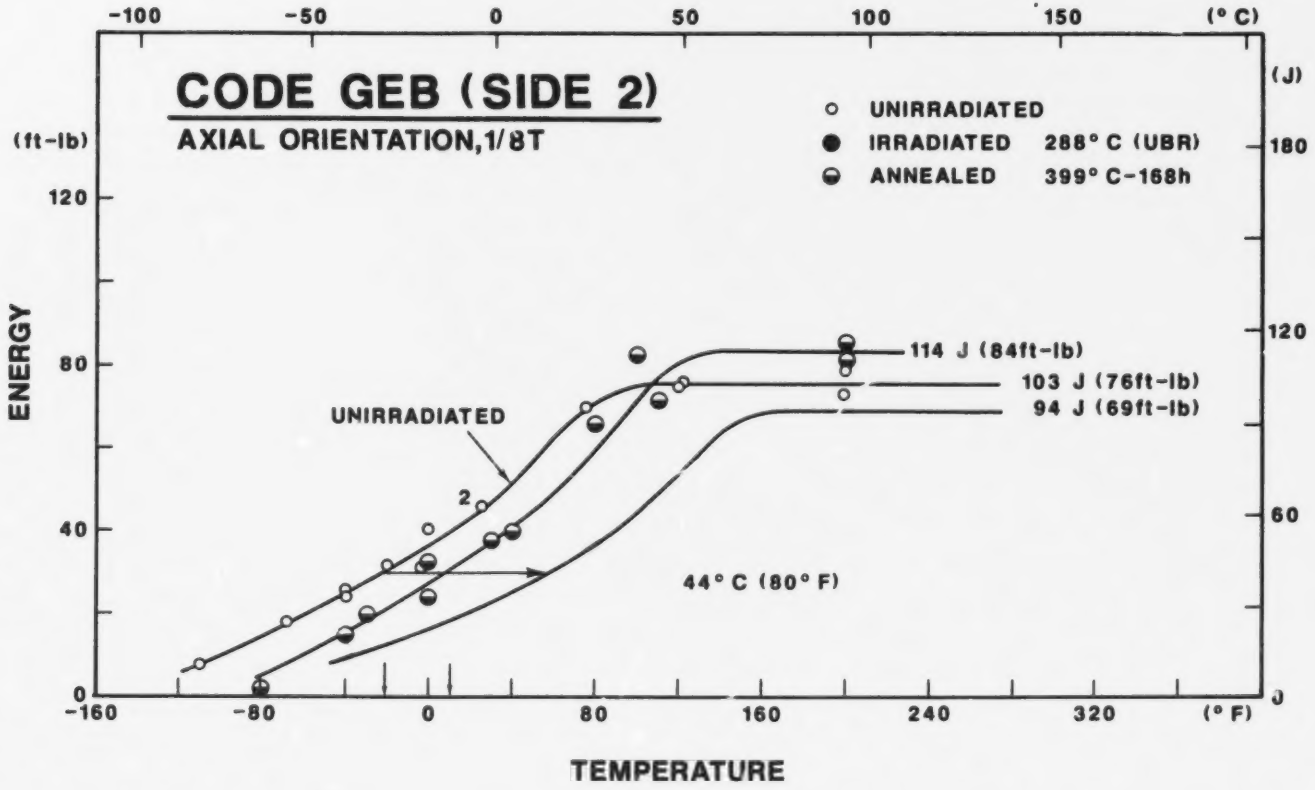

Fig. 1-17 Charpy-V notch ductility of archive ring forging, GEB (side 2) before and after irradiation at 288°C (550°F) and after postirradiation annealing at 399°C (750°F) for 168 h.

BEST COPY AVAILABLE

42

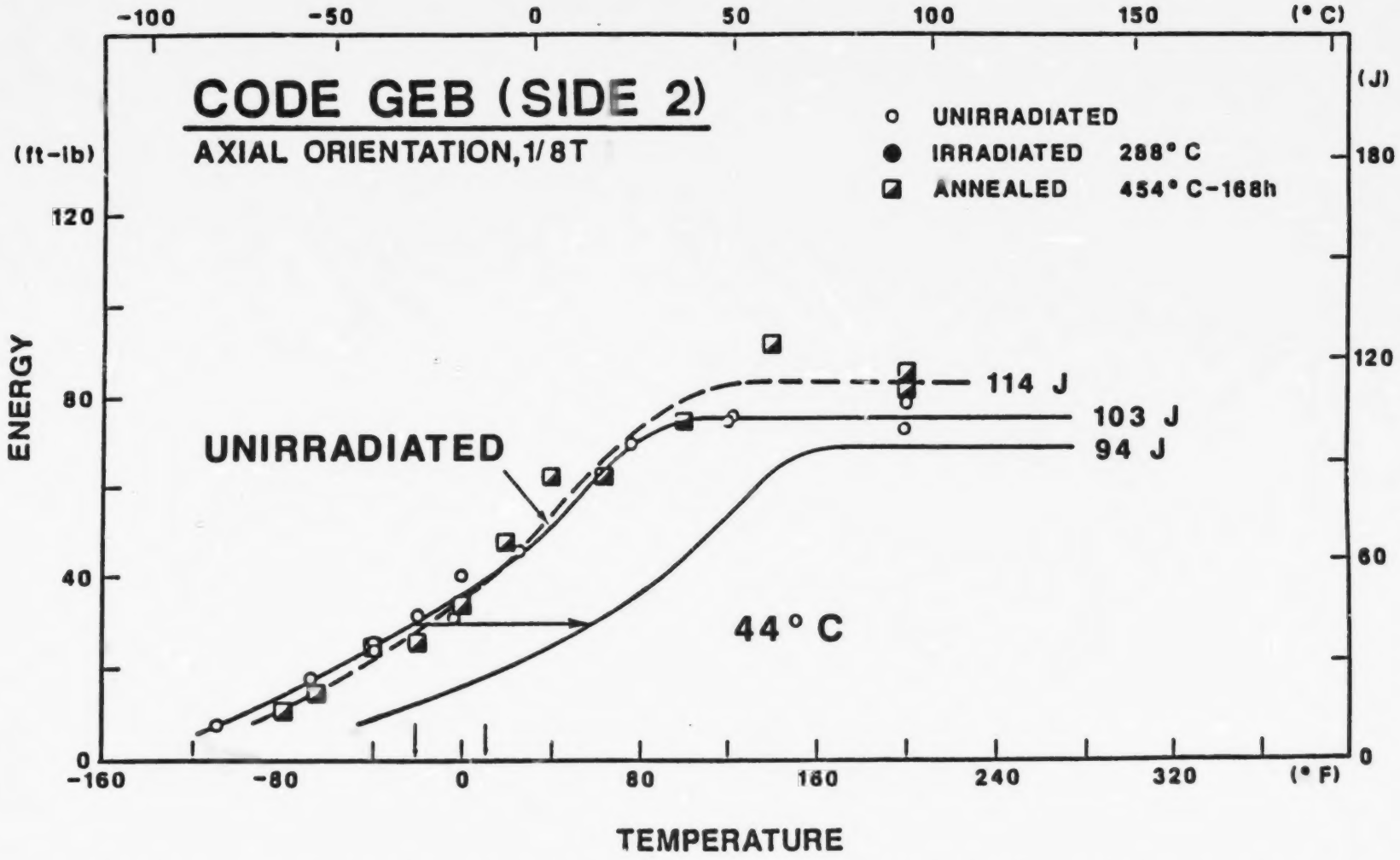

Fig. 1-18 Charpy-V notch ductility of archive ring forging, GEB (side 2) before and after irradiation at 288°C (550°F) and after postirradiation annealing at 454°C (850°F) for 168 h.

BEST COPY AVAILABLE

Table 1-7 Postirradiation Charpy-V Test Results for KRB-A Vessel Archive Material (1/8 T location in forging, UBR-68 irradiation assembly)

Test Condition	Specimen Number	Location in[a] Forging (Block No.)	Temperature		Energy		Expansion		Shear
			(°C)	(°F)	(J)	(ft-lb)	(mm)	(mils)	(%)
As-Irradiated	97	4B-F	-40	-40	15	11	0.229	9	--[b]
	94	4B-F	-18	0	19	14	0.356	14	--
	90	4B-R	-12	10	24	18	0.406	16	--
	78	4A-F	4	40	39	29	0.636	27	--
	107	4C-F	10	50	38	28	0.711	28	--
	83	4A-R	27	80	50	37	0.838	33	--
	104	4C-R	27	80	49	36	0.838	33	--
	117	4D-F	38	100	66	49	1.118	44	--
	112	4D-R	49	120	66	49	1.194	47	--
	110	4C-F	93	200	94	69	1.575	62	98
	113	4D-R	116	240	98	72	1.549	61	100
	77	4A-F	127	260	91	67	1.524	60	100
Postirradiation Annealed (399°C-168 h)	114	4D-R	-62	-80	3	2	0.000	0	--
	98	4B-F	-40	-40	20	15	0.254	10	--
	102	4C-R	-34	-30	27	20	0.508	20	--
	91	4B-R	-18	0	33	24	0.584	23	--
	118	4D-F	-18	0	45	33	0.559	22	--
	80	4A-F	-1	30	52	38	0.813	32	--
	82	4A-R	4	40	54	40	0.813	32	--
	100	4C-R	27	80	90	66	1.270	50	--
	95	4B-F	38	100	113	83	1.727	68	--
	175	5A-F	43	110	98	72	1.346	53	--
	76	4A-F	93	200	117	86	2.007	79	100
	86	4A-R	93	200	111	82	1.803	71	100

[a] MEA drawing 433-C0-5004 Rev. 0

[b] Not yet available

Table 1-7 Postirradiation Charpy-V Test Results for KRB-A Vessel Archive Material (1/8 T location in forging, UBR-68 irradiation assembly)

Test Condition	Specimen Number	Location in[a] Forging (Block No.)	Temperature		Energy		Expansion		Shear
			(°C)	(°F)	(J)	(ft-lb)	(mm)	(mils)	(%)
Postirradiation	116	4D-F	-62	-80	15	11	0.178	7	--
Annealed	106	4C-F	-54	-65	20	15	0.356	14	--
(454°C-168 h)	81	4A-F	-40	-40	34	25	0.559	22	--
	93	4B-F	-29	-20	35	26	0.533	21	--
	87	4A-R	-18	0	46	34	0.711	28	--
	92	4B-R	-7	20	65	48	0.991	39	--
	79	4A-F	4	40	85	63	1.168	46	--
	120	4D-F	16	60	85	63	1.448	57	--
	84	4A-R	38	100	102	75	1.829	72	90
	109	4C-F	60	140	125	92	1.600	63	98
	103	4C-R	93	200	110	81	1.803	71	100
	99	4C-R	93	200	115	85	1.702	67	100

[a] MEA drawing 433-CO-5004 Rev. 0 [b] Not yet available

45

thermal aging (288°C and 288°C + 454°C) without irradiation be investigated for the archive material to explore one possible explanation for the upper shelf difference. The three sets of C_v data were developed with the same impact test machine.

With the CT specimen tests, the elevation in the 100-MPa$\sqrt{m}$ transition temperature matched well that found in C_v tests (Fig. 1-19). Tests of CT specimens in 399°C and 454°C annealed conditions are illustrated in Figs. 1-20 and 1-21. In each case, inconsistent recovery is observed. For the 399°C anneal, two specimens indicated no recovery referenced to the mean irradiated condition curve; four other specimens indicated up to 80% recovery in 100-MPa$\sqrt{m}$ temperature. For the 454°C anneal, each specimen indicated some recovery; the K_J value for one specimen fell to the left of the unirradiated curve denoting 100% recovery. The reason(s) for the inconsistencies has not been revealed to date.

Tests of tensile specimens yielded the information in Table 1-8. The irradiation exposure produced a 76 MPa increase in yield strength and a 59 MPa increase in ultimate tensile strength. The 399°C anneal produced a 70% recovery in yield strength; full recovery in yield strength was obtained with the higher temperature anneal. These results follow well the C_v 41-J transition temperature indications; that is, the 454°C anneal but not the 399°C anneal produced full 41-J transition temperature recovery.

Separate from the UBR-68 experiment, MEA working with EG&G Idaho, Inc. (J. W. Rogers) made fluence determinations for the reactor vessel material. The material analyzed was a slice from a vessel trepan provided by MPA. Results are illustrated in Fig. 1-22. Notice that the fluence to the inner wall surface is much less than the original estimate (1×10^{19} n/cm^2) of the inner wall fluence made at the time of vessel decommissioning and the 8×10^{18} n/cm^2 fluence target for the UBR-68 experiment. Accordingly, a 1:1 comparison of embrittlement produced by a given fluence from a test reactor vs. KRB-A service cannot be accomplished at this time. To further complicate the issue, the reanalysis of vessel operating temperature by the utility indicates a service temperature of 279°C for the vessel belt-line region. This best estimate was derived from downcomer water temperature information only. MEA proposed two new irradiation experiments to the NRC to resolve the attendant uncertainties. These are (1) an irradiation at 288°C to a low fluence matching the measured fluence for the 1/8T location of the vessel trepans, i.e., 2.8×10^{18} n/cm^2, E > 1 MeV and (2) an irradiation at 275°C to 8.7×10^{18} n/cm^2, E > 1 MeV. Results from the first experiment coupled with the data of Fig. 1-16 would show the fluence dependency of embrittlement and would enable a closer comparison of embrittlement produced by test reactor vs. power reactor environments. The second experiment represents a test of the temperature dependency of embrittlement and will help ascertain the significance of the current uncertainty on the vessel in-wall temperature. The NRC has approved both experiments for 1987.

Results obtained by MPA for Trepan G and C materials for the C-L orientation (thickness layer no. 2) at a fluence of 2.7×10^{18} n/cm^2

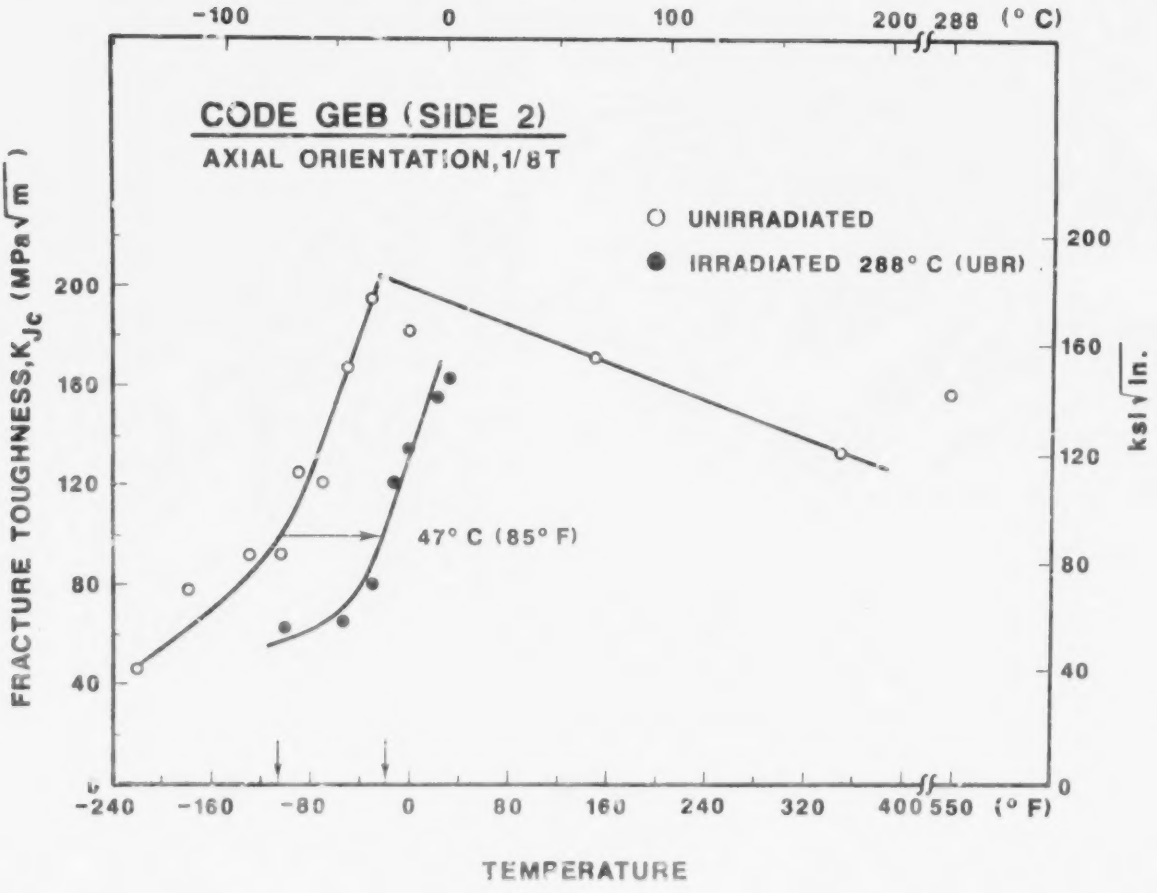

Fig. 1-19 Fracture toughness of archive ring forging, GEB (side 2) before and after irradiation at 288°C (550°F) to 8.6×10^{18} n/cm^2, E > 1 MeV. The specimens were irradiated in the light-water-cooled and moderated UBR.

BEST COPY AVAILABLE

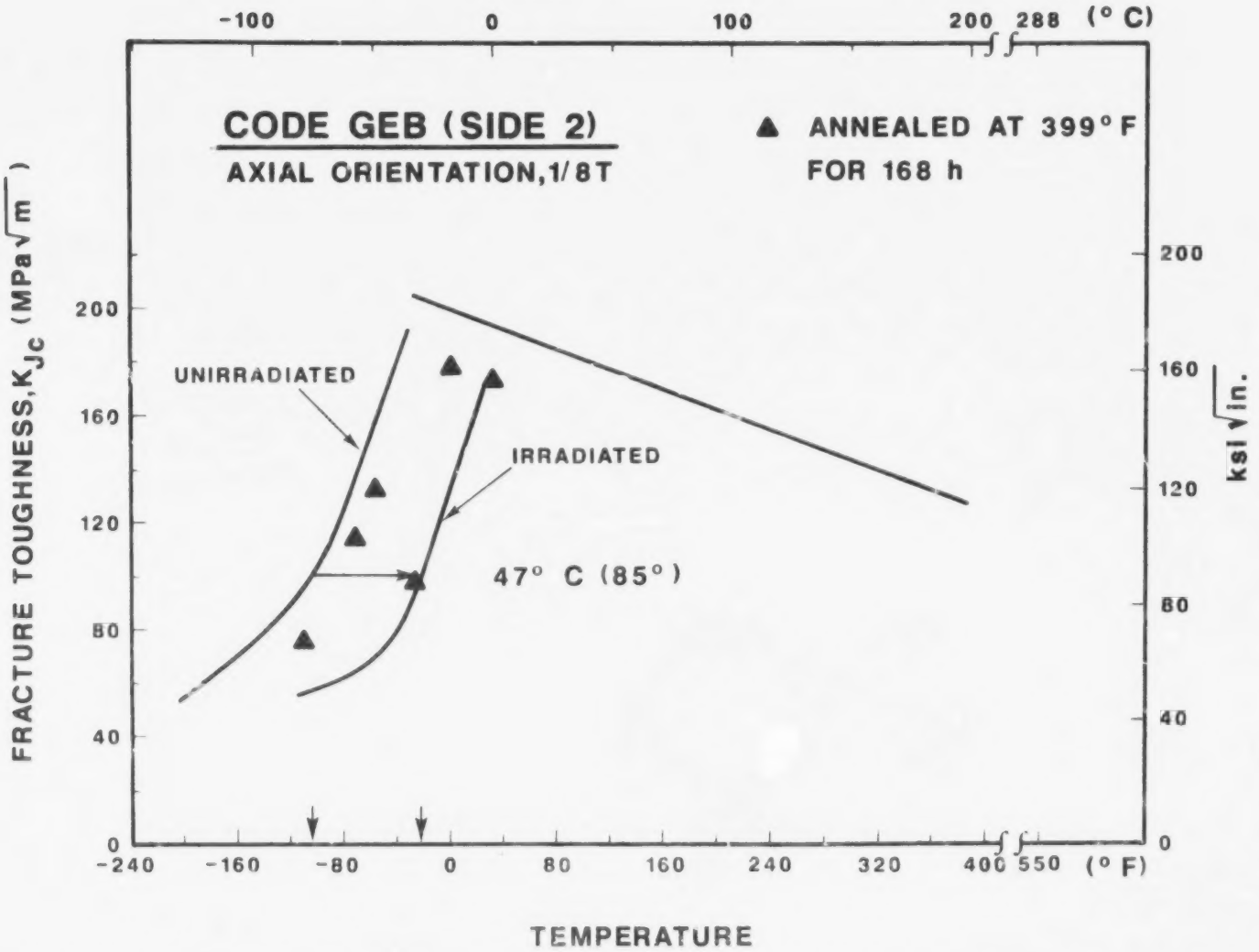

Fig. 1-20 Postirradiation annealing at 399°C for 168 h results in no recovery or up to 80% recovery.

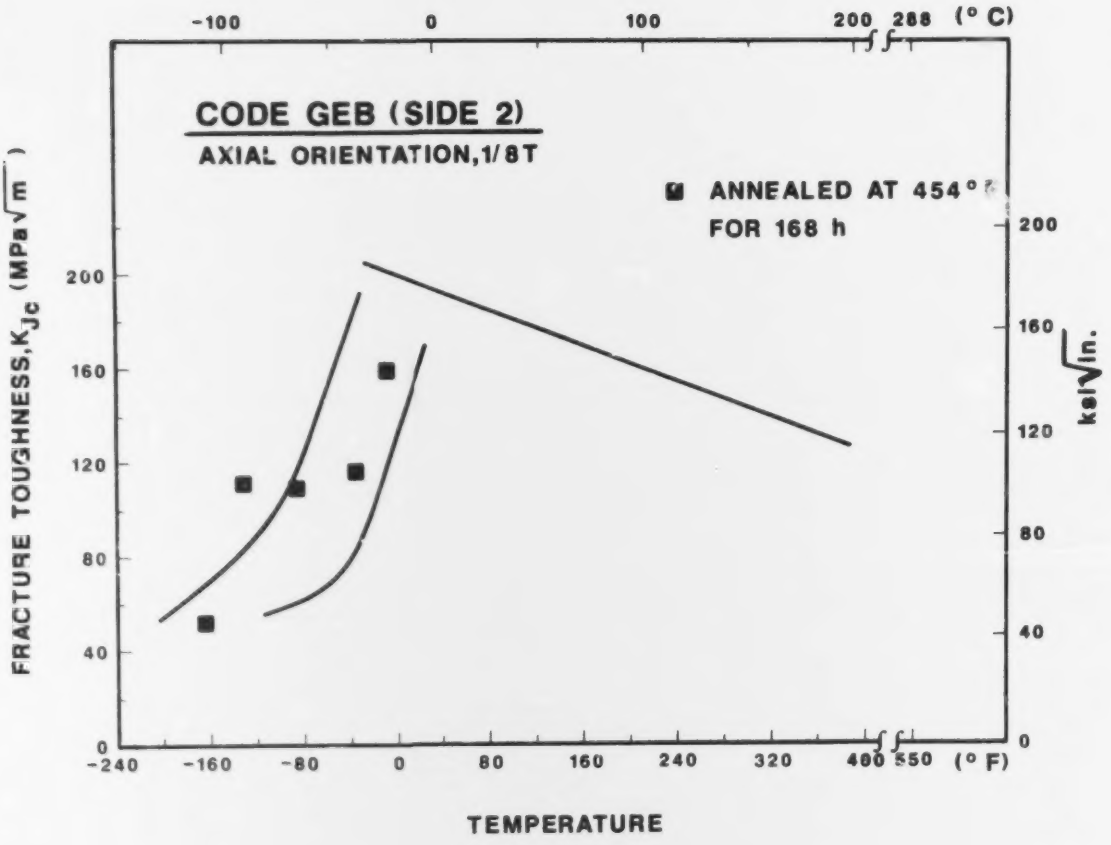

Fig. 1-21 Postirradiation annealing at 454°C for 168 h provides at least partial recovery in every case, although the amount of recovery indicated by individual specimens is not the same. The reason(s) for the inconsistency is not known.

Table 1-8 Postirradiation 24°C Tensile Test Results for Archive Material GEB (Side 2) (5.74-mm diameter specimens, 1/8T location, TL orientation)

Material Condition	Specimen Number	Yield Strength		Tensile Strength		Elongation	Reduction in Area
		(MPa)	(ksi)	(MPa)	(ksi)	(%)	(%)
Unirradiated Reference	GEB-T9	488[a]	70.8	633	91.8	38.4[b]	61.1
	GEB-T10	488[a]	70.8	633	91.8	39.6[b]	65.4
	Average	488	70.8	633	91.8	39.0	63.3
Irradiated	GEB2-16	564	81.8	692	100.3	----[c]	----[c]
	Increase	76	11.0	59	8.5		
	GEB2-19[d]	463	67.1	649	94.1	----[c]	----[c]
Annealed 399°C-168 h	GEB2-17	511	74.1	647	93.8	----[c]	----[c]
	Decrease	53	7.7	45	6.5		
	% Decrease		70.0		76.5		
	GEB2-20[d]	448	65.0	626	90.8	----[c]	----[c]
Annealed 454°C-168 h	GEB2-18	484	70.2	632	91.6	----[c]	----[c]
	Decrease	80	11.6	60	8.7		
	% Decrease		100.0		100.0		
	GEB2-21[d]	430	62.3	676	89.1	----[c]	----[c]

[a] 12.7 mm gage length extensometer, 0.2% offset

[b] Elongation in 12.7-mm gage length

[c] Not yet available

[d] 288°C test

FLUENCE ASSESSMENTS - TREPAN "G"
(EG&G IDAHO, J. W. ROGERS)

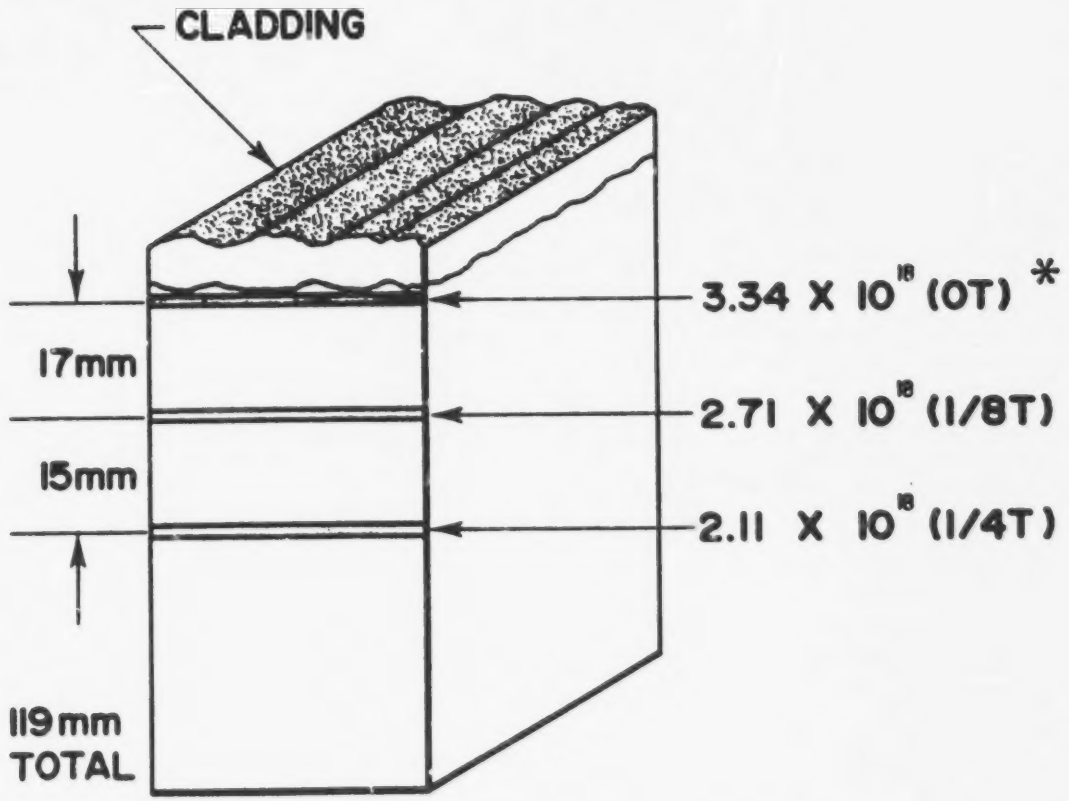

* FISSION SPECTRUM ASSUMPTION

Fig. 1-22 Through-thickness determinations by MEA/EG&G Idaho, Inc. for vessel trepan material.

BEST COPY AVAILABLE

describe a 60°C increase in 41-J temperature and a 50-J decrease in C_v upper shelf energy (USE), when referenced to the preirradiation properties of the archive material (Fig. 1-23). In contrast, only a 30°C increase in C_v 41-J temperature and a < 10-J decrease in C_v USE were found for the L-C orientation. The C-L vs. L-C results appear anomalous. At MEA's recommendation a few C_v samples were annealed at 454°C for 168 h. The C_v USE values did not rise up to MEA's archive material preirradiation (or postirradiation annealed) values. In fact, MPA reported very little recovery in trepan upper shelf levels.

The overall inequality of trepan vs. archive behavior in the C-L orientation is not understood at this time, especially since the C-L vs. L-C relationships are opposite to experience for other materials irradiated in various test reactors. This anomaly is a primary focus of continuing efforts by MPA and others.

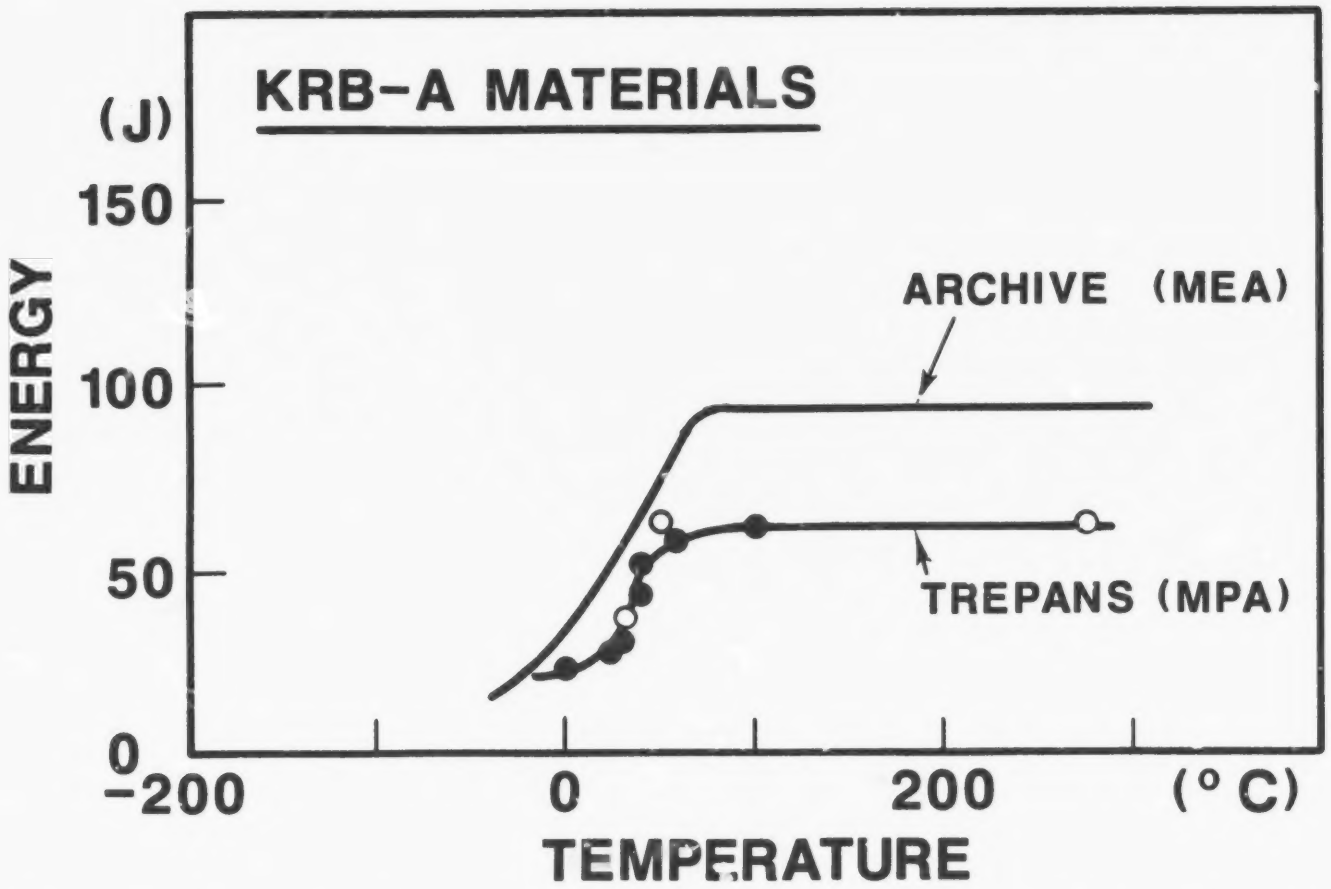

Fig. 1-23 Comparison of as-irradiated condition Charpy-V test results for MEA archive material (test reactor irradiation) and MPA trepan material (KRB-A vessel service). The trepan material which received a much lower fluence than the archive material has poorer notch ductility properties (courtesy MPA).

BEST COPY AVAILABLE

2. ENVIRONMENTALLY-ASSISTED CRACK GROWTH IN LWR MATERIALS

2.1 Environmental Degradation of Fatigue Life

J. B. Terrell

2.1.1 Background

The design requirements for Class 1 piping systems in nuclear power plants are contained in Section III, Subsection NB of the ASME Boiler and Pressure Vessel Code (Ref. 17). Article NB-3650 pertains to the analysis of piping products including the fatigue analysis, which assesses the accumulation of fatigue damage due to the variation of pressure, moment, and thermal loadings during operation of the system.

The ASME Code provides procedures that combine the various types of loadings with both piping geometry considerations and a set of piping system analysis rules. The end result is an estimation of a value for alternating stress amplitude which can be used in conjunction with an ASME S-N curve for a particular class of materials, e.g., carbon steels, to determine the allowable number of cycles a structural member can undergo before fatigue failure becomes imminent.

Section III of the Code contains reference curves for stress-life (S-N) behavior for various LWR steels and alloys. The Code also formulates a built-in factor of safety for each class of steels by means of the ASME design curve. The design curve is more conservative than its corresponding S-N mean data line by either a safety factor of two on stress or twenty on life, whichever is greater. For example, the use of the design curve should provide a margin of safety from unforeseen deleterious effects that could arise from such things as environment, surface finish, material variability, residual stresses, size effects, and statistical scatter of data. However, the ASME Code does not cite data to support these safety factors (Ref. 18). Furthermore, Reference 19 shows BWR environment fatigue results that fall clearly below the design curve, yielding nonconservative life estimates.

An experimental program at MEA has been designed to assess the behavior of LWR piping steels and weldments when cyclically loaded in the presence of simulated PWR environments. Part of the program will examine the effects of low dissolved oxygen PWR environments on the S-N behavior of SA 106 Gr. B steel with and without nuclear grade weldments. The end result of the work should lead to the development of a data base that could be used to formulate revisions to the ASME S-N design curves.

2.1.2 Summary of Results

During 1986, several accomplishments which facilitated the execution of the more difficult aspects of the S-N testing program were achieved. The first involved the compressive buckling problem with S-N specimens when high stress amplitudes were employed. It was found

necessary to stiffen the load train such that lateral movement would be restricted to a minimum. A system was developed that allows the load train to reciprocate axially at maximum testing loads with a minimum of friction while allowing only 0.4 mm (0.0015 in.) lateral movement of the load train at the test specimen gage length. With this improved system notched specimens were tested at loads high enough to cause failures at 125 cycles without any apparent deleterious buckling or bending of the specimen.

The second accomplishment involved building a facility capable of automatically monitoring and controlling a PWR environment for the S-N tests. The duration of the low frequency tests could be as long as six weeks per test and would obviously require a self-contained test facility capable of shutting itself down automatically if either the test terminates or a system malfunction develops. A facility has been constructed that provides high temperature, reactor-grade water to two S-N miniautoclave test systems. The facility also monitors pH, dissolved oxygen content, and conductivity of the test environment. An intricate interlock system provides a series of safeguards that protect important components of the control console against damage that could occur from conditions such as water loss, furnace overheating, jammed valves, overpressure, etc.

The miniautoclave system, used for testing both smooth and notched S-N specimens in a PWR environment, became operational this year and is working very well (Fig. 2-1).

The testing of stress-life ASME SA 106-B steel specimens has included the items listed in Table 2-1. In 1986, Items 3 through 8 were completed and Items 9 and 13 represent work in progress. S-N plots of the results can be found in Figs. 2-2 through 2-4. Figure 2-2 shows a comparison between unnotched and notched specimens tested in 288°C air, with the notched data remaining uncorrected for notch effects. This particular figure plots "net section stress amplitude" instead of pseudostress amplitude values typical of ASME design curve plots. From this figure, a two observations can be made:

(1) All of the notched data appear to fall on the same curve, with the $K_t = 2$ data possibly exhibiting slightly higher values for stress amplitudes for a given number of cycles to failure.

(2) A considerable difference between the smooth and notched data can be seen at long lives ($N_f > 10^4$ cycles). However, as higher stress amplitudes are employed, all of the data tend to converge as N_f approaches 1.

BLANK PAGE

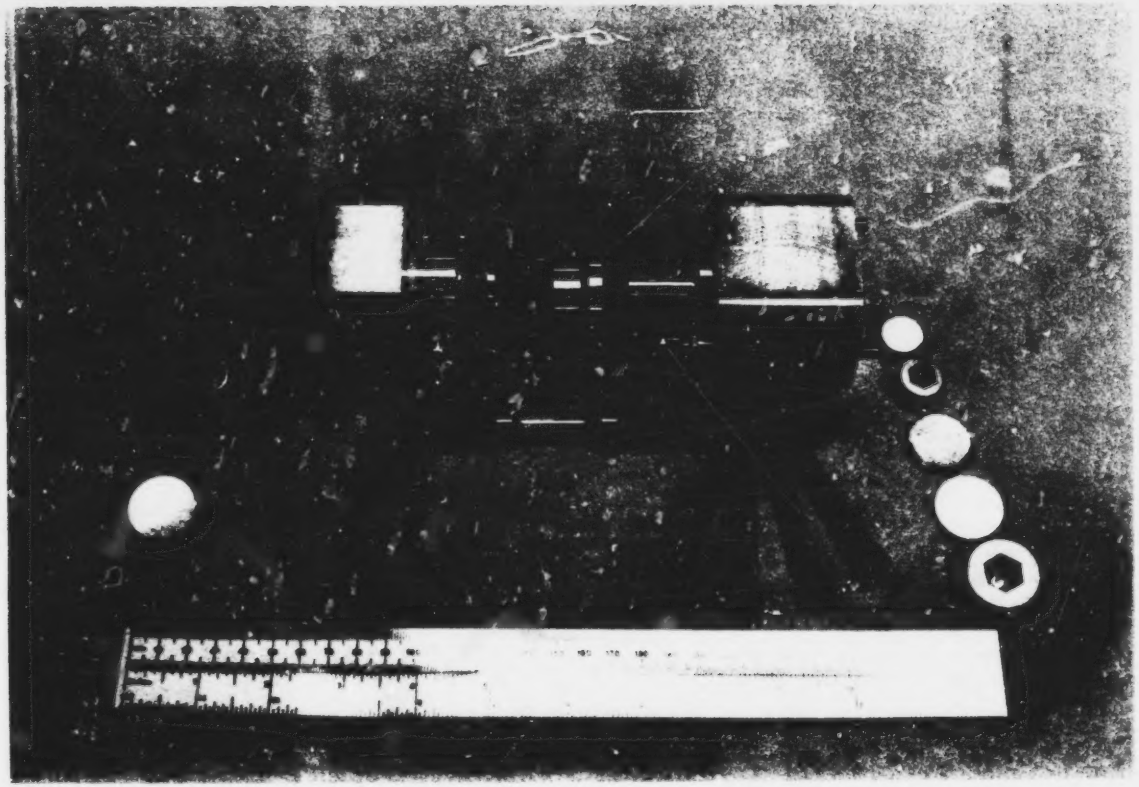

Fig. 2-1 S-N miniautoclave system.

BEST COPY AVAILABLE

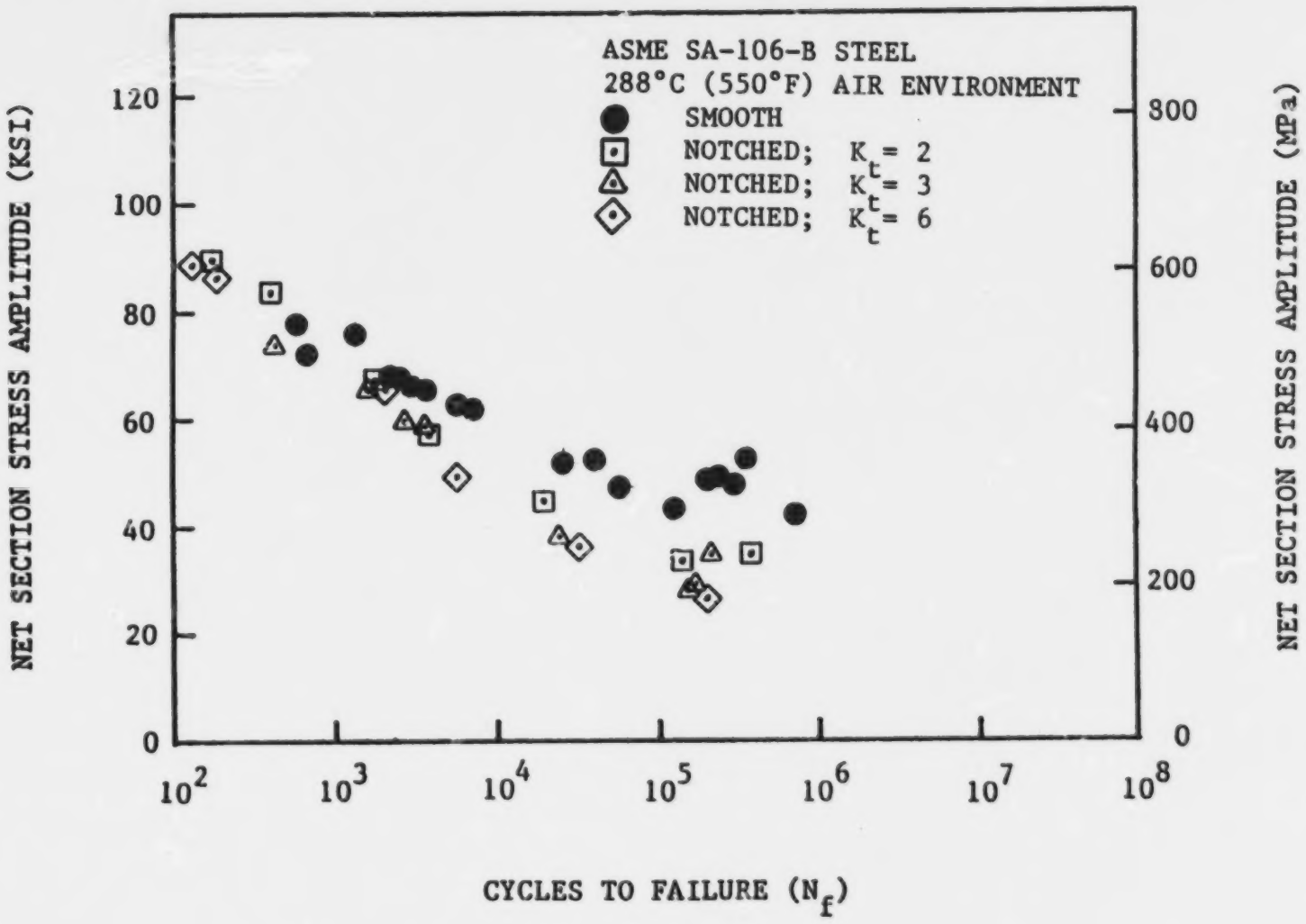

Fig. 2-2 Stress-life plot of notched and unnotched SA 106-B specimens tested in 288°C (550°F) air.

BEST COPY AVAILABLE

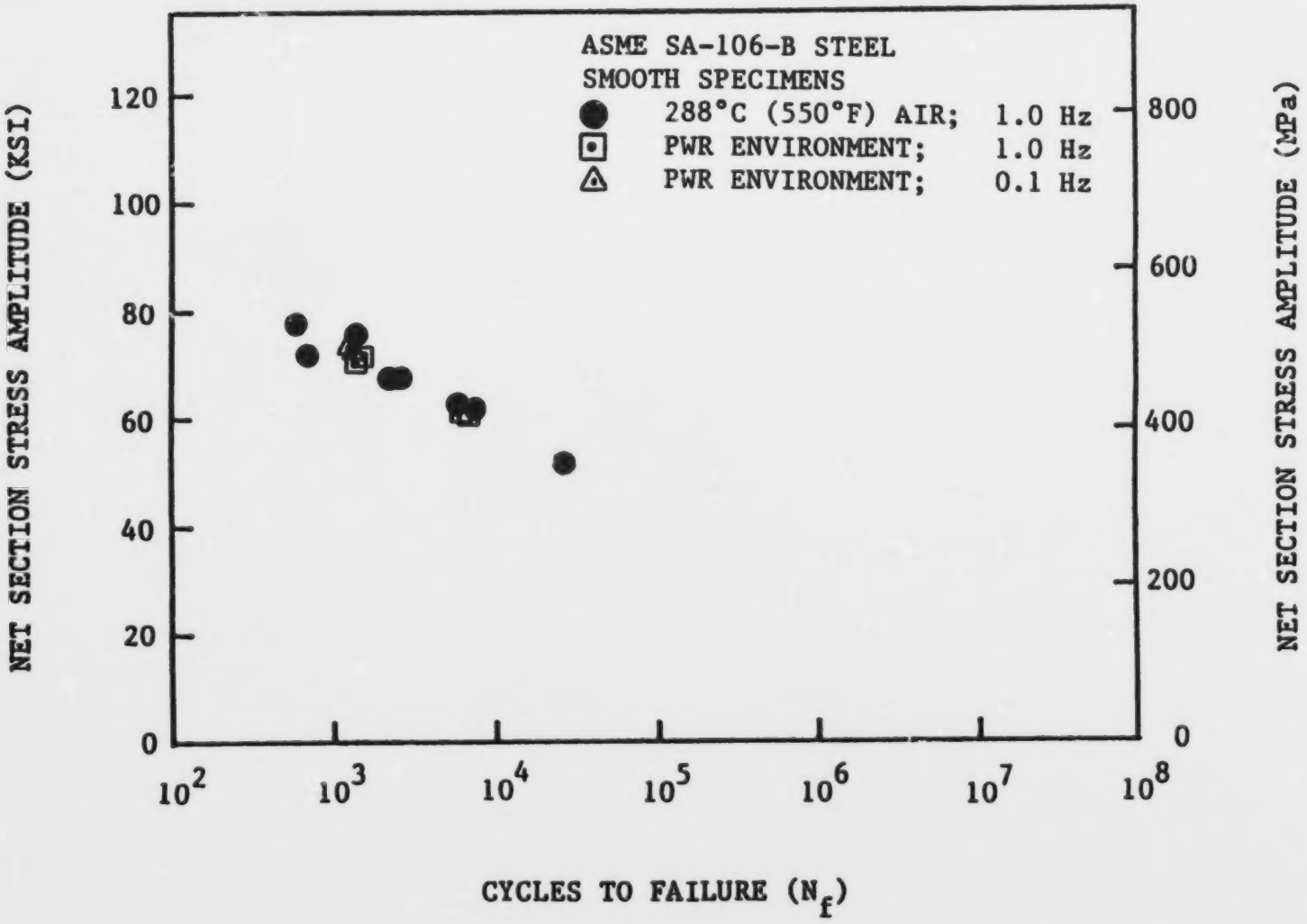

Fig. 2-3 Stress-life plot of unnotched SA 106-B specimens tested in 288°C (550°F) air and PWR environments. Frequency sensitivity study.

BEST COPY AVAILABLE

58

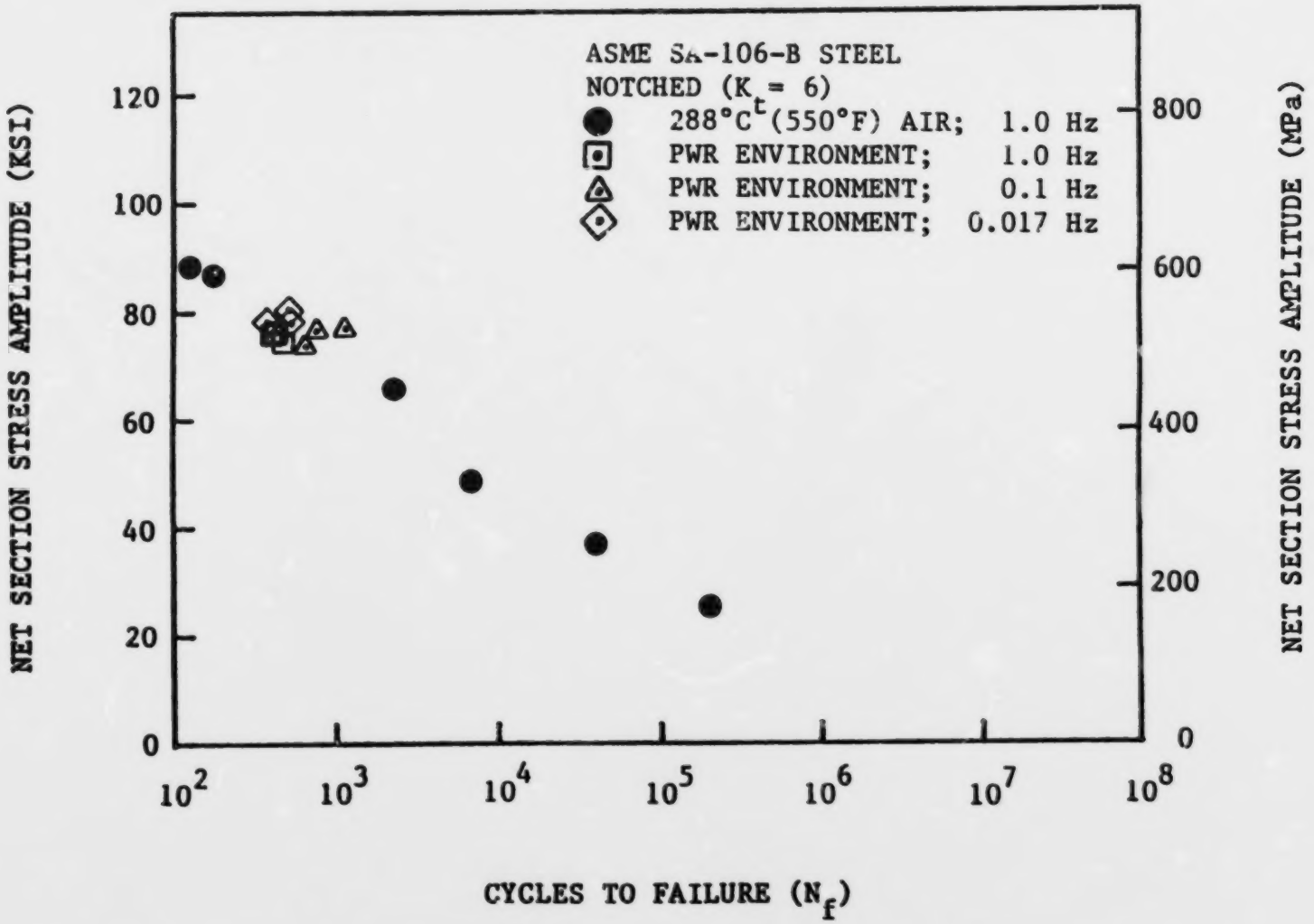

Fig. 2-4 Stress-life plot of notched (K_t = 6) SA 106-B specimens tested in 288°C (550°F) air and PWR environments. Frequency sensitivity study.

BEST COPY AVAILABLE

Table 2-1 Summary of Completed Testing

No.	Metal Type	Environment	K_t	Frequency (Hz)	Strain Ratio	Completed (%)
1	Base	24°C air	1	1	-1.00	100
2	Base	288°C air	1	1	-1.00	100
3	Base	288°C air	1	1	0.05	100
4	Base	288°C air	1	1	0.50	100
5	Weld	288°C air	1	1	-1.00	100
6	Base	288°C air	2	1	-1.00	100
7	Base	288°C air	3	1	-1.00	100
8	Base	288°C air	6	1	-1.00	100
9	Base	PWR	1	1	-1.00	50
10	Base	PWR	1	0.1	-1.00	50
11	Base	PWR	6	1	-1.00	50
12	Base	PWR	6	0.1	-1.00	50
13	Base	PWR	6	0.017	-1.00	50

The small difference in N_f values between data points having different notch severities is a result of mild steels exhibiting considerable ductility which causes notch blunting and subsequent relief of stresses in a sharp notch if insufficient constraint is present. The difference in the stress amplitude values in the 10^7 cycle regime supports Peterson's expression for K_f, the fatigue strength reduction factor (Ref. 20):

$$K_f = 1 + \frac{K_t - 1}{1 + \sqrt{\frac{a}{r}}} \qquad (2\text{-}1)$$

where K_t is the theoretical elastic notch factor, r is the notch root radius, and a is a characteristic material thickness based on the mechanical properties of the material. If the stress amplitude values for the notched specimen data points at lives greater than 10^7 cycles are multiplied by their respective K_f values, then the notched data would match the smooth specimen data. Moreover, K_f decreases in value for data whose lives are $< 10^7$ until data points from notched specimens match those from smooth specimens at $N_f = 1$ (Ref. 21). This trend can also be observed in Fig. 2-2.

If notched specimen data points were plotted on an ASME-style pseudostress-amplitude vs. cycles-to-failure graph, then an actual strain would have to be obtained and subsequently multiplied by the elastic modulus to obtain a pseudostress value. The practical means by which to obtain actual notch strain data are from approximate methods, such as finite-element analysis or Neuber analysis. Neuber's Theory (Ref. 22), being the simpler of the two methods, states that the geometric mean of the elastic notch factors for both stress and strain is equal to the theoretical notch factor, or:

$$K_\sigma K_\varepsilon = K_t^2 \qquad (2\text{-}2)$$

Accordingly, the stress and strain amplitudes at the root of the notch ($\Delta\sigma/2$ and $\Delta\varepsilon/2$) can be related to K_t by the following equation:

$$\frac{\Delta\sigma}{2}\frac{\Delta\varepsilon}{2} = \frac{K_t\left(\frac{\Delta S}{2}\right)^2}{E} \qquad (2\text{-}3)$$

where $\Delta S/2$ is the global or nominal stress amplitude.

Application of Neuber's Rule to the fatigue data results in S-N data points that appear to be much too high and fit a data curve situated well above the ASME mean data line for three reasons. First, Neuber's Rule tends to be conservative in that it predicts higher than actual stress and strain values which actually exist at the notch (Ref. 23). Second, it has been shown that a limiting notch root radius exists in notched fatigue tests below which no further influence of the notch stress concentration factor is observed in the fatigue life results (Ref. 24).

In order to plot notched S-N results on a pseudostress-amplitude vs. cycles-to-failure plot such as on an ASME Section III fatigue curve, the "worst-case notch" concept may have to be applied. This entails the application of both Neuber's Rule and a fracture mechanics description of sharp notches. Current efforts are directed to this methodology so that notched S-N results can be displayed on the ASME fatigue curve plot.

The results of PWR environment testing are presented in Figs. 2-3 and 2-4. Figure 2-3 shows the results (to date) from the frequency sensitivity study performed on smooth specimens. Little effect has been found for frequencies of 1 Hz and 0.1 Hz at higher stress amplitudes. Figure 2-4 shows the results (to date) for the frequency sensitivity study performed on notched specimens ($K_t = 6$) at 1 Hz, 0.1 Hz, and 0.017 Hz. The evidence indicates that 1.0 Hz may result in the shortest times to failure. However, no conclusions can be reached until the sensitivity study has been completed. Testing on S-N specimens is expected to proceed without incident.

2.2 Mechanisms and Models for Environmentally-Assisted Fatigue Crack Growth

W. H. Cullen, H. Hanninen, and G. Gabetta

2.2.1 Background

There are many contrasts between the applied load-environment characteristics of a power plant component and the load-environment parameters of a laboratory test. While every attempt is made to provide as much similarity between the two as possible, there are variables, such as load range, temperature, water chemistry, and flow rate, which are usually controlled at a constant value in the laboratory, but which vary over an allowable range in a power reactor. In addition, the load spectrum in the laboratory is usually characterized by a constant amplitude and frequency or is a relatively simple variable amplitude spectrum. The cyclic period of laboratory tests ranges from about 1 mHz to 20 Hz, while cyclic frequencies in the power plants will range down to the microhertz regime for the start-ups, power loadings and unloadings which may consume several hours of clock time. In addition, about 95% or more of the power reactor load cycles will occur at very high load ratios, approximately 0.95 to 0.99 as compared with laboratory tests, usually carried out at lower load ratio regimes. Clearly, the laboratory tests are carried out as a best-effort approximation to the power plant application and are often aimed at determining the worst-case or most conservative boundaries for environmentally-assisted fatigue crack growth behavior. Understandably, the laboratory data sets will often lack a definitive connection with the engineering application in one or more respects.

The theoretical solution to this dilemma is to identify the one or more micromechanisms, in the atomistic or electrochemical sense, and provide a calculational model, based on first principles of materials science, mechanics, and corrosion chemistry, which can be used to predict the environmentally-assisted fatigue crack growth rates for the case of the widely varying, reactor-typical situation. The ideal model would allow for growth rate prediction when two or more variables are simultaneously changing, such as temperature and load, as well as for the extrapolation of effects to regimes for which laboratory tests cannot be reasonably conducted, such as near-threshold stress factor or ultra-high load ratio values. The objective of this subtask is to identify, describe, and refine the micromechanistically based model which best explains the characteristics of environmentally-assisted fatigue crack growth rates in LWR pressure vessel and piping steels. This is being accomplished by continuing to observe the phenomenological effects of critical variables on fatigue crack growth rates, by maintaining cognizance of the work in this area which is being carried out at other laboratories and by carrying out a series of laboratory experiments and analyses which will serve to identify better the mechanisms, rate-determining parameters and calculational approaches to the problem of understanding high-temperature corrosion fatigue crack growth. Much of the progress on this subtask is contributed by visiting scientists who are experts in calculational modeling and micromechanistic studies of the environmentally-assisted cracking processes.

Substantial progress was attained in this area during 1986. A study of strain rate models and their applicability to the base of fatigue crack growth rate data in PWR environments which has been obtained under NRC contracts at the Naval Research Laboratory and MEA has been completed. Through the use of a crack-tip strain rate model and a two-mechanism formulation of the environmental processes which contribute to fatigue crack growth rates in PWR environments, it was shown that many of these results, including the temperature dependence of crack growth rates in A 508-2 steel could be successfully included within the predictive abilities of the model. A NUREG report was published which describes the derivation and application of this model (Ref. 25).

While the derivation of fatigue crack growth rates is the primary result of the investigations into environmentally-assisted cracking of LWR materials in PWR environments, much information has been gained from fractographic analyses, electrochemical testing, and constant extension rate testing. For the last several years, MEA has carried out, with the help of the Technical Research Centre of Finland, a series of investigations of the morphology and constitution of the oxide formation on the fatigue fracture surfaces. It is hoped that post-test interpretation of the oxide characteristics will assist in the accurate understanding of the crack-tip processes which led to the particular oxide compositions found on the flanks of the fatigue crack. One promising technique for the determination of trace elements which are present in the oxides is X-ray Photoelectron Spectroscopy (XPS). In this technique, a few Angstroms of oxide thickness is analyzed, then ion-sputtering is used to remove a thin layer of oxide (5 to 50 Å is customary), and the procedure is repeated. In this way, the oxide composition may be determined as a function of depth. While XPS uses characteristic X-radiation lines to excite photoelectrons, Auger Electron Spectroscopy (AES) uses an electron beam to excite and eject core electrons from the substance under analysis. The subsequent electronic transitions which occur in order to fill that electronic state result in the ejection of Auger electrons, which carry an energy specific to the atom from which they originated. Together XPS and AES are powerful tools for the analysis of surface films and diffusion gradients near surfaces. The results of several such XPS and AES analyses, spanning a wide range of pressure vessel materials and crack growth rates, have been assembled; and a NUREG report (Ref. 26) was published which describes the results of this research.

For many years, researchers have attempted to determine a phenomenological link between constant extension rate testing (CERT) and fatigue crack growth rates in LWR materials. For the most part, the CERT tests have been successful in providing information about the electrochemical potential required for stress-corrosion cracking in certain material/environment combinations, but considerably less than successful in providing a useful relationship between cracking rates in the CERT test and environmentally-assisted crack growth rates from a conventional FCGR test. This discrepancy is most acute for PWR environments, which exhibit generally low cracking potentials; CERT tests in PWR environments have often failed to produce any cracking at

all, but rather ductile failures which yield little information about environmental assistance or its characterization. There are a number of factors which may be responsible for this ineffective coupling, but all reduce to the general observation that CERT tests have not, in general, been designed to duplicate accurately the crack-tip conditions. Specifically, (1) the test specimens are customarily of virgin material, not cyclically plasticized, as is the crack-tip plastic zone material; (2) the environments are typical of bulk environments, not crack-tip environments; and (3) the stress state is uniaxial and not the multiaxial state which must obtain at the crack tip. MEA has devised a test matrix which addresses all of these issues and is carrying out a series of CERT tests using cyclically prestrained piping steels, with a variety of notch geometries to simulate various crack-tip opening displacements and stress states, and environments which are saturated with manganese sulfide, as the environment in the crack-tip enclave may well be.

2.2.2 Summary of Results

A combined summary of the two NUREG reports which have resulted from this work and a brief description of the objectives and approach of the CERT test matrix are given below.

2.2.2.1 A Two-Mechanism Model for Fatigue Crack Growth

In the following, a model will be described with features that are substantially those of a time base, crack-tip strain rate model. This model was derived originally at CISE from experimental data evaluation and was presented for the first time in 1984*. Since then, further work and an ongoing comparison with other developing models and with experimental data (obtained either at CISE from specially designed experiments or from data bases generated at other laboratories) gave the confidence that by using the proper data analysis several of the questions about effects of critical variables can be answered; moreover, although no definite conclusions can be made about the mechanisms involved, several suggestions on the nature of the observed enhancement come out through the model application.

Superposition models for corrosion fatigue have been already proposed several years ago (Refs. 27 and 28) Currently, the following components are considered:

(1) A purely mechanical fatigue crack growth component.
(2) A "true corrosion fatigue" component.
(3) A "stress corrosion" component.

An accurate description of a three-component model has been made by Austen (Ref. 29), as shown schematically in Fig. 2-5. The crack growth rate vs. ΔK plot for a metal in an inert environment follows

---

*G. Gabetta, ICCGR Spring Meeting, Daresbury, June 1984.

the Paris law (at ΔK above the threshold value). The presence of an aggressive environment causes an increase in crack growth rate that can be due to "true corrosion fatigue" (Fig. 2-5a), with crack growth rate still following Paris law or can be due to "stress corrosion", introducing a plateau-like component (Fig. 2-5b). Both "true corrosion fatigue" and "stress corrosion" components can be present, as shown in Fig. 2-5c.

This last situation is found when testing medium- to high-sulfur level A 533-B pressure vessel steel in either PWR or BWR water. Therefore, to predict the maximum crack growth rate one can expect for given set of test conditions, quantitative evaluation of both of the processes involved is required. The model approach proposed here is to separate the different components and try to construct a quantitative evaluation for each of them, which could be used for the prediction of further results. The approach is quite empirical, and the parameters are derived by mathematical fits to the existing data base. The two environmental components of crack growth rate are treated separately; for the stress corrosion component, the classical stress corrosion approach based on strain rate is used.

True Corrosion Fatigue Component

As already mentioned, the true corrosion fatigue component is expected to give rise to a da/dN plot that follows the Paris law; experimental results have confirmed that when only this component is present, da/dN is ΔK dependent, while little or no time-based effects are noticed. For instance, frequency effects are very small, as for air data. Moreover, the SEM examination of fracture surfaces reveals features usually indicated as "ductile" (Refs. 30 and 31), similar in appearance to fracture surfaces of specimens tested in air. For a quantitative evaluation of the true corrosion fatigue component on A 533-B specimens tested at 288°C in reactor grade water, the ductile fracture surface appearance has been used as proof that only true corrosion fatigue was present. The da/dN vs. ΔK values of test sections showing that type of fractographic appearance reside on a line whose equation has been fitted with a least-squares linear best fit:

$$da/dN = 3.41 \times 10^{-8} \Delta K^{2.575} \text{ (mm/cycle)} \qquad (2\text{-}4)$$

This line is shown in Fig. 2-6. This equation will be referred to as the "CISE ductile base line" and is used in this report as a baseline to evaluate the magnitude of the stress corrosion component from experimental data. This equation is intended to be valid for the pressure vessel steel/pure water system at 288°C. It is also very close to the baseline equation proposed by J. Gilman (Ref. 32), obtained from constant ΔK experimental data*.

---

*W. Van Der Sluys and R. Emanuelson, EPRI Program Review, Battelle,

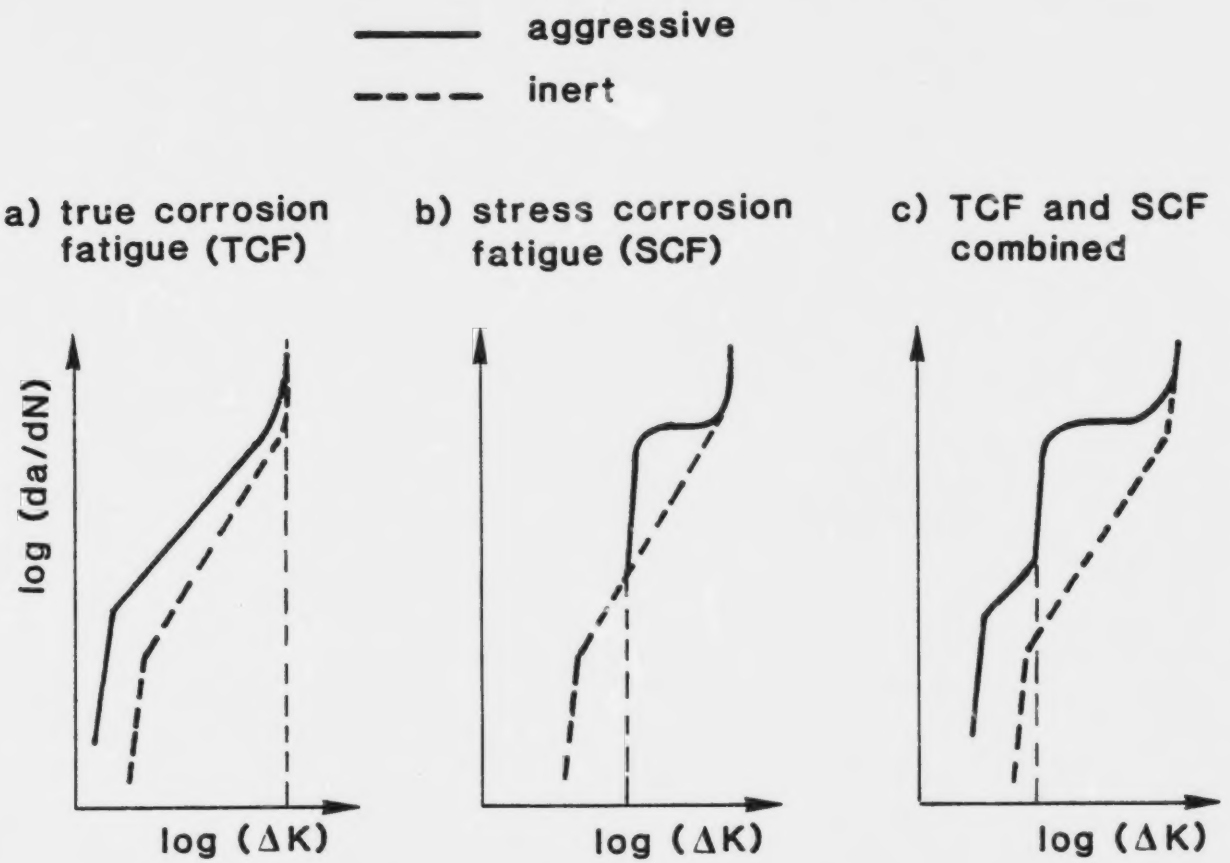

Fig. 2-5 Schematic of the three-component model for environmentally-assisted crack growth (Ref. 29).

BEST COPY AVAILABLE

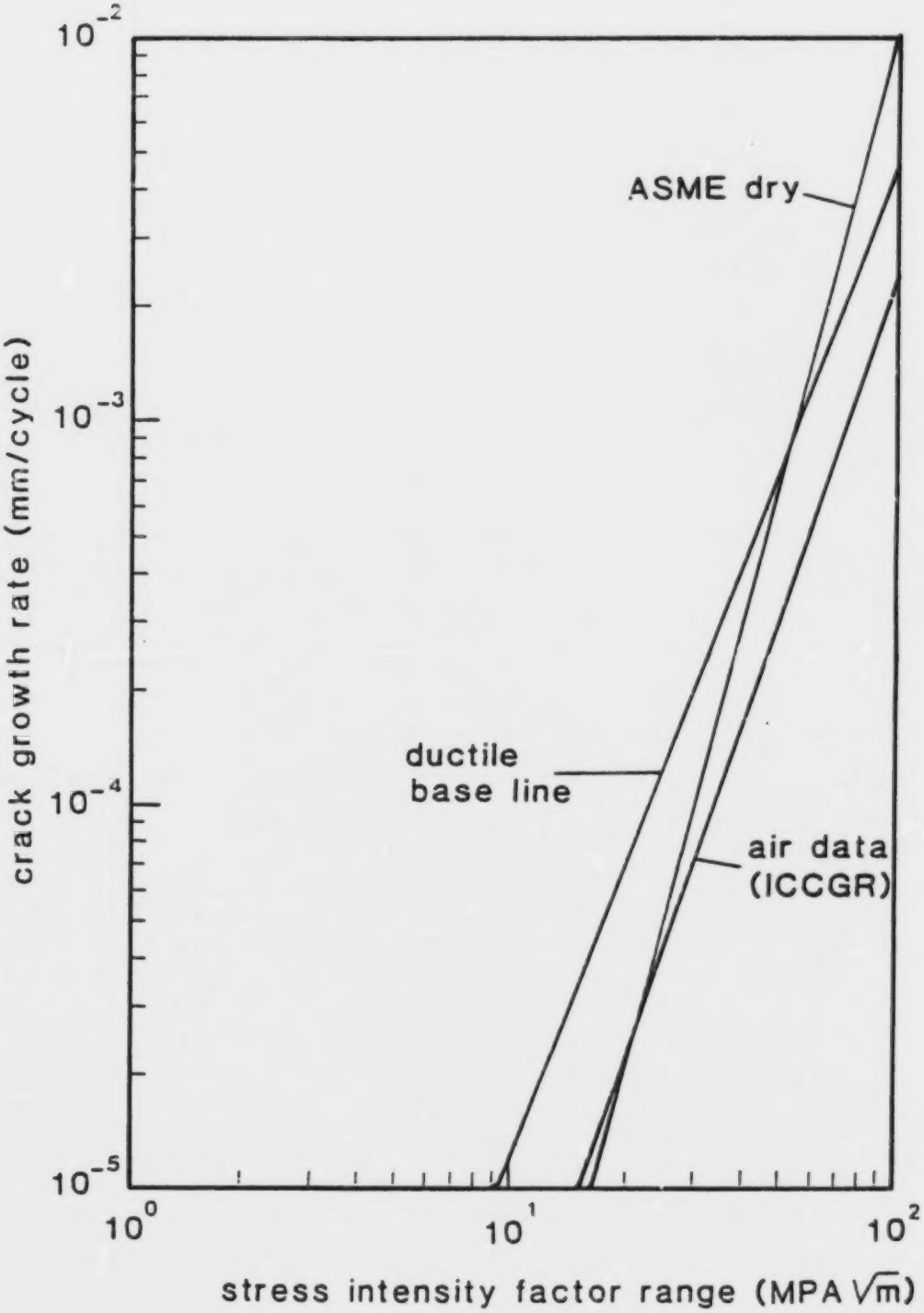

Fig. 2-6 CISE ductile baseline for fatigue crack growth, compared with the ASME code dry line and with air data from ICCGR.

BEST COPY AVAILABLE

In Fig. 2-6, the air line curve, as obtained by best-fitting data from several laboratories (Ref. 33) is reported. All data are from pressure vessel steels tested at 288°C. The two lines are almost parallel, the ductile baseline in water showing higher crack growth rates due to the environmental enhancement. The ASME XI Code line for air data, also reported for comparison, has a different slope.

Stress Corrosion Component

The so-called "stress corrosion component," introduces a plateau-like behavior in the da/dN vs. ΔK plot. This plateau indicates a region where dependence on ΔK does not exist. The existence of that plateau was shown several years ago by stress corrosion specialists who worked with precracked specimens (see Fig. 2-7). Such a plateau can be found in crack growth rate results obtained from A 533-B in pure water at 288°C, when in presence of some peculiar material/environment conditions, i.e., a sulfur content in excess of a minimum value, a laminar flow rate, and so on. When those conditions are present, an approach similar to the one used for a traditional stress corrosion test is supposed to be useful to account on a quantitative basis for this crack growth rate component. In this approach, crack-tip strain rate must be known.

The true corrosion fatigue component has been quantitatively evaluated for A 533-B tested in reactor grade water at 288°C, as described in the preceeding section. Thus, the stress corrosion component of the average crack growth rate during each loading period at a given stress intensity factor was evaluated by:

$$(da/dt)_{scc} = [(da/dN)_{tot} - (da/dN)_{tcf}]/\text{loading time} \qquad (2\text{-}5)$$

It has been found from CISE environmental fatigue data*, that $(da/dt)_{scc}$ has about the same value for a wide range of frequencies (0.5 to 0.00017 Hz) and applied loads. This value is about 10^{-4} mm/s and seems to be independent of oxygen content (between 2 and 200 ppb) and of the applied ΔK. About the same value of da/dt (10^{-4} to 10^{-5} mm/s) has been measured by Speidel (Ref. 35) on double cantilever beam specimens in water environment. This is also very close to what has been measured by J. Gilman, from constant ΔK environmental fatigue tests (Ref. 32).

Crack-Tip Strain Rate Evaluation

To define crack-tip strain rate for a compact tension specimen, a very simple approach has been used, which has been already described completely in a previous report (Ref. 36). The strain is assumed to

---

*G. Gabetta, ICCGR Spring meeting, Fontainebleau, France, May 1986.

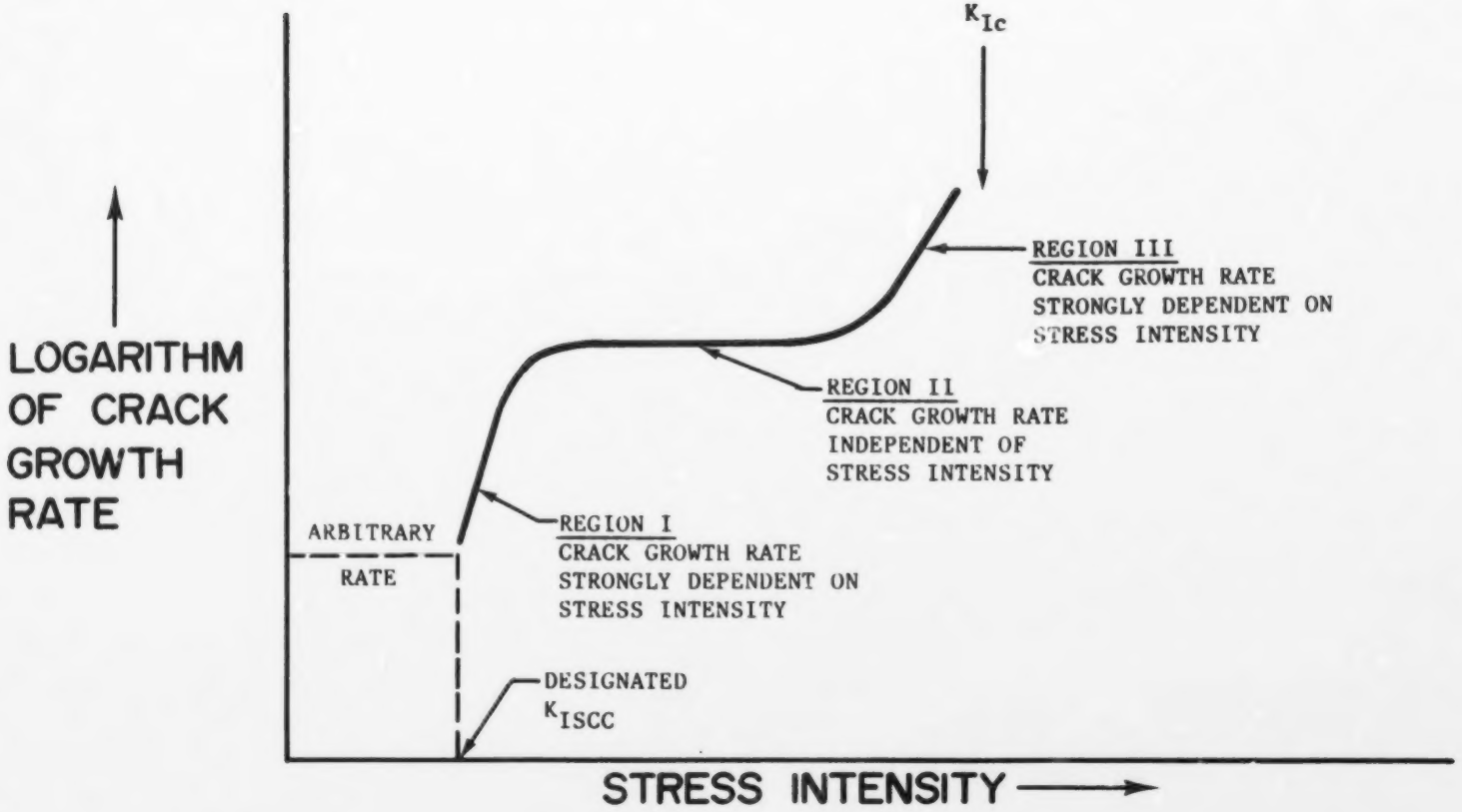

Fig. 2-7 Schematic representation of stress corrosion crack growth rates as a function of applied stress intensity factor, showing three regions which can be visibly and mechanistically differentiated. Figure adapted from Reference 27.

BEST COPY AVAILABLE

be uniformly distributed over a large zone ahead of the crack tip. The dimension of this process zone (the gage length) has been estimated as equal to the distance between the crack tip and the specimen center of rotation (x_o-a) (Ref. 37). The strain is therefore proportional to the ratio between crack-tip opening displacement (CTOD) and that gage length (x_o-a). The strain rate is calculated as the average value during rise time:

$$\dot{\varepsilon} = [(CTOD_{max} - CTOD_{min})/(\text{loading time})(x_o\text{-a})]\ (s^{-1}) \qquad (2\text{-}6)$$

A typical plot of $(da/dt)_{scc}$ vs. crack-tip strain rate is shown in Fig. 2-8 for A 533-B steel weld tested at 288°C in pure water. The plateau in this plot shows the presence of stress corrosion susceptibility for this material during fatigue tests in the environment indicated in the upper left. Moreover, this plot indicates that the SCC component during fatigue is active in a well-defined range of crack-tip strain rate. To obtain a quantitative prediction of the maximum crack growth rate, the following must be defined:

(1) The maximum cyclic crack growth rate that can be reached when all three components are active.

(2) The strain rate range (and corresponding ΔK range) where that maximum crack growth rate can be expected.

When steps 1 and 2 are known, in the presence of a material/environment couple that is stress corrosion susceptible, it will be possible to predict the maximum crack growth rate one can observe in corrosion fatigue. As the SCC component has a constant rate (constant da/dt, as shown before) for a material-environment that is susceptible to intergranular SCC (IGSCC), the maximum cyclic crack growth rate is expected to be a function of frequency.

For pressure vessel steels tested in reactor grade water, the maximum predicted crack growth rate as a function of frequency (Ref. 28), follows the equation:

$$(da/dN)_{max} = (da/dN)_{tcf} \times 10^{-4} \times (\text{loading time})\ (\text{mm/cycle}) \qquad (2\text{-}7)$$

A family of limit values for da/dN is shown in Fig. 2-9. Each curve corresponds to a different loading frequency and represents the upper limit for crack growth rate in a subcritical regime. The knowledge of the strain rate and/or of the ΔK range where that maximum value can be reached represents the second step for the superposition model.

Mechanisms of Environmentally Enhanced Crack Growth

From a mechanistic point of view, this model supports the idea that each component of crack growth rate is caused by a different mechanism. Because two components have been identified, in addition to the

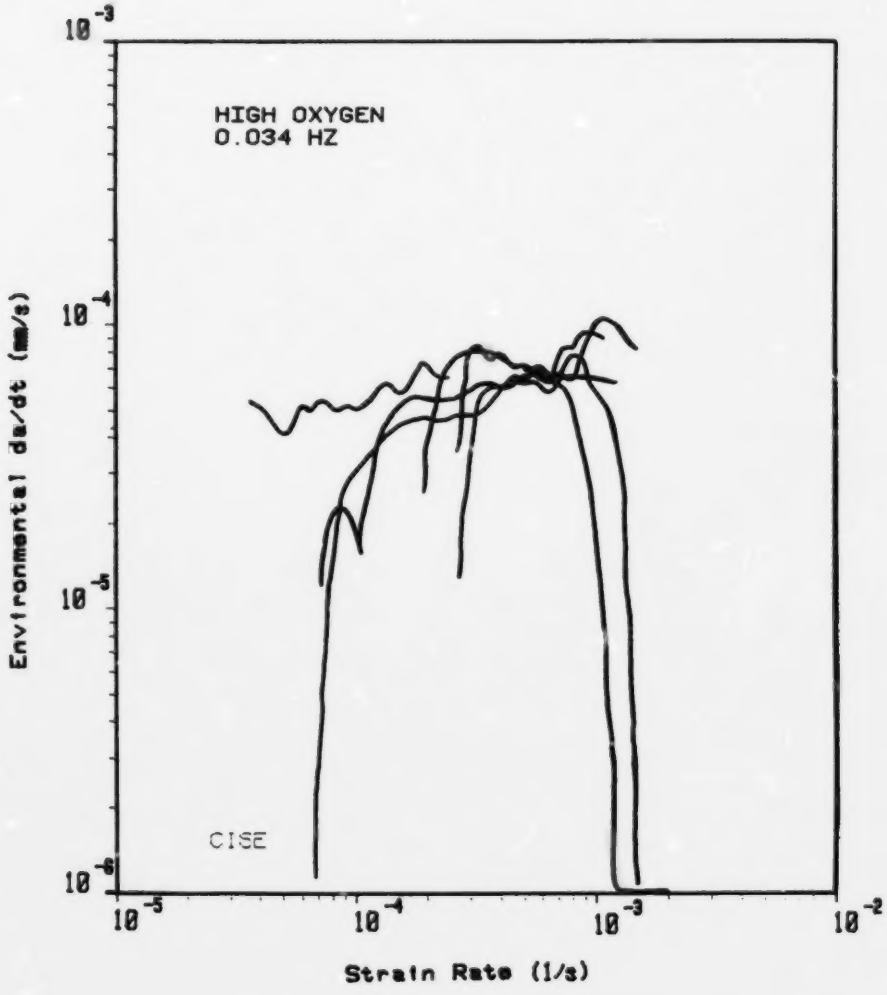

Fig. 2-8 Stress corrosion component of fatigue crack growth rate as a function of crack-tip strain rate, for tests of a pressure vessel steel in oxygenated, high-temperature water.

BEST COPY AVAILABLE

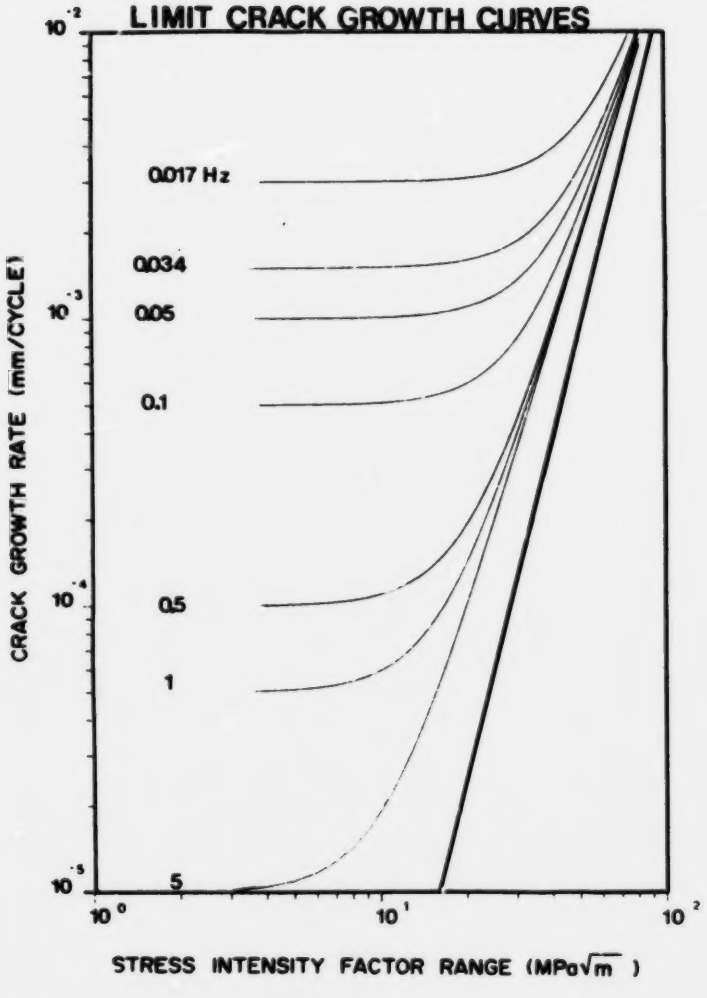

Fig. 2-9 Calculated limit curves for the maximum expected crack growth rate (empirical approach).

BEST COPY AVAILABLE

purely mechanical crack growth rate, two different mechanisms are likely to be active. In the following, they are indicated as "Mechanism A" and "Mechanism B." Mechanism A will be related to the true corrosion fatigue component, while Mechanism B is assumed to be active during stress corrosion.

Mechanism "A"

Mechanism A is always active for tests in noninert environments, at least at ΔK levels above the mechanical threshold; crack growth rate is dependent on ΔK and follows the Paris law. There is well-defined evidence that A is active also in air because:

(1) The fractography of specimens tested in air is similar to the fractography of specimens tested in water, when only true corrosion fatigue is present.

(2) Crack growth rates measured in vacuum have been found to be consistently lower than crack growth rates measured in air*.

(3) Air data have been used by Gilman (Ref. 32) to estimate the true corrosion fatigue baseline; the equation of that line is very similar to the one obtained by G. Gabetta** for the ductile baseline.

Mechanism "B"

Mechanism B causes transgranular stress corrosion (TGSCC). TGSCC has been found during SSR tests on 316 NG stainless steel, when sulfate impurities are present and no IGSCC takes place (Ref. 39). In this case, the crack velocity has been found to be linearly dependent on strain rate: tests on A 533-B have already shown that a minimum strain rate is necessary to activate the B mechanism, which causes a constant crack growth rate. When the strain rate is above a certain threshold, however, a few conditions must be fulfilled in order to observe the higher crack growth rate; one of them is that the sulfur content in the material must exceed a minimum value (Ref. 40). Moreover, it is possible that a long incubation time is required to get the cracking process started. That might be attributed to the time required for the building up at the crack tip of an aggressive environment; the amount of time required is dependent possibly on inclusion shape, size, and distribution in the material, on electrochemical conditions, and on water flow rate past the specimen mouth.

The most characteristic feature of Mechanism B is that it produces a constant crack growth rate with respect to a time base. While the estimation of this constant rate can be affected by the baseline equation that is selected (the baseline is calculated empirically, from best-fitting data; it is assumed to be frequency and R ratio

---

*L. James, ICCGR Fall Meeting, Akron, OH, Oct. 1984.
**G. Gabetta, ICCGR Spring Meeting, Fontainebleau, France, May 1986.

independent, which is likely to be not completely true), fractographic evidence does support that hypothesis* very well when showing that the spacing of brittle striations is proportional to the loading rise time.

Model Application to Fatigue Crack Growth Data

When trying to apply the model described above to corrosion fatigue data, the problem one is faced with is how to separate the true corrosion fatigue component from the stress corrosion component. As each one seems to correspond to a different crack growth mechanism, the dependence of each parameter on critical variables can be expected to be very different. Since several parameters are involved in corrosion fatigue, it can be very difficult to be able to understand the singular role of any one.

A simple dependence is assumed to exist between crack growth rate (on a time base) and crack-tip strain rate, but in addition two different mechanisms, corresponding to two different relationships between those variables, are supposed to be active. An example of da/dt vs. crack-tip strain rate is shown in Fig. 2-10, for MEA data obtained at a temperature of 288°C. In that plot, it is fairly easy to recognize the presence of a straight line, with a superposed plateau-like component. As a first approach, an empirical separation has been used by simply drawing a line to separate the two fields where, respectively, true corrosion fatigue and stress corrosion are supposed to be dominant on the basis of a visual examination of the plot.

Analytical Formulation of the Strain Rate Model

A few analytical remarks are important here. A straight line on the log/log plot of da/dt vs. crack-tip strain rate has an equation such as the following:

$$da/dt = A * \dot{\varepsilon}^{n} \qquad (2\text{-}8)$$

where A and n are mathematically determined constants. As da/dt and crack-tip strain rate are usually calculated as average values, one can multiply both sides of Eq. 2-8 by the rise time T, and substitute the analytical expression for strain rate, obtaining:

$$da/dN = A\left[\left(\frac{R+1}{R-1}\right)\left(\frac{1}{\sigma_y E}\right)\left(\frac{1}{x_o - a}\right)\right]^{n} \Delta K^{2n} \qquad (2\text{-}9)$$

---

*C. Rinaldi and G. Gabetta, ICCGR Spring Meeting, Fontainbleau, France, May 1986.

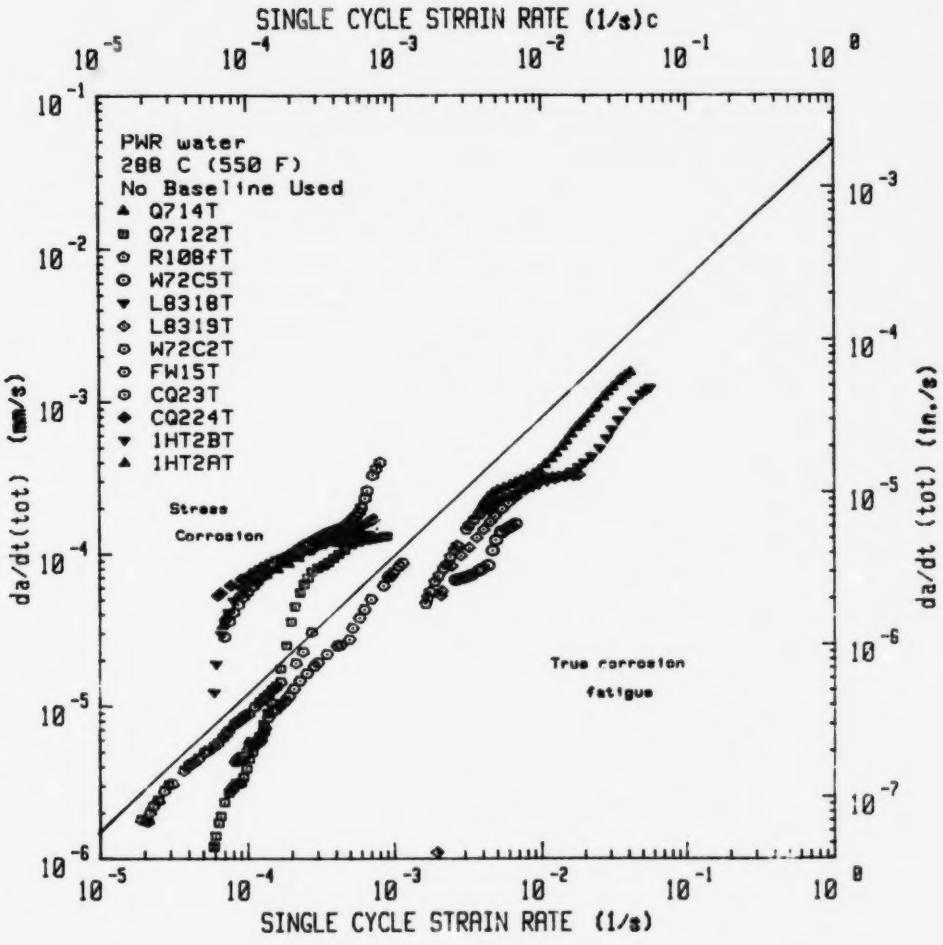

Fig. 2-10 Plot of time-based, total crack growth rate vs. crack-tip strain rate for MEA data at 288°C.

BEST COPY AVAILABLE

in which σ_y is yield stress and E is Young's modulus. Equation 2-9 is again a linear plot in log (da/dN) vs. log (ΔK), for each given R ratio and crack length [crack length is accounted for by the term (x_o-a)]. This slope is twice the slope of the da/dt vs. strain rate plot, and the intercept is a function of both strain rate and crack length. In fact for a constant load amplitude fatigue test at a fixed R ratio, as the crack length increases, the value of the intercept changes continuously, so that the result in terms of crack growth rate vs. ΔK is not a completely straight line, but is slightly curved.

When a "plateau-like" component is present, as for high temperature data, a baseline is needed to separate the two crack growth rate components. For CISE data, the calculation has been made empirically, with the help of fractographic observations. In the Gilman model, best-fit air data sets have been used.

A fairly simple analytical approach will be attempted here. As shown in Fig. 2-10, high temperature data can be separated into two parts by simply drawing a line to divide the stress corrosion from the true corrosion fatigue component. A linear best-fit has been calculated through all the points lying below the arbitrarily chosen line. The line obtained is shown in Fig. 2-11. Its equation is the following:

$$da/dt = 1.637 \times 10^{-2} \dot{\varepsilon}^{0.853} \qquad (2\text{-}10)$$

Figure 2-12 shows the data points that are supposed to be due to the stress corrosion effect, i.e., the points lying above the arbitrarily chosen line. The best-fit line through this set of points has the equation:

$$da/dt = 1.406 \times 10^{-2} \dot{\varepsilon}^{0.604} \qquad (2\text{-}11)$$

The slope of this line is close to the value found in Ref. 39 for slow strain rate (SSR) tests on smooth specimens of 316 stainless steel. The value obtained from those tests was about 0.5. The same slope on a da/dt vs. strain rate plot is found for both IGSCC and TGSCC, so that the authors of Reference 39 proposed the idea that the same mechanism is active in both cases. Using this approach, it is seen that the two different slopes found for corrosion fatigue test results do confirm the presence of two different mechanisms. Moreover, the fact that the slope relative to the "stress corrosion component" is very close to the one found during SSR tests, confirms the presence of a stress corrosion kind of phenomenon, as proposed by the model, and that this phenomenon can be present and coupled with any type of mechanical straining, monotonic or cyclic, provided that suitable environmental conditions are present. As the cyclic straining is likely to produce an even higher crack growth rate than a monotonic load, it is possible that the higher mechanical component is responsible for the higher slope found during fatigue tests. Another reason that might account for this difference is, of course, the difference

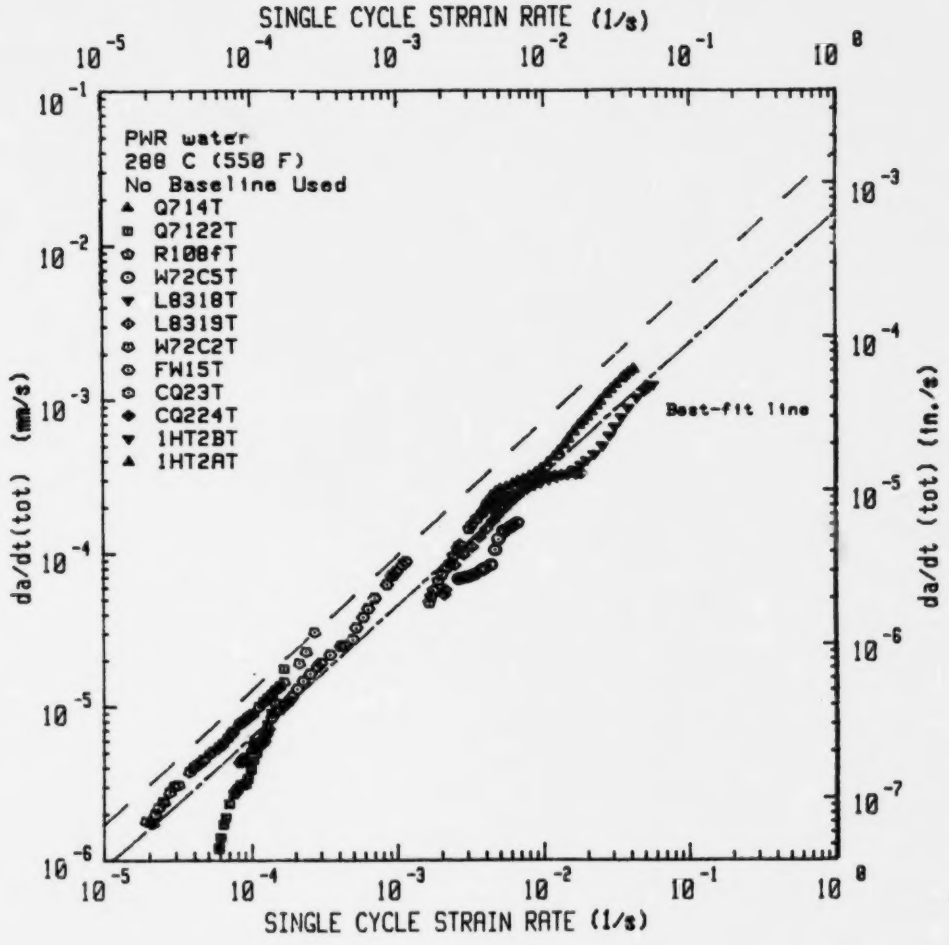

Fig. 2-11 Plot of the arbitrarily chosen true corrosion fatigue part of data shown in Fig. 2-10. The best-fit line of the included data set is also shown.

BEST COPY AVAILABLE

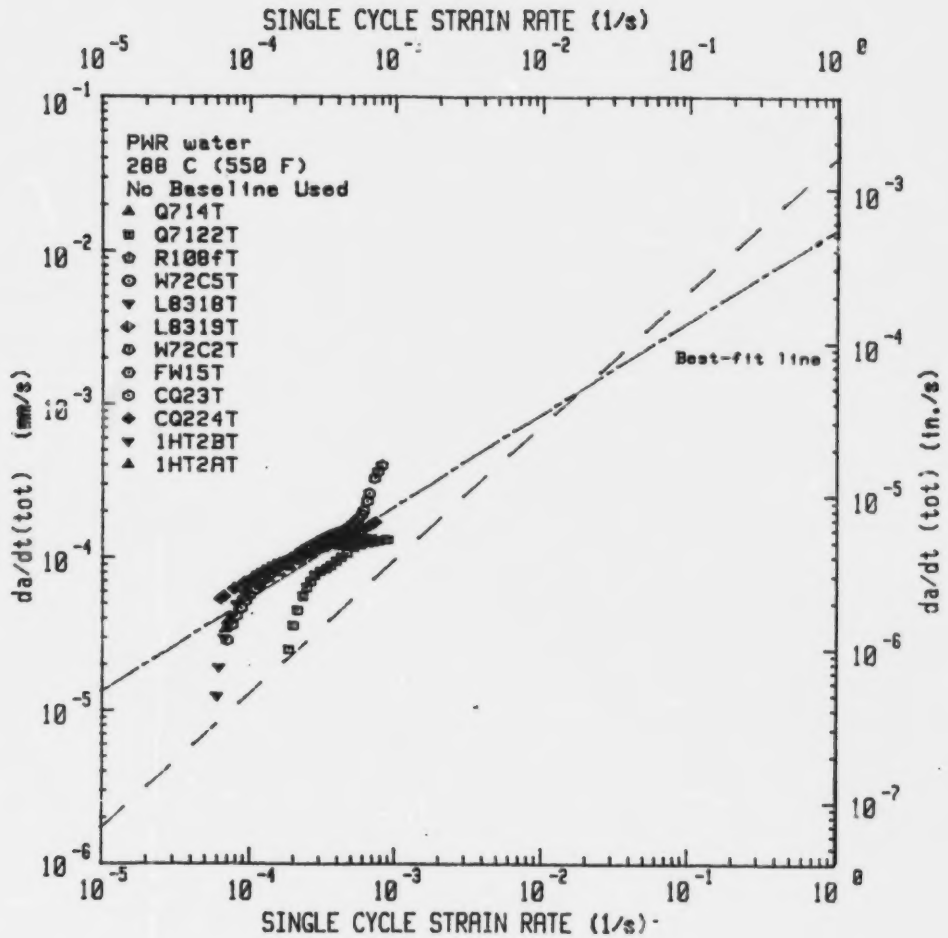

Fig. 2-12 Plot showing only the stress corrosion component of crack growth rate, as calculated by using the analytical baseline, for MEA data at 288°C.

BEST COPY AVAILABLE

in material. However, this very simple empirical way of separating the two components is probably not capable of yielding very accurate values. A base line in terms of da/dt vs. strain rate must be determined. Anyway, the comparison with SSR test data is very important because it confirms the validity of the model.

Returning to the da/dN vs. ΔK plot, the true stress corrosion fatigue component can be described by the following equation:

$$da/dN = 1.637 \times 10^{-2} \left(\frac{R + 1}{R - 1}\right) \left(\frac{1}{\sigma E}\right) \left(\frac{1}{x_o - a}\right)^{0.853} \Delta K^{1.706} \quad (2\text{-}12)$$

Using Eq. 2-12, a family of lines can be drawn by varying crack length and R ratio. Figure 2-13 shows that plot for R = 0.2 and 0.7. Each line in a group corresponds to a constant load amplitude, fatigue crack growth rate test running from a/W = 0.3 to a/W = 0.7. The ductile baseline, as calculated by CISE experimental data, has been superposed on that plot, together with the CISE data points used to calculate the best-fit. A good correspondence is shown between the analytical and the empirical baseline, which has been calculated by data obtained mainly at an R = 0.2 (a few points at R = 0.7 were nevertheless taken into account).

As Mechanism A is assumed to be active in air, it is interesting here to compare the extensive study of air data made by Eason*, with the baseline Eq. 2-12. One difference is found in the fact that while no frequency effect is supposed to be due to Mechanism A, a small, but calculable effect of frequency has been found by Eason through an analytical treatment of data supplied by several laboratories. On the other hand, a comparison of the R ratio correction factor proposed by this author, with the R ratio correction factor as contained in Eq. 2-12, is shown in Fig. 2-14. The agreement between the two is quite good, at least for R ratios less than 0.8.

2.2.2.2 Results of XPS Studies of Fatigue Fracture Surfaces

Sulfur content of the pressure vessel steels has been established to be one of the major variables in determining the corrosion fatigue crack growth in LWR environments (Refs. 40 to 44). The chemistry and electrochemistry inside the crack is affected by the dissolution of the MnS inclusions of the steel. Exposure of the MnS inclusions at the crack tip is affected by many additional parameters like the form, size, and amount of MnS inclusions on the crack path. The MnS inclusions dissolve in LWR water (Refs. 45 and 46) and form sulfur ions inside the crack. Moreover, the impurities from bulk water can migrate into the crack, affect the crack-tip chemistry, and form stable corrosion products.

---

*E. Eason, ICCGR Spring Meeting, Fontainebleau, France, May 1986

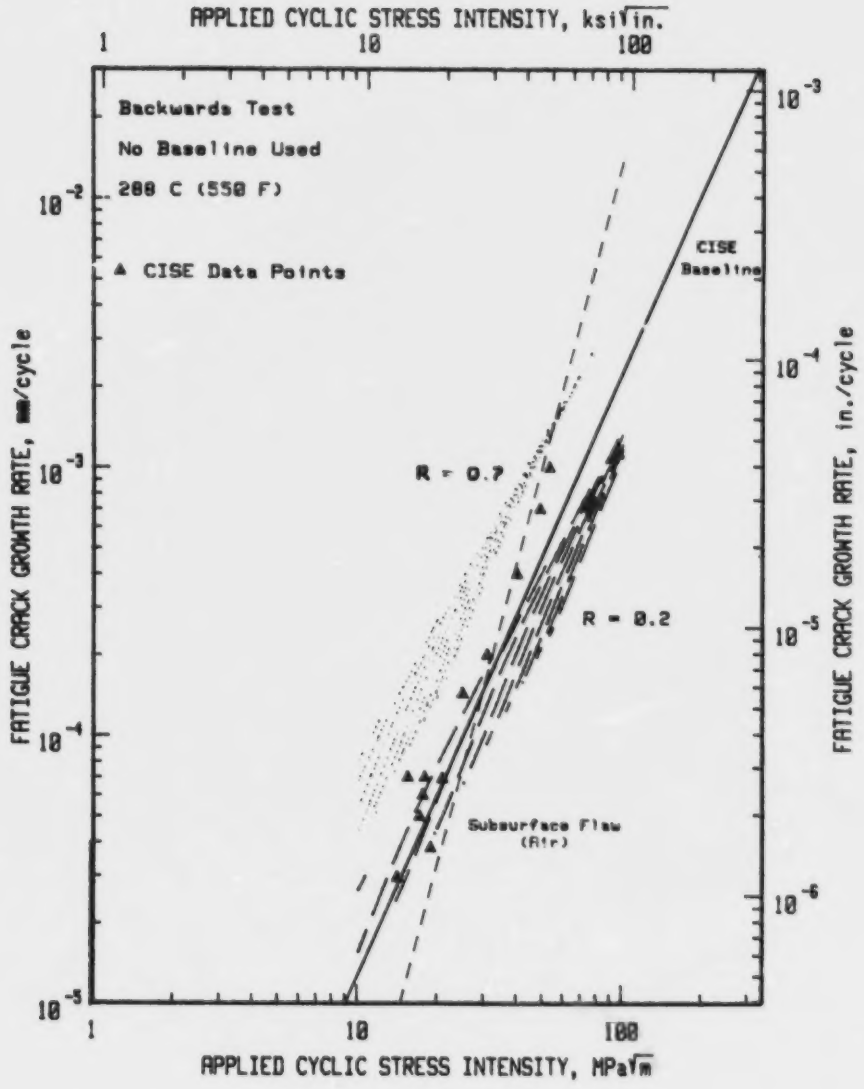

Fig. 2-13 Family of baselines obtained analytically from MEA data at 288°C. The CISE empirical baseline is included also for comparison.

BEST COPY AVAILABLE

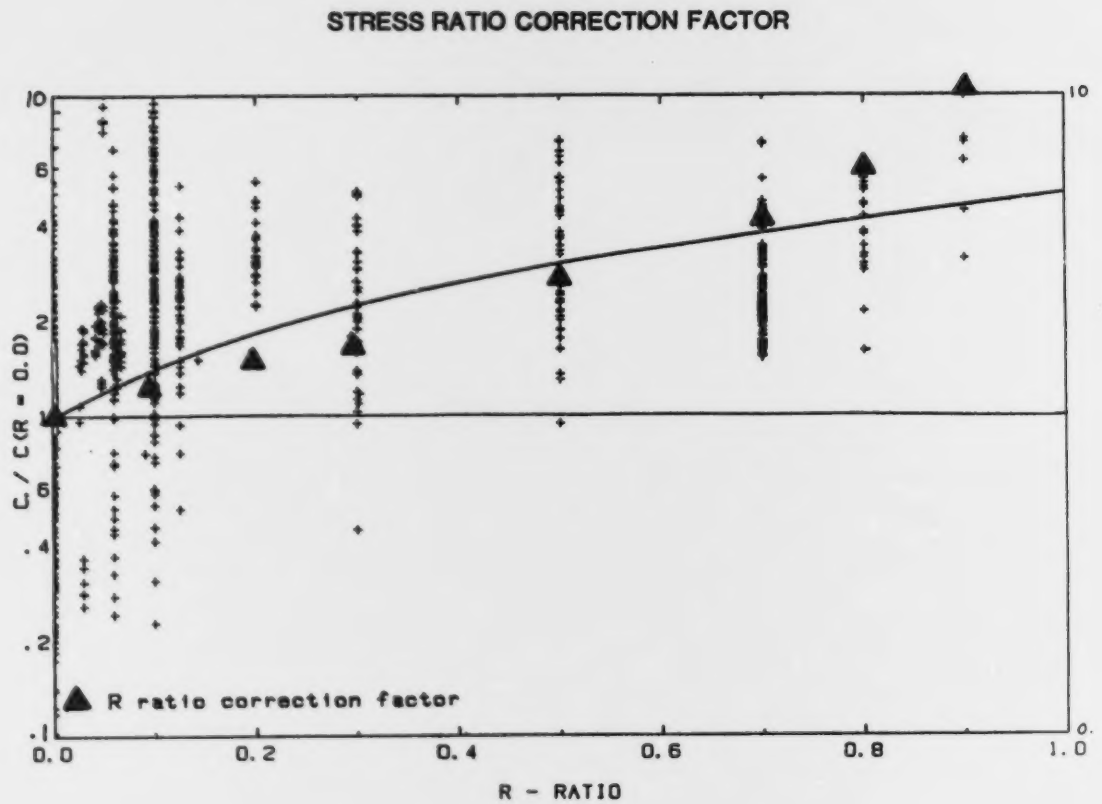

Fig. 2-14 Correction factor for R ratio, based on a synthesis of data by Eason (Reference: E. Eason, ICCGR Spring Meeting, Fontainebleau, France, May 1986).

BEST COPY AVAILABLE

Auger Electron Spectroscopy (AES) and X-ray Photoelectron Spectroscopy (XPS) have proven to be of great value in corrosion science because of their shallow detection depth (generally of the order of 1 nm). Thus, the surface sensitivity of these techniques is orders of magnitude better than that of the typical Energy Dispersive X-ray analysis (EDS) performed by Scanning Electron Microscope (SEM) (typically of the order of 1 μm depth). XPS can detect all important elements heavier than hydrogen, whereas AES detects those heavier than lithium. This is an improvement over the normal (windowed) EDS techniques which are sensitive only to elements heavier than nitrogen. Analysis of a corrosion product film to a depth greater than 1 to 3 nm (depth profiling) usually involves ion bombardment (sputtering) coupled with simultaneous analysis by AES or sequential analysis by XPS.

The objective of this study is to analyze the composition and structure of the corrosion products on corrosion fatigue fracture surfaces formed in PWR conditions during fatigue crack growth rate testing in real crack-tip environments using XPS and AES. The environmental conditions inside the corrosion fatigue cracks are evaluated based on these results.

The samples studied belonged to three different research programs: samples 1HT-34, 1HT-41, 1HT-44, and 1HT-84 were part of the International Cyclic Crack Growth Rate Group round robin utilizing test specimens provided by Electric Power Research Institute (EPRI) (Ref. 47); samples V82-3, V82-4, and V82-5 as well as CQ2-3 and W7-2C-14 were corrosion fatigue tested at MEA (Refs. 42 and 48); and samples AP-1 and AP-1.1 were corrosion fatigue tested by Technical Research Centre of Finland (VTT) (Refs. 43 and 49). The 1HT, CQ2, and W7 samples were A 533-B plate; the V82 samples were A 508-2 forging; and the AP samples were a Cr-Mo-V steel forging. The chemical compositions of these steels are given in Table 2-2.

Table 2-2 Chemical Compositions of the Tested Steels (Wt-%)

Code	C	Mn	P	S	Si	Ni	Cr	Mo	Cu	V
A 533-B										
1HT	0.19	1.28	0.009	0.013	0.25	0.61	0.04	0.55	0.10	0.004
W7-2C	0.23	1.40	0.005	0.004	0.25	0.70	——	0.57	——	——
CQ2	0.21	1.28	0.006	0.012	0.24	0.56	——	0.53	0.12	——
A 508-2										
V82	0.19	0.69	0.007	0.009	0.31	0.82	0.38	0.62	0.13	0.010
Cr-Mo-V										
AP	0.16	0.47	0.012	0.014	0.34	0.28	2.75	0.63	0.100	0.300

For this study, specimens were selected which represented both the high and low crack growth rates of the similar steels. This study allowed comparison of fracture surfaces of low sulfur and medium sulfur steels, as well as steels with different MnS particle sizes and distributions. Also, artificial crack-simulating specimens were studied.

The oxide on the corrosion fatigue fracture surface formed in PWR-water conditions of the steels studied was found to be Fe_3O_4 (magnetite), as is expected on the basis of the electrochemical data. Sulfur was observed on the top of the oxide surface mainly as a sulfate which probably was an artifact due to oxidation during the post-test exposure to the aerated conditions. Analysis of the Fe $2p_{3/2}$ line (Fig. 2-15) showed that the major sulfur species was FeS_2. Also FeS was observed after sputtering, but because its line is very near the line of FeO (which is known to result from the sputtering of Fe_3O_4), it was not certain from which phase the information came. This finding confirms the earlier electrochemical findings (Refs. 50 to 52) that the electrochemical conditions inside the crack are in the area of Fe-S-H_2O Pourbaix diagram where both Fe_3O_4 and FeS_2 are stable phases (Fig. 2-16) (Ref. 53). In addition, in these conditions Mn is soluble, as can be seen from the Mn-S-H_2O Pourbaix diagram (Fig. 2-17)*. Therefore, Mn was not generally observed to be present in the oxide phase of the corrosion fatigue fracture surfaces.

Generally, the amount of sulfur in the oxide layer was about 3 at. %, and sulfur seemed to be present deep in the oxide phase. However, some exceptions to this were found. The corrosion fatigue fracture surface of specimen V82-3 showed about 6 at. % S, but specimen V82-4 only about 0.5 at. % on a very thin surface layer. From the crack growth behavior, just the opposite concentrations could have been expected. One explanation for this type of XPS observation can be the possibly different surface treatment of the specimens after fracture; but because of the thinness of the sulfur layer in specimen V82-4, this perhaps is not the right explanation. Possibly, it could be this specimen has been cut from the plate so that locally the sulfur content has been low on the crack path, which then results in low amounts of sulfur in the fracture surface oxide. This hypothesis was tested by examining low S (0.004 wt. % S) and medium S (0.012 wt. % S) steel specimens. Unfortunately, the medium S specimen fractured during corrosion fatigue testing and the corrosion fatigue fracture surface was further oxidized in the bulk water environment, thus preventing the reliable comparison of the fracture surface compositions. However, the fracture surface oxide of the low sulfur steel contained 1 to 4 at. % S without showing any marked enhancement in the crack growth rate. Therefore, it cannot be concluded, based on these results, if there are any critical amounts of sulfur in the oxide phase which is needed for enhancing the corrosion fatigue crack growth rate.

---

* P. Scott, Communication at ICCGR Meeting, Warrington, UK, May 1984.

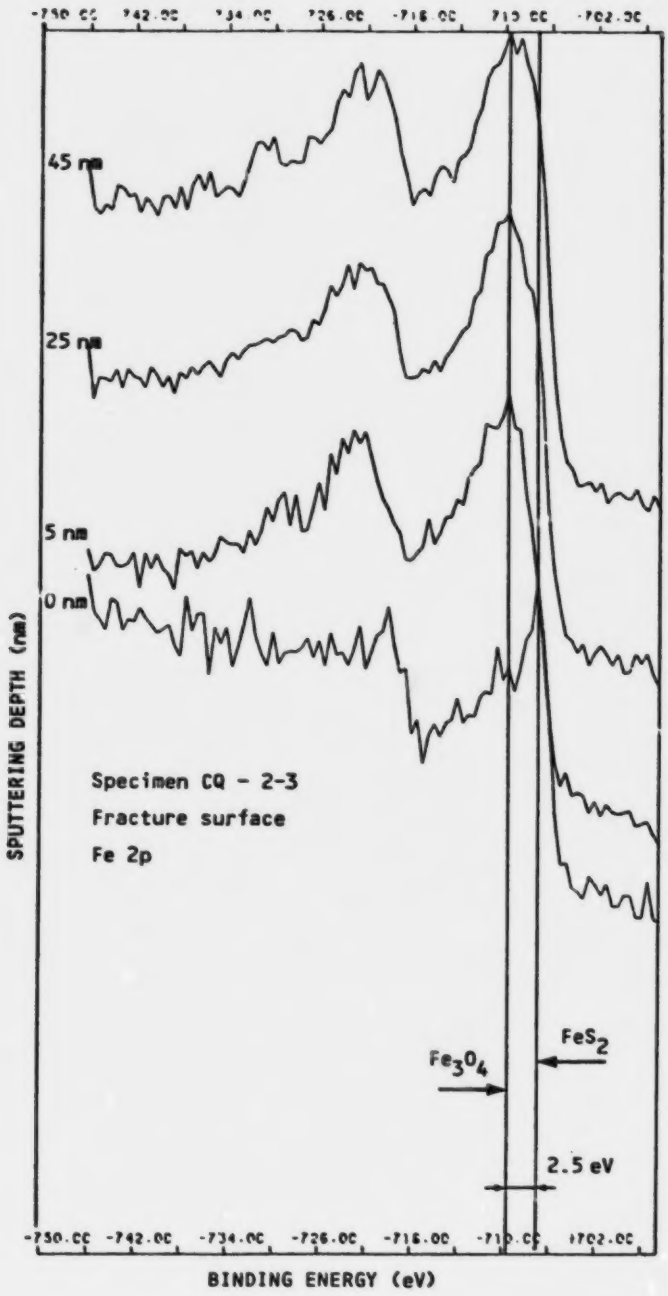

Fig. 2-15 Fe 2p spectra of specimen CQ2-3 from the fracture surface (II).

BEST COPY AVAILABLE

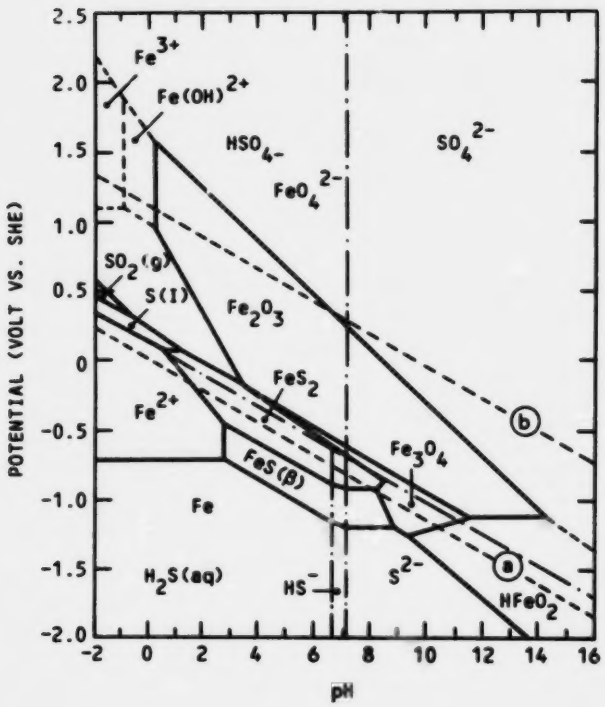

Fig. 2-16 Potential-pH diagram for Fe-S-H_2O at 300°C: a(ion) = 10^{6}, a(dissolved sulfide) = 10^{-1}, a(gas) = 1, and a(solid) = 1 (Ref. 26).

BEST COPY AVAILABLE

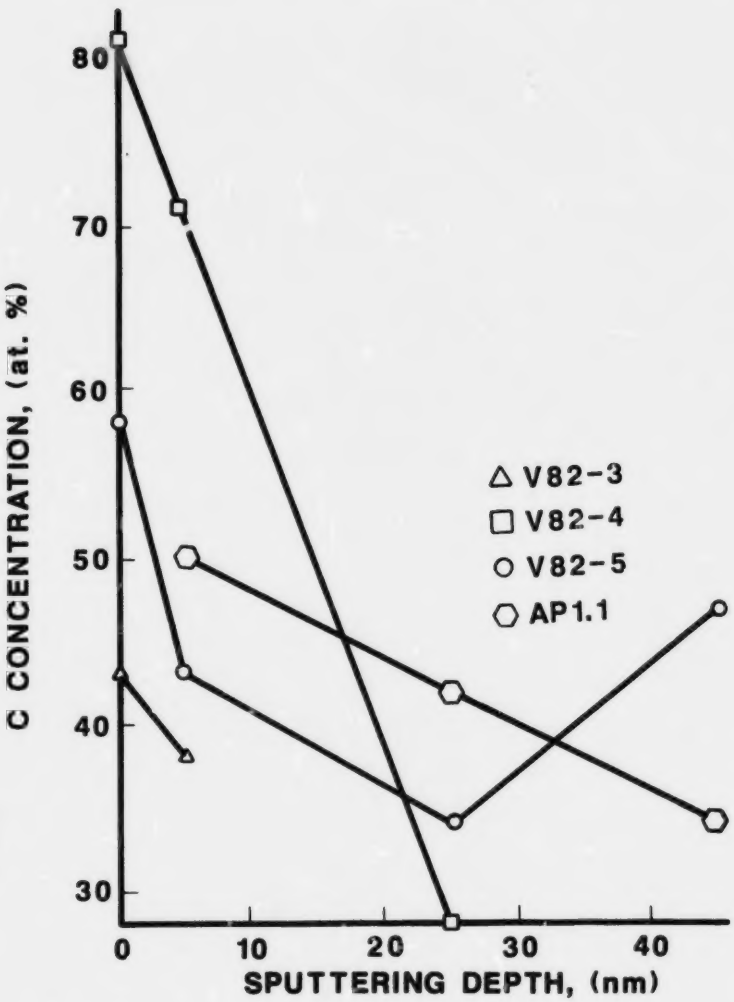

Fig. 2-17 Carbon concentration in fatigue fracture surface oxides as a function of depth as determined by AES.

BEST COPY AVAILABLE

Marked amounts of C were always observed on the top of the analyzed fracture surfaces (Fig. 2-17). The form of carbon was basically the same as graphite, but it could not be stated definitely if there were also some kind of C compounds present. After sputtering, the amount of carbon decreased rapidly at first, but then stayed at the same level. Since sputtering is known to force penetration of carbon deeper into the oxide, therefore it cannot be concluded for sure if the carbon content arises from some external source, such as the anti-corrodent spray, or whether it is forming during corrosion fatigue. In the latter case, carbon could come from the steel itself, e.g., as a result of decarburisation. However, this type of phenomenon has not been observed. Due to the low testing temperature, very high hydrogen fugacities would be needed probably for this to occur. Therefore, the authors anticipate that most of the carbon comes from the application of hydrocarbon based anticorrodents following the corrosion fatigue test. Even though this is subsequently removed, e.g., by methyl-ethyl-ketone solvent as in this study, marked amounts of carbon can still be left as in the case of specimen V82-4, where it probably disturbed significantly the reliable analysis of the corrosion product layer.

Chlorine and boron were found to be present in the oxide phases. As shown in Fig. 2-18, generally about 5 to 6 times more boron was found than chlorine. Both of these elements were found deep in the oxide which probably means that they are incorporated into the oxide phase during its growth. Boron comes from the boric acid used and chlorine is an impurity in the water chemistry. High amounts of chlorine were found especially in specimens 1HT-84 and V82-3. Specimen V82-4 also showed marked amounts of additional impurities Na and Ca in its XPS spectra. The origin of these species could not be traced back in this study.

Conclusions of XPS and AES Investigations

Based on the XPS and AES spectroscopic observations of corrosion fatigue fracture surfaces of various pressure vessel steel specimens tested in the PWR-water conditions, the following conclusions may be drawn:

- The oxide of the corrosion fatigue fracture surfaces was always in the form of magnetite (Fe_3O_4).
- Sulfur was found to be basically in the form of FeS_2, but existence of FeS could not be excluded.
- In specimens where a high crack growth rate was observed, the amount of sulfur generally at the crack tip was double that in the middle of the fracture surface behind the crack tip.
- Based on the presence of magnetite and FeS_2, the crack-tip conditions can be located in the potential-pH diagram indicating neutral or slightly acid conditions where the corrosion potential is around -500 mV (SHE) or less.

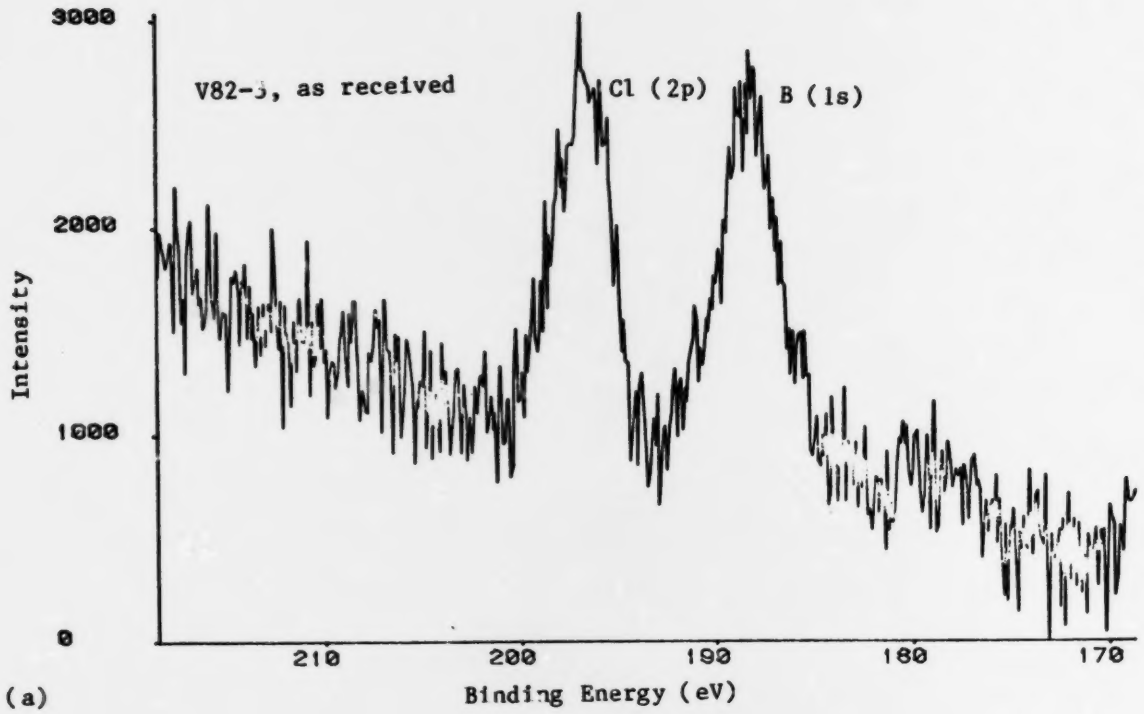

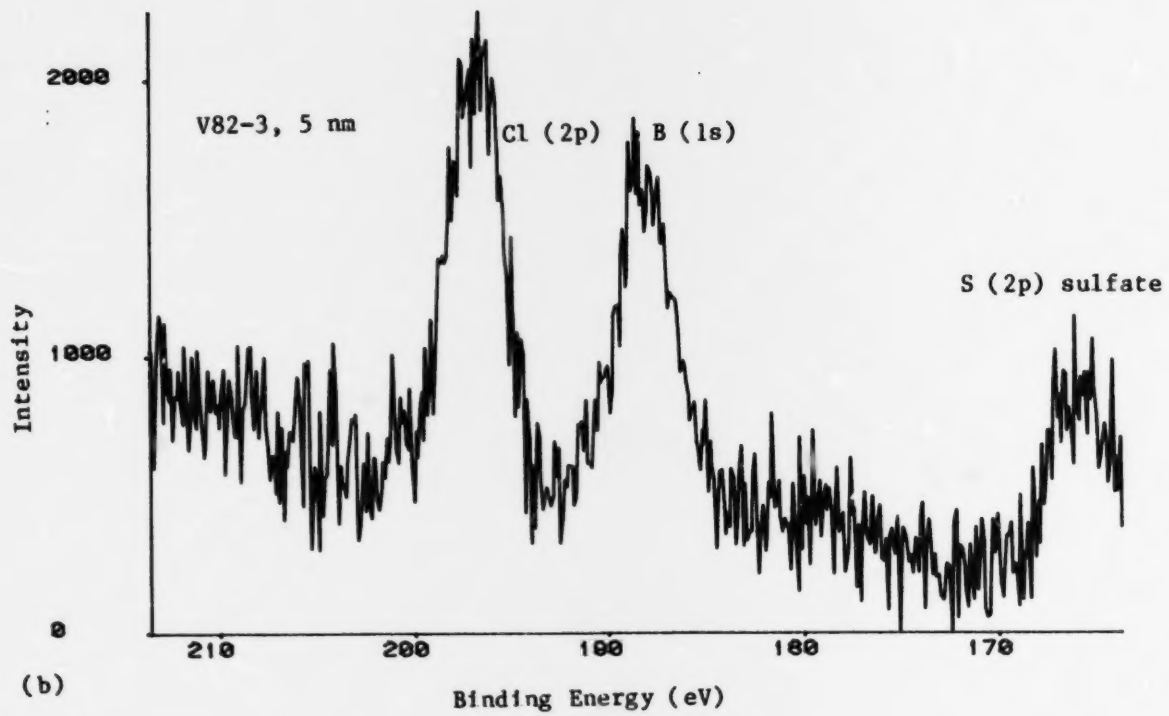

Fig. 2-18 XPS spectra of Cl 2p and B 1s of V82-3 specimen: (a) as-received condition and (b) after 5 nm sputtering.

BEST COPY AVAILABLE

- The critical amount of sulfur in the oxide phase required to produce the high corrosion fatigue crack growth rates could not be revealed. By analysis of carefully made specimens, this, however, could be possible.

- Boron and chlorine were also present in the oxide. They seem to be incorporated in the oxide during the growth of the oxide since sputtering revealed about constant values of these specie.

- Impurities in the water chemistry can be observed by analyzing the oxides with XPS and AES spectroscopies; in this study, Na and Ca were observed in some specimens in addition to Cl which was present in different amounts on the oxide surfaces of all specimens.

- The high carbon content on the top of the oxide layers made the quantitative analysis of the surface layers difficult. Therefore, in future studies, contamination of the surfaces to be analyzed should be avoided as much as possible. Also, the extended post-test exposure of the specimens to high temperature water should be avoided since the oxides continue to grow, and perhaps the most interesting layers will be covered by other layers of oxide, preventing accurate analysis of crack growth-related corrosion products.

2.2.2.3 Constant Extension Rate Testing of Cyclically Prestrained Carbon Steels in Crack-Tip Environments

The objective of this part of the mechanisms' studies is to conduct CERT tests which are designed to have a significantly higher degree of correspondence with the actual fatigue crack-tip characteristics than have CERT tests which have been conducted to the present time. In order to accomplish this, a "dogbone" type of specimen has been designed in order to cyclically prestrain large volumes [about 20,000 mm^3 (about 1.2 $in.^3$ for each specimen)] of carbon steel. Following the cyclic prestraining, this specimen, shown in Fig. 2-19, will be machined into notched CERT specimens, shown in Fig. 2-20. The notched geometries will be designed so that the notch factor ranges from K_t of 2 to a K_t of 6. This is deliberately coincident with the notch geometries of the stress-life specimens designed for use in the fatigue life work described in Section 2.1. The reduced gage section and the notch in the CERT specimen will be centered in the fully plasticized region of the dogbone panel specimen.

The tests will be conducted in miniature autoclaves fabricated of zirconium metal which will be oxidized to provide an electrically insulating layer so that the test specimen will be electrically isolated from the test system. The specimen will be cathodically polarized, in some of the tests, using conventional potentiostatic

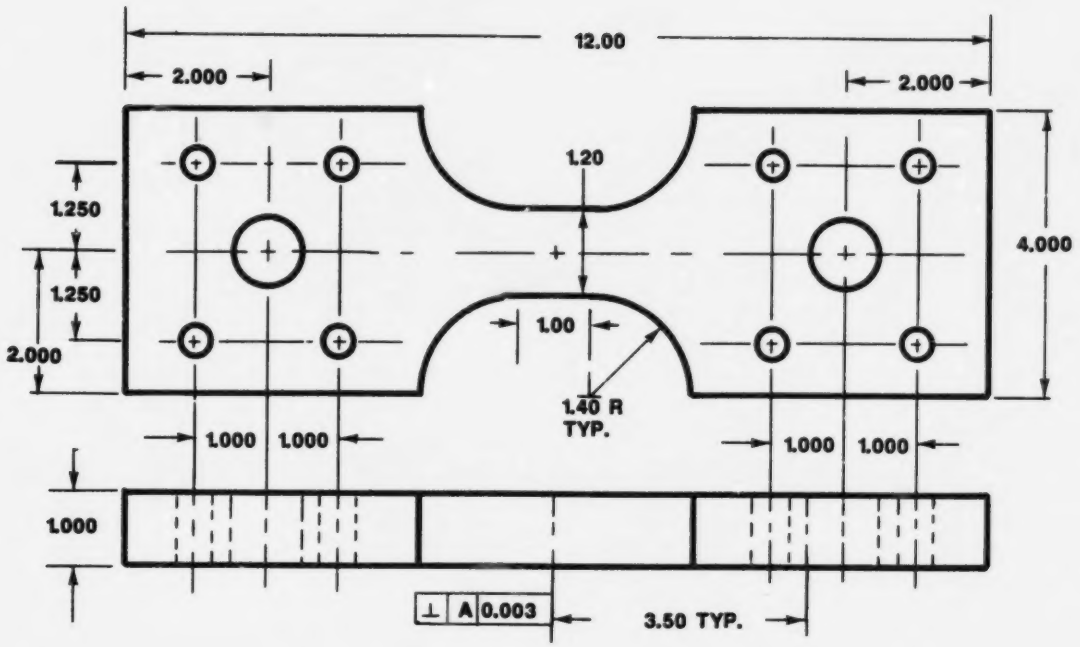

1 in. = 25.4 mm

GRINDING DIRECTION

Fig. 2-19 Specimen used to cyclically prestrain A 516 Gr. 70 carbon steel before converting material to CERT specimens.

BEST COPY AVAILABLE

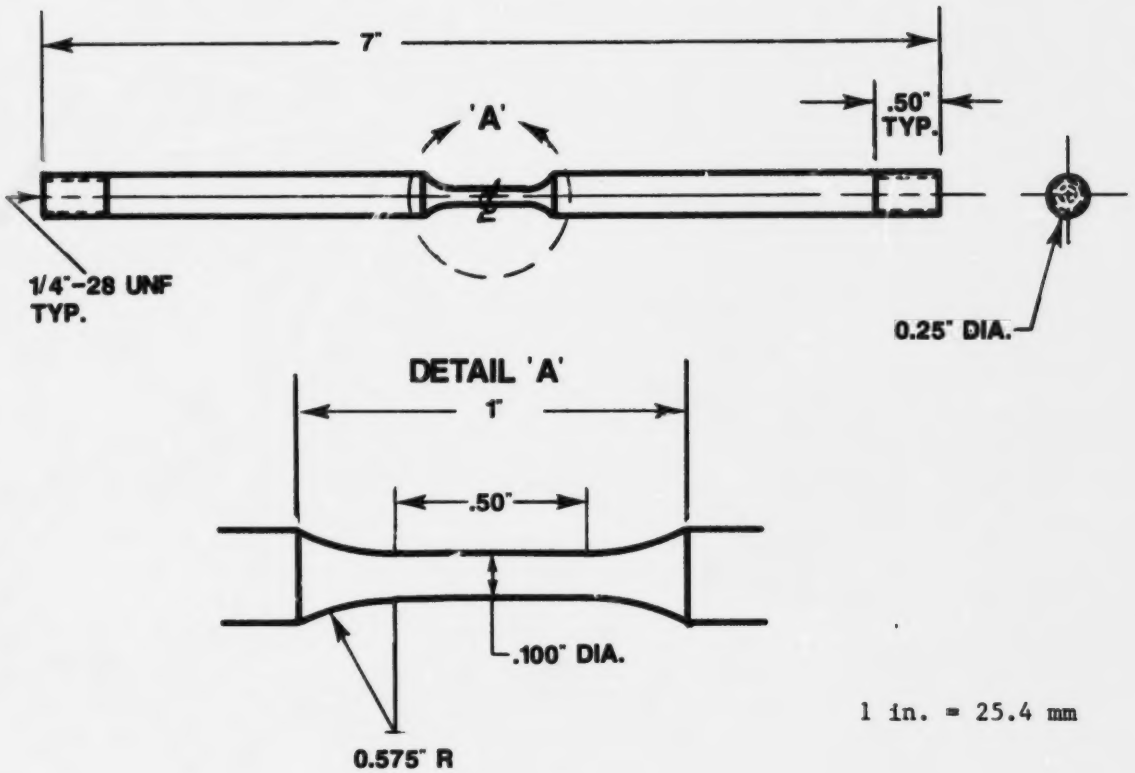

Fig. 2-20 Constant extension rate specimen to be used in this study.

BEST COPY AVAILABLE

instrumentation. The specimen will be statically pressurized with deoxygenated water which will be saturated with manganese sulfide. A water-cooled sliding seal in the bottom of the autoclave will allow straining of the specimen with a minimal loss of load due to friction. A schematic assembly drawing of the autoclave system is shown in Fig. 2-21.

The test matrix will consist of tests (a) with the various notch factors, (b) at a variety of strain rates, representing a range of strain rates likely to be obtained at the crack tip, and (c) over a temperature range of 93°C to 288°C. Cathodic potentials will be applied to simulate and extend the expected electrochemical conditions in the crack-tip enclave. The use of various notch factors not only provides the obvious range of stress concentration factors, but also results in a shift of the location of maximum triaxiality in the notch region. This, in turn, may yield a return of information on the way in which internal hydrogen (if hydrogen is the detrimental species) interacts with the steel to cause cracking.

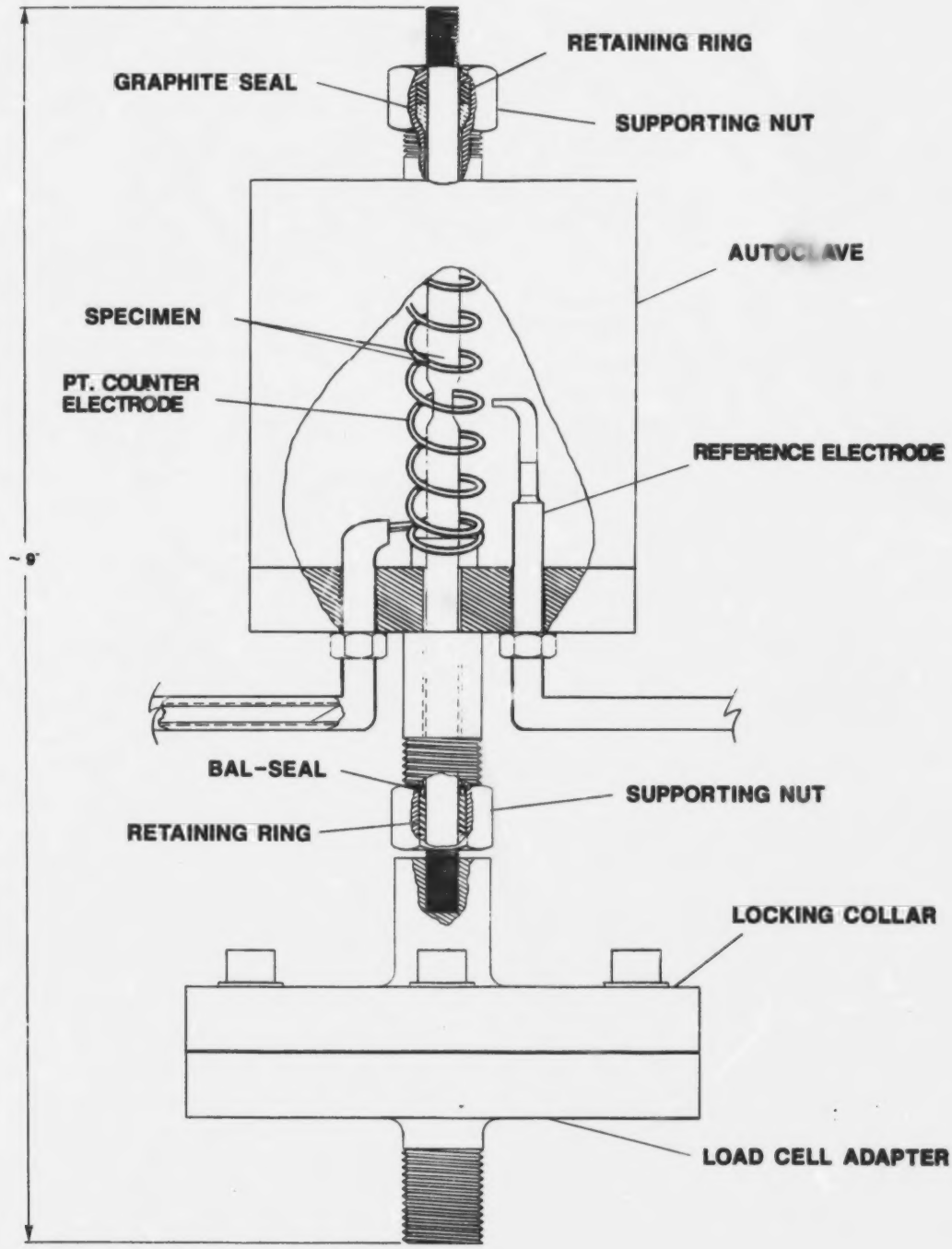

Fig. 2-21 Schematic of the autoclave used in the CERT program.

BEST COPY AVAILABLE

2.3 Cumulative Damage Factor for Environmentally-Assisted Fatigue Crack Growth

W. H. Cullen and D. R. Broek

2.3.1 Background

The in-service loading of the primary boundary is characterized by variable loads and variable frequencies, due to the pressure-, vibration-, and thermal-induced stresses acting on the system components. In contrast, most of the laboratory tests conducted to date involve constant load amplitude and frequency, in order to provide a greater opportunity to understand the effects and interactions of the critical variables. The conduct of spectrum tests in aqueous environments is not as well established a science as spectrum testing in ambient environments, although both the marine-related industries (shipping, offshore technology) provide important incentives. In those systems in which environment does not come into play, sufficiently large (but still elastic) peak loads in a multiload-level test generally cause a retardation in crack growth rates, although the amount and cyclic duration of the retardation are functions of the magnitude of the overload and the material properties, particularly the strain hardening index. Conversely, underloads or compressive loads often cause an acceleration in subsequent crack growth rates. There is very little research evidence available for variable-amplitude tests of environmentally sensitive steels conducted in aqueous environments. In the absence of a definitive micromechanistic model, there is no way to speculate on the response of pressure vessel and piping steels to variable load amplitude sequences.

Because the reference lines shown in Appendix A of ASME Section XI (Ref. 54) are based on constant amplitude crack growth rates, use of these or of constant amplitude data in general, will not provide an accurate assessment of crack extension under realistic operating conditions. Consideration of accelerations or retardations in growth rates due to load interactions will provide a more accurate assessment; incorporation of environmental effects will improve that even more. Accurate calculations of crack extension for plant-life extension or in-service inspection applications will benefit considerably from development of a data base and an algorithm for improved analysis of random load and environmental interactions.

The approach of this subtask is to perform fatigue crack growth rate tests in pressurized, high-temperature water, using loading waveforms with simple overload spectra and to attempt to develop a predictive capability for determination of growth rates incorporating the combined effects of environment and loading spectra. Initially, baseline tests are being conducted in 288°C helium gas environments, in order to ascertain the degree of retardation and acceleration which are typical of pressure vessel steels. Tests will then be carried out in high-temperature water environments, for the same patterns of waveform but at an appropriately lower frequency.

2.3.2 Summary of Results

During 1986, the balance of the simple overload and underload tests in both high-temperature helium gas and high-temperature water were completed, along with a series of three tests of the ICCGR waveform described in the previous annual report (Ref. 55) and in Reference 56. The first of the ICCGR tests was conducted in helium gas and the last two in PWR water environments with the loading rates characterized by two different cyclic frequencies. Figure 2-22 shows the crack extension results from these ICCGR tests, showing clearly that there is little difference between the test in the gaseous environment and the tests in PWR environment. The relatively small differences are due possibly to the relatively high test frequency, allowing for only a small environmental effect. Much of the calculational model development and refinement occurred during 1986, and a summary of this development and a demonstration of the results of fitting this model to the ICCGR test results are given below.

2.3.2.1 Interpretation of Constant Amplitude Data

A major problem often hampering validation and verification of crack growth load-interaction models is the representation of constant amplitude rate data. Every model needs constant amplitude data as input; if these data are an inadequate representation of constant amplitude behavior, the sometimes subtle load-interaction effects may be obscured.

The above statement may seem trivial, yet constant amplitude data are quite often misrepresented. Rate data often show considerable scatter, and it is commonly assumed that a best fit of the rate data is the best representation. However, this may or may not be the case. The criterion should not be whether the rate data set is fitted well, but whether crack growth is predicted well. A best fit of the rate data set does not necessarily give the best reproduction of the original crack growth curve. If it does not, the rate data set is misrepresented, no matter how well it was fitted.

An example is shown in Figs. 2-23 and 2-24. The regression fit of the rate data (line in Fig. 2-23) upon reintegration produces the Paris equation illustrated by the dashed line in Fig. 2-24. Clearly, this is not an ideal representation. A slight adjustment of the rate line produces the solid line in Fig. 2-24. The main cause of errors during fitting of rate data (whether the fit is linear or not is immaterial) is often due to the fact that data at high rates get the same weight as data at low rates. Yet, the high rate data represent only a small portion of total life. Thus, the bias causes errors at low rates, where most of the life is spent.

Apparently, representation of rate data is a more subtle problem than is often thought, the best fit being the one that gives the best results in use, not the one that looks best in the rate diagram. There is only one way to obtain this best fit, namely trial and error, i.e., iteration. One starts with a regression fit to the rate data.

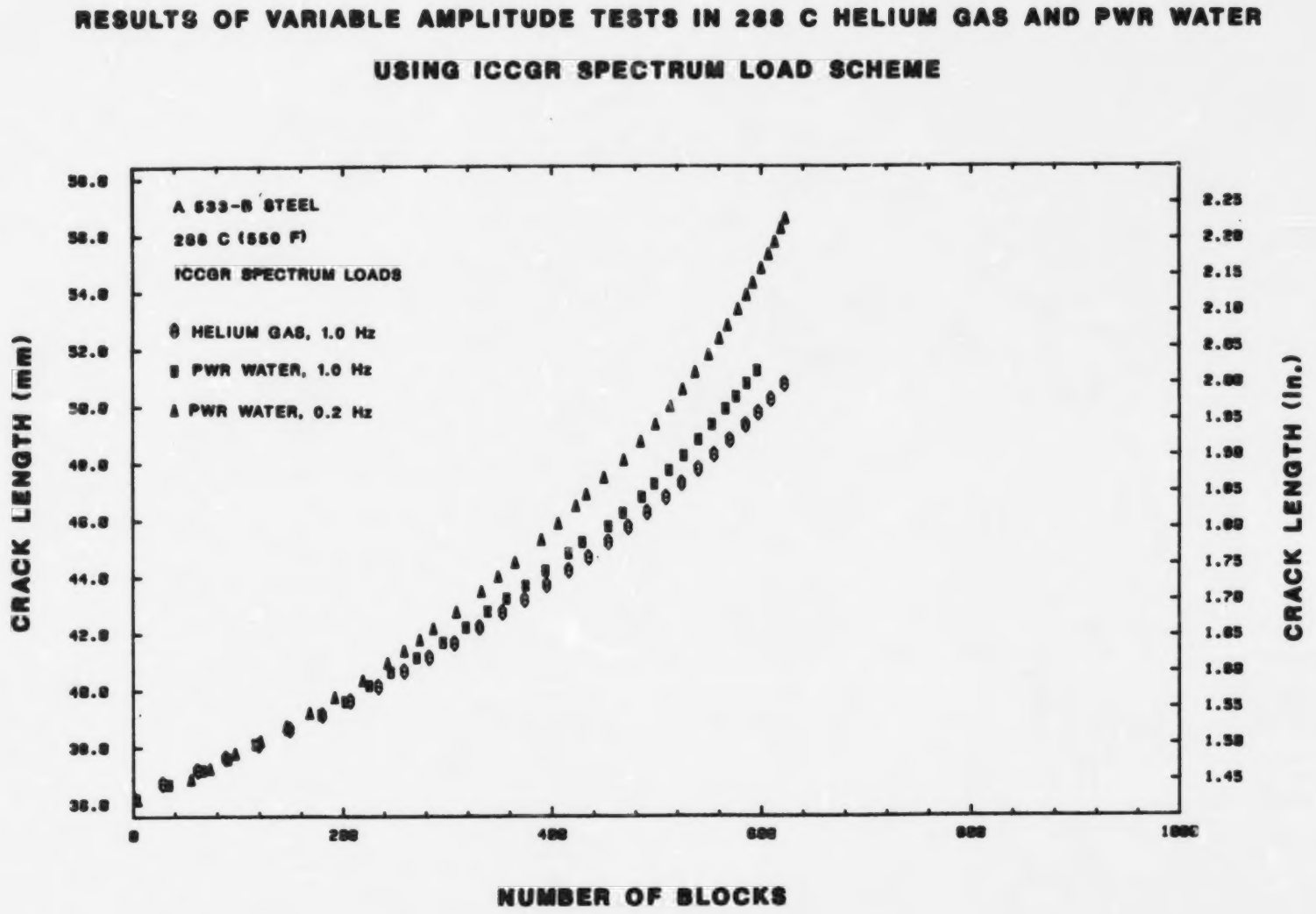
RESULTS OF VARIABLE AMPLITUDE TESTS IN 288 C HELIUM GAS AND PWR WATER
USING ICCGR SPECTRUM LOAD SCHEME
A 533-B STEEL
288 C (550 F)
ICCGR SPECTRUM LOADS
HELIUM GAS, 1.0 Hz
PWR WATER, 1.0 Hz
PWR WATER, 0.2 Hz
CRACK LENGTH (mm)
CRACK LENGTH (in.)
NUMBER OF BLOCKS

Fig. 2-22 Crack extension vs. cyclic count for tests of A 533-B using the ICCGR spectrum, but MEA specimens and test procedures as described in the text. Specimen W8R-13 was tested in 288°C helium gas and specimens W8R-17 and W8R-18 were tested in PWR water using cyclic frequency components of 1 Hz and 0.2 Hz, respectively.

BEST COPY AVAILABLE

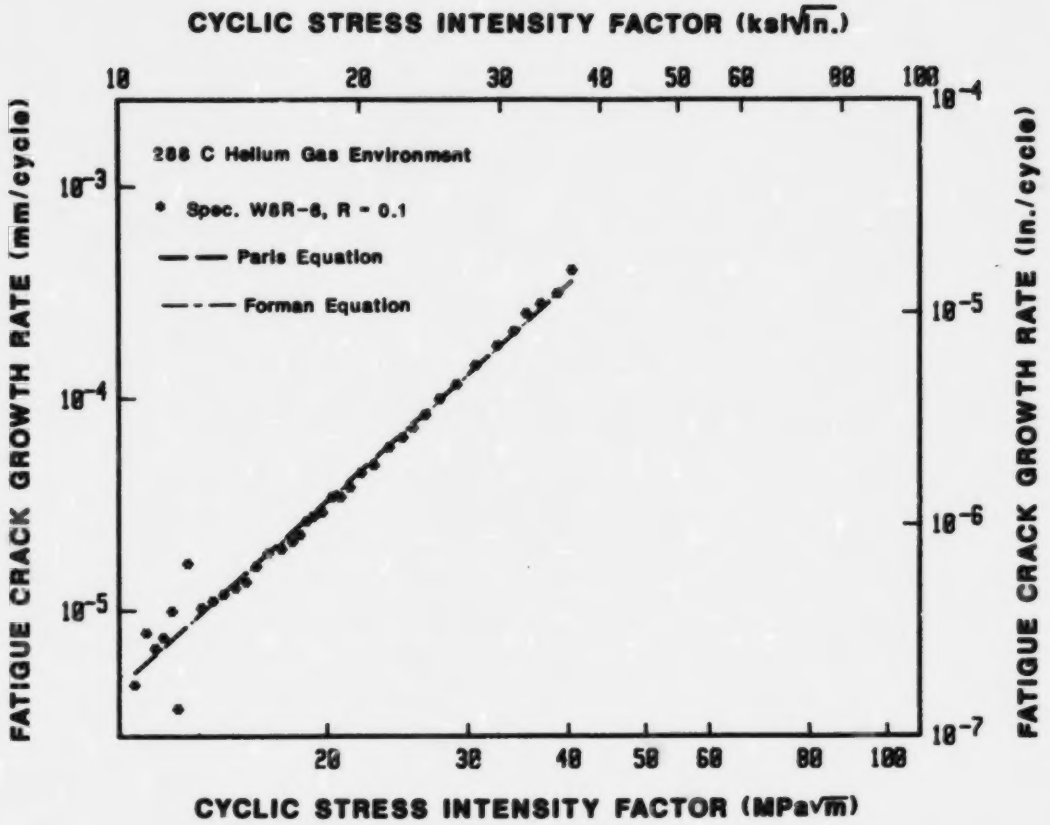

Fig. 2-23 Fatigue crack growth rate vs. applied cyclic stress intensity factor for the test of W8R-6 at R = 0.1 together with the linear best-fit results to a Paris equation.

BEST COPY AVAILABLE

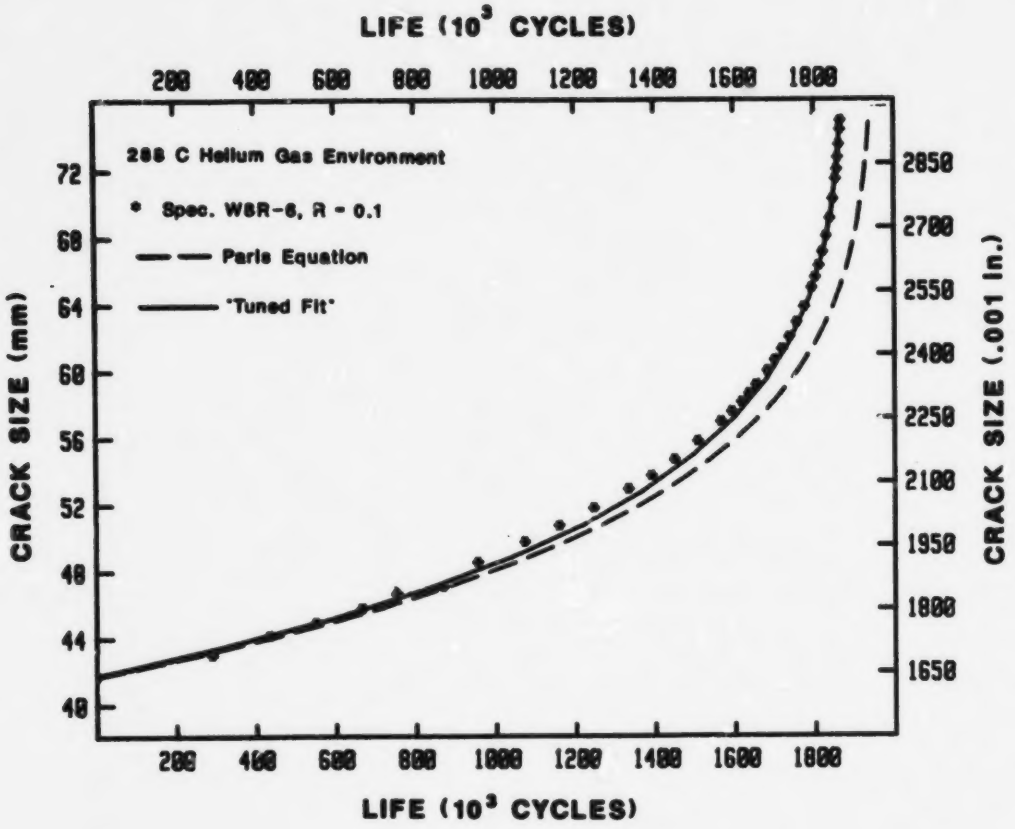

Fig. 2-24 Regeneration of the crack extension vs. cyclic count for the test of W8R-6, together with the original test data, showing that the best-fit using the growth rate data and a Paris equation can be substantially improved ("tuned") by working with the crack extension data alone, and iteration techniques.

BEST COPY AVAILABLE

Then reintegration is performed to check the fit to the original crack growth curve. If there is a discrepancy and the convexity of the curve is correct, the rate curve needs repositioning to higher or lower rate values. If the convexity is wrong, the slope of the curve through the rate data, or parts of it, require adjustment. Whether the rate data are expressed in equational form or used in tabular form, the problem is always the same. In view of this, the presentation of rate data alone in the literature is poor practice. For anyone to use these data, the goodness of fit can never be checked unless the original test data of crack size vs. cycles are given as well.

The service simulation loading considered in the present work contains cycles at three different amplitudes and R values. Due to load-interaction effects, some cycles may be effectively modified to other amplitudes and R, but at least the basic three components should be represented as well as can be achieved; otherwise, the verification of any load-interaction model will be useless: any discrepancies found could just as well be due to bias in input data as due to inadequacy of the model. Data for the four constant amplitude tests were obtained, fitted, and fine-tuned with individual Paris equations (Ref. 57):

$$\frac{da}{dN} = C\ \Delta K^n \qquad (2\text{-}13)$$

where C and n are fitting parameters. The data were then tabulated and used in tabular form in the analysis. The resulting data are shown in Table 2-3, while Fig. 2-25 shows how reintegration leads to an essentially perfect fit of the original tests.

Table 2-3 Evaluation of Best-Fit Crack Growth Rate Curves

ΔK ($MPa\sqrt{m}$)	da/dN (mm/cycle)			
	R = 0.10	R = 0.20	R = 0.70	R = 0.90
1.1	0.174×10^{-8}	0.983×10^{-8}	0.465×10^{-7}	0.737×10^{-7}
11.0	0.447×10^{-5}	0.800×10^{-5}	0.109×10^{-4}	0.112×10^{-4}
22.0	0.475×10^{-4}	0.599×10^{-4}	0.564×10^{-4}	0.505×10^{-4}
54.9	0.108×10^{-2}	0.864×10^{-3}	0.495×10^{-3}	0.373×10^{-3}
109.9	0.115×10^{-1}	0.650×10^{-2}	0.257×10^{-2}	0.169×10^{-2}

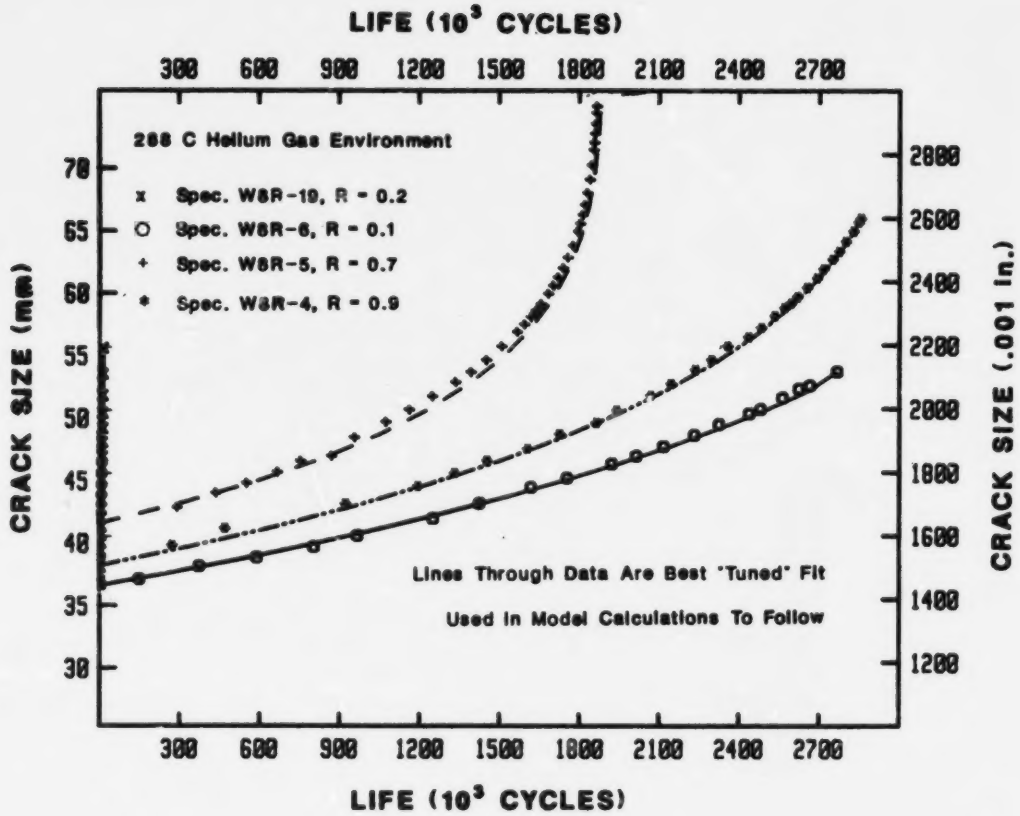
LIFE (10^3 CYCLES)
300 600 900 1200 1500 1800 2100 2400 2700
288 C Helium Gas Environment
x Spec. W8R-10, R = 0.2
O Spec. W8R-6, R = 0.1
+ Spec. W8R-5, R = 0.7
* Spec. W8R-4, R = 0.9
CRACK SIZE (mm)
70 65 60 55 50 45 40 35 30
2800 2600 2400 2200 2000 1800 1600 1400 1200
CRACK SIZE (.001 in.)
Lines Through Data Are Best "Tuned" Fit
Used In Model Calculations To Follow
300 600 900 1200 1500 1800 2100 2400 2700
LIFE (10^3 CYCLES)

Fig. 2-25 Regeneration of the crack extension vs. cyclic count for all the constant amplitude tests conducted in 288°C helium gas, together with the original test data, showing that in each case an adequate fit using a Paris-type equation is satisfactory, although "tuning" may be necessary.

BEST COPY AVAILABLE

In order to demonstrate the effect of a poor fit, some predictions were made using a Walker equation (Ref. 58):

$$\frac{da}{dN} = B \quad \Delta K^{k} \; K^{l}_{max} \qquad (2\text{-}14)$$

where B, k, and l are fitting parameters.

Forcing data for different R values to fit one equation is seldom satisfactory; no matter how complicated the equation, none can cover all data sets properly. Although the rate data seem to be fairly well covered by the equation as appears from Fig. 2-26, reintegration leads to disaster, as is demonstrated well in Fig. 2-27. Fortunately, there is no need for an equation. Fatigue crack growth analysis is invariably done by a computer which is just as capable of using tabular data as equations. The Walker equation was carried along here, just to demonstrate this point. The values of B, k, and l are shown in the caption of Fig. 2-27. Other values were tried, but those shown were optimal.

2.3.2.2 Predictive Model Development

A multitude of load-interaction models have been published, from the very simple, yet elegant (Refs. 59 and 60) to the more complicated (Refs. 61 to 68). Some account for retardation only, some also cover acceleration after underloads. Because a pure fundamental treatment is quite difficult, most models contain unknown parameters or include a calibration parameter. In either case, the parameter must be obtained experimentally, by adjusting its value until the results fit the data of a certain random or variable amplitude test. There can be no objection against empirical calibration, provided that the model once calibrated, can be used for predictions of other cases. Fundamentalists raising objections should realize that the rate data are obtained from experiments as well. (Even Hooke's law is empirical, and stress analysis would be impossible without empirically obtained values for modulus and Poisson's ratio.) Empiricism is not a measure; generality is the criterion. In view of this, all models are useful, provided they have generality and lead to practically usable answers (Refs. 69 and 70).

As a consequence, it makes little difference which model one chooses. The choice may be mostly a matter of familiarity; the better the user knows the model and its intricacies and peculiarities, the less likely is misuse and misinterpretation. For this reason, the Broek model (Refs. 67 and 68) was used here, further developed to account for underload effects. The background of the model was extensively explained in the references cited, and it was shown that the effective K_{max} is given as:

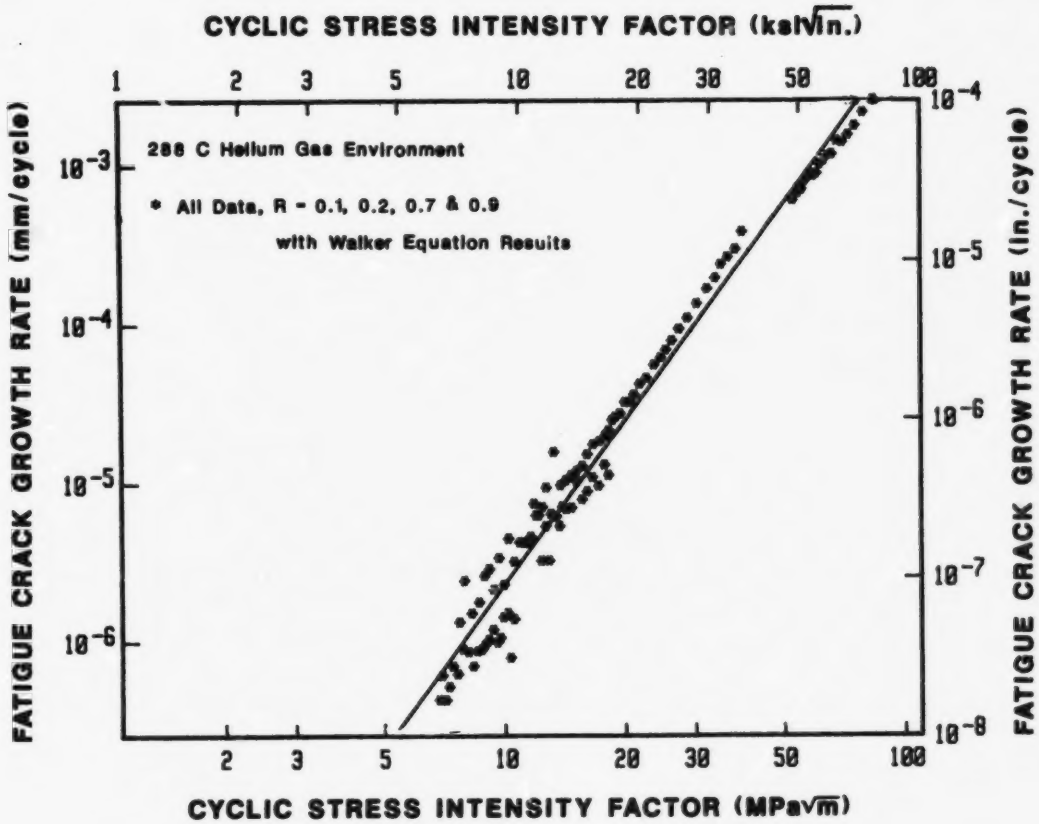

Fig. 2-26 Cumulative plot of fatigue crack growth rate vs. applied maximum stress intensity factor for all the tests conducted in 288°C helium gas, together with the results of fitting the Walker equation. The fit seems excellent, but temporarily serendipitious nonetheless, as shown in the next figure.

BEST COPY AVAILABLE

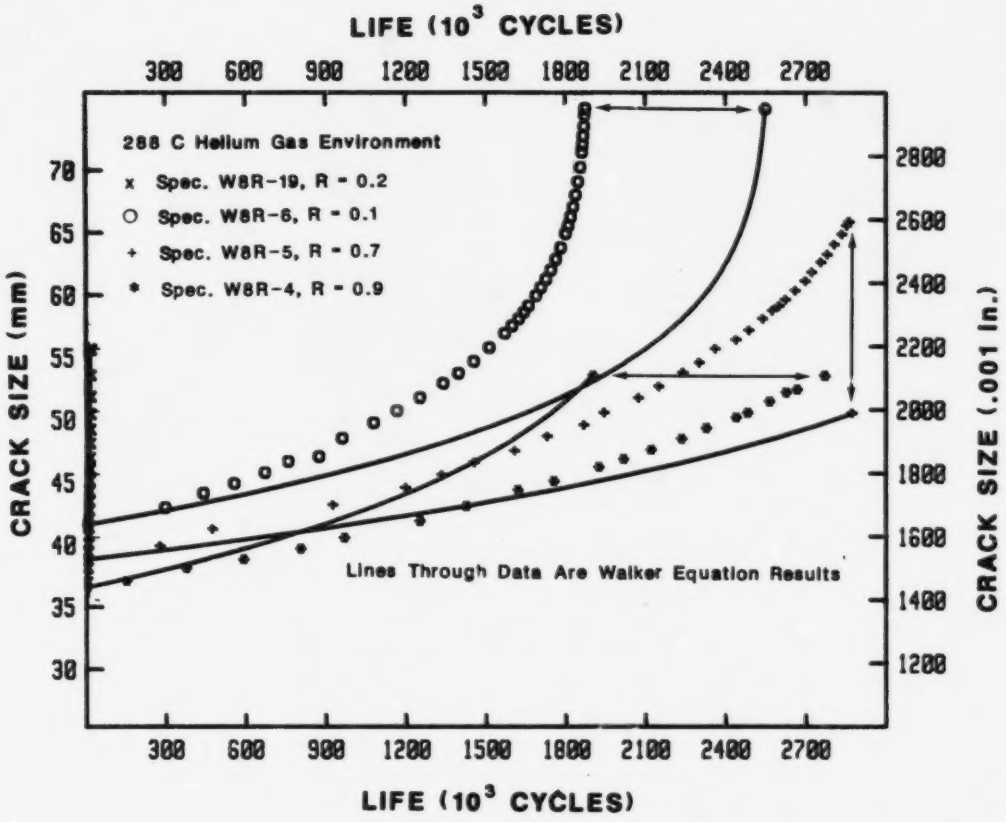
LIFE (10^3 CYCLES)
300 600 900 1200 1500 1800 2100 2400 2700
288 C Helium Gas Environment
x Spec. W8R-19, R = 0.2
O Spec. W8R-6, R = 0.1
+ Spec. W8R-5, R = 0.7
* Spec. W8R-4, R = 0.9
Lines Through Data Are Walker Equation Results
CRACK SIZE (mm)
70 65 60 55 50 45 40 35 30
CRACK SIZE (.001 in.)
2800 2600 2400 2200 2000 1800 1600 1400 1200
LIFE (10^3 CYCLES)

Fig. 2-27 Regeneration of the crack extension vs. cyclic count for all the constant amplitude tests conducted in 288°C helium gas using the Walker equation, together with the original test data, showing that the quality of the fit is not good. The coefficients are: $C = 4.29 \times 10^{11}$, $m = 2.55$, and $n = 0.90$.

BEST COPY AVAILABLE

$$K_{max,eff} = \frac{1 - \frac{2}{\pi}\sqrt{\frac{2}{\alpha}}\sqrt{\frac{\rho}{r_{\rho c}}}}{1 - \frac{2}{\pi}\sqrt{\frac{2}{\alpha}}} K_{max} \qquad (2\text{-}15)$$

where ρ is furthest plastic boundary established by any previous overload, $r_{\rho c}$ is the plastic zone at the current load, and α is 6 for plane strain and 2 for plane stress.

New to this model is the accounting for underloads. During a normal cycle, the material at the crack tip undergoes a stress-strain loop (Refs. 67 and 68) as shown in Fig. 2-28. At the maximum stress, point A is reached and point C at the minimum stress. If the next cycle is an underload, the strain moves beyond point C toward point B. This new return point can be calculated so that the increased loop size after the underload is then known (the above effective K_{max} is based on the decreased loop size after an overload). However, it is not determined easily how the original loop size after an underload is restored gradually. An assumption on this matter would be necessary. In view of this, the problem was approached somewhat more pragmatically.

From point A in Fig. 2-28, an underload type of excursion in strain (or stress) $\Delta\varepsilon_p$ is made corresponding to K_u where K_u is the stress intensity range of the underload. Starting from point A as zero, the stress has to decrease by σ_{ys} (accounting in an approximate manner for the Bauschinger effect, σ_{ys} being the yield stress), before reversed yielding occurs. Hence, the zone undergoing reversed plastic deformation, r_{du}, is given by (assuming plane strain):

$$r_{du} = \frac{\Delta K_u^{\,2}}{24\pi\,\sigma_{ys}^{\,2}} \qquad (2\text{-}16)$$

During "normal" loading, the zone with reversed plasticity is r_{de}, also given by Eq. 2-16 if ΔK_u is replaced by ΔK of the "normal" loading, i.e., the current load cycle.

Crack growth will be affected by the underload as long as the crack tip is inside r_{de} (Fig. 2-29). The closure level initially will be reduced to that of the underload but be gradually restored to the "normal" level. Then the effective minimum value of K_{min} in subsequent cycling will be:

$$K_{min,eff} = K_{min,eff,pr} + \eta\,(K_{min} - K_{min,eff,pr}) \qquad (2\text{-}17)$$

where pr stands for previous cycle.

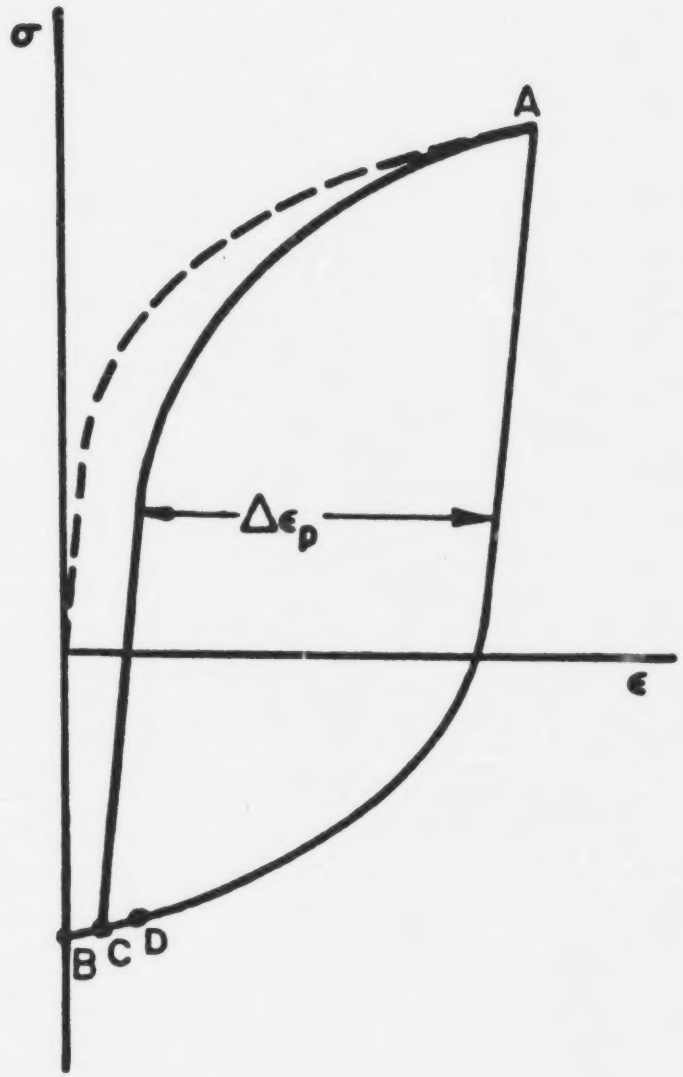

Fig. 2-28 Schematic of the stress-strain excursion of previously unstrained material near the crack tip during one and one-half fatigue cycles. Sequencing is O-A-C-A. The return to B is not possible because of plasticity.

BEST COPY AVAILABLE

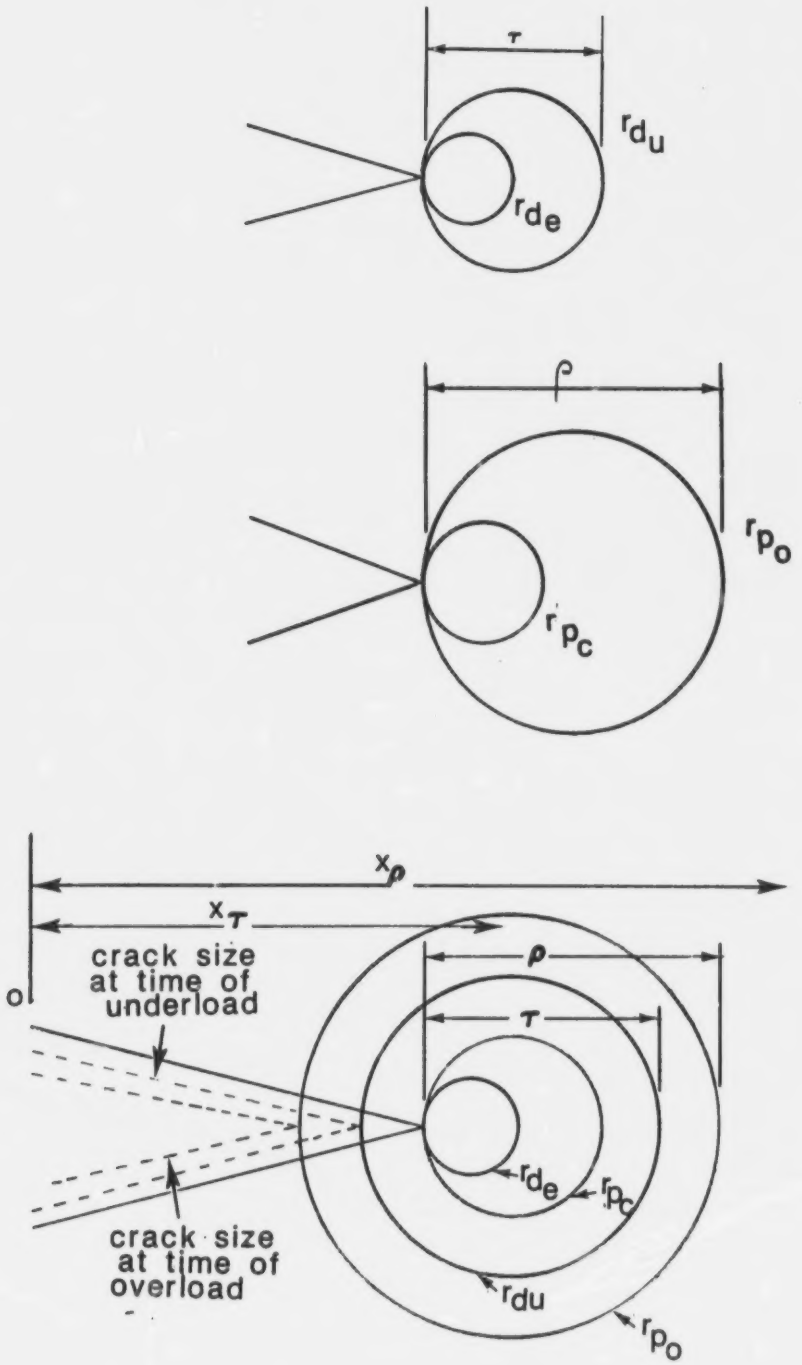

Fig. 2-29 Schematic and nomenclature of the plastic zones which are necessary to characterize a crack tip in materials subject to overloads and underloads.

BEST COPY AVAILABLE

As a first approximation η was defined as:

$$\eta = \frac{r_{de}}{\tau} \qquad (2\text{-}18)$$

This means that the (effective) K_{min} must be adjusted every cycle on the basis of Eq. 2-16, 2-17, and 2-18. Simultaneously, K_{max} must be adjusted on the basis of Eq. 2-15. This requires recalculation of the farthest boundaries of material that was once plastic (τ) and of material that once underwent reversed plasticity (ρ). If any of these two change in any cycle, the new value must be kept in memory. The accounting is shown in Table 2-4. Should $K_{max,c}$, where c stands for current, be associated with an overload, then ρ changes; should $K_{min,c}$ be associated with an underload then τ changes, or both. If neither is the case and there have been no previous underloads or overloads that affected the plastic or reverse plastic enclaves, then $\rho = r_{pc}$ and $\tau = r_{de}$, so that the effective values remain equal to the current values.

Since the conditions can change at any time, the above must be checked in every cycle; the integration must be performed in a cycle-by-cycle manner. For the present analysis, the commercially available computer program RECYCL was used. It already included the overload model as described; it was modified to account for underloads as well.

The model as used does not require any calibration. Obviously, the introduction of a calibration parameter could help in improving accuracy. At this time, since the number of test data sets against which to check the model are still limited, the use of a calibration factor would always prove the model correct. If with limited data, good results are obtained without a calibration factor, at least reasonable modeling can be claimed.

Table 2-4 Conditions For Interaction Effects
(see also Fig. 2-29)

r_{pc}	$= K^2_{max,c} / \alpha \pi \sigma^2_{ys}$ ($\alpha = 6$ for plane strain)
$X_{\rho,new}$	$= a_c + r_{pc}$ (a_c is current crack size)
	if $X_{\rho,new} > X_\rho$ then $X_\rho = X_{\rho,new}$
ρ	$= X_\rho - r_{pc}$
$K_{max,eff}$	$= \psi(\rho)$ (see Eq. 2-16)
r_{de}	$= \Delta K^2_c / 24\pi \sigma^2_{ys}$
$X_{\tau,new}$	$= a_c + r_{de}$
	if $X_{\tau,new} > X_\tau$ then $X_\tau = X_{\tau,new}$
τ	$= X_\tau - r_{de}$
η	$= \tau / r_{de}$
$K_{min,eff}$	$= \psi(\eta)$ (see Eqs. 2-17 and 2-18)
ΔK_{eff}	$K_{max,eff} - K_{min,eff}$
R_{eff}	$= K_{min,eff} / K_{max,eff}$

2.3.2.3 Prediction of Service Simulation Test Results -- Linear Analysis

The service simulation load history was discussed earlier. A tabulation of the load values is presented in Table 2-5. Note that these loads are the result of a rainflow count of the history. Tests with this history were performed at 288°C (550°F) in helium as well as in a reactor-water environment. Previously, similar tests were performed with different values of the loads.

Table 2-5 Loads for One Block As Applied (Rainflow Counted)

Occurrence Cycles	Minimum Stress/Load (MPa)	Maximum Stress/Load (MPa)
1500	233.0	258.9
29	205.0	286.9
1	205.0	258.9
1	49.2	286.9

The service-simulation tests were analyzed in various ways. In the first place, the analysis was done linearly, i.e., any load-interaction effects were ignored. For this purpose, the commercially available computer program LICAFF was used. It operates in the same manner as RECYCL but does not account for load interaction effects so that it can employ a much faster integration routine.

The analytical results for test W8R-13 are compared with the test data in Fig. 2-30. With the best-fit rate data (see Table 2-4), the life is overpredicted by a factor of almost two. Better agreement was obtained with the Walker equation, but this was fortuitous, because the equation is a poor fit of constant amplitude behavior. This shows that a poor representation of constant amplitude data sets may lead to unwarranted conclusions. It should be noted that the da/dN reference lines proposed in ASME Section XI give the poorest fit and are the most unconservative.

Figure 2-30 is of interest because it shows that acceleration due to underloads is more important than effects due to overloads. If it had been the other way, the predictions would have been conservative. In that case, there would have been little use for a predictive model because a conservative linear integration would be acceptable for practical use. However, if a simple linear prediction is unconservative, better procedures are necessary.

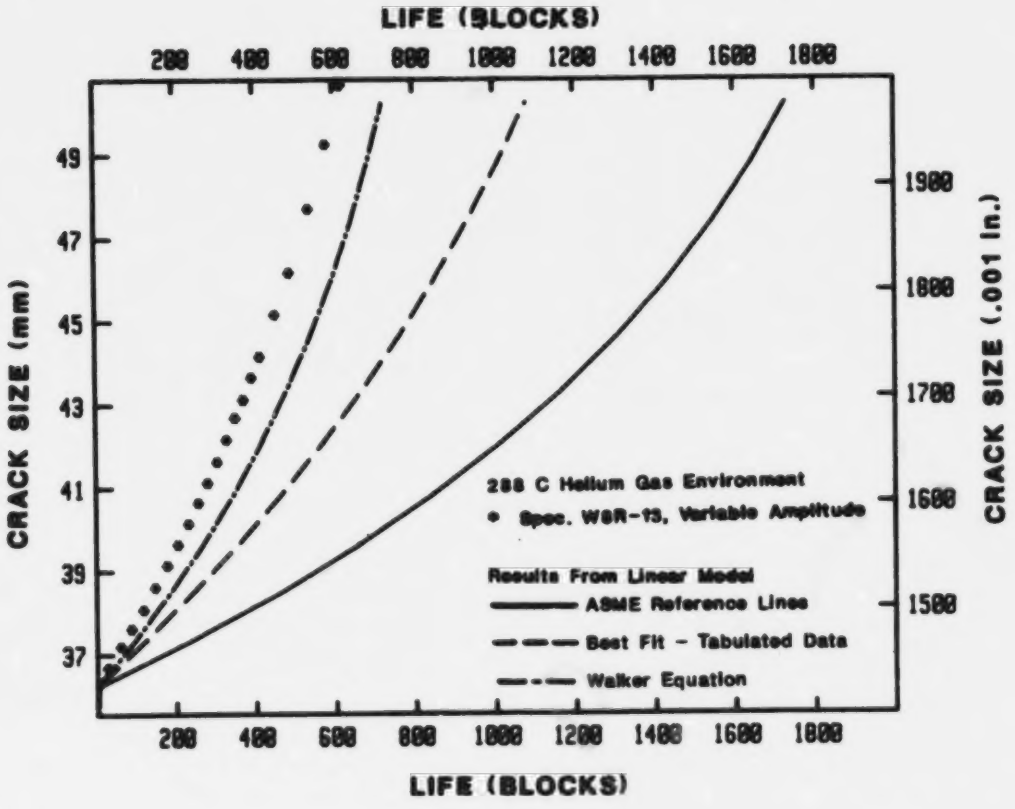

Fig. 2-30 Analytical results using linear analysis for the crack extension vs. cyclic count for the test of W8R-13, showing that data input in any form leads to a nonconservative prediction of life.

BEST COPY AVAILABLE

Previous service simulation tests were analyzed as well with linear integration. As before, similar discrepancies were observed. In all cases, the predictions were unconservative. Although a complete set of constant amplitude data in the reactor-water environment was not available, the service load simulation tests performed in reactor water at 0.2 and 1 Hz were analyzed as well. For this purpose, the constant amplitude data were approximated as follows. Data for one test for constant amplitude at R = 0.9 were available. These data points are shown in Fig. 2-31, where they are compared with data obtained at the same loads and load ratio in helium. Reintegration results are presented in Fig. 2-32: apparently a good rate data fit was obtained.

The test data for water show an average increase of rates by a factor of 1.4, as compared to those in helium. This factor was applied to helium data for other load ratios (0.2, 0.7) to obtain a complete data set appropriate to water environment. The resulting tabular rate data are provided in Table 2-6. These were used for the analysis of the service simulation tests.

The results of the linear analysis are shown in Fig. 2-33. Because only one rate data set was available, the prediction for both the test at 1 Hz and that at 0.2 Hz are the same. Again the predicted curves are unconservative. The use of the environmental data proposed in ASME Section XI on the other hand produce extremely overly conservative predictions.

Table 2-6 da/dN-ΔK Table for Water Environment

ΔK	da/dN (mm/cycle)			
(MPa$\sqrt{m}$)	R = 0.10	R = 0.20	R = 0.70	R = 0.90
1.1	0.243×10^{-8}	0.138×10^{-7}	0.650×10^{-7}	0.211×10^{-7}
11.1	0.625×10^{-5}	0.112×10^{-4}	0.152×10^{-4}	0.192×10^{-4}
22.0	0.665×10^{-4}	0.838×10^{-4}	0.790×10^{-4}	0.150×10^{-3}
54.9	0.151×10^{-2}	0.121×10^{-2}	0.701×10^{-3}	0.226×10^{-2}
109.1	0.161×10^{-1}	0.909×10^{-2}	0.358×10^{-2}	0.176×10^{-1}

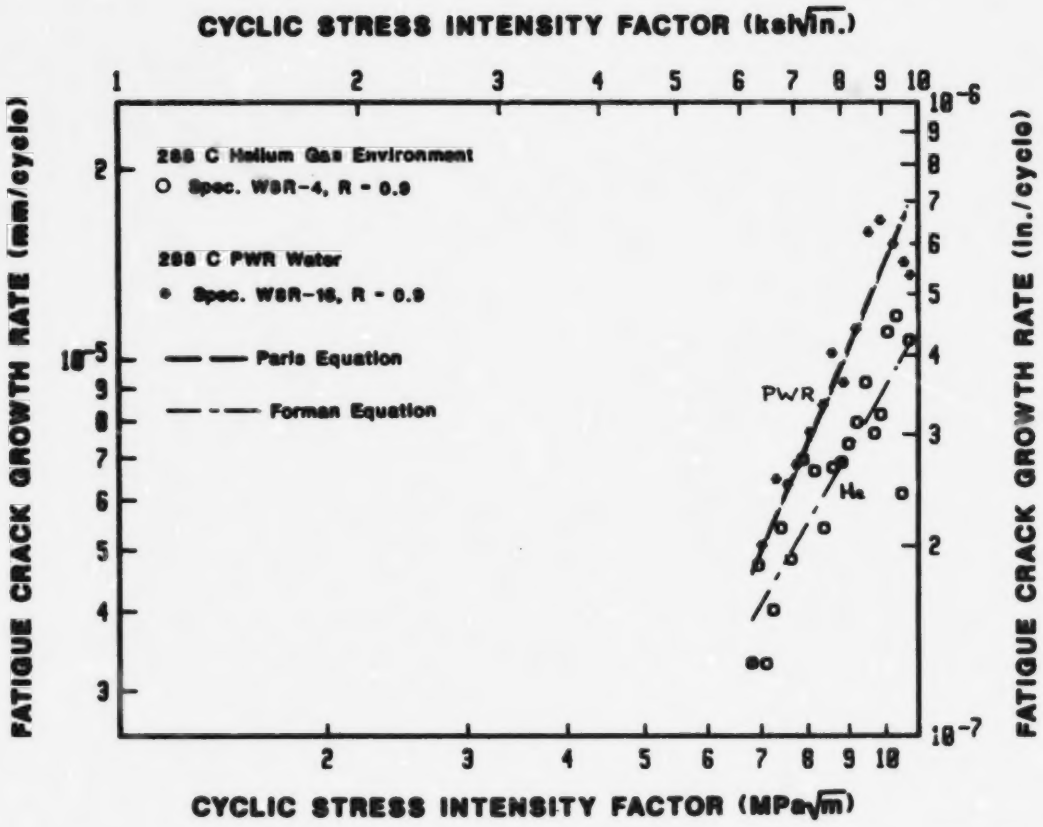

Fig. 2-31 Fatigue crack growth rate vs. applied cyclic stress intensity factor for the tests of W8R-4 (helium gas, see Fig. 2-25) and W8R-16 (PWR) conducted at R = 0.9 together with the linear best-fit results to a Paris equation.

BEST COPY AVAILABLE

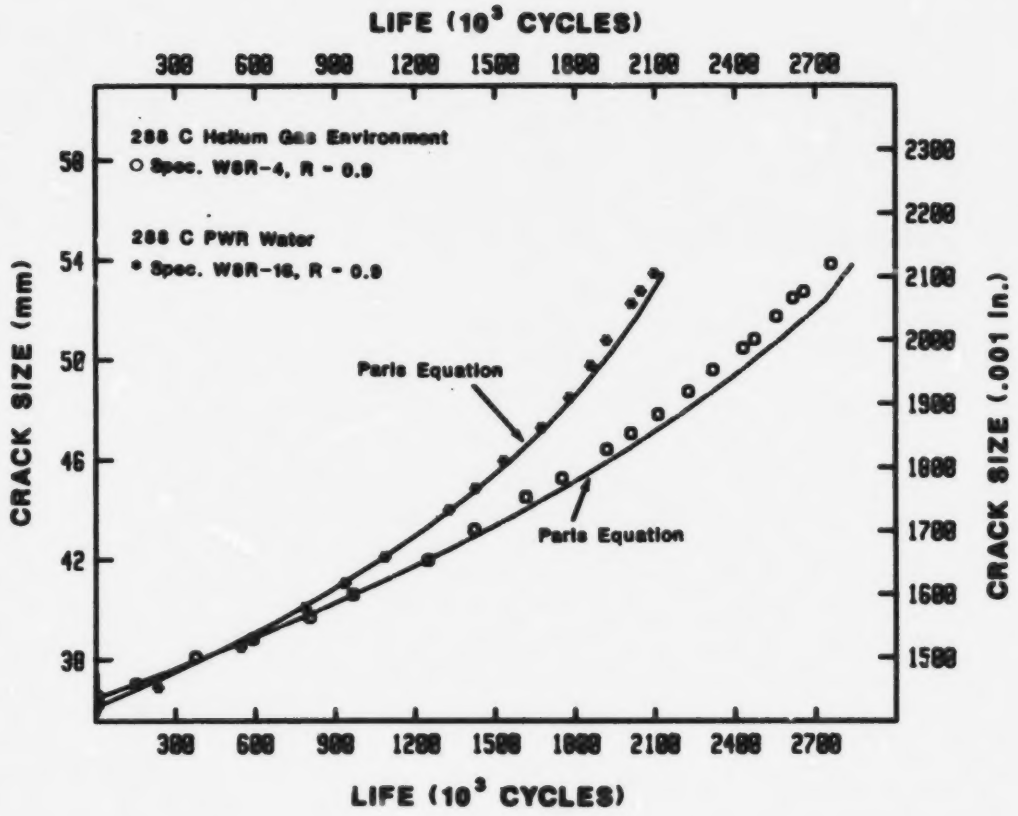

Fig. 2-32 Regeneration of the crack extension vs. cyclic count for tests at R = 0.9 of W8R-4 (helium gas) and W8R-16 (PWR water).

BEST COPY AVAILABLE

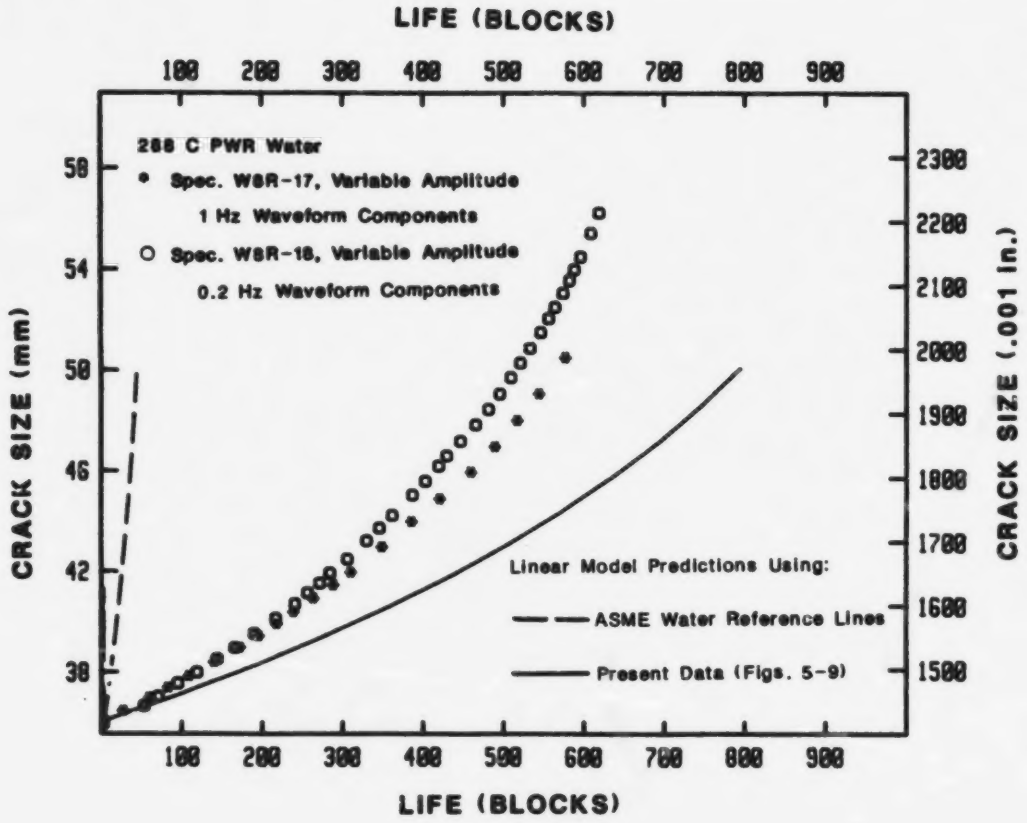

Fig. 2-33 Analytical results using linear analysis for the crack extension vs. cyclic count for the PWR environment tests of W8R-17 (1 Hz) and W8R-18 (0.2 Hz), showing that data input either as real test data or in the form of the ASME reference lines leads to a inaccurate prediction of life.

BEST COPY AVAILABLE

2.3.2.4 Application of the Present Model

The prediction of service simulation tests with the load-interaction model, including retardation and acceleration effects as discussed are shown in Figs. 2-34 and 2-35. The agreement with test data is very good at low da/dN but less than excellent in the high da/dN regime. The latter may be due to the fact that at longer cracks there is no longer plane strain, so that the calculation of plastic zone sizes becomes somewhat less accurate. Plastic zone sizes govern the problem; overall, the agreement is satisfactory.

2.3.3 Conclusion and Anticipated Progress

With the use of a load-interaction model accounting for overload and underload effects, crack growth during service (simulation) loading can be predicted with sufficient accuracy for practical use. A model accounting for load-interaction is necessary, because linear integration is unconservative by as much as a factor of two. Apparently, the reactor-load history is much more prone to cause acceleration than retardation. If it were the other way, linear analysis would always be conservative, and there would be little need for a load-interaction model.

The advantage of the present model is that is needs no calibration parameter. However, more checks are necessary with different kinds of load histories. It is expected that these will necessitate further development and refinement and possibly a calibration factor. Be that as it may, it is not the rigor of the model that counts, but its practical usefulness. In order to provide the results needed to check on the accuracy of the model as it has been presented here, tests with random mixing of cyclic components are underway. These components will range from the set of three used in the ICCGR waveform to random mixing of a more comprehensive set of components taken from the design specifications for operating PWR's.

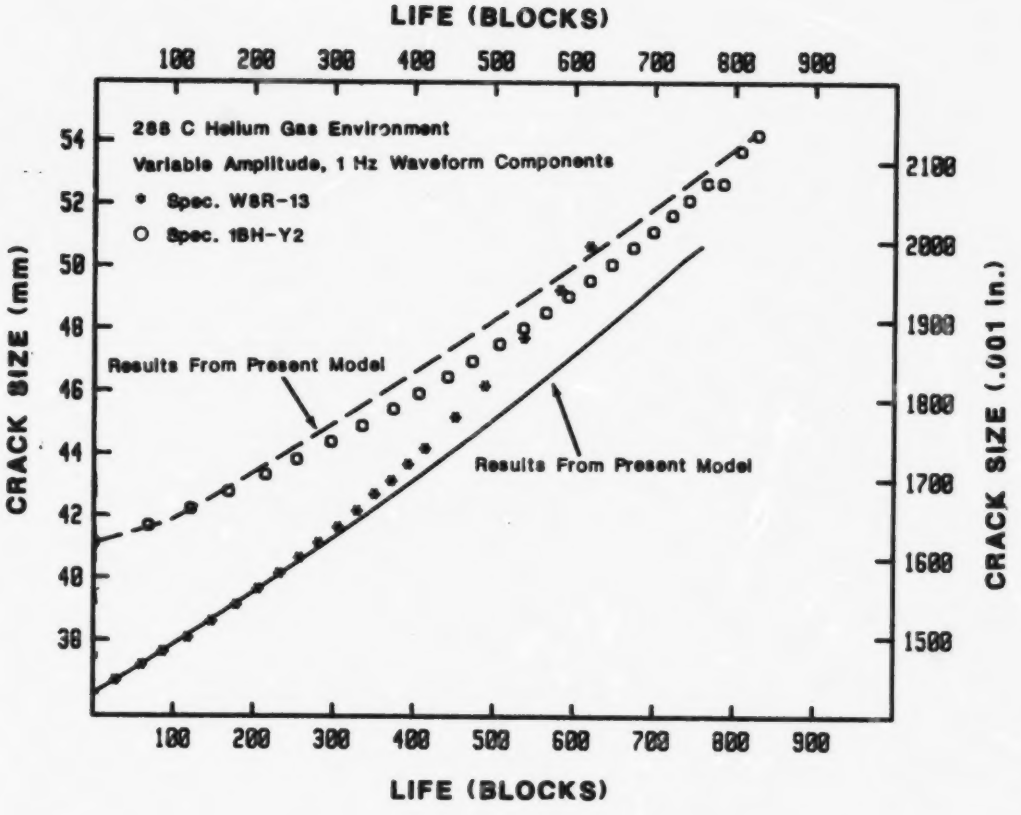
LIFE (BLOCKS)
100 200 300 400 500 600 700 800 900
288 C Helium Gas Environment
Variable Amplitude, 1 Hz Waveform Components
* Spec. W8R-13
O Spec. 1BH-Y2
Results From Present Model
Results From Present Model
CRACK SIZE (mm)
54 52 50 48 46 44 42 40 38
CRACK SIZE (.001 in.)
2100 2000 1900 1800 1700 1600 1500
100 200 300 400 500 600 700 800 900
LIFE (BLOCKS)

Fig. 2-34 Analytical results for the tests of W8R-13 and 1BH-Y2, both conducted with the ICCGR round robin spectrum but with different loads and initial crack lengths. The model incorporating acceleration and retardation effects was used.

BEST COPY AVAILABLE

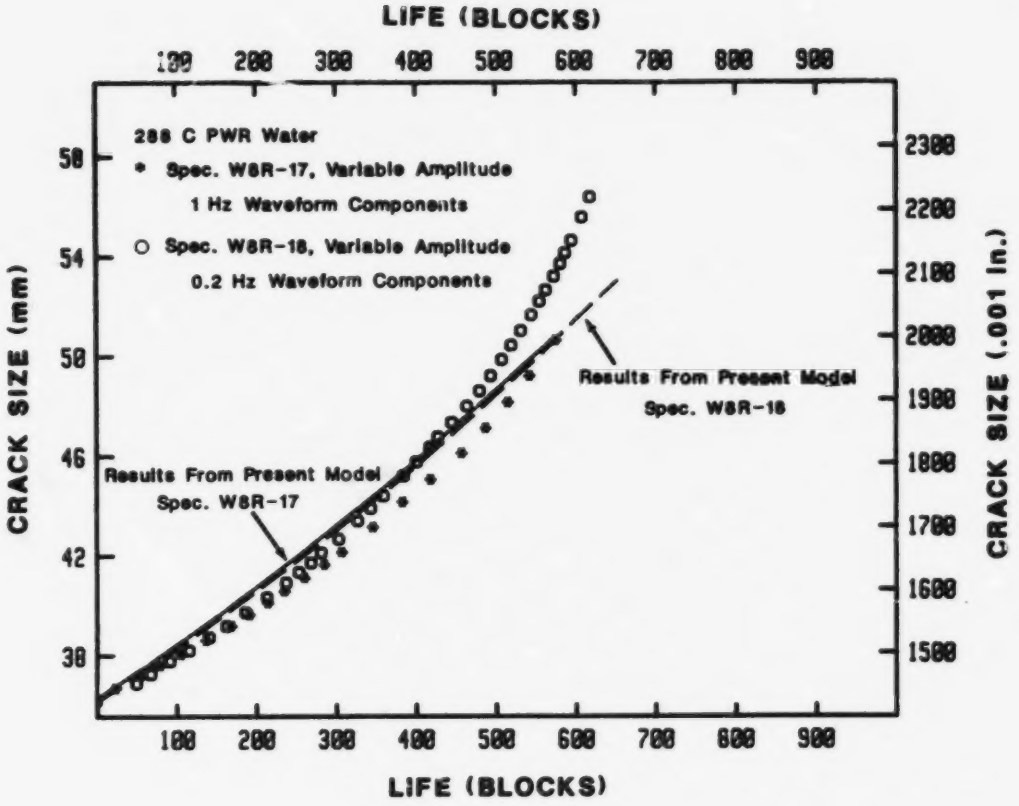

Fig. 2-35 Analytical results for the tests of W8R-17 and W8R-18, both conducted in PWR water with the ICCGR round robin spectrum. The model incorporating acceleration and retardation effects was used, and the degree of fit is very good.

BEST COPY AVAILABLE

2.4 Evaluation of the Effects of Environment and Cladding on the Growth of Surface Flaws

W. H. Cullen and M. I. Jolles

2.4.1 Background

Testing with through-cracked specimens, principally of the compact tension (CT) design, has been the backbone of the data base development of fatigue crack growth data for pressure vessel and piping steels in reactor-grade water environments. However, it has long been recognized that this one-dimensional flaw geometry is not typical of in-service cracks. The latter are usually semicircular or semielliptical (two dimensional) when still in the early stages of development and are faced with stainless steel cladding for many of the primary loop components. It has been assumed generally that the CT specimen design does provide conservative data. However, as technology has developed, a number of questions have arisen concerning the (a) potential for the CT specimen to be conservative, or (b) the applicability of test results of a homogeneous material to an engineering design incorporating a bimetallic composite.

There are three areas of difference (mechanical, metallurgical, and environmental) between one- and two-dimensional cracks in clad and unclad materials.

(1) Mechanical: In part-through cracks, the stress intensity factor (K) varies along the crack front and, especially near the clad interface, may be strongly affected by the residual stresses induced by the thermal expansion differences between the clad and the base plate. The magnitude of these residual stresses will be a function of the test temperature, and the shape of the crack will be a function of the local stress state, in addition to the global (applied) stress.

(2) Metallurgical: Orientation effects can result in differences in fatigue crack growth rates, especially in aqueous environments (Ref. 71). Growth rates along the two orthogonal axes which define the through-thickness and surface traces of a part-through crack will probably reflect these orientation-dependent growth rate differences. For clad test specimens, the situation is more complex, because growth rates in stainless steel are different from those in base plate materials, especially in aqueous environments (Ref. 72), and the growth rates in the dilution zone which defines the clad-base interface have never been measured.

(3) Environmental: As the electrochemistry of the environmentally-assisted fatigue crack growth rate process becomes better understood, there is growing evidence that the electrochemical potential of the specimen and crack-tip electrolyte inside a tight crack is substantially different from that which is (most commonly) measured for a specimen and the bulk environment. In general, it is expected that crack-tip electrochemical

potentials will be lower than those measured in the bulk, but substantiation of this fact is very difficult.

The presence of clad will alter further the electrochemical potential. Because of its different plastic flow characteristics, the clad may exhibit a different crack-mouth opening displacement and thus affect the mass transport of ions in and out of the crack-tip enclave. Lastly, the nearly pure tensile stress state surrounding the crack in a part-through crack specimen, as compared with the combined tensile stress and bending moment of a compact specimen, offers a different distribution of the triaxial stresses near the tip of the crack. If environmentally-assisted growth is due, even in part, by interstitial hydrogen, then environmentally-assisted crack growth differences may be expected between one- and two-dimensional crack growth specimens.

The principal objective of this program is to assess the adequacy of current procedures in Sec. XI of the ASME Boiler and Pressure Vessel Code for predicting the growth of defects found in operating plants. The data in Sec. XI are based exclusively on the results of CT specimen testing. In the present program, PTC specimens (clad and unclad) are utilized to investigate the differences in growth between one- and two-dimensional cracks. The final step in the assessment of the Sec. XI procedures is to examine the growth of surface cracks introduced into a typical component, i.e., a heavy-wall pipe, and to predict this growth from CT specimen data in a way which is analogous to the methods of Section XI, Appendix A (Ref. 54).

2.4.2 Summary of Results

2.4.2.1 High Temperature Studies -- Base Plate Specimens

Having ascertained that initial notch shape resulted in negligible differences in crack growth rates (Ref. 73), the high temperature tests were conducted with a semicircular notch, which has a greater chance of lending itself to an analytical evaluation of potential drop vs. crack extension and geometry. Samples of the three materials were prepared, precracked, and tested with mixed results. The first test of low sulfur A 533-B was completed satisfactorily, but the initial tests of the higher sulfur A 533-B and the A 106-B yielded highly asymmetric crack extension and the electric potential drop data could not be processed satisfactorily. Visual observation indicated that the problem was that the precrack had not nucleated uniformly and the asymmetry carried on into the testing phase as well. Subsequently, a V-notch geometry was introduced into the remainder of the specimens, and repeat tests of these two materials proved to be acceptable.

The first test in the series was of the low sulfur (0.004%) A 533-B steel coded W7. Figures 2-36, 2-37, and 2-38 show a post-test macrophotograph of the specimen, the crack lengths "a" and "c" vs. cyclic count plots, and the fatigue crack growth rate vs. applied cyclic stress intensity factor plots for this test. Figure 2-39 shows the fatigue crack growth rate vs. applied cyclic stress intensity

PART-THROUGH CRACK GROWTH IN A 533-B TESTED AT 288 C (550 F)

R = 0.2 3 Hz Sinusoidal Waveform

Fig. 2-36 Photograph of the fatigue surface from the test of specimen code W7-24-10, A 533-B steel, 0.004% sulfur. Specimen tested at 288°C, R = 0.2, 3-Hz sinusoidal, room air environment.

BEST COPY AVAILABLE

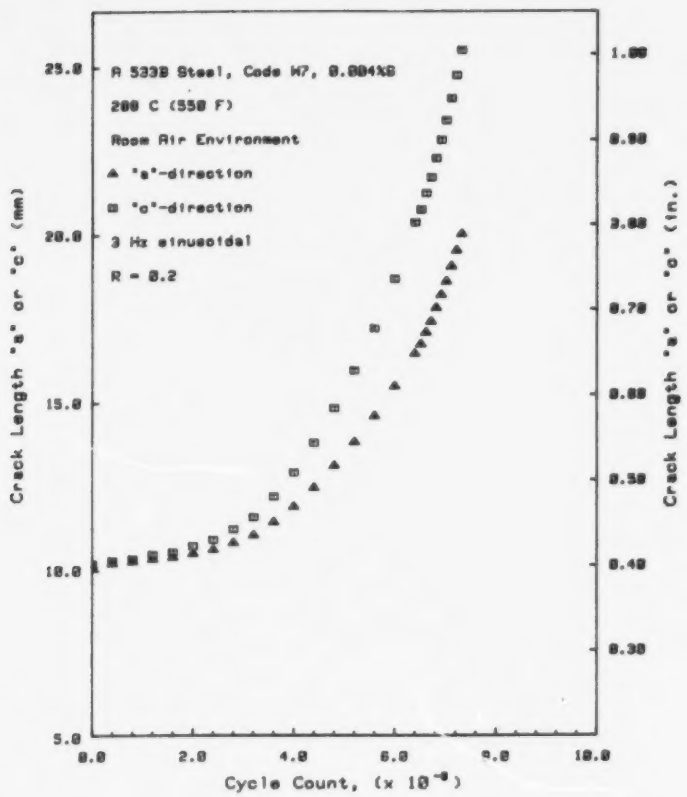

Fig. 2-37 Crack length vs. cyclic count for the "a" and "c" directions for the test of specimen W7-24-10.

BEST COPY AVAILABLE

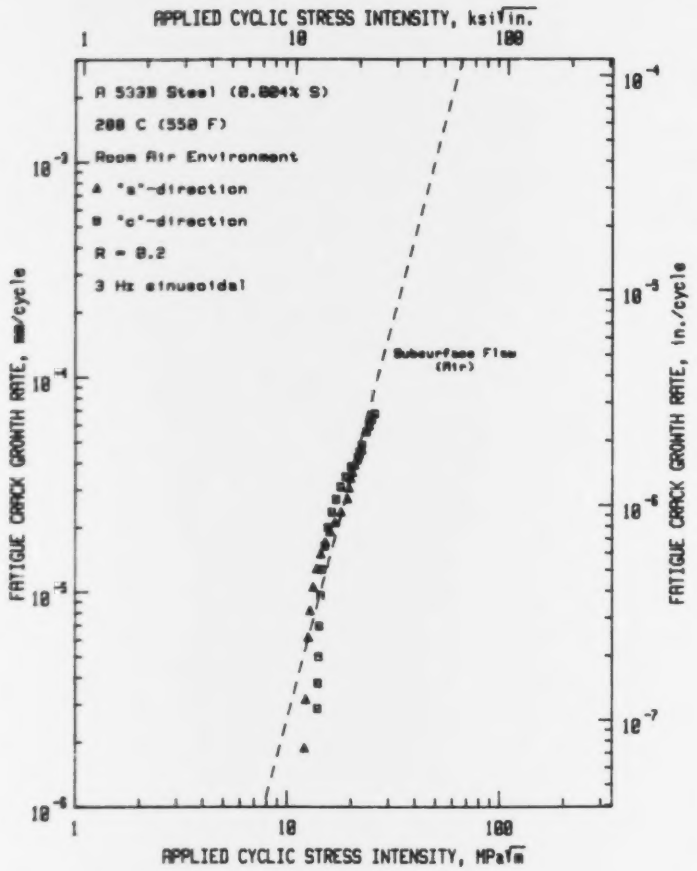

Fig. 2-38 Fatigue crack growth rate vs. applied cyclic stress intensity factor for the test of specimen W7-24-10.

BEST COPY AVAILABLE

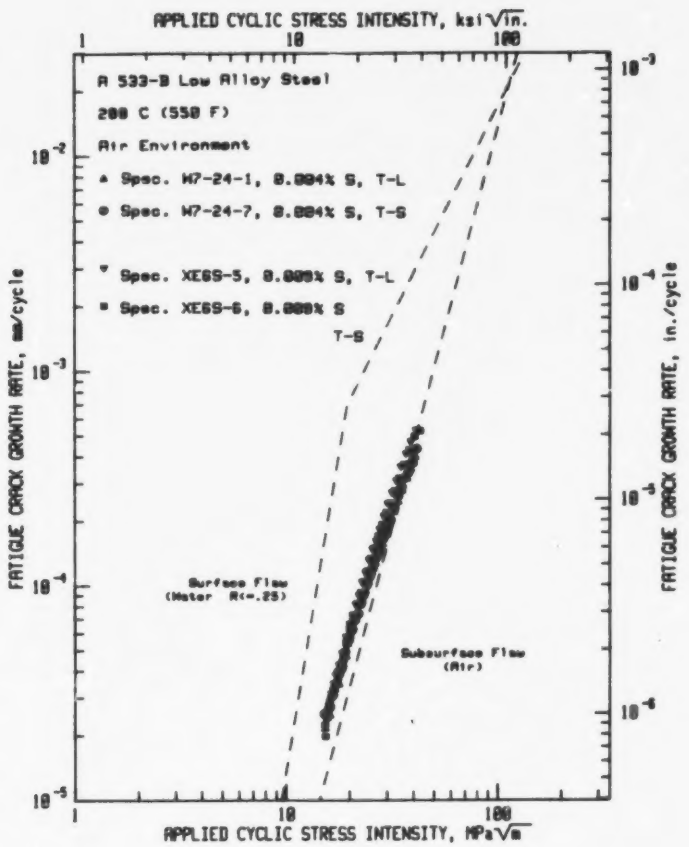

Fig. 2-39 Fatigue crack growth rate vs. applied cyclic stress intensity factor for the tests of A 533-B steel from the same plate as specimen W7-24-10 and specimens XE4S-1 and XE4S-4. These are compact specimen results for orientations which are collinear with the "a" and "c" growth directions in the part-through cracked specimen.

BEST COPY AVAILABLE

factor plots for the companion compact specimens of this material as well as the higher sulfur A 533-B, coded XE2, XE4, or XE6, in the TL and TS directions which are parallel to the "a" and "c" directions in the part-through crack specimen.

The second set of results presented here corresponds to the test of the higher sulfur A 533-B. The first attempt to test this material was not successful because of highly asymmetric crack extension due to nonuniform nucleation of the precrack from the initial notch. Figures 2-40, 2-41, and 2-42 show a post-test macrophotograph of the specimen, the crack lengths "a" and "c" vs. cyclic count plots, and the fatigue crack growth rate vs. applied cyclic stress intensity factor plots for this test.

The third set of results presented here corresponds to the test of the A 106 Gr. B steel. As in the case above, the first attempt to test this material was not successful because of highly asymmetric crack extension due to nonuniform nucleation of the precrack from the initial notch. Figures 2-43, 2-44, and 2-45 show a post-test macrophotograph of the specimen, the crack lengths "a" and "c" vs. cyclic count plots, and the fatigue crack growth rate vs. applied cyclic stress intensity factor plots for this test. Figure 2-46 shows the fatigue crack growth rate vs. applied cyclic stress intensity factor plots for the companion compact specimens of this material, in the LR and LC directions which are parallel to the "a" and "c" directions in the part-through crack specimen.

2.4.2.2 Clad Specimen Studies

Single tests of clad specimens were conducted at both room temperature and at 288°C in order to ascertain the effect of cladding on the fatigue crack growth rates and fatigue crack front morphology. Both were identically instrumented with six potential-drop probes; no surface crack sensing foil gages were used in either the room temperature or high temperature test. Test loads were the same in both cases. Figures 2-47a, 2-47b, 2-48a, and 2-48b show the macrophotographs and accompanying schematics of the fatigue fracture surfaces from the two tests. It is evident that the crack extended preferentially near the clad-to-base plate interface during the precracking phase of these two tests. The major difference in the two samples is in the extension of the crack along the surface of the two specimens. Evidently, the tensile residual stresses in the clad at room temperature have caused the crack to extend more rapidly along the surface at the lower temperature than at the test temperature of 288°C. Figures 2-49 and 2-50 give the crack length vs. cyclic count plots for these two tests, which were carried out using the same test loads in both cases, thus enabling direct comparison of the results. Figures 2-51 and 2-52 give the fatigue crack growth rate vs. applied cyclic stress intensity factor plots for the two tests.

Fig. 2-40 Photograph of the fatigue fracture surface from the test of specimen code XE4S-5, A 533-B steel, 0.009% sulfur. Specimen tested at 288°C, R = 0.2, 3-Hz sinusoidal, room air environment.

BEST COPY AVAILABLE

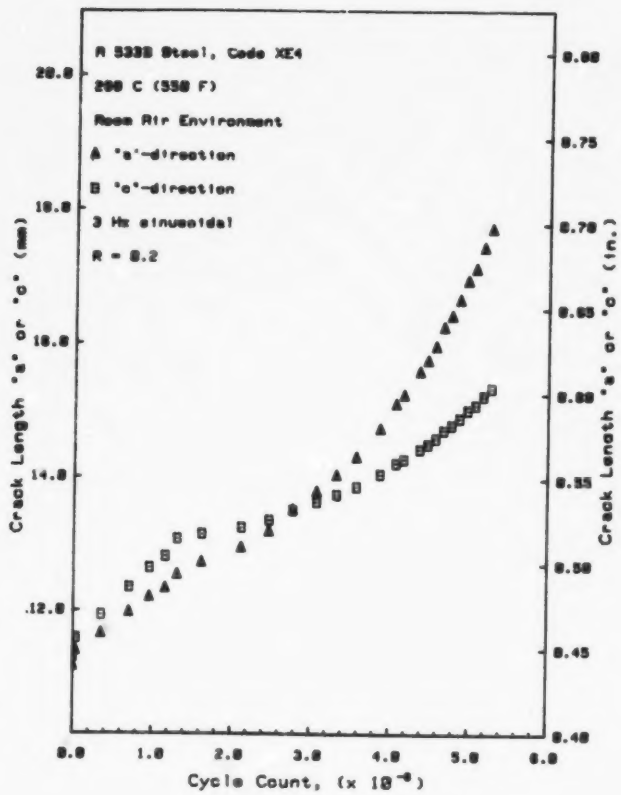

Fig. 2-41 Crack length vs. cylic count for the "a" and "c" directions for the test o specimen XE4S-5.

BEST COPY AVAILABLE

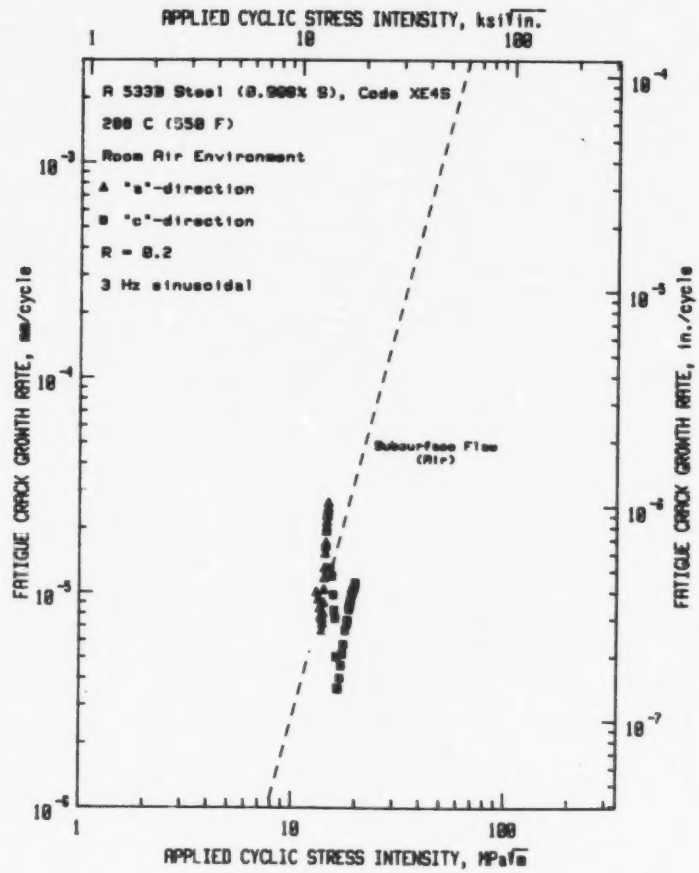

Fig. 2-42 Fatigue crack growth rate vs. applied cyclic stress intensity factor for the test of specimen XE4S-5.

BEST COPY AVAILABLE

PART-THROUGH CRACK GROWTH IN A 106-B TESTED AT 288 C (550 F)

R = 0.2 3Hz SINUSOIDAL WAVEFORM

Fig. 2-43 Photograph of the fatigue fracture surface from the test of specimen code A 106-R2-B, A 106 Gr. B steel, 0.021% sulfur. Specimen tested at 288°C, R = 0.2, 3-Hz sinusoidal, room air environment.

BEST COPY AVAILABLE

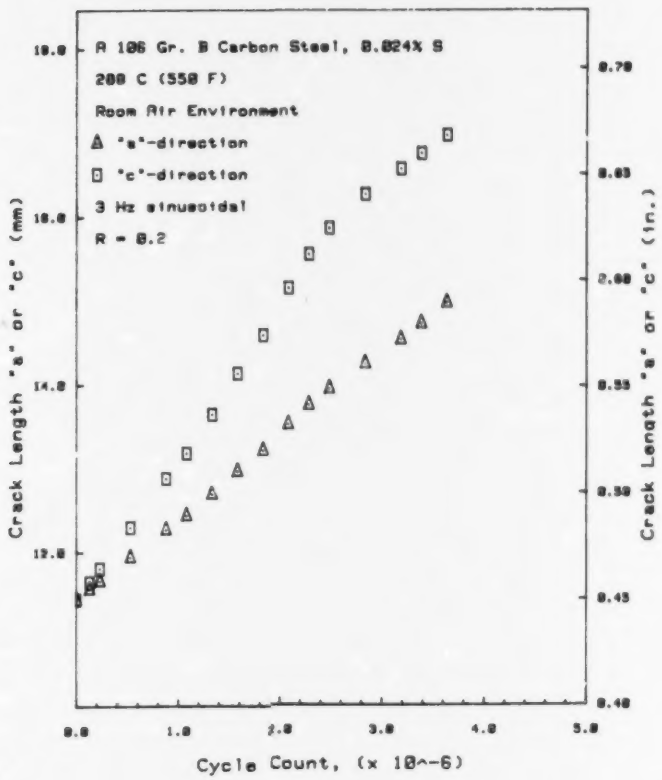

Fig. 2-44 Crack length vs. cyclic count for the "a" and "c" directions for the test of specimen A 106-R2-B.

BEST COPY AVAILABLE

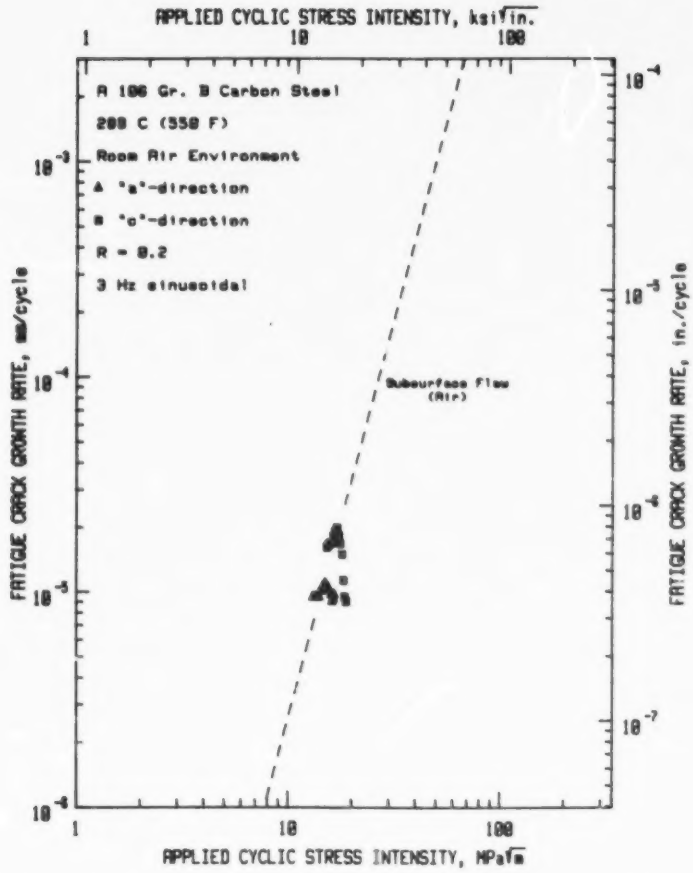

Fig. 2-45 Fatigue crack growth rate vs. applied cyclic stress intensity factor for the test of specimen A 106-R2-B.

BEST COPY AVAILABLE

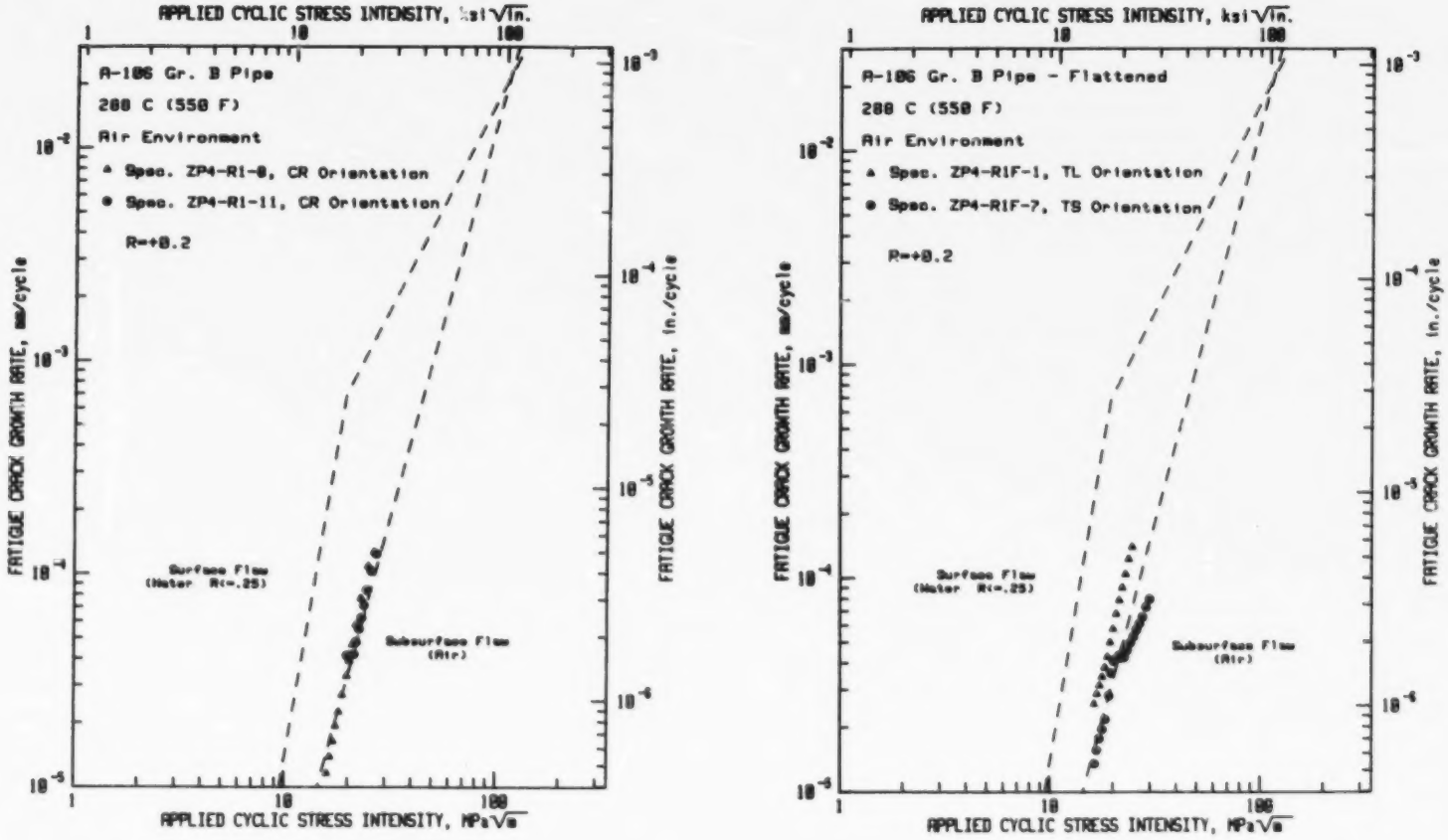
APPLIED CYCLIC STRESS INTENSITY, ksi√in.
A-106 Gr. B Pipe
288 C (550 F)
Air Environment
▲ Spec. ZP4-R1-8, CR Orientation
● Spec. ZP4-R1-11, CR Orientation
R=+0.2
Surface Flaw (Water R=.25)
Subsurface Flaw (Air)
FATIGUE CRACK GROWTH RATE, in./cycle
APPLIED CYCLIC STRESS INTENSITY, MPa√m
A-106 Gr. B Pipe - Flattened
288 C (550 F)
Air Environment
▲ Spec. ZP4-R1F-1, TL Orientation
● Spec. ZP4-R1F-7, TS Orientation
R=+0.2
Surface Flaw (Water R=.25)
Subsurface Flaw (Air)
FATIGUE CRACK GROWTH RATE, in./cycle
APPLIED CYCLIC STRESS INTENSITY, MPa√m

Fig. 2-46 Fatigue crack growth rate vs. applied cyclic stress intensity factor for the tests of A 533-B steel from the same plate as specimen A 106-R2-B. These are compact specimen results for orientations which are collinear with the "a" and "c" growth directions in the part-through cracked specimen.

BEST COPY AVAILABLE

FATIGUE CRACK GROWTH IN CLAD A 533-B

SPECIMEN XE2S-C-4 ~ 25 C (77 F)

SPEC Nº XE2SC-4

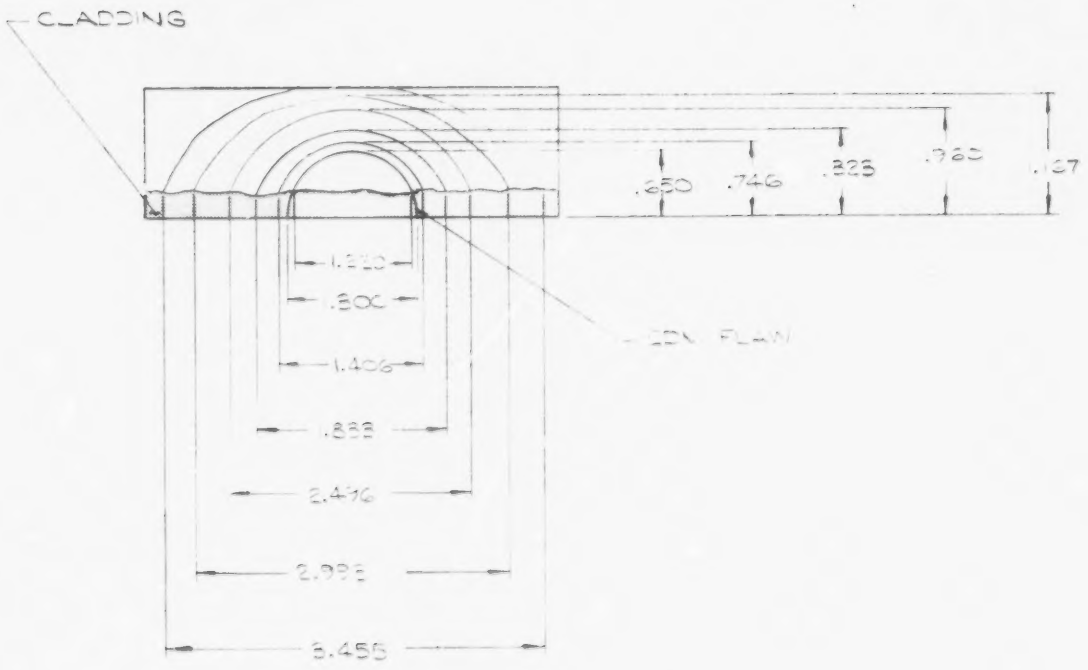

Fig. 2-47 Photograph and accompanying schematic of the fatigue fracture surface from the clad specimen test at room temperature.

BEST COPY AVAILABLE

SPECIMEN XE2S-C-1 288 C (550 F)

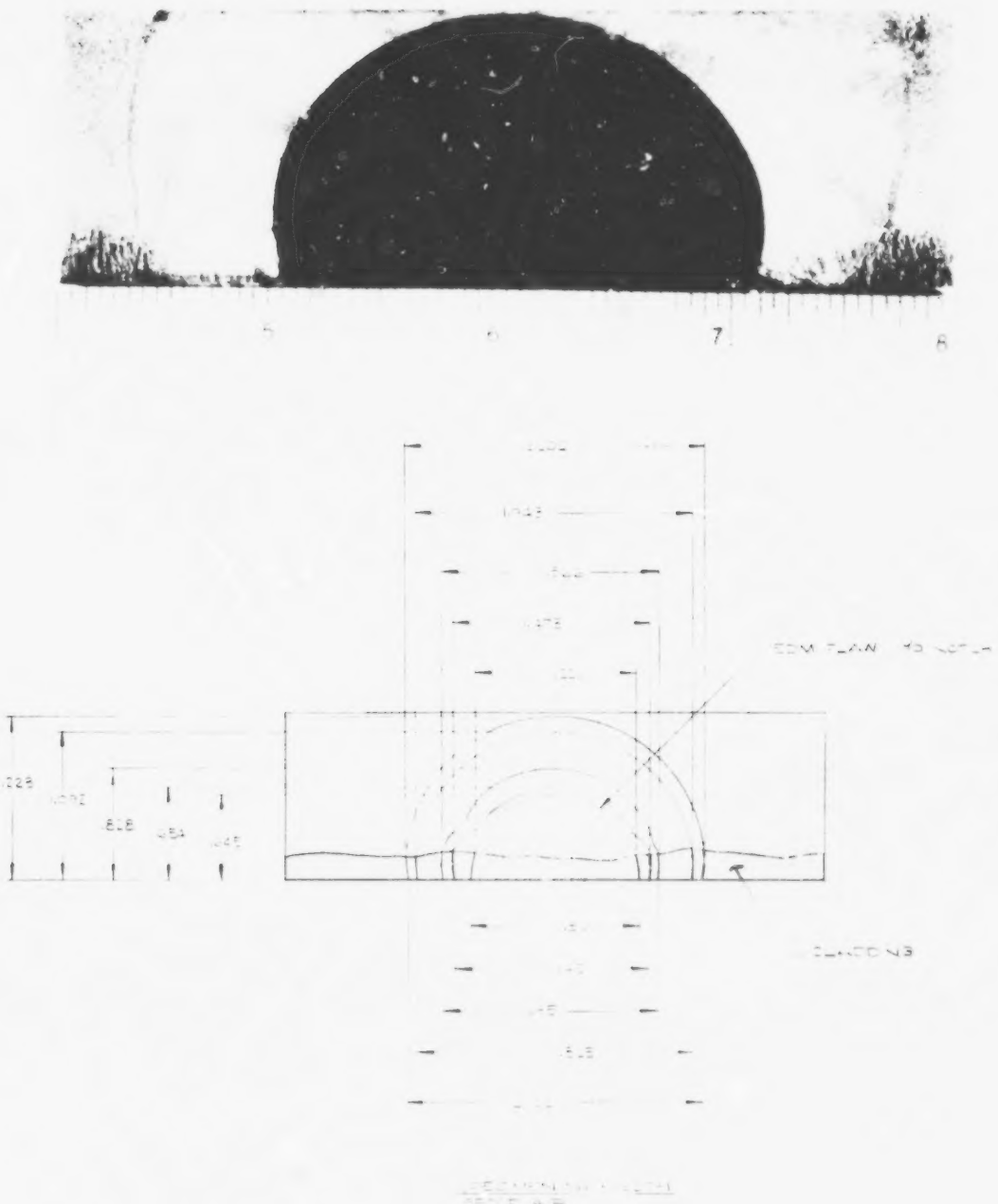

Fig. 2-48 Photograph and accompanying schematic of the fatigue fracture surface from the clad specimen test at 288°C (550°F). Note that the surface crack length for the room temperature test (Fig. 2-47) is proportionately much longer than for the high temperature test.

BEST COPY AVAILABLE

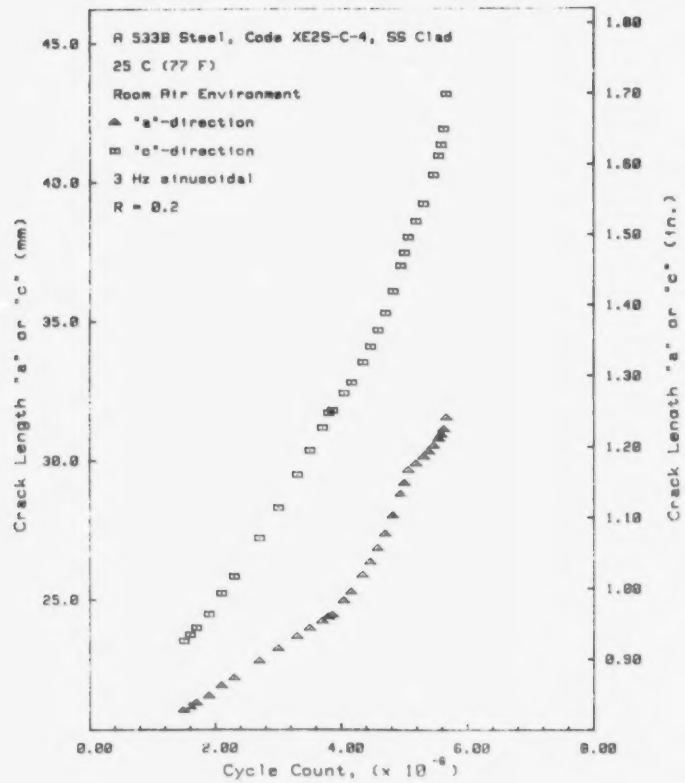

Fig. 2-49 Crack length vs. cyclic count for the "a" and "c" directions for the test of clad specimen XE2-SC4, tested at room temperature.

BEST COPY AVAILABLE

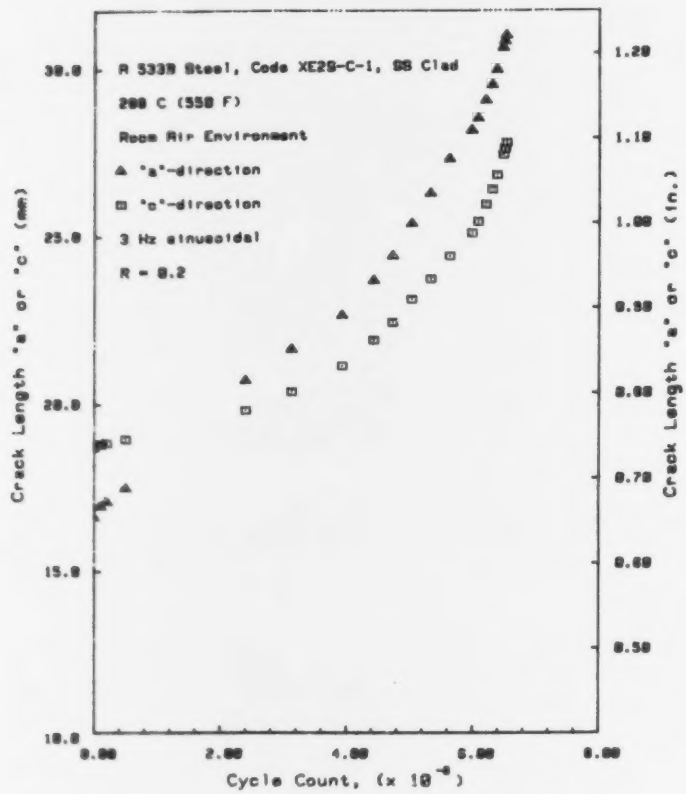

Fig. 2-50 Crack length vs. cyclic count for the "a" and "c" directions for the test of clad specimen XE2-SC1, tested at 288°C (550°F).

BEST COPY AVAILABLE

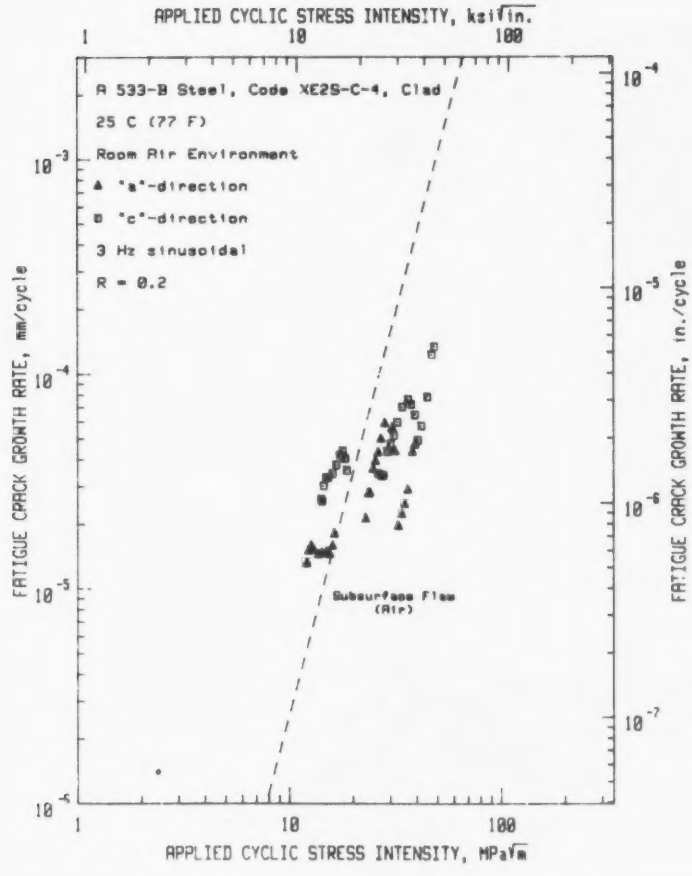

Fig. 2-51 Fatigue crack growth rate vs. applied cyclic stress intensity factor for the test of clad specimen XE2-SC4, tested at room temperature.

BEST COPY AVAILABLE

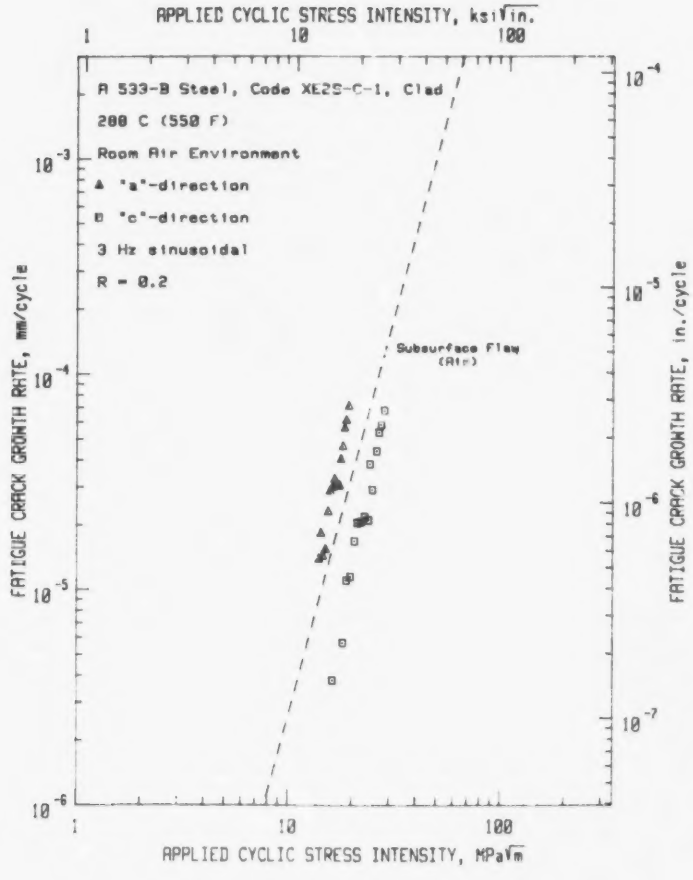

Fig. 2-52 Fatigue crack growth rate vs. applied cyclic stress intensity for the test of clad specimen XE2-SC1, tested at 288°C (550°F).

BEST COPY AVAILABLE

2.4.3 Discussion

The fatigue crack growth rate results from the unclad PTC specimens at both high and low temperatures are reasonable, in agreement with companion results from CT specimens, and do not warrant any further discussion. The original intent of this phase of the work was not in anticipation of determining any such differences, but in the development of the methodology required to perform the PWR environment tests which will follow. However, the differences in the crack shape in the clad PTC specimens for tests conducted at room temperature and 288°C do present some interesting questions on the role of local residual stresses in the fatigue crack extension process.

The residual stresses arise from the difference in thermal expansion coefficients between the clad and the base plate. As the clad metal on the base plate cools from the fusion temperature of the clad layer, the clad contracts approximately 50% more than the base plate, thus giving rise to a tensile field in the clad, balanced by a compressive field in the base plate. The purpose of the stress relief treatment is to alleviate these stresses through thermal activation of dislocations at the stress relief temperature. The hypothesis is that the residual stresses will be reduced to the value of the yield stresses of the base metal and clad, repectively, which is appropriate to the stress relief temperature, assuming that time is sufficiently long to allow this thermal activation to proceed to a reasonable stage. In this case, from Table AHA-2, Part AM of Reference 74, the yield stress of stainless steel of this composition should be about 138 MPa (20.1 ksi) at 621°C (1150°F). Upon cooling (or heating), the thermal contractions (or expansions) lead to changes in stress level ($\Delta\sigma$) given by the formula:

$$\Delta\sigma = E\ \Delta l = E\ \alpha\Delta T \qquad (2\text{-}18)$$

in which Δl is the change in length, ΔT is the change in temperature, E is the elastic modulus, and α is the coefficient of expansion. The constants to be used are appropriate to either the base plate or clad materials for the appropriate temperatures. A simple calculation shows that large stresses result from from the cool-down from the stress relief temperature to room temperature, and it is likely that further deformation will occur during this cool-down. Suffice it to say that at room temperature the stresses at the interface will be well above normal yield for the clad stainless. This is borne out by the study of Reference 75.

This situation at the test temperature of 288°C is confused by the unknown amount of yielding which may have occurred during the cool-down from the stress relief temperature, but generally speaking, during the temperature increase from ambient to 288°C, the high stresses present at room temperature will be reduced to some extent. It is remotely possible that the residual stresses might be reduced to an essentially insignificant value. Adding to this possibility is the fact that the test specimen is held at 288°C for several days in order

to complete the test. Even though the thermal activation of dislocations is not statistically rapid at that temperature, the duration of the test is favorable to at least some additional stress relief.

There are two other factors which must be considered in the explanation of the shape of the fatigue cracks in the clad specimens. A plastic zone is formed at the tip of the fatigue crack. This results in plasticity along both flanks of the crack leading to crack closure. This phenomenon can be related to the compressive stresses in the plastically deformed regions, balanced by tensile stresses just outside this region. For calculational purposes, these plasticity-induced stresses are superposed on the residual stresses. However, the fatiguing process must simulate something analogous to a "shakedown" of the localized residual stress field, perhaps eliminating many of the potential effects of the residual stress field. In a similar vein, one must also consider that the net unflawed test section is subjected to the elastic stress of the test loads applied to the specimen, in this case about 96 MPa (14 ksi). If the clad is already essentially at the yield point before the test loads were applied, then the additional stress is going to take the clad beyond yield on the first applied fatigue cycle. The resultant strains serve to further reduce the effectiveness of the residual stress.

The second factor which could potentially come into play is the fatigue crack growth rate differences in the clad and base plate materials as a function of temperature. In actuality, this should not be a large effect, since for stainless steels, there is only a slight elevation in crack growth rates corresponding to the difference in ambient temperatures and 288°C (Ref. 76), while for the base plate material, there is little change in crack growth rates over the same temperature range. The point is that the rapid extension of the fatigue crack parallel to the clad-base plate interface in the room temperature test cannot be attributed predominately to a difference in the fatigue crack growth rates between clad and base plate materials.

This leaves only the crack closure/plastic-zone argument and the cool-down/plastic yielding/cyclic loading argument to explain why there is such a strong similarity between the crack shapes for the high temperature tests of both unclad and clad materials. It is not possible within the context of this study to examine these relationships any further. The observation and rationalization given above does tend to suggest that the residual stresses are ineffective vis-a-vis fatigue crack growth at temperatures of 288°C.

From these results and discussion, the following observations may be drawn:

(1) Crack growth rates in room air environments, at both room temperature and 288°C are very similar to those obtained in compact specimens of similar or identical materials. If there is any interaction between the growth rates in the "a" and "c" directions, it is not sufficiently large to impact these data sets, at least in terms of fatigue crack growth rates.

(2) The rapid growth of the crack in the clad and along the clad-to-base plate interface at room temperature results in a large difference in the eccentricity of clad specimen cracks for specimens tested at room temperature and 288°C. Bearing in mind that the clad plates were stress relieved at a little over 600°C prior to specimen fabrication, it is interesting to note that at 288°C, the shape of the crack in the clad specimen is virtually identical to the shape of the crack in a companion unclad specimen, indicating that the residual stresses which remain in the specimens at the test temperature of 288°C are not sufficiently high to affect crack growth rates or shape.

(3) Future tests in a water environment should prove to be especially interesting since it is clear that the "canoe-shaped" profile of the part-through cracks developed during the higher tests is nearly ideal for trapping the aqueous environment, possibly leading to the stagnation and contaminent specie build-ups which might in turn lead to enhancement of the environmental-assistance component of the fatigue crack growth rates.

(4) Fatigue crack growth rates in the piping steels are of about the same magnitude as those in the pressure vessel steels. The only significant difference which has been noted is the slightly greater variability in the crack growth rates in the specimens taken from the flattened product as compared with those specimens taken from the unflattened piping steel.

2.5 Environmentally-Assisted Fatigue Crack Growth

W. H. Cullen

2.5.1 Background

Fatigue crack growth and stress-corrosion cracking programs utilizing conventional specimens have been the backbone of the NRC-sponsored program on environmental effects since its inception in the mid-1970's. Use of these specimens in several investigations with difference test parameter matrices has resulted in the identification of several critical variables and their range of influence. Among these are the influence of waveform, test frequency, material chemistry, irradiation, temperature, and load ratio. The objective of this task has been to continue this ongoing program aimed at the development of da/dN vs. ΔK for a wide variety of pressure vessel and piping steels. The emphasis is on extending the range of selected variables for the materials being tested, particularly load ratio, test frequency, and material chemistry. A test matrix of pressure vessels steels, including welds and heat-affected zone material, and addressing critical variables such as material chemistry, load ratio, test frequency, and specimen orientation was initiated in 1980 and concluded in 1985. A test matrix addressing load ratio, temperature, and test frequency effects in piping steels was initiated in 1982 and was concluded also in 1985. Carbon steels, such as A 106 Gr. C and A 516 Gr. 70, and a cast stainless steel, A 351-CF8A, were incorporated into this study. Topical reports describing these studies are available (Refs. 71 and 72).

2.5.2 Summary of Results

During 1985, fatigue crack growth rate tests of A 106 Gr. C carbon steel, A 508-2 and A 533-B, as well as tests of submerged-arc weld metal were completed. Completion of these tests represented the last of the piping and pressure vessel steel tests to be carried out under the guidelines of the test matrices developed at the beginning of the program. During 1986, a report was issued (Ref. 77) which (a) gave a concise review of the significant critical variables for fatigue crack growth, (b) presented the data sets from the 1985 tests, and (c) indicated those research and engineering areas for which data sets were few in number, or nonexistent altogether. All of these areas are critical for the application of Section XI of the ASME Boiler and Pressure Vessel Code, or similar life assessment calculations, to various situations or to certain materials categories.

Among these topics suggested as necessary for continued improvement of the Code are the following:

(1) Research at higher load ratios. Although the research techniques are available, it is technologically more difficult to conduct fatigue crack growth rate tests at very high load ratios and the concomitantly much reduced ΔK range. Unfortunately, it is well known that the bulk of the reactor operating transients

occur at high load ratio, so the data base is weakest in exactly that area in which the need is greatest.

(2) Research into temperature effects as a function of load ratio. Temperature effects for cast stainless steels (Ref. 72), carbon steels (Ref. 71), and irradiated and unirradiated A 508-2 low alloy steels of medium sulfur content (Refs. 78 and 79) were determined in the early 1980's within the context of this NRC program. In 1977, the temperature dependence of A 533-B was established by researchers at Central Electricity Research Laboratories (Ref. 80). However, all of these data sets were derived for a load ratio of 0.2. These data sets have proven to be of great importance in understanding the mechanisms of environmentally-assisted fatigue crack growth rates, and in the refinement of strain rate models for calculating fatigue crack growth rates of pressure vessel steels. For this reason, and in conjunction with the discussion above of the general need for high load ratio crack growth rate research, it is important to continue to expand the matrix of test results which will establish more generally the effects of temperature and higher load ratios on fatigue crack growth rates.

(3) Research on the correlation of sulfur chemistry, inclusion morphology, and crack growth rate effects. It is generally acknowledged that increased sulfur content results in increased fatigue crack growth rates in PWR environments. However, the more local kinetics of the crack growth mechanisms are not understood. Enough research has been completed to know that there are some cases of low sulfur steels exhibiting high growth rates and high sulfur steels exhibiting low growth rates. Since many reactor materials have through-thickness sulfur gradients and since the thermal mechanical processing often results in fine grain structure and small inclusion particles near the surface of thick sections, it can be expected that fatigue crack growth rates will be as dependent on location and local microstructural character, as on environmental and loading parameters. Any serious attempt to develop predictive models for the calculation of fatigue cracking needs a much improved data base and mechanistic understanding than that which currently exists.

(4) Research on stainless steels. At present, there is available only a bare minimum of fatigue crack growth data for cast or wrought stainless steels in pressurized, high-temperature water. It is interesting to note that the environmental effects are nearly nonexistent at a load ratio of 0.2 but increase dramatically as the load ratio increases (Ref. 71). Additionally, even though the proportion of environmental enhancement of crack growth rates at $R = 0.2$ is small, the effect on the fractography is extremely large. The fractographic features on the cast stainless tested at $R = 0.2$ show that brittle-appearing areas cover nearly all of the fatigue fracture surface. The fractography at $R = 0.2$ is qualitatively the same as that at $R = 0.7$ and $R = 0.85$. The implication here

is that for all load ratios, the fractographic features show strong effects of the environmental presence, yet the crack growth data only reveal that presence at the higher load ratios. Clearly, there is a mechanism active at the load ratio of 0.2 which causes the fractographically brittle-like appearance, without causing the increase in growth rates. Alternatively, the choice of test frequency, waveform, or other test variable is suppressing the environmental component of the crack growth rates, without suppressing the crack-tip mechanism which is producing the brittle-like appearance. In any case, there is something here which is not understood well and which could be a potential problem in the accurate prediction of stainless steel component life.

3. RADIATION SENSITIVITY AND POSTIRRADIATION PROPERTIES RECOVERY

3.1 Effect of Temperature on Annealing for Alleviating Radiation-Induced Embrittlement

J. R. Hawthorne

3.1.1 Background

Postirradiation heat treatment has been shown effective in mitigating radiation-induced embrittlement in low alloy steels and welds such as those forming early production (pre-1972) reactor pressure vessels. Moreover, the method has been applied successfully to the vessels of two light-water-cooled and moderated power reactors. These are the Army SM-1A and the Belgian BR-3 reactors whose rate of embrittlement accrual exceeded initial estimates. Their vessel service temperatures of 224°C and 260°C, respectively, are lower than the service temperatures of large commercial power reactors, nominally 288°C; nonetheless, their anneals demonstrate that the method can be applied to certain power reactor vessels to reduce embrittlement if needed.

Studies to date have focused on 399°C annealing; however, the consensus of a 1984 MEA survey of reactor vessel fabricators and steam system suppliers was that higher temperature annealing such as 454°C annealing may be feasible for some vessels now in service. The practical temperature limit is governed in part by the thermal behavior of piping, supports, and the biological shield adjacent to the vessels.

Data from studies of 454°C annealing are limited but suggest that in addition to the possibility for a high percentage recovery in vessel properties, material resistance to reirradiation embrittlement may be significantly different from that following 399°C annealing. Also, certain data suggest that embrittlement saturation occurs with reirradiation and that the embrittlement level at saturation is lower than that immediately preceding the anneal. If confirmed for highly radiation-sensitive steels and welds, such a characteristic would have a major impact on future vessel operations and annealing decisions, especially where plant lifetime extension (PLEX) are of concern. One complication is the known variability in steel and weld metal responses to 399°C and 454°C. Composition aspects are investigated by MEA separately in an effort to isolate the source(s) of the differences in annealing recovery (see section 3.2 below).

In 1984, a study of irradiation-annealing (IA) and irradiation-annealing-reirradiation (IAR) behavior of weld metals was mounted to resolve three issues: firstly, the extent of difference between and the variability of 454°C vs. 399°C annealing recovery in welds typical of early vessel fabrication; secondly, the reembrittlement trends and rates following 454°C vs. 399°C annealing; and lastly, the significance of material type and fabrication history to the recovery obtainable with each treatment and to reirradiation behavior. A critical test of welding flux type vs. recovery was among specific objectives.

In 1985, welds encompassing the four generic types found in early vessels were acquired (Table 3-1). All four weld deposits contain a high copper content or an intermediate copper content, synonomous with high radiation sensitivity. Other factors such as nickel content (high or low) and weldment flux type (Linde 80, Linde 0091 or Linde 124) depict the range of materials found in early vessel welding. In the case of the weld code WW7, the nonavailability of high copper, low nickel welding filler wire required MEA fabrication of a new weld using welding equipment specially reactivated for the project. Progress in 1985 also included the 288°C irradiation of one experiment assembly containing Charpy-V (C_v) and tensile specimens.

Table 3-1 Submerged-Arc Weld Deposit Materials

Weld No.	MEA Code	Nominal Composition (Wt-%)		Welding Filler	Welding Flux
		Cu	Ni		
1	W8A	0.39	0.65	MnMoNi	Linde 80
2	W9A	0.39	0.65	MnMoNi	Linde 0091
3	WW4	0.15	0.65	MnMoNi	Linde 124
4	WW7	0.35	0.11	MnMo	Linde 80

3.1.2 Summary of Results

Figures 3-1 and 3-2 illustrate schematically the series of irradiation, annealing, and reirradiation tests planned for the four welds. The Irradiation (I), Irradiation-Anneal (IA), and Reirradiation (IAR) exposures of the four welds were completed in 1986. All irradiations were at a controlled temperature of 288°C nominal. The target first cycle fluence was 1.2×10^{19} n/cm^2, E > 1 MeV; the target reirradiation fluence was 0.3×10^{19} n/cm^2 or 0.7×10^{19} n/cm^2. Tests of the C_v and tensile specimens from all but one assembly were completed in this reporting period also. C_v results are illustrated in Figs. 3-3 to 3-16; tensile test findings are listed in Table 3-2. The untested assembly (HTA-3) represents the higher fluence IAR condition.

The welds exhibited a range of radiation embrittlement sensitivities. Typically, high sensitivity was found with a high copper content. High copper content coupled with a high nickel content, as expected, proved particularly detrimental to weld metal radiation resistance. For example, weld code W8A (high nickel) exhibited a much greater C_v 41-J transition temperature elevation than weld code WW7

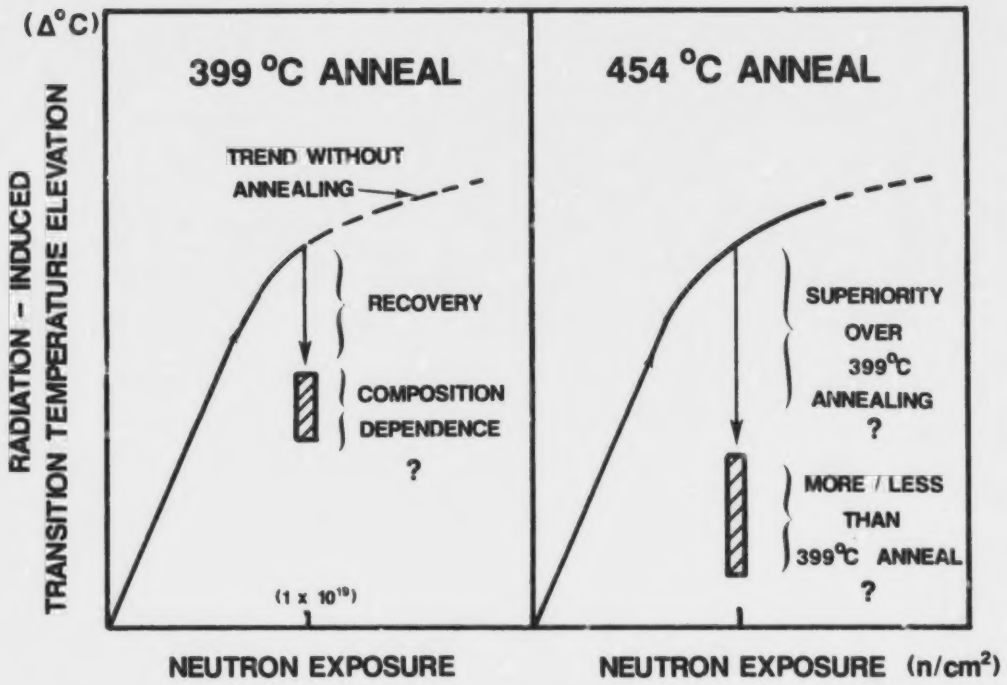

Fig. 3-1 Plan for Phase 1 investigations (I and IA conditions).

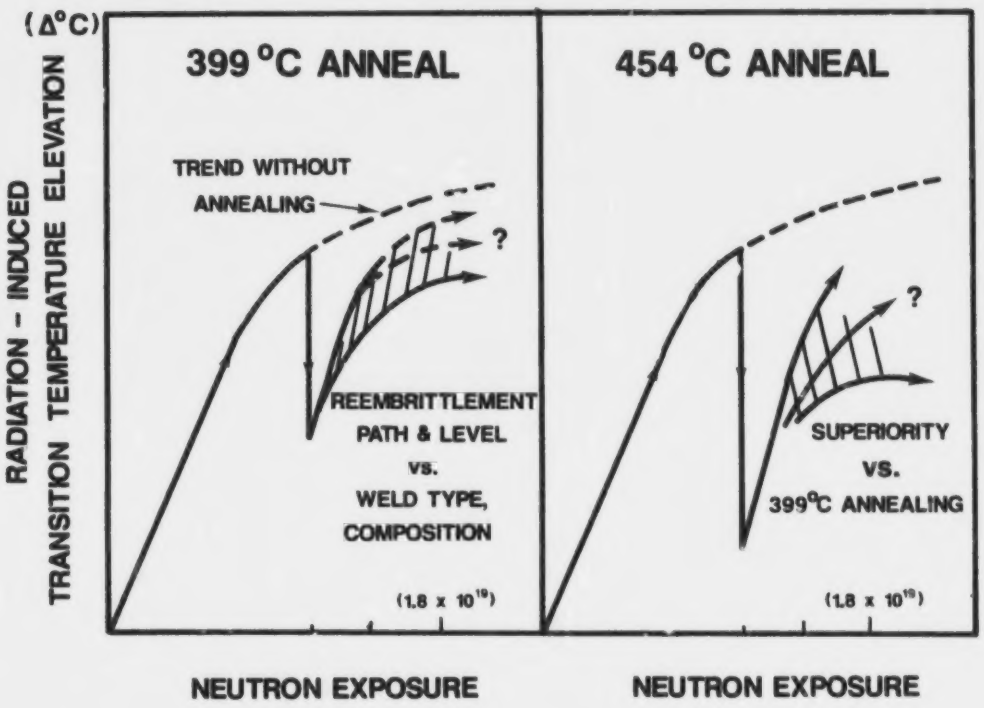

Fig. 3-2 Plan for Phase 2 investigations (two IAR fluence conditions).

BEST COPY AVAILABLE

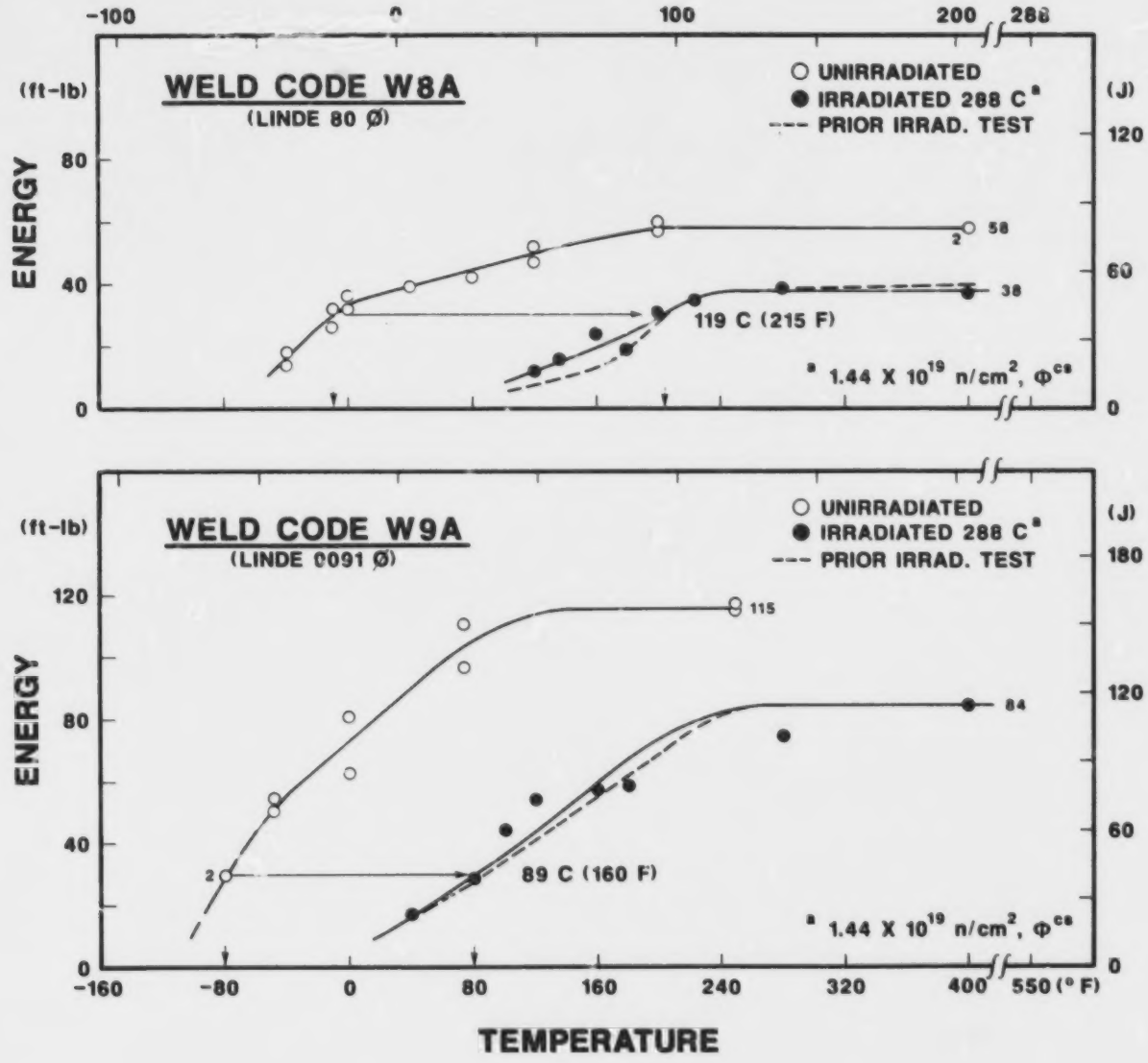

Fig. 3-3 Charpy-V notch ductility of submerged-arc welds, code W8A (upper graph) and code W9A (lower graph), before and after irradiation in assembly HTA-1 (UBR-62). The welds were made with the same lot of copper-coated weld filler wire but with different fluxes: Linde 80 and Linde 0091, respectively. The data points for the irradiated condition agree well with the data trend for a prior irradiation test at about the same fluence (dashed curve) in each case.

BEST COPY AVAILABLE

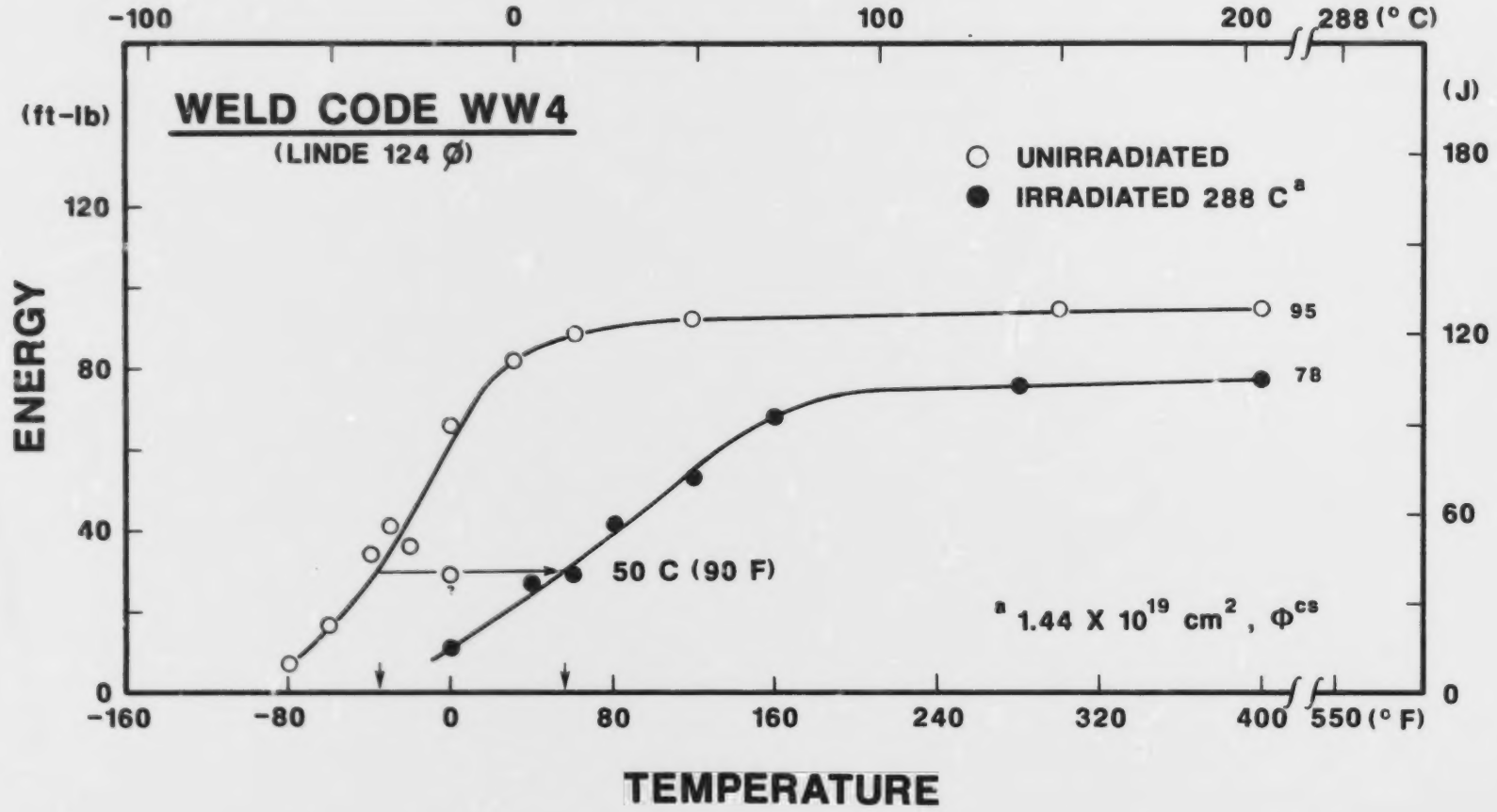

Fig. 3-4 Charpy-V notch ductility of submerged-arc weld, code WW4, before and after irradiation in assembly HTA-1 (UBR-62). Specimens for this weld were commingled with specimens of weld codes W8A and W9A of Fig. 3-1.

BEST COPY AVAILABLE

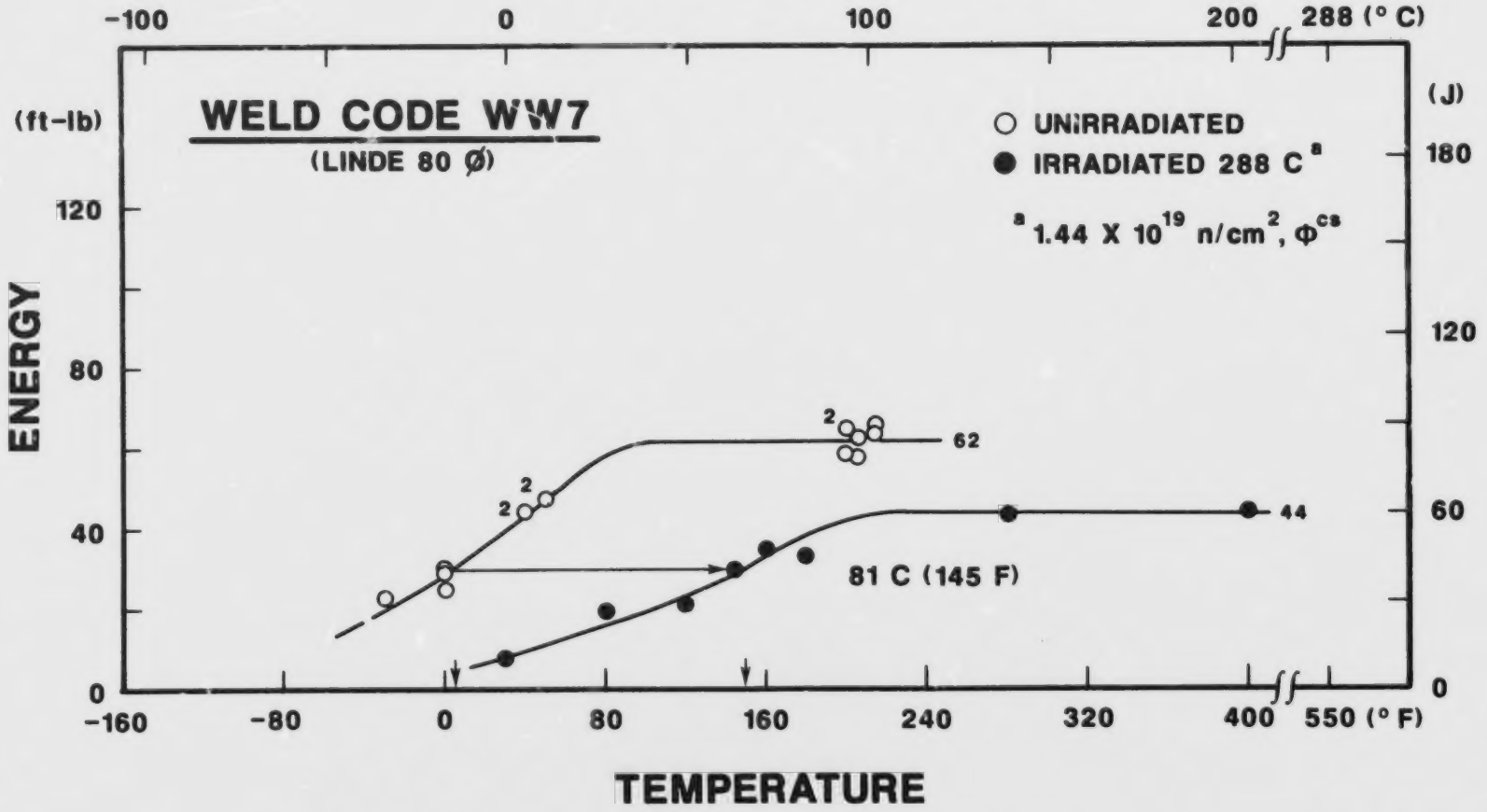

Fig. 3-5 Charpy-V notch ductility of submerged-arc weld, code WW7, before and after irradiation in assembly HTA-1. Specimens of this weld were commingled with specimens of weld codes W8A, W9A, and WW4 of Figs. 3-1 and 3-2.

BEST COPY AVAILABLE

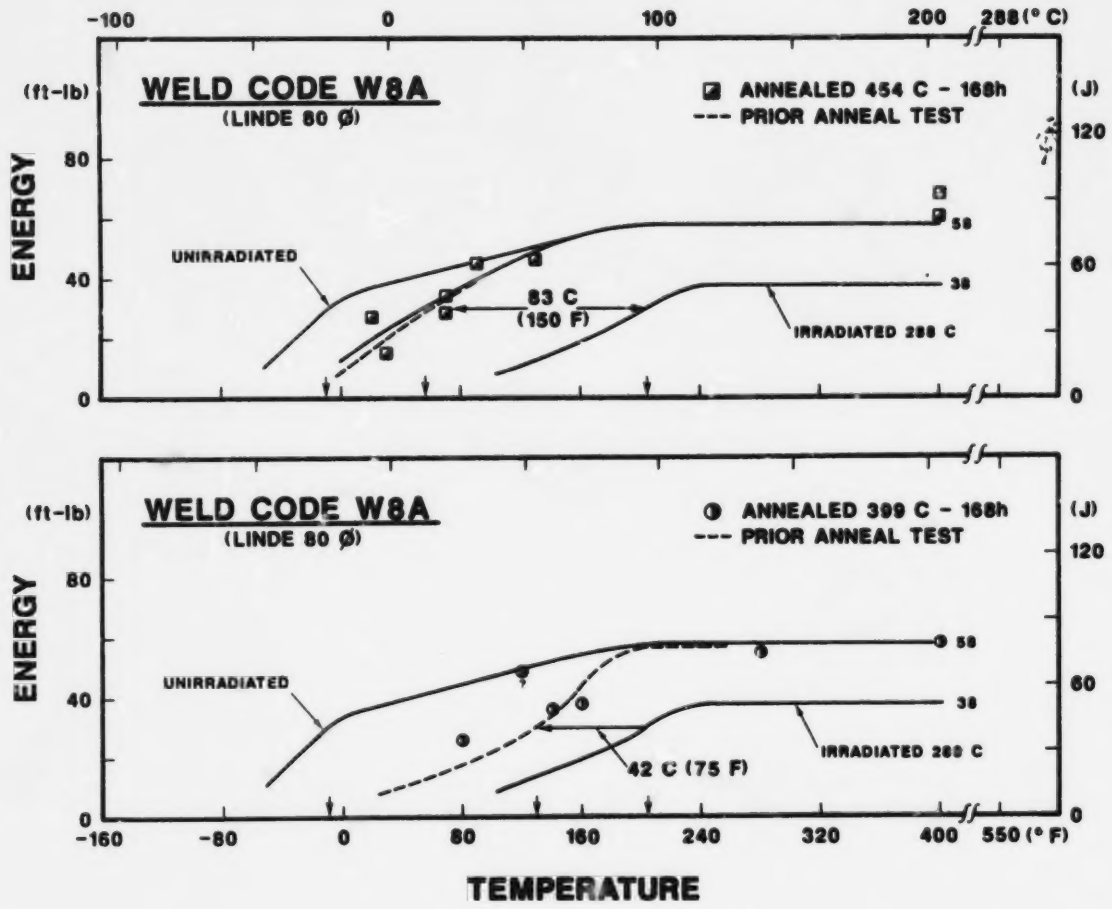

Fig. 3-6 Charpy-V notch ductility of submerged-arc weld, code W8A, before and after irradiation and after postirradiation annealing at 454°C (upper graph) and at 399°C (lower graph) (Assembly HTA-1).

BEST COPY AVAILABLE

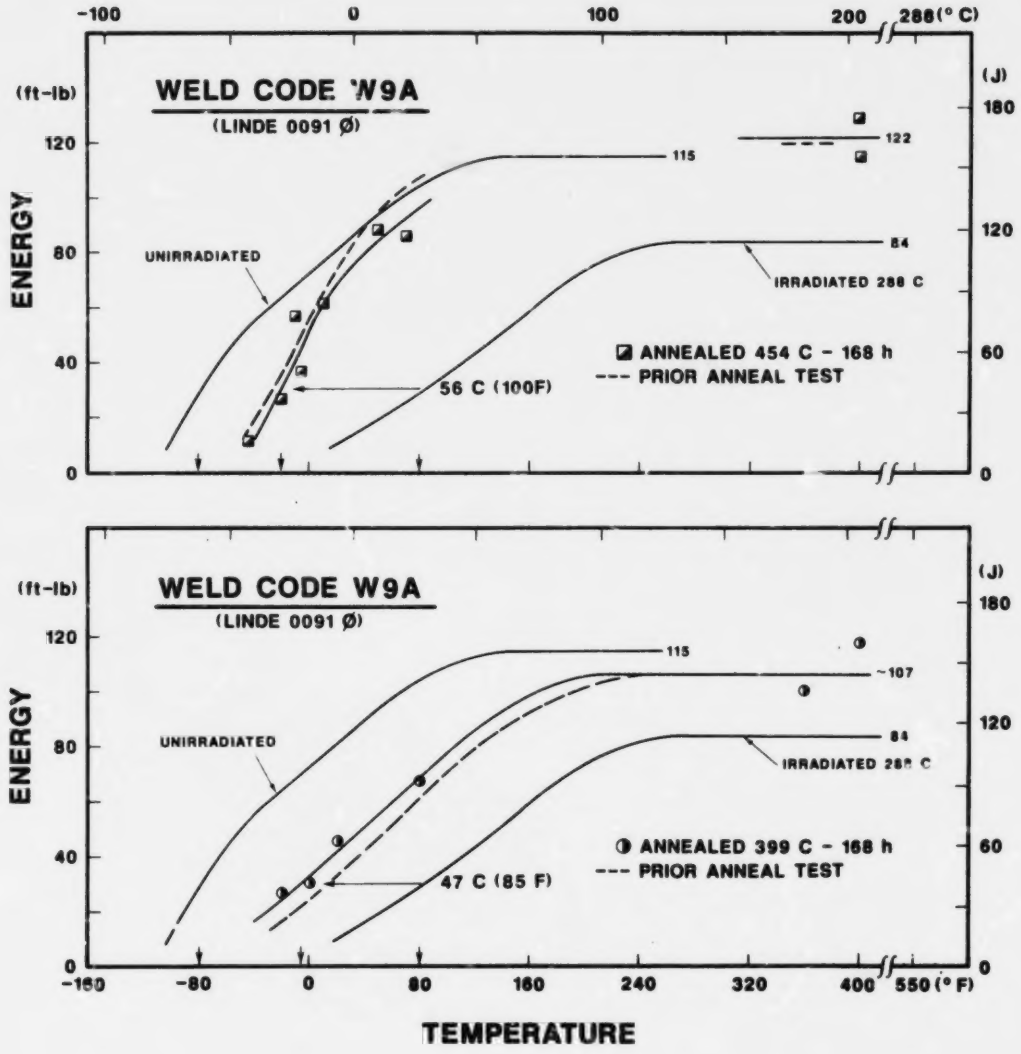

Fig. 3-7 Charpy-V notch ductility of submerged-arc weld, code W9A, before and after irradiation and after postirradiation annealing at 454°C (upper graph) and at 399°C (lower graph) (Assembly HTA-1).

BEST COPY AVAILABLE

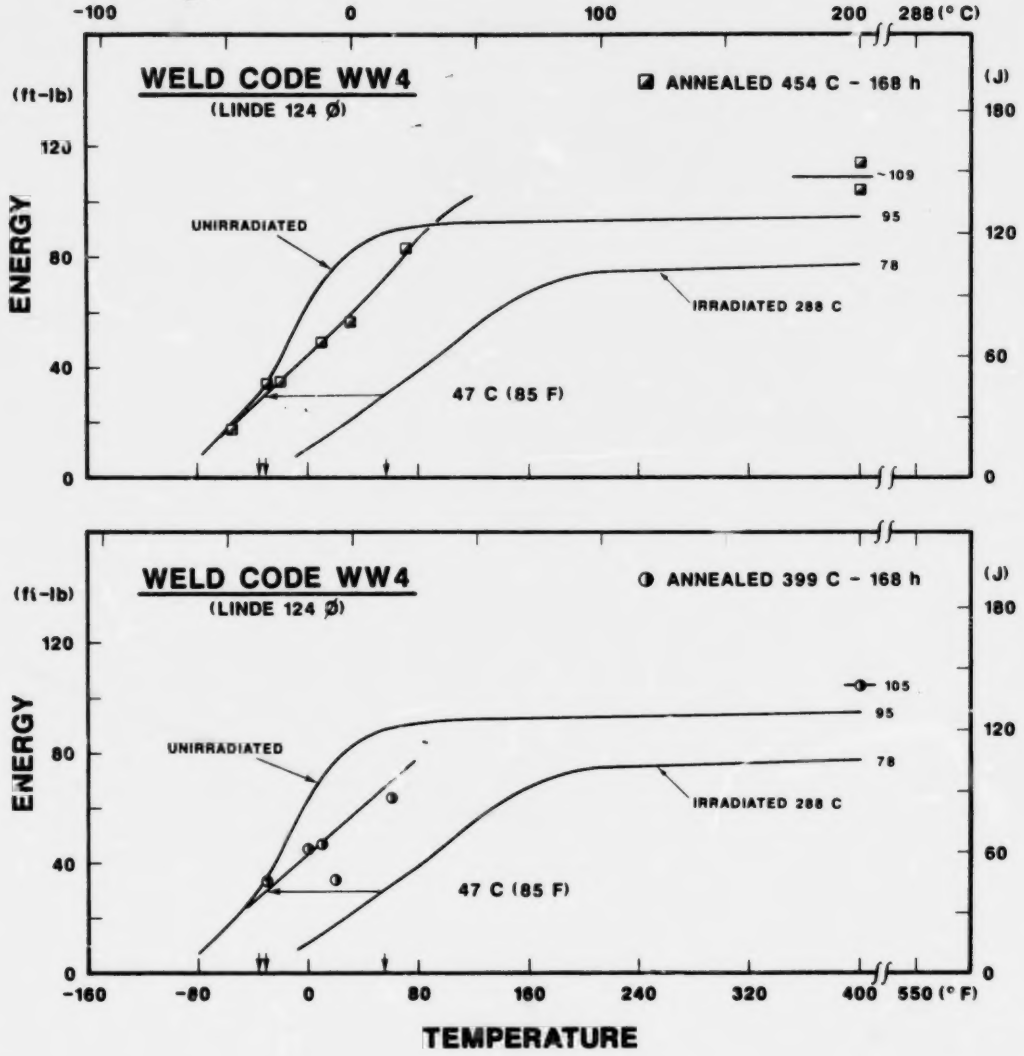

Fig. 3-8 Charpy-V notch ductility of submerged-arc weld, code WW4, before and after irradiation and after postirradiation annealing at 454°C (upper graph) and at 399°C (lower graph) (Assembly HTA-1).

BEST COPY AVAILABLE

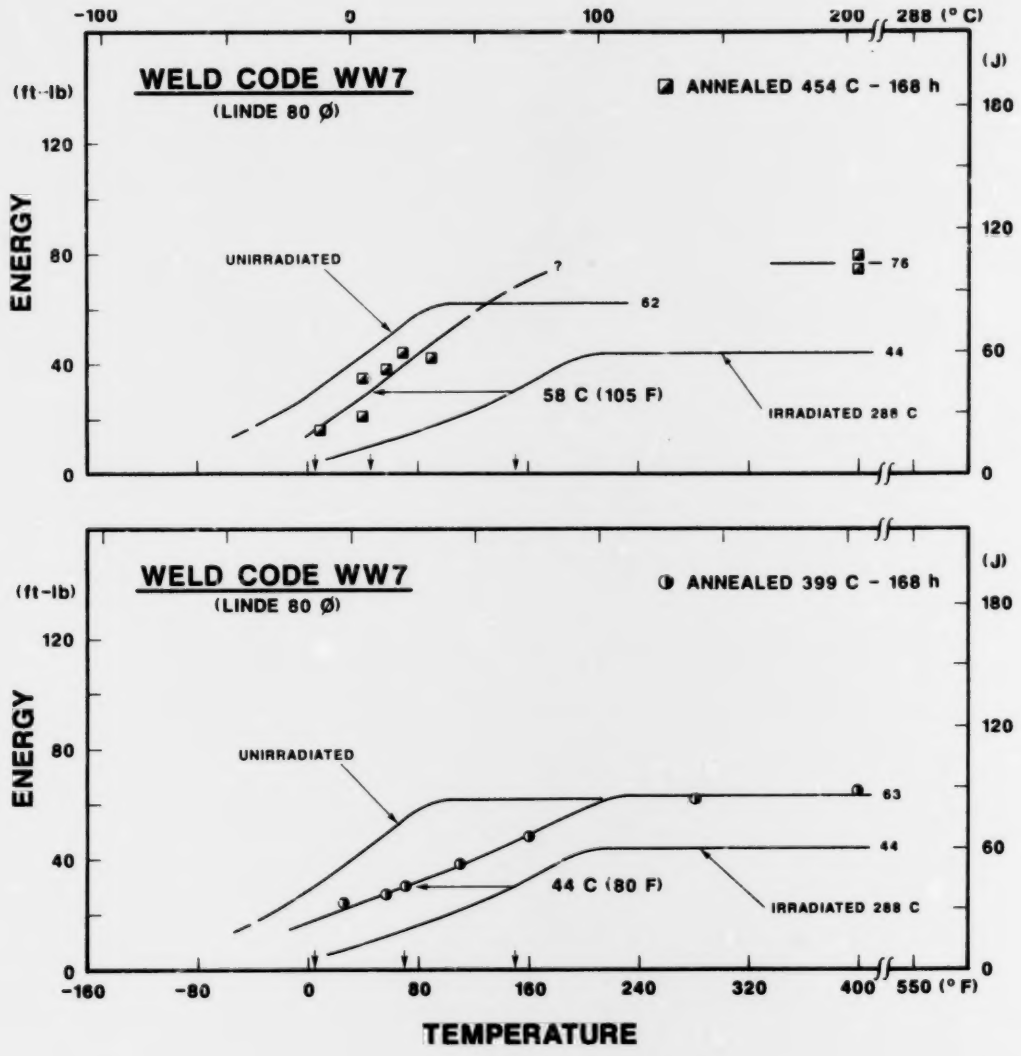

Fig. 3-9 Charpy-V notch ductility of submerged-arc weld, code WW7, before and after irradiation and after postirradiation annealing at 454°C (upper graph) and at 399°C (lower graph) (Assembly HTA-1).

BEST COPY AVAILABLE

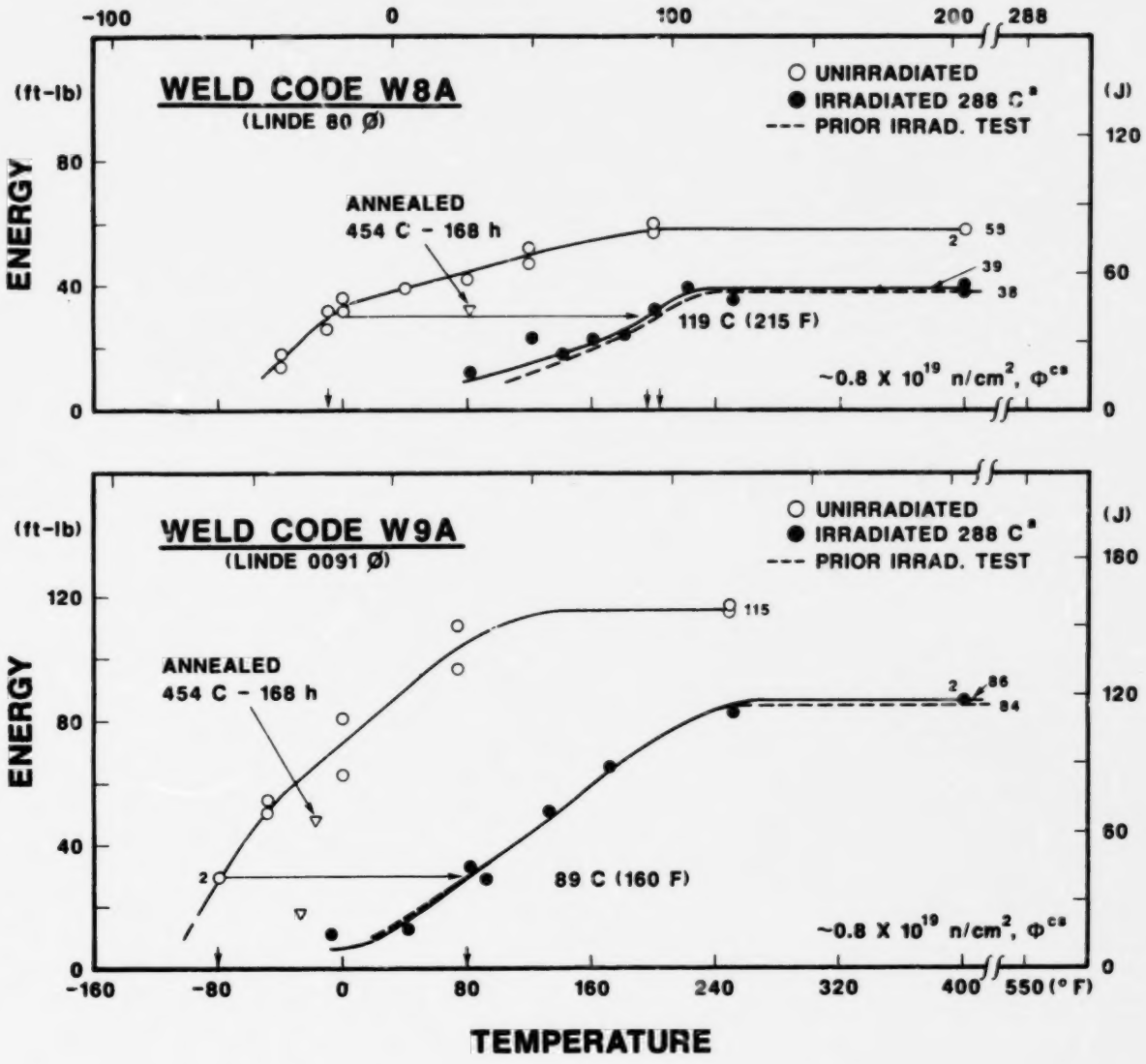

Fig. 3-10 Charpy-V notch ductility of submerged-arc weld, code W8A (upper graph) and code W9A (lower graph), before and after irradiation to ~ 8 x 10^{19} n/cm^2, E > 1 MeV (preliminary fluence estimate) (Assembly HTA-4, UBR-72A).

BEST COPY AVAILABLE

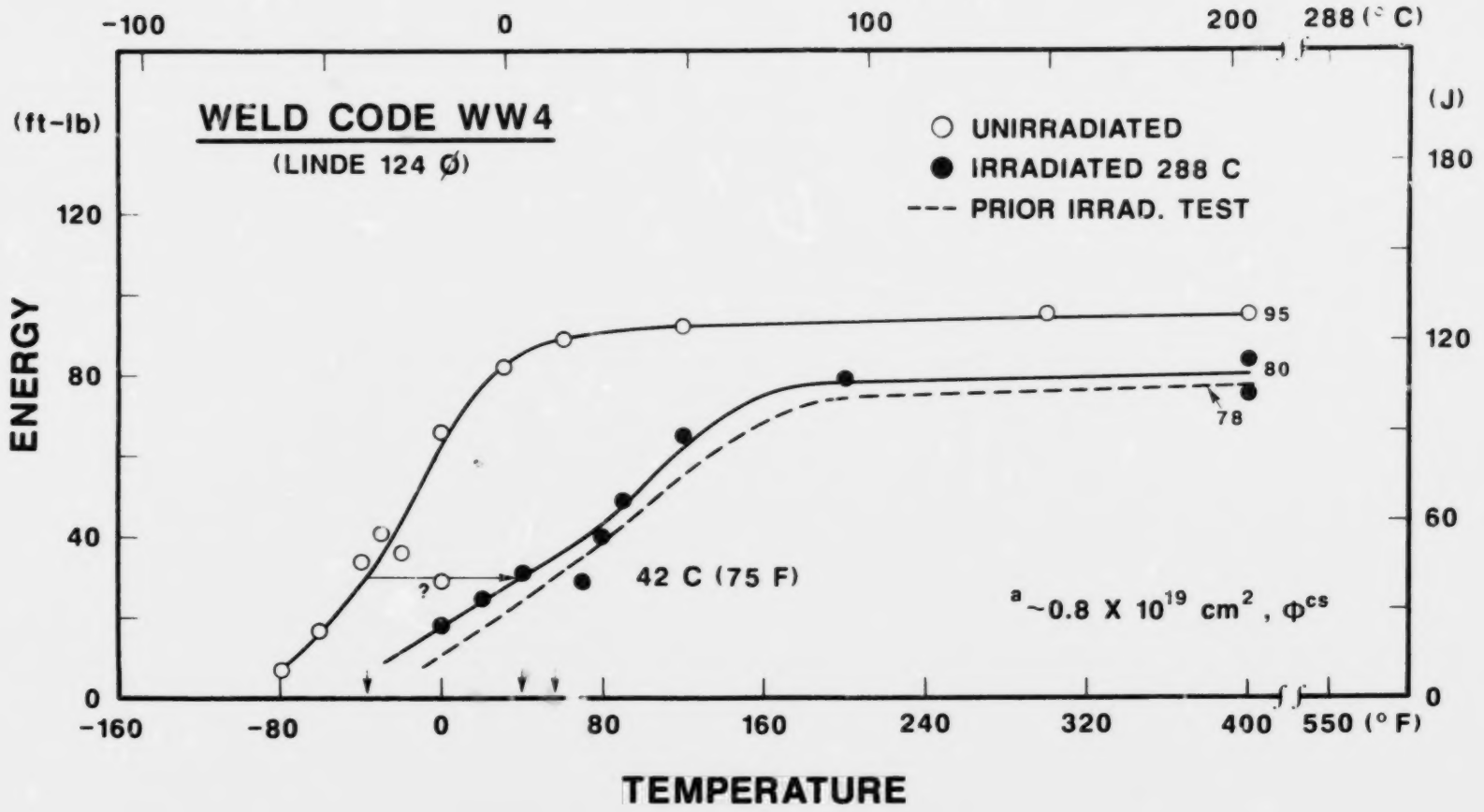

Fig. 3-11 Charpy-V notch ductility of submerged-arc weld, code WW4, before and after irradiation to ~ 8 x 10^{18} n/cm^2, E > 1 MeV (Assembly HTA-4, UBR-72A).

BEST COPY AVAILABLE

155

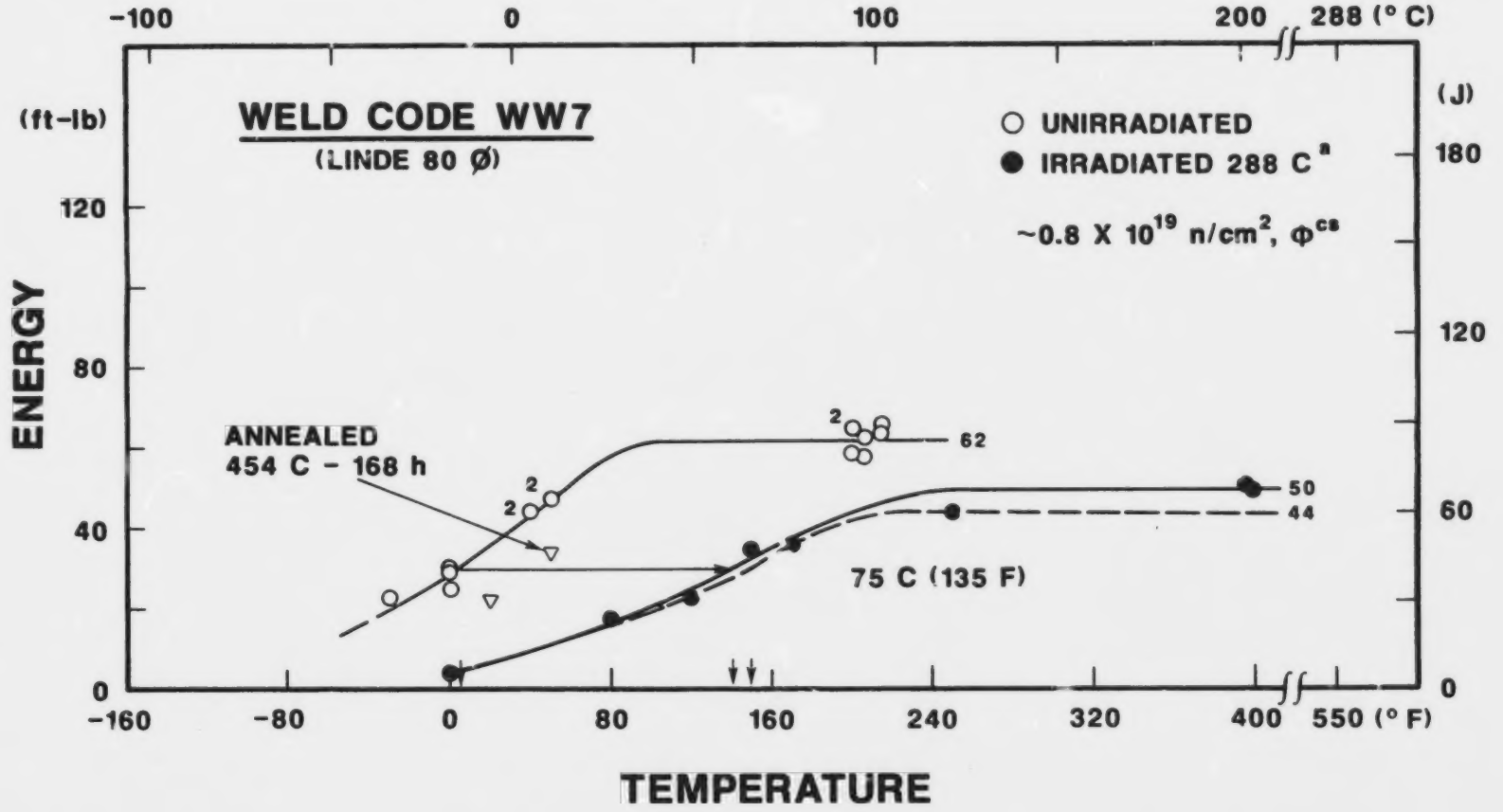

Fig. 3-12 Charpy-V notch ductility of submerged-arc weld, code WW7, before and after irradiation to ~ 8 x 10^{18} n/cm^2, E > 1 MeV (Assembly HTA-4, UBR-72A).

BEST COPY AVAILABLE

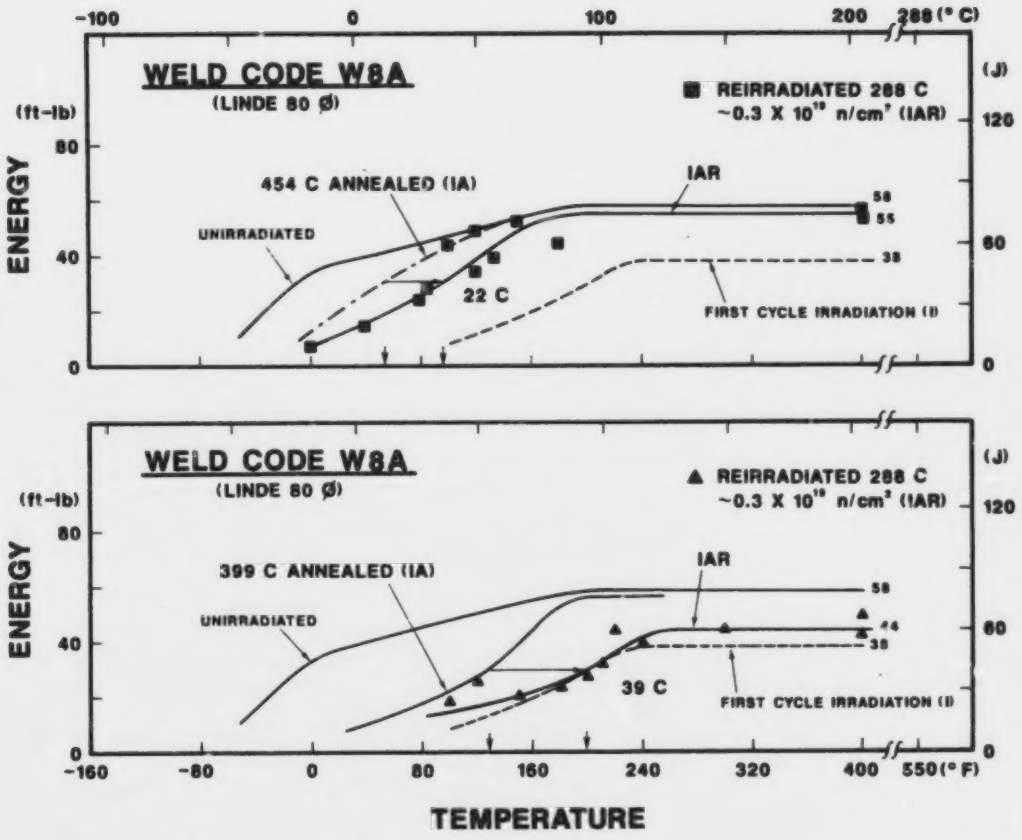

Fig. 3-13 Charpy-V notch ductility of submerged-arc weld, code W8A, after reirradiation following a 454°C intermediate anneal (upper graph) and after reirradiation following a 399°C intermediate anneal (lower graph). Trend lines for the I and IA condition are also shown for reference (Assembly HTA-3, UBR-70).

BEST COPY AVAILABLE

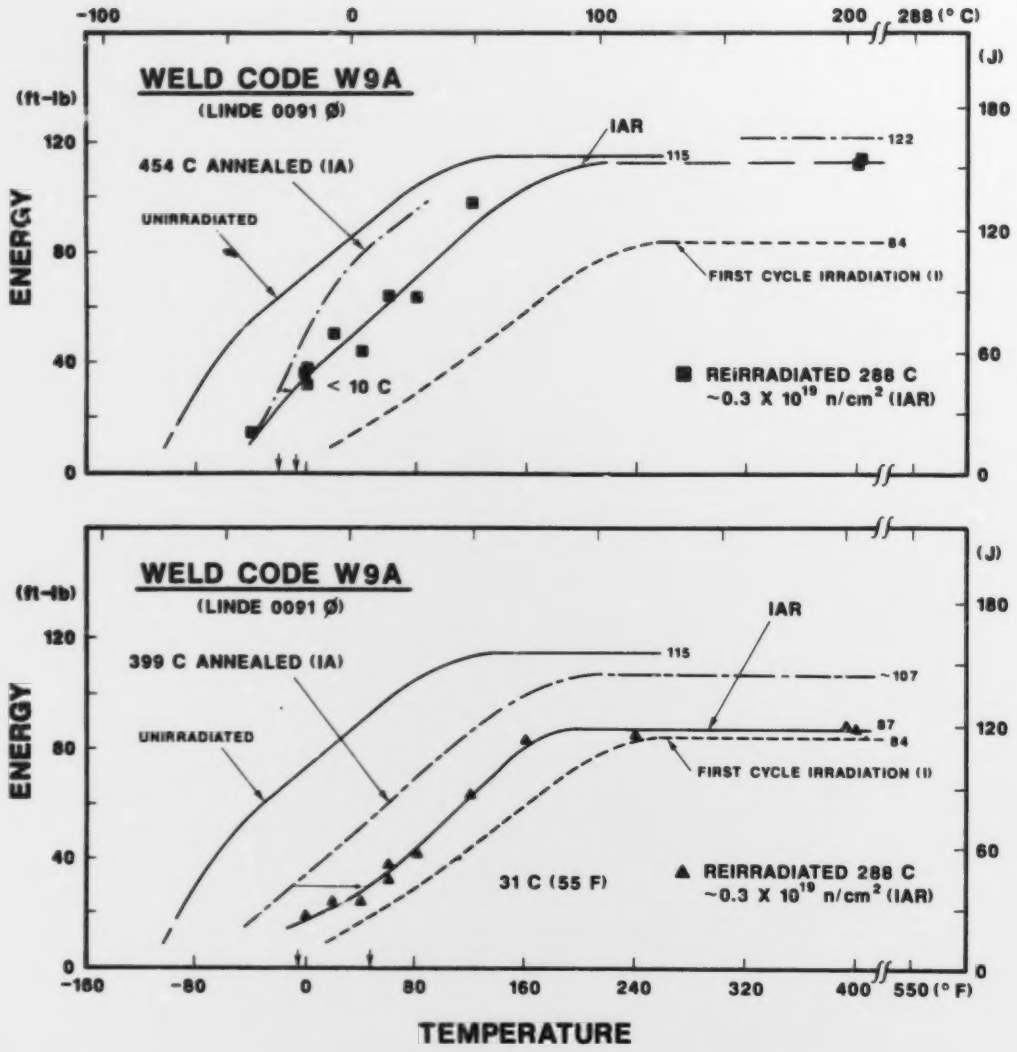

Fig. 3-14 Charpy-V notch ductility of submerged-arc weld, code W9A, after reirradiation following a 454°C intermediate anneal (upper graph) and after reirradiation following a 399°C intermediate anneal (lower graph). Trend lines for the I and IA condition are also shown for reference (Assembly HTA-3, UBR-70).

BEST COPY AVAILABLE

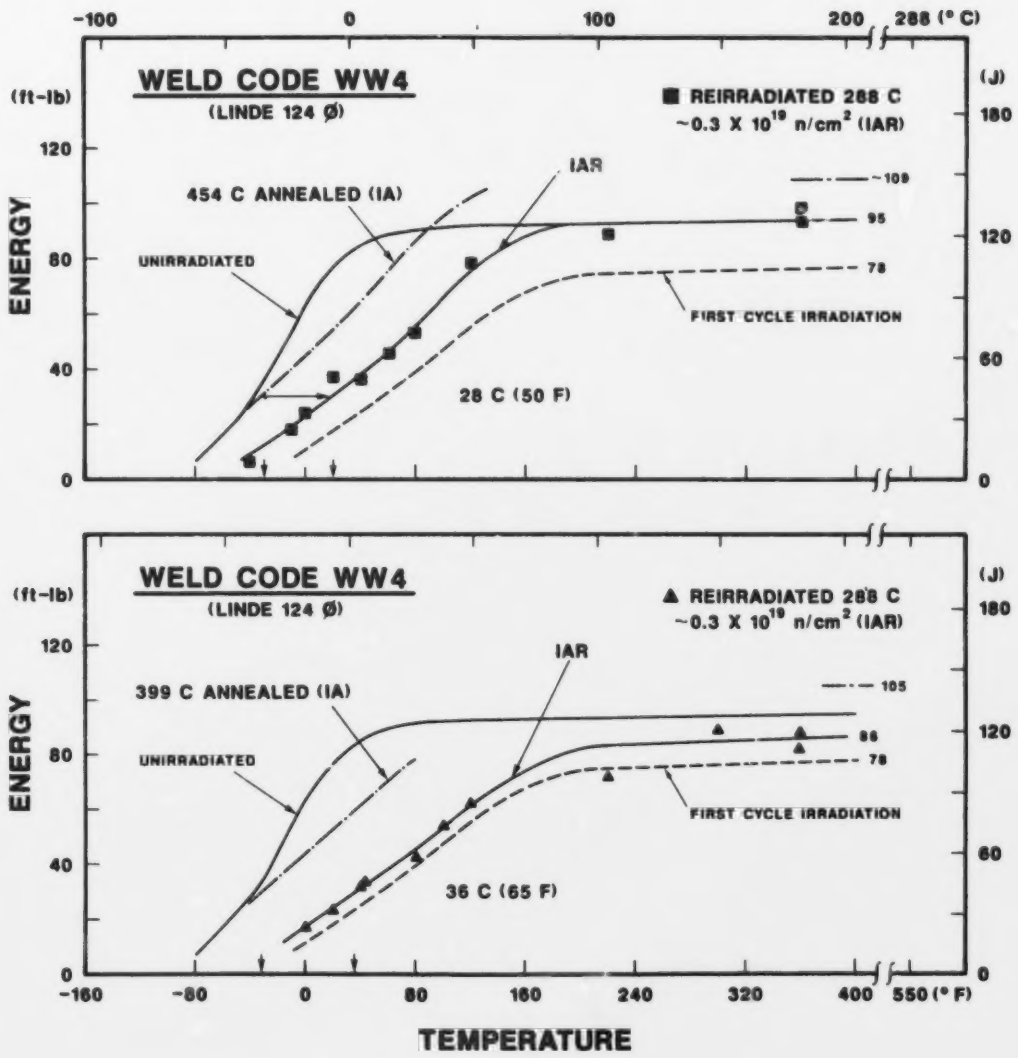

Fig. 3-15 Charpy-V notch ductility of submerged-arc weld, code WW4, after reirradiation following a 454°C intermediate anneal (upper graph) and after reirradiation following a 399°C intermediate anneal (lower graph). Trend lines for the I and IA condition are also shown for reference (Assembly HTA-3, UBR-70).

BEST COPY AVAILABLE

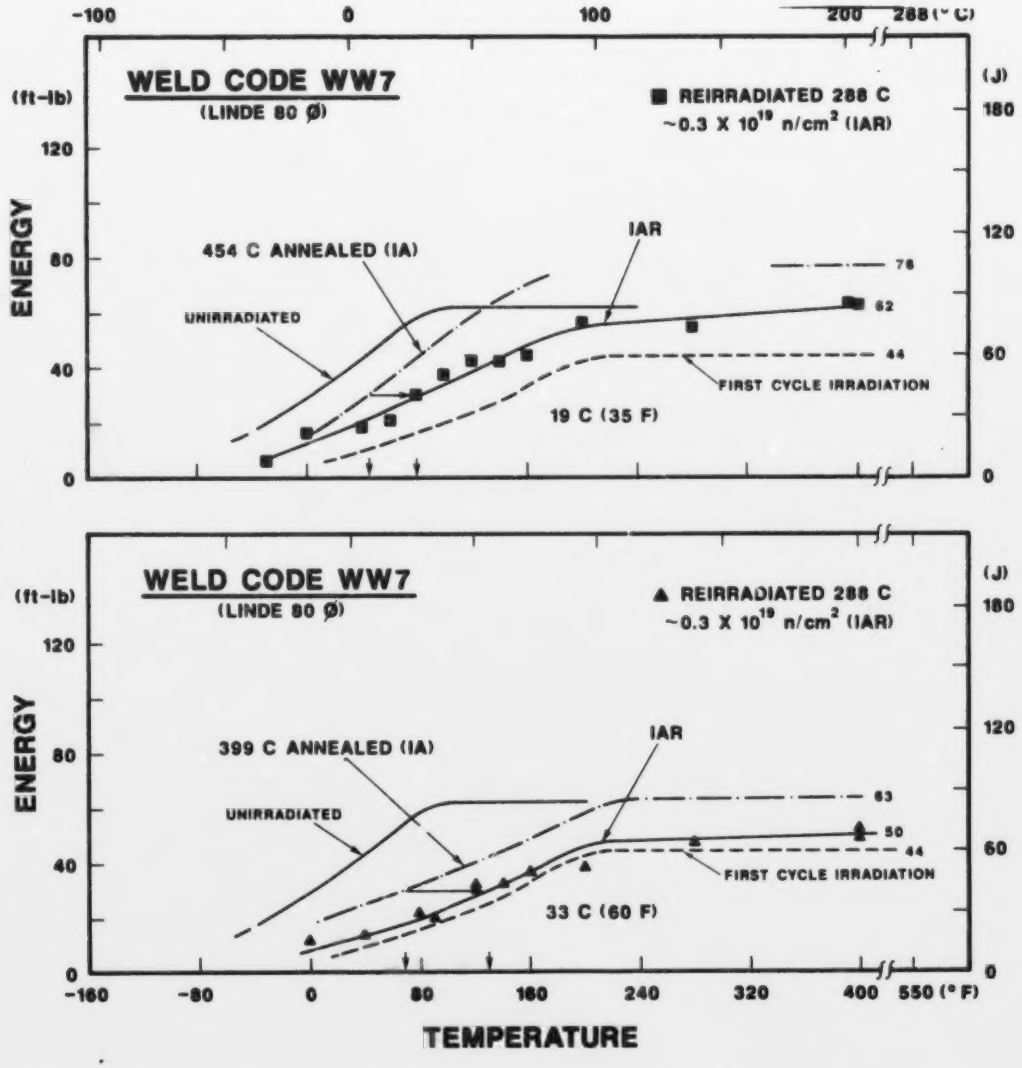

Fig. 3-16 Charpy-V notch ductility of submerged-arc weld, code WW7, after reirradiation following a 454°C intermediate anneal (upper graph) and after reirradiation following a 399°C intermediate anneal (lower graph). Trend lines for the I and IA condition are also shown for reference (Assembly HTA-3, UBR-70).

BEST COPY AVAILABLE

Table 3-2 Postirradiation 24°C Tensile Test Results for Submerged-Arc Welds (HTA Irradiation Series; 5.76-mm diameter specimens)

Weld Code	Welding Flux	HTA Assembly	Material Condition	Specimen Number	Yield Strength (MPa)	Yield Strength (ksi)	Tensile Strength (MPa)	Tensile Strength (ksi)	Elongation (%)	Reduction in Area (%)
W8A (0.39 Cu, 0.65 Ni)[a]	Linde 80	——	Unirradiated	3	494	71.6	616	89.3	23.8	61.1
				4	502	72.8	618	89.7	23.9	60.0
				Average	498	72.2	617	89.5	23.9[b]	60.6
		HTA-4 (UBR-72)	Irradiated	509	625	90.6	721	104.6	——[c,d]	——[c,d]
				Increase	127	18.4	104	15.1	——	——
		HTA-1 (UBR-62)	Annealed 399°C-168 h	485	568	82.4	678	98.3	——	——
				Residual Increase	70	10.2	61	8.8	——	——
			Annealed 454°C-168 h	471	521	75.5	635	92.1	——	——
				Residual Increase	23	3.3	18	2.6	——	——
		HTA-2 (UBR-70A)	IAR 399°C Anneal	473[e]	596	86.5	705	102.3		
				Increase[e]	28	4.1	27	4.0	——	——
				Total Increase	98	14.3	88	12.8	——	——
		(UBR-70B)	IAR 454°C Anneal	497[e]	532	77.2	649	94.1	——	——
				Increase[e]	11	1.7	14	2.0	——	——
				Total Increase	34	5.0	32	4.6	——	——
		HTA-3 (UBR-71A)	IAR 399°C Anneal	459	623	90.3	719	104.3	——	——
				Increase	55	7.9	41	6.0	——	——
				Total Increase	125	18.1	102	14.8	——	——
		(UBR-71B)	IAR 454°C Anneal	483	558	80.9	660	95.7	——	——
				Increase	37	5.4	25	3.6	——	——
				Total Increase	60	8.7	43	6.2	——	——

[a] Nominal composition [b] Elongation in 25.4 mm [c] Not available [d] Test planned [e] Increase over annealed condition

161

Table 3-2 Postirradiation 24°C Tensile Test Results for Submerged-Arc Welds (HTA Irradiation Series; 5.76-mm diameter specimens)

Weld Code	Welding Flux	HTA Assembly	Material Condition	Specimen Number	Yield Strength (MPa)	Yield Strength (ksi)	Tensile Strength (MPa)	Tensile Strength (ksi)	Elongation (%)	Reduction in Area (%)
W9A (0.39 Cu, 0.65 Ni)[a]	Linde 0091	——	Unirradiated	3	576	83.5	658	95.5	22.6	67.4
				4	572	83.0	654	94.9	21.8[b]	69.4
				Average	574	83.3	656	95.2	22.2[b]	68.4
		HTA-4 (UBR-72)	Irradiated	425	704	102.1	771	111.8	——[c,d]	——[c,d]
				Increase	130	18.8	115	16.6	——	——
		HTA-1 (UBR-62)	Annealed 399°C-168 h	389	644	93.4	728	105.6	——	——
				Residual Increase	70	10.1	72	10.4	——	——
			Annealed 454°C-168 h	375	581	84.3	681	98.7	——	——
				Residual Increase	7	1.0	25	3.5	——	——
		HTA-2 (UBR-70A)	IAR 399°C Anneal	387[e]	665	96.5	753	109.2	——	——
				Increase[e]	21	3.1	25	3.6	——	——
				Total Increase	91	13.2	97	14.0	——	——
		(UBR-70B)	IAR 454°C Anneal	411[e]	597	86.6	696	101.0	——	——
				Increase[e]	16	2.3	15	2.3	——	——
				Total Increase	23	3.3	40	5.8	——	——
		HTA-3 (UBR-71A)	IAR 399°C Anneal	377	666	96.6	756	109.6	——	——
				Increase	22	3.2	26	4.0	——	——
				Total Increase	92	13.3	99	14.4	——	——
		(UBR-71B)	IAR 454°C Anneal	401	613	88.9	705	102.3	——	——
				Increase	32	4.6	25	3.6	——	——
				Total Increase	39	5.6	49	7.1	——	——

[a] Nominal composition [b] Elongation in 25.4 mm [c] Not available [d] Test planned [e] Increase over annealed condition

162

Table 3-2 Postirradiation 24°C Tensile Test Results for Submerged-Arc Welds (HTA Irradiation Series; 5.76-mm diameter specimens)

Weld Code	Welding Flux	HTA Assembly	Material Condition	Specimen Number	Yield Strength (MPa)	Yield Strength (ksi)	Tensile Strength (MPa)	Tensile Strength (ksi)	Elongation (%)	Reduction in Area (%)
WW4 (0.15 Cu, 0.65 Ni)[a]	Linde 124	———	Unirradiated	2	487	70.6	593	86.0	23.8	69.1
				3	472	68.4	590	85.6	23.9	68.7
				Average	479	69.5	592	85.8	23.9	68.9
			288°C	1	394	57.1	538	78.0	19.8	64.1
				4	418	60.6	541	78.4	20.6	62.6
				Average	406	58.9	540	78.2	20.2	63.4
			Aged	5	467	67.8	592	85.8	22.5	66.4
			550°F-90 days	10	476	69.1	596	86.5	22.3	68.9
				Average	472	68.5	594	86.2	22.4	67.7
		HTA-4 (UBR-72)	Irradiated	95	527	76.5	630	91.4	——[c,d]	——[c,d]
				Increase	48	7.0	38	5.6	——	——
		HTA-1 (UBR-62)	Annealed 399°C-168 h	47	474	68.8	590	85.5	——	——
				127	485	70.3	596	86.5	——	——
				Average	480	70.0	593	86.0	——	——
				Residual Increase	1	0.5	1	0.2		
			Annealed 454°C-168 h	87	461	66.8	578	83.9	——	——
				137	460	66.7	577	83.7	——	——
				Average	461	66.8	578	83.8		
				Residual Increase	-18	-2.7	-14	-2.0		
		HTA-2 (UBR-70A)	IAR 399°C Anneal	89	532	77.1	632	91.7	——	——
				Increase[e]	52	7.1	39	5.7	——	——
				Total Increase	53	7.6	40	5.9	——	——
		(UBR-70B)	IAR 454°C Anneal	103	508	73.7	609	88.3	——	——
				113	502	72.8	606	87.9	——	——
				Average[e]	505	73.3	608	88.1	——	——
				Increase[e]	44	6.5	30	4.3	——	——
				Total Increase	26	3.8	16	2.3	——	——
		HTA-3 (UBR-71A)	IAR 399°C Anneal	129	543	78.7	643	93.2	——	——
				Increase	60	8.7	50	7.2	——	——
				Total Increase	63	9.2	51	7.4	——	——
		(UBR-71B)	IAR 454°C Anneal	105	516	74.8	621	90.1	——	——
				111	531	77.0	624	90.5	——	——
				Average	523	75.9	623	90.3	——	——
				Increase	63	9.1	45	6.5	——	——
				Total Increase	44	6.4	31	4.5	——	——

[a] Nominal composition [b] Elongation in 25.4 mm [c] Not available [d] Test planned [e] Increase over annealed condition

163

Table 3-2 Postirradiation 24°C Tensile Test Results for Submerged-Arc Welds (HTA Irradiation Series; 5.76-mm diameter specimens)

Weld Code	Welding Flux	HTA Assembly	Material Condition	Specimen Number	Yield Strength (MPa)	Yield Strength (ksi)	Tensile Strength (MPa)	Tensile Strength (ksi)	Elongation (%)	Reduction in Area (%)
WW7 (0.35 Cu, 0.11 Ni)[a]	Linde 80	——	Unirradiated (All weld metal specimen, 5.74-mm gage diameter)	1	505	73.3	611	88.6	43.6	62.9
				4	512	74.3	613	88.9	39.8	62.7
				Average	509	73.8	612	88.8	41.7	62.8
		HTA-4 (UBR-72)	Irradiated	120	617	89.5	710	103.0	——[c,d]	——[c,d]
				Increase	108	15.7	99	14.2	——	——
		HTA-1 (UBR-62)	Annealed 399°C-168 h	37	578	83.8	679	98.5	——	——
				Residual Increase	69	10.0	67	9.7	——	——
			Annealed 454°C-168 h	29	531	77.0	639	92.7	——	——
				Residual Increase	22	3.2	27	3.9		
		HTA-2 (UBR-70A)	IAR 399°C Anneal	68	603	87.4	698	101.2	——	——
				Increase[e]	25	3.6	19	2.7	——	——
				Total Increase	94	13.6	86	12.4	——	——
		(UBR-70B)	454°C Anneal	81	553	80.1	653	94.7	——	——
				89	559	81.0	659	95.6	——	——
				Average	556	80.6	656	95.2		
				Increase[e]	25	3.6	17	2.5	——	——
				Total Increase	47	6.8	44	6.4	——	——
		HTA-3 (UBR-71A)	IAR 399°C Anneal	94	604	87.6	701	101.6	——	——
				Increase	26	3.8	21	3.1	——	——
				Total Increase	95	13.8	88	12.8	——	——
		(UBR-71B)	IAR 454°C Anneal	107	564	81.8	663	96.1	——	——
				115	560	81.2	663	96.1	——	——
				Average	562	81.5	663	96.1	——	——
				Increase	31	4.5	23	3.4	——	——
				Total Increase	53	7.7	50	7.3	——	——

[a] Nominal composition [b] Elongation in 25.4 mm [c] Not available [d] Test planned [e] Increase over annealed condition

164

(low nickel). Also, an influence of welding flux on irradiation performance was observed. The data for weld code W8A and weld code W9A, made with the same lot of filler wire, illustrate the effect of using a Linde 80 flux vs. a Linde 0091 flux. Flux type, in part, governs the as-deposited weld metal composition which itself has a direct effect on radiation resistance. Weld metal compositions are listed in Table 3-3.

A key determination from the 454°C vs. 399°C postirradiation annealing data is that C_v 41-J transition temperature recovery may or may not be significantly greater with a 454°C anneal (Fig. 3-17). However, reembrittlement of the welds was significantly less after a 454°C anneal compared to a 399°C anneal (Fig. 3-18). In turn, the benefit of IAR procedures appears to be greater with the higher temperature anneal (Fig. 3-19). Properly applied, IAR procedures may be a means of avoiding PTS concerns and for achieving PLEX in many cases.

Referring to Table 3-2, the measured changes in yield strength in general agree with the findings on C_v notch ductility, including variable radiation sensitivity and variable annealing recovery among the materials. More important to the present study, a superior effect of a 454°C anneal compared to that of a 399°C anneal is evident in both the IA and the IAR condition results.

The data suggest strong weld metal tendencies toward radiation embrittlement saturation in IAR-treated material. The one remaining (untested) IAR assembly which received a 0.7×10^{19} n/cm^2 reirradiation fluence is designed to verify these indications for the prototypic welds. Information from this assembly will be available by mid-1987.

Table 3-3 Compositions of Submerged-Arc Weld Deposits

Weld Code	Chemical Composition (Wt-%)									
	C	Mn	Si	P	S	Ni	Cr	Mo	Cu	Sn
Weld W8A (Linde 80 ϕ)	0.079(min)[a]	1.27	0.71	0.010	0.012	0.55	0.10	0.42	0.37	0.002
	0.096(max)	1.36	0.79	0.017	0.019	0.68	0.13	0.50	0.42	0.004
Weld W9A (Linde 0091 ϕ)	0.19(min)	1.21	0.23	0.008	0.005	0.64	0.10	0.49	0.35	0.003
	0.19(max)	1.27	0.23	0.012	0.010	0.77	0.11	0.50	0.43	0.004
Weld WW7 (Linde 80 ϕ)	0.08	1.56	0.60	0.013	0.008	0.10	0.12	0.54	0.35	0.002
Weld WW4 (Linde 124 ϕ)	0.08	1.38	0.49	0.013	0.018	0.65	0.10	0.44	0.16	0.004

[a] Range (min/max) observed, multiple test locations in 1.83-m long weld seam

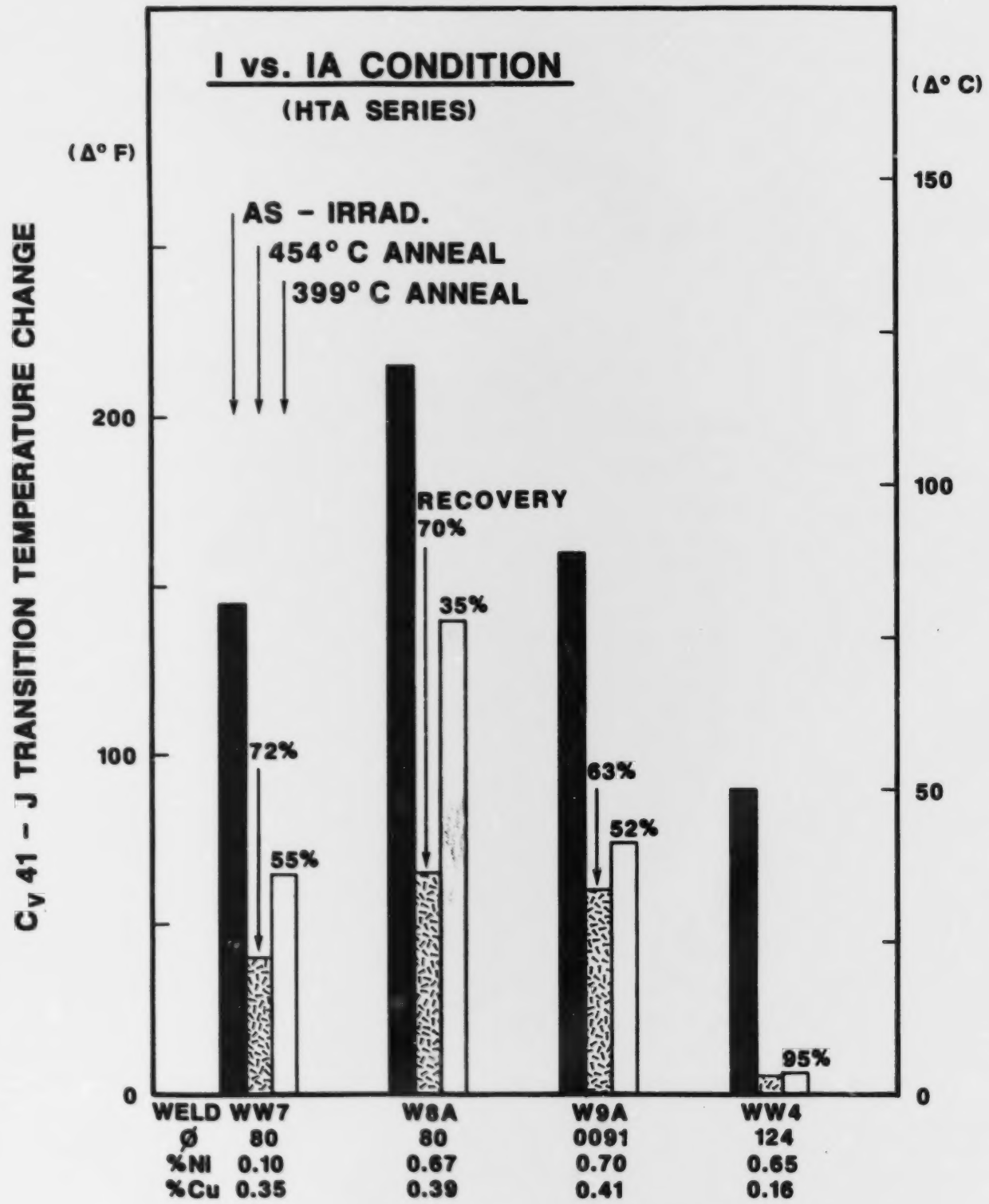

Fig. 3-17 Summary of notch ductility changes observed for weld codes W8A, W9A, WW4, and WW7 after irradiation and after postirradiation annealing at 454°C and 399°C.

BEST COPY AVAILABLE

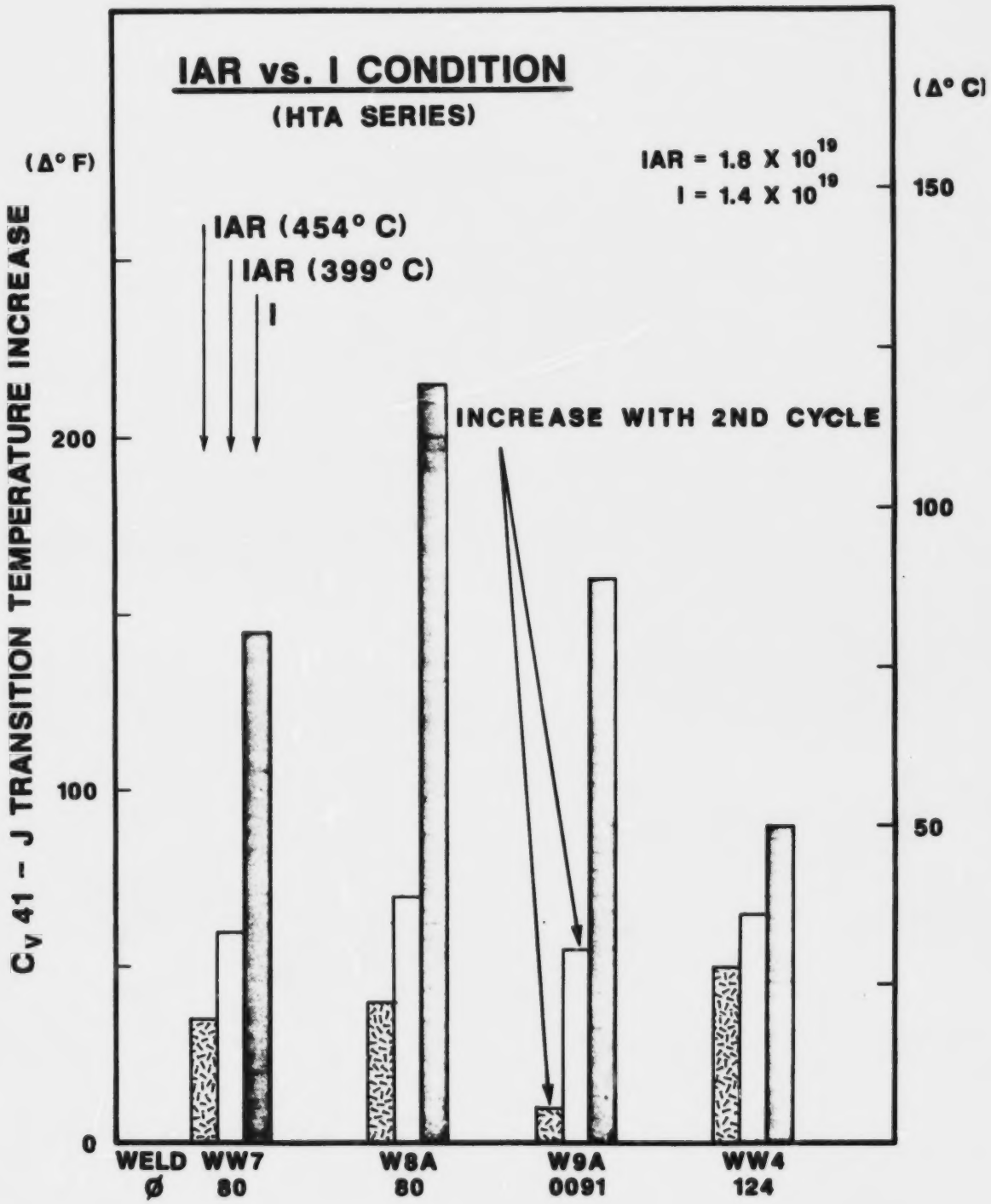

Fig. 3-18 Summary of notch ductility changes observed for weld codes W8A, W9A, WW4, and WW7 after reirradiation following a 454°C or 399°C intermediate anneal. The left hand and center bars indicate the increase in transition temperature by the second exposure cycle only.

BEST COPY AVAILABLE

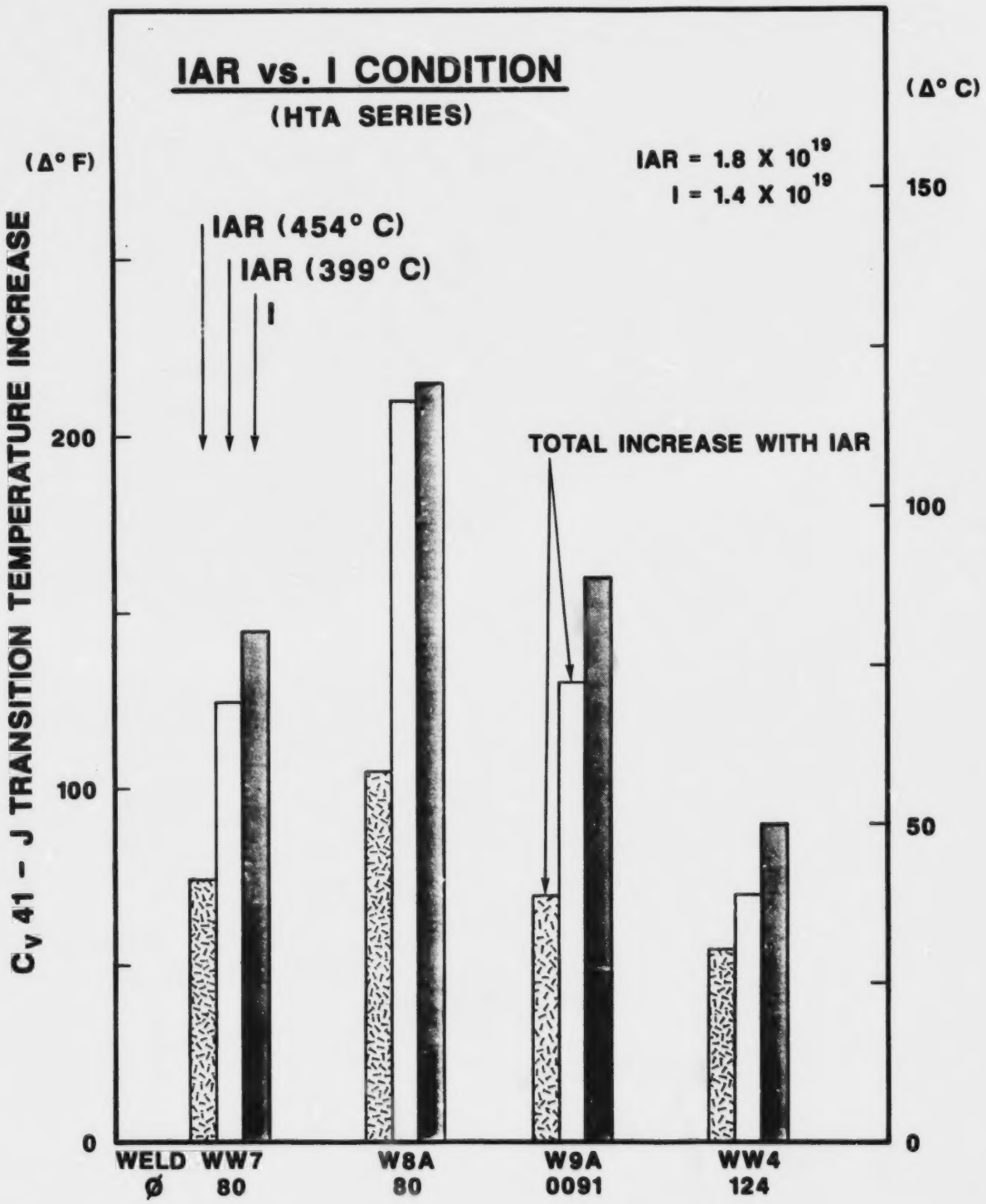

Fig. 3-19 Summary of notch ductility changes observed for weld codes W8A, W9A, WW4, and WW7 after reirradiation following a 454°C or 399°C intermediate anneal. The left hand and center bars indicate the total transition temperature elevation with the IAR treatment.

BEST COPY AVAILABLE

3.2 Influence of Steel Composition on Embrittlement Relief by Post-irradiation Heat Treatment

J. R. Hawthorne

3.2.1 Background

Metallurgical influences on mechanical properties recovery by postirradiation annealing have not been investigated in detail but obviously form a prerequisite to NRC's weighing of commercial annealing applications. Studies of heat treatment for the mitigation of radiation-induced embrittlement are finding increasing evidence of an effect of material composition on the amount of notch ductility recovery obtained. The large scatter observed in percentage recovery with 399°C annealing is a particularly clear indication of a composition dependency of some type.

The present investigation, undertaken for the NRC in 1984, employs ten plates from laboratory melts having statistical variations in copper, nickel, and phosphorus content. The elements, singly or in combination, have known contributions to radiation sensitivity behavior. Whether or not the influences of these elements, singly or in combination, carry over into recovery behavior is one question addressed here.

Irradiation and anneal tests of one group of materials completed in 1985, revealed that copper but not phosphorus has a strong influence on embrittlement relief by 399°C annealing. The results confirm initial NRC/MEA suspicions that composition must be treated as a potentially critical variable influencing both recovery and the degree of residual embrittlement after the anneal.

3.2.2 Summary of Results

The second group of materials in the experiment matrix has now been evaluated for composition effects on recovery. Here, the focus was on the influence of variable nickel content and the nickel/copper content ratio.

The material codes investigated were 5C, 5D, 6A, 6B, 6C; individual compositions of the plates are listed in Table 3-4. Except for material code 6C, the base composition for melting was A 302-B. That for material code 6C was A 533-B. Microstructures were tempered upper bainite with traces of free ferrite and were similar in character. Preirradiation tensile strengths also were comparable (Table 3-5). Accordingly, comparisons for judgments of annealing response were much simplified. Results for the 288°C irradiated condition and the 288°C irradiated + 399°C annealed conditions are summarized in Table 3-6 and are illustrated in Figs. 3-20 and 3-21, respectively. C_v test results for the individual plates in the preirradiation and postirradiation conditions are shown in Figs. 3-22 to Fig. 3-26.

Table 3-4 Chemical Compositions of Plates from Laboratory (4-Way Split) Melts of Steel (A 302-B or A 533-B Base Composition, Vacuum Induction Melts)

Melt	Plate/Cast No.[a]	Chemical Composition (Wt-%)									
		C	Mn	P	S	Si	Cu	Ni	Cr	Mo	Sn
5	5C	0.24	1.30	0.002	0.014	0.21	0.16	0.27	0.003	0.53	0.004
	5D	0.24	1.30	0.002	0.014	0.21	0.16	0.27	0.003	0.53	0.004
6	6A	0.23	1.29	0.002	0.013	0.22	0.28	0.05	-----	0.53	0.004
	6B	0.23	1.29	0.002	0.013	0.22	0.28	0.27	-----	0.53	0.004
	6C	0.23	1.29	0.002	0.013	0.22	0.28	0.69	-----	0.53	0.004

[a] Heat Treatment: 899°C-1 h, AC; 649°C-1 h, WQ.

171

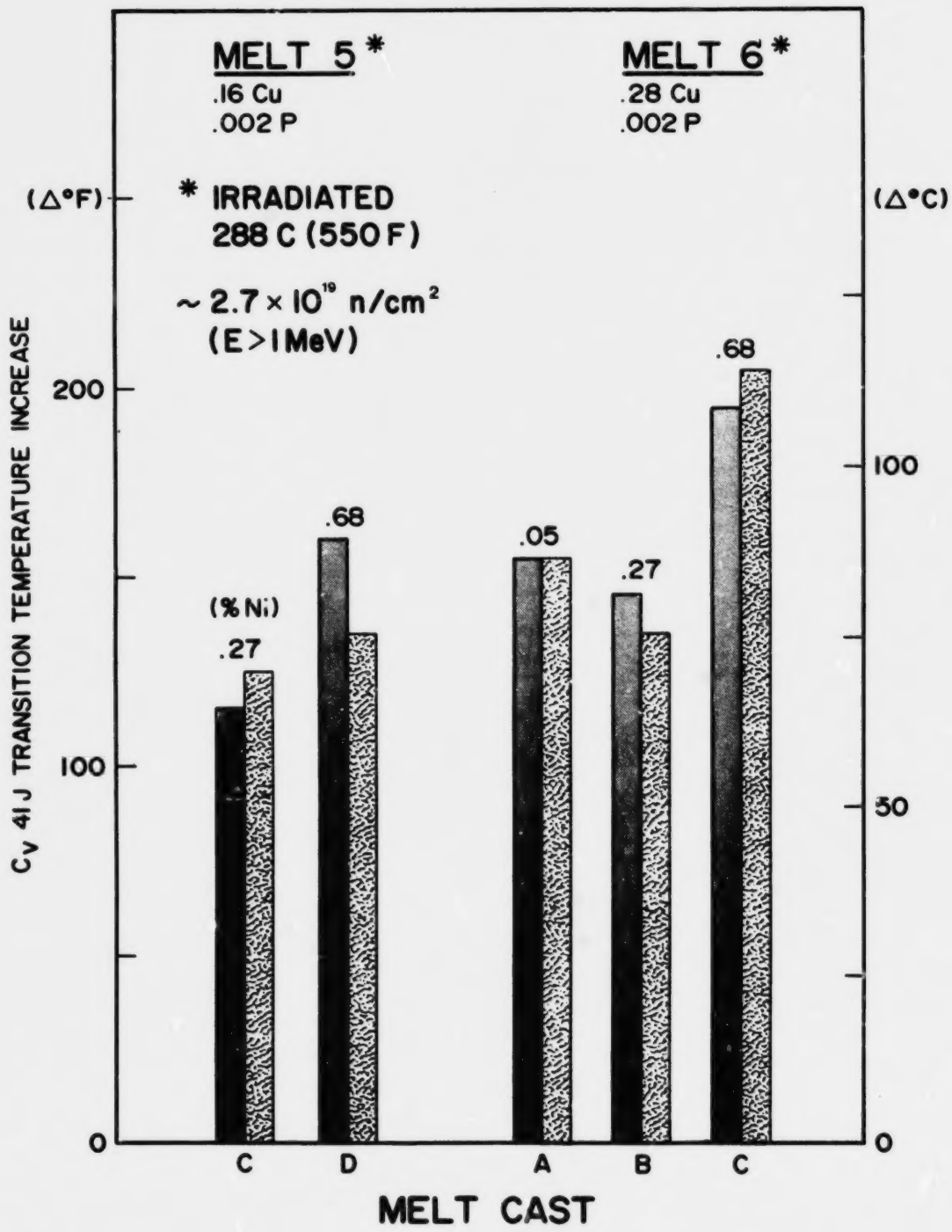

Fig. 3-20 Comparison of transition temperature increases observed for five materials from two separate reactor irradiation experiments.

BEST COPY AVAILABLE

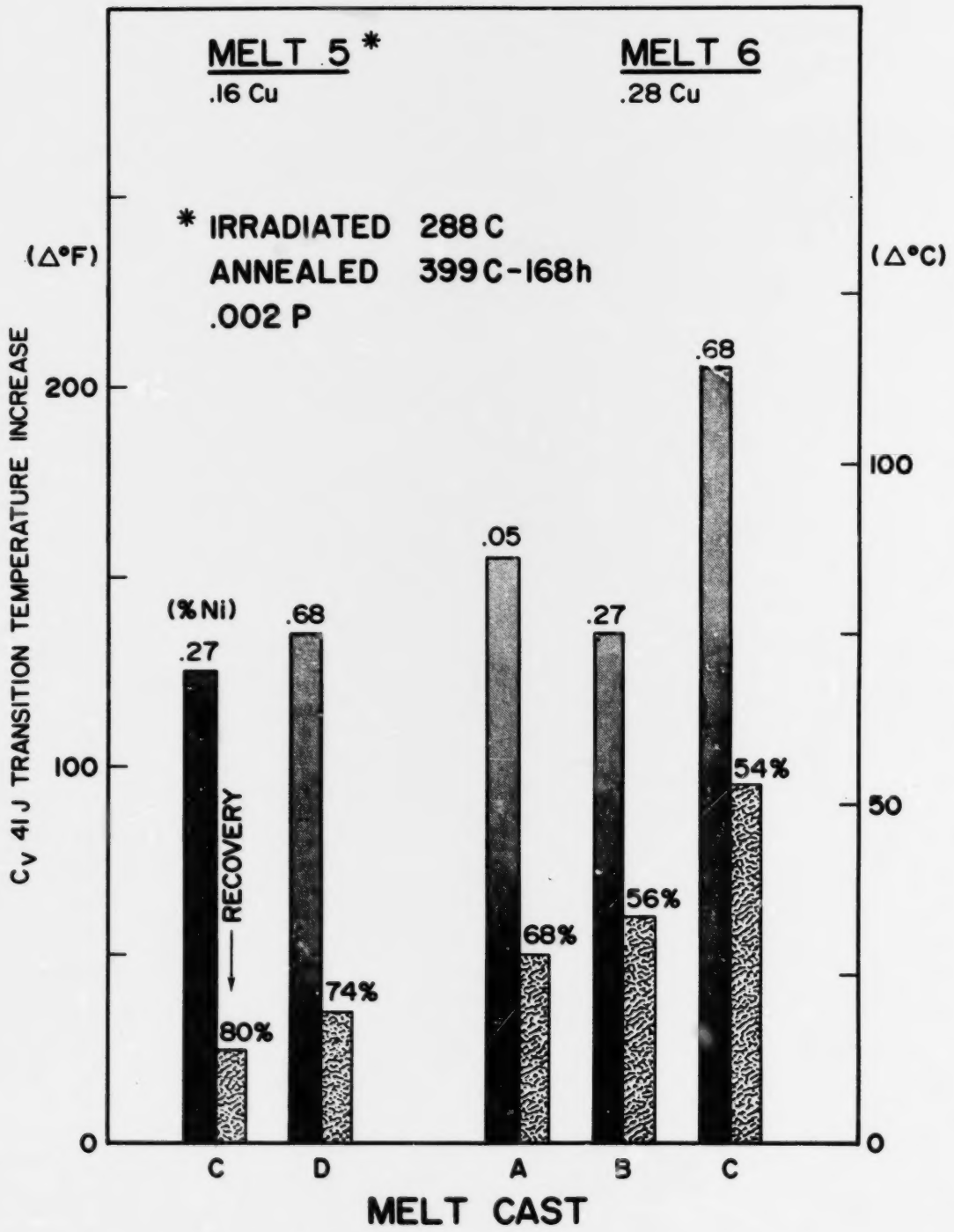

Fig. 3-21 Comparison of transition temperature recovery by postirradiation annealing (399°C-168 h).

BEST COPY AVAILABLE

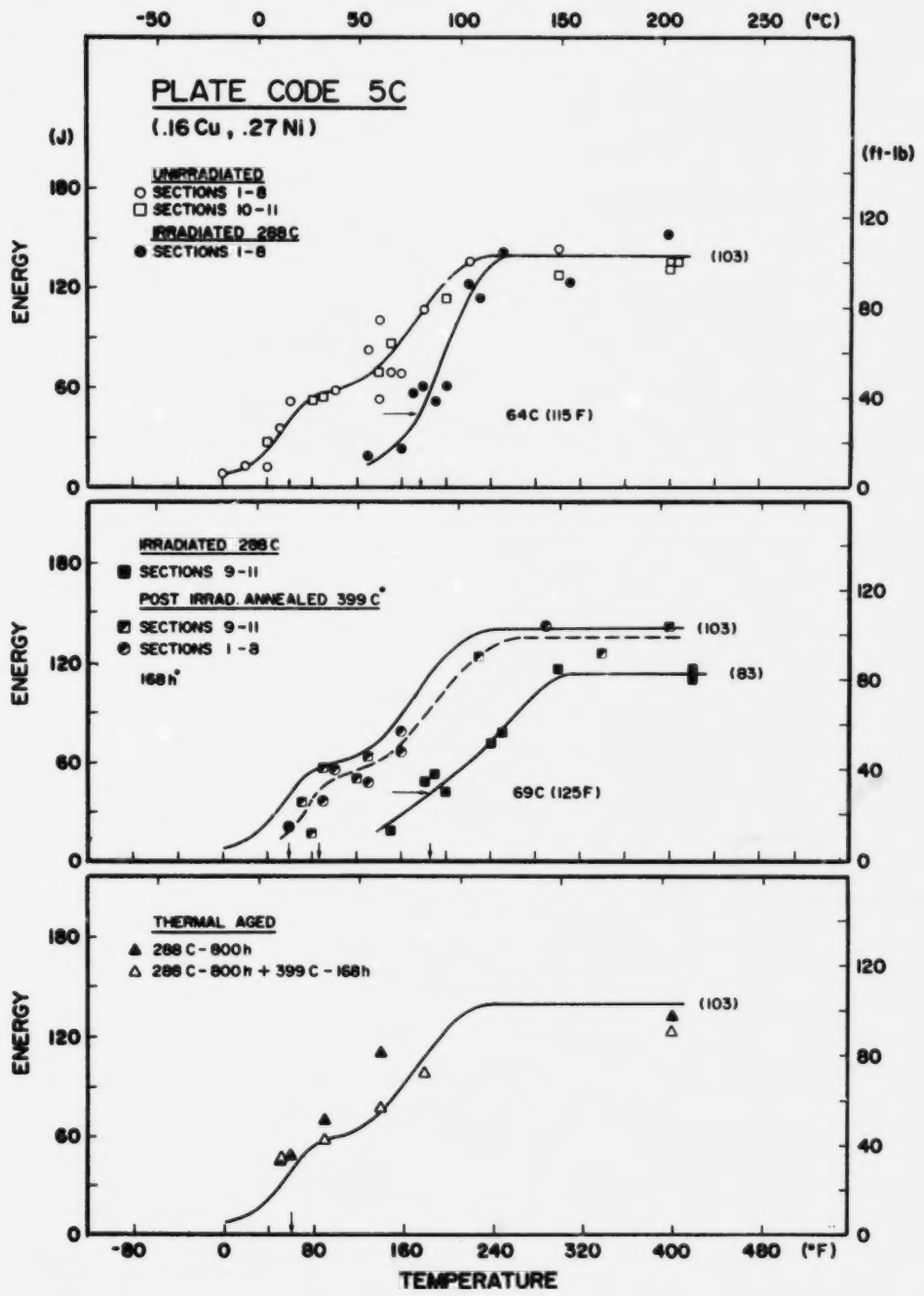

Fig. 3-22 Irradiation and postirradiation annealing data for plate 5C obtained from two separate reactor irradiation experiments. Long-term thermal conditioning data (aging) are also shown.

BEST COPY AVAILABLE

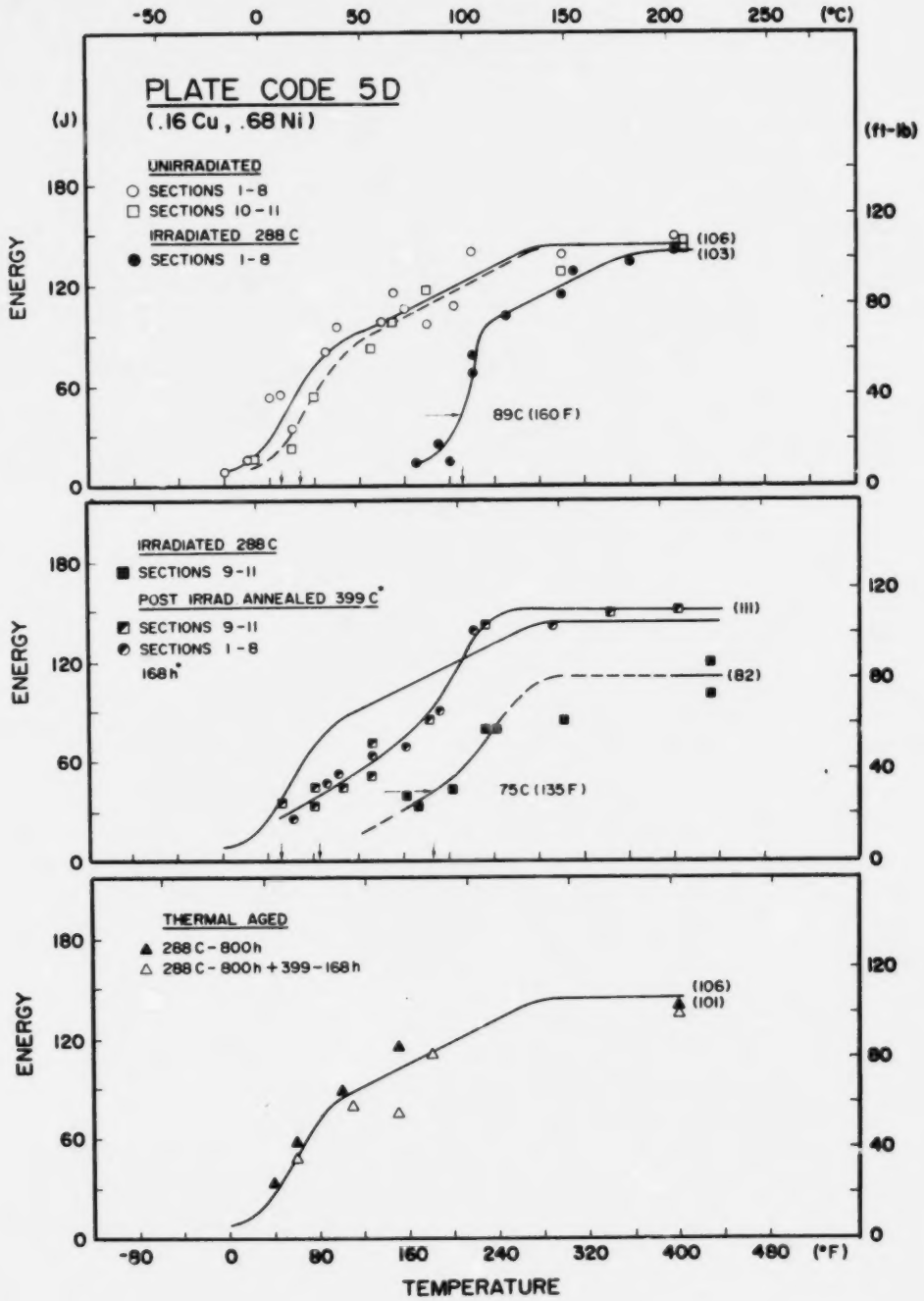

Fig. 3-23 Irradiation and postirradiation annealing data for plate 5D obtained from two separate reactor irradiation experiments. Long-term thermal conditioning data (aging) are also shown.

BEST COPY AVAILABLE

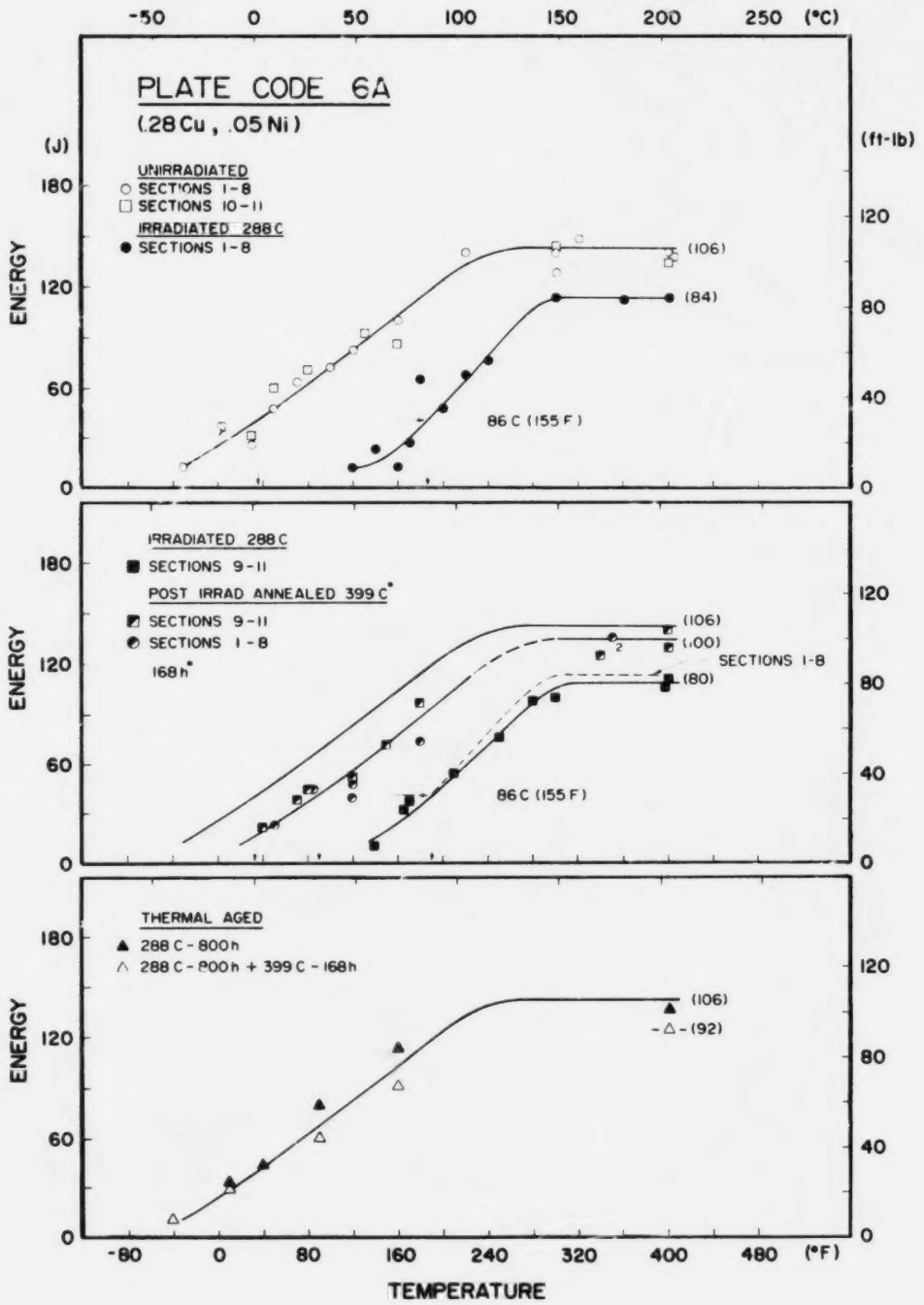

Fig. 3-24 Irradiation and postirradiation annealing data for plate 6A obtained from two separate reactor irradiation experiments. Long-term thermal conditioning data (aging) are also shown.

BEST COPY AVAILABLE

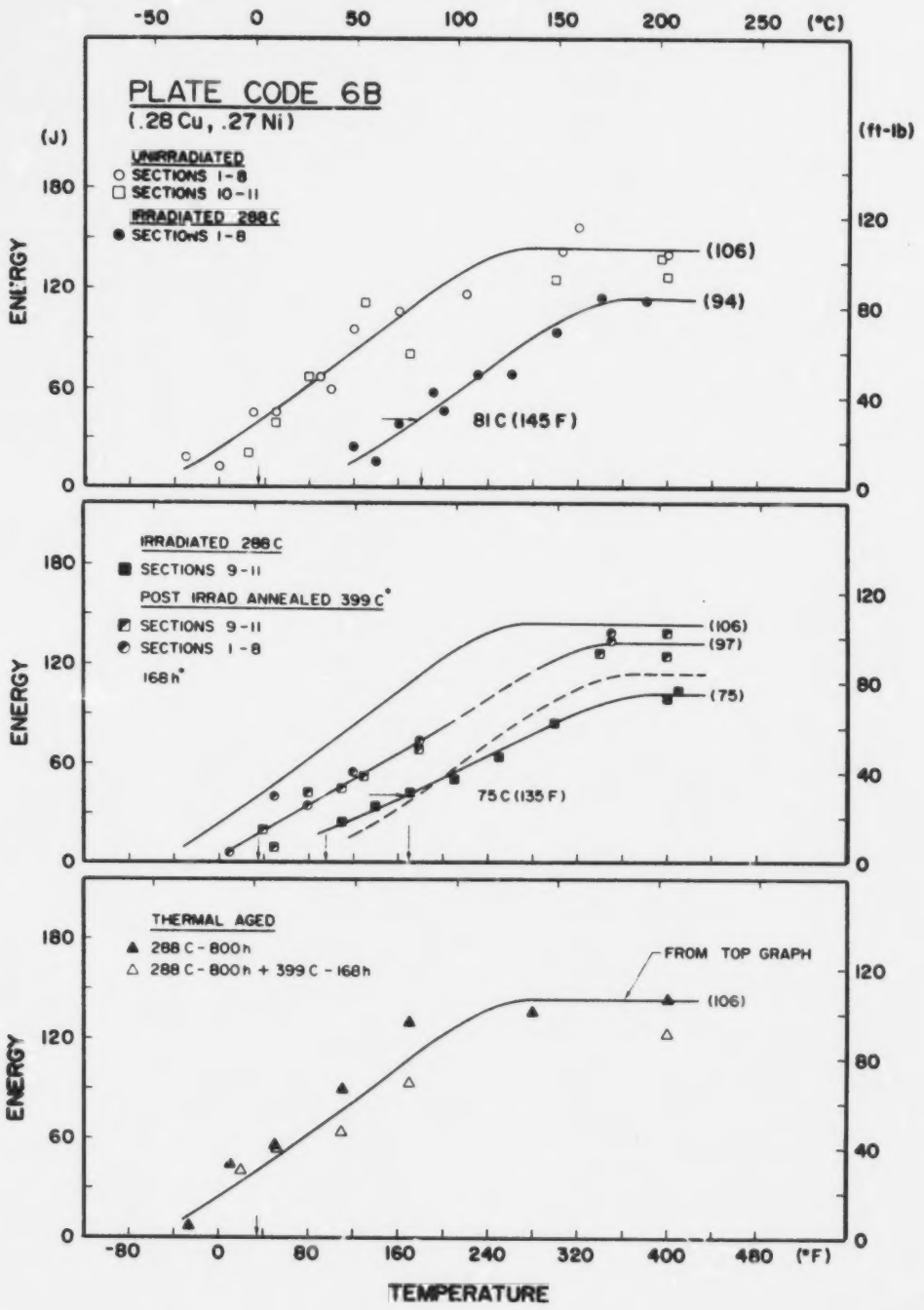

Fig. 3-25 Irradiation and postirradiation annealing data for plate 6B obtained from two separate reactor irradiation experiments. Long-term thermal conditioning data (aging) are also shown.

BEST COPY AVAILABLE

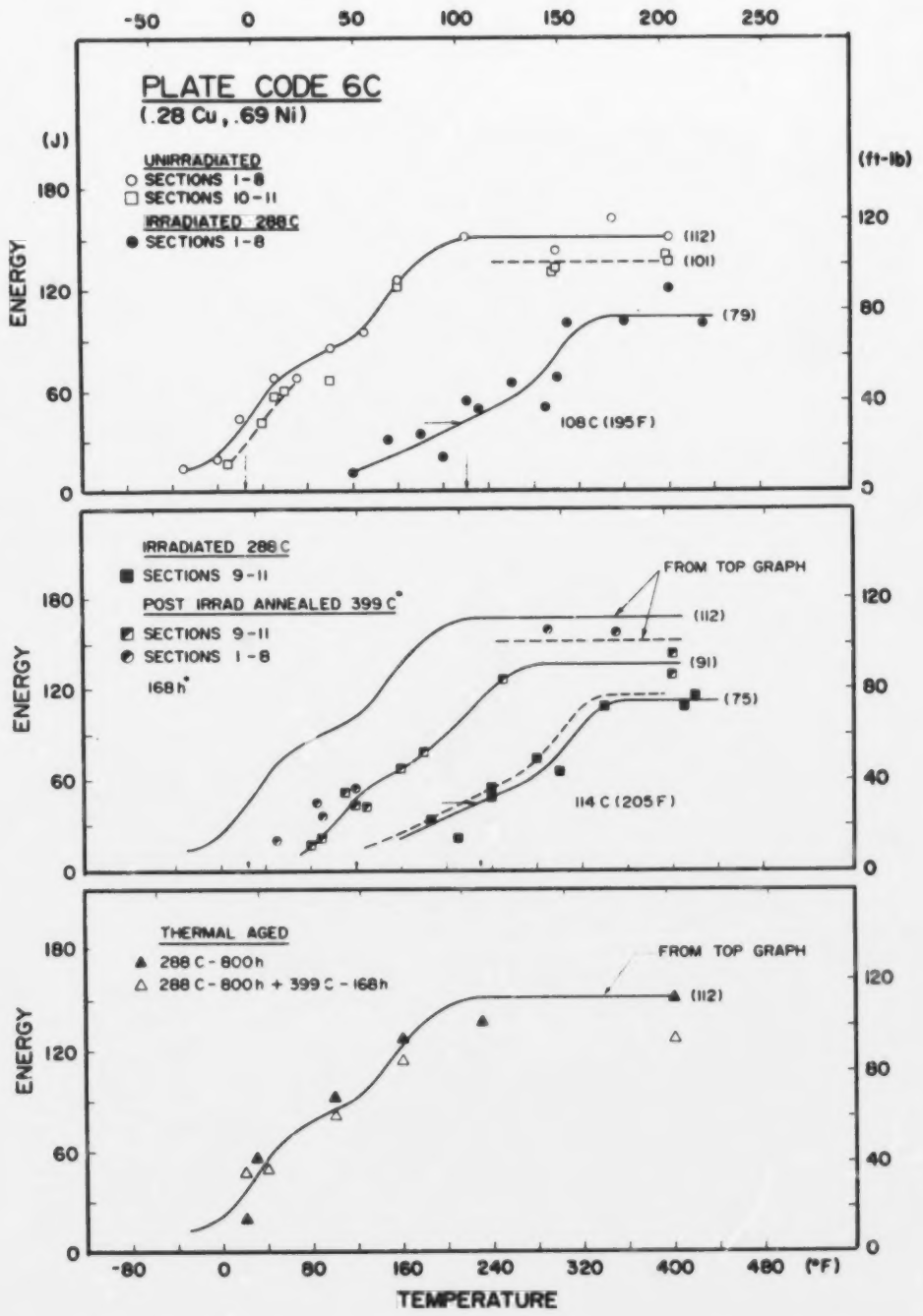

Fig. 3-26 Irradiation and postirradiation annealing data for plate 6C obtained from two separate reactor irradiation experiments. Long-term thermal conditioning data (aging) are also shown.

BEST COPY AVAILABLE

Table 3-5 Preirradiation Tensile Properties of Test Plates from Melts 5 and 6 (Ambient temperature tests)

Melt No.	Plate No.	Yield Strength[a] 0.2% Offset (MPa)	Tensile Strength (MPa)	% Elongation in 25.4 mm (%)
5	5C	536	667	22.2
	5D	550	690	22.9
6	6A	550	685	22.3
	6B	561	697	22.4
	6C	587	719	22.4

[a] Average of duplicate tests; 6.4-mm diameter x 31.8 gage length specimens

The anneal temperature of 399°C was chosen for the study because a higher temperature heat treatment conceivably could produce too great a recovery for a meaningful comparison of materials in many instances. Also, annealing at temperatures higher than 399°C (e.g., 454°C) has produced anomalous results in some investigations which still bear explanation. As noted in the figures, the effects of thermal aging without irradiation were also studied. Results are discussed in a later paragraph.

Radiation sensitivity and annealing recovery relative to transition behavior was judged from C_v 41-J transition temperature changes. Only limited tests of the irradiated condition were performed to maximize the number of specimens available for annealing evaluations. In general, 8 to 10 specimens were used to establish as-irradiated condition properties. To guide the selection of postirradiation test temperatures, prior irradiation results cited in Reference 83 were utilized. Because the plate sections used for the original as-irradiated condition properties determinations were not immediately adjacent to those sections used for the present study, a limited number of "check tests" were performed as a precaution to verify the original set of data. In some cases, significant properties differences were revealed (see data for plate codes 67B and 67C as examples). An across-plate properties gradient is the obvious cause; test procedures are not responsible since the same equipment was used throughout.

In Fig. 3-20, radiation-induced elevations in 41-J temperature observed with the current irradiation test and the earlier irradiation test are compared. For plate codes 5C and 5D, the two sets of data in general appear comparable. For plate code 5D, the difference is 14°C. The data figures for these plates, however, show a significant difference in the shape of the transition curves for the two separate

Table 3-6 Notch Ductility Determinations for A 302-B and A 533-B Plates in Irradiation Assemblies CNI-1, -2 and CEA-2

Plate Code[a]	Percent Ni	Percent Cu	Plate Sections	Exp. No.	Fluence[b] ($\times 10^{19}$)	Charpy-V 41-J Temperature						
						Initial	Irrad.	ΔT	Annealed[c]	ΔT_{Rec}	ΔT_{Res}	Percent Rec
5C	0.27	0.16	1-8	CNI-1 (UBR-33)	2.4	16°C (60°F)	80°C (175°F)	64°C (115°F)	29°C (85°F)	51°C (90°F)	13°C (25°F)	78.3
			9-11	CEA-2 (UBR-63)	2.78	16°C (60°F)	85°C (185°F)	69°C (125°F)	29°C (85°F)	56°C (100°F)	14°C (25°F)	80.0
5D	0.68	0.16	1-8	CNI-1 (UBR-33)	2.4	10°C (50°F)	99°C (210°F)	89°C (160°F)	29°C (85°F)	70°C (125°F)	19°C (35°F)	78.1
			9-11	CEA-2 (UBR-63)	2.78	10°C (50°F)	85°C (185°F)	75°C (135°F)	29°C (85°F)	56°C (100°F)	19°C (35°F)	74.0
6A	0.05	0.28	1-8	CNI-2 (UBR-34)	2.6	2°C (35°F)	88°C (190°F)	86°C (155°F)	29°C (85°F)	59°C (105°F)	27°C (50°F)	67.7
			9-11	CEA-2 (UBR-63)	2.78	2°C (35°F)	88°C (190°F)	86°C (155°F)	29°C (85°F)	59°C (105°F)	27°C (50°F)	67.7
6B	0.27	0.28	1-8	CNI-2 (UBR-34)	2.6	2°C (35°F)	82°C (180°F)	80°C (145°F)	35°C (95°F)	47°C (85°F)	34°C (60°F)	58.6
			9-11	CEA-2 (UBR-63)	2.78	2°C (35°F)	76°C (170°F)	74°C (135°F)	35°C (95°F)	41°C (75°F)	34°C (60°F)	55.6
6C	0.69	0.28	1-8	CNI-2 (UBR-34)	2.6	-4°C (25°F)	104°C (220°F)	108°C (195°F)	48°C (120°F)	56°C (100°F)	52°C (95°F)	51.3
			9-11	CEA-2 (UBR-63)	2.78	-4°C (25°F)	110°C (230°F)	114°C (205°F)	48°C (120°F)	62°C (110°F)	52°C (95°F)	53.7

[a] 0.002% P

[b] n/cm^2, E > 1 MeV (calculated spectrum) at 288°C

[c] 399°C (750°F)-168 hr anneal

[d] Not applicable

[e] Approximate due to initial USE uncertainty

Table 3-6 Notch Ductility Determinations for A 302-B and A 533-B Plates in Irradiation Assemblies CNI-1, -2 and CEA-2 (Part 2)

Plate Code[a]	Percent P	Percent Cu	Plate Sections	Exp. No.	Fluence[b] ($\times 10^{19}$)	Charpy-V Upper Shelf Energy						
						Initial	Irrad.	ΔUSE	Annealed[c]	ΔUSE_{Rec}	ΔUSE_{Res}	Percent Rec
5C	0.27	0.16	1-8	CNI-1 (UBR-33)	2.4	140 J (103 ft-lb)	140 (103)	~0 (~0)	140 (103)	——[d] ——	——[d] ——	——[d]
			9-11	CEA-2 (UBR-63)	2.78	140 J (103 ft-lb)	113 (83)	27 (20)	~134 (~ 99)	~21 (~16)	~6 (~4)	80.0
5D	0.68	0.16	1-8	CNI-1 (UBR-33)	2.4	144 J (106 ft-lb)	140 (103)	~4 (~3)	144 (106)	~4 (~3)	0 0	100
			9-11	CEA-2 (UBR-63)	2.78	144 J (106 ft-lb)	111 (82)	33 (24)	151 (111)	40 (29)	0 0	100
6A	0.05	0.28	1-8	CNI-2 (UBR-34)	2.6	144 J (106 ft-lb)	114 (109)	30 (22)	136 (100)	22 (16)	8 (6)	72.7
			9-11	CEA-2 (UBR-63)	2.78	144 J (106 ft-lb)	109 (80)	35 (26)	136 (100)	27 (20)	8 (6)	76.9
6B	0.27	0.28	1-8	CNI-2 (UBR-34)	2.6	144 J (106 ft-lb)	114 (84)	30 (22)	136 (100)	22 (16)	8 (6)	72.7
			9-11	CEA-2 (UBR-63)	2.78	144 J (106 ft-lb)	102 (75)	42 (31)	132 (97)	30 (22)	12 (9)	62.9[e]
6C	0.69	0.28	1-8	CNI-2 (UBR-34)	2.6	152 J (112 ft-lb)	104 (77)	48 (35)	144 (106)	40 (29)	8 (6)	82.9
			9-11	CEA-2 (UBR-63)	2.78	137 J (101 ft-lb)	102 (75)	35 (26)	124 (91)	22 (16)	13 (10)	61.5

[a] 0.002% P

[b] n/cm^2, E > 1 MeV (calculated spectrum) at 288°C

[c] 395°C (750°F)-168 hr anneal

[d] Not applicable

[e] Approximate due to initial USE uncertainty

181

tests. An explanation for the anomaly cannot be offered. In contrast, the postirradiation trend curves for the remaining three materials show good agreement.

The annealing data for the materials (Fig. 3-21) permit two important observations. A nickel content of 0.68% (with a high copper content) exerts a detrimental effect on notch ductility recovery. This nickel content is toward the upper end of the allowable range for A 533-B steel. An increase in nickel content from 0.05 to 0.27% nickel, on the other hand, had no major effect on apparent recovery in terms of the residual embrittlement observed (compare melt no. 6, cast A vs. cast B). This spread in nickel content is within the allowable range for ASTM A 302-B steel. Accordingly, nickel content shows a capability for influencing the annealing response of one type steel but not the other. Referring to copper content, the detrimental effect of this impurity on radiation sensitivity and recoverability in fracture resistance is consistent with the reported observations with the first group of materials (Ref. 84).

The lower portion of the three-part data figures compares the thermal aging data to the unirradiated condition trend line reproduced from the upper illustration. Specimens were aged at 288°C for 800 h, comparable to the irradiation time at temperature or were given a duplex heat treatment of 288°C-800 h + 399°C-168 h comparable to the thermal history of irradiated and annealed specimens. For the single heat treatment condition, a trend toward a slight improvement of notch ductility properties was noted in those cases where changes were found. Upper shelf improvement is the most obvious change. In contrast, specimens given the duplex heat treatment showed tendencies toward a slight degradation in notch ductility, that is, the data points fell to the right and somewhat below the data for the 288°C aging treatment. In the transition region, the duplex aging data remained within the data scatter band for the unirradiated (reference) condition. For the upper shelf regime, however, the values for duplex aging were lower than those for the reference condition, especially for plate codes 6A, 6B, and 6C.

If one takes into account the effect of the duplex heat treatment on the unirradiated material, the postirradiation anneal produced essentially full upper shelf recovery for all five composition variations. On the other hand, incomplete recovery would be the conclusion if the unirradiated condition is the baseline for judging recovery. Obviously, more needs to be known about the metallurgical effects to RPV materials by duplex heat treatments in the absence of irradiation.

In summary, this particular investigation clearly demonstrated that composition effects (and interactions) must be understood to properly assess plant-specific annealing applications to the NRC.

3.3 Mechanisms of Irradiation Damage for Reactor Vessel Steels

J. R. Hawthorne

3.3.1 Background

The present investigation to isolate and model radiation effects mechanisms in RPV steels was undertaken by MEA in FY 1985. Experimental phases are being performed largely by subcontractors under MEA guidelines. Additional work is being done through cooperative programs with certain overseas laboratories (VTT, Finland; CEN, Belgium). Objectives are to apply advanced microscopy for purposes of (a) confirmation of the basic mechanism for the copper content contribution to radiation sensitivity development, (b) definition of the mechanism by which nickel alloying reinforces the copper content effect, and (c) isolation of the mechanism of the phosphorus contribution to radiation sensitivity.

Materials under investigation are from pedigreed laboratory melts of low alloy steels previously irradiated by MEA for composition effects determination, and two split-laboratory melts of iron binary and ternary alloys made in 1985. The latter melts were produced with composition variations in copper, nickel, copper + nickel, phosphorus, and phosphorus + nickel, and phosphorus + copper content (Table 3-7). Laboratory melting provides a high degree of metallurgical control over the resultant materials and allows 1:1 comparisons normally unattainable with large commercial production melts. Chemical compositions of the plates produced from the iron alloy melts are listed in Table 3-8.

Table 3-7 Matrix for Melting Iron-Binary and Iron-Ternary Alloys

Melt	Cast	Target Composition
1	A	Fe + 0.01% Cu
	B	Fe + 0.30% Cu
	C	Fe + 0.30% Cu + 0.4% Ni
	D	Fe + 0.30% Cu + 0.7% Ni
2	A	Re (Reference)
	B	Fe + 0.7% Ni
	C	Fe + 0.7% Ni + 0.025% P
	D	Fe + 0.7% Ni + 0.025% P + 0.30% Cu

Table 3-8 Chemical Compositions and Heat Treatments of Laboratory-Melted Plates

Melt	Cast	Composition (Wt-%)[a]						Normalizing Heat Treatment[b]
		C	Mn	P	Ni	Cu	Al	
1	A	0.010	0.031	0.004	< 0.010	0.006	< 0.005	1698
	B	0.013	0.013	0.004	0.012	0.280	0.007	1698
	C	0.010	0.017	0.003	0.370	0.270	< 0.005	1685
	D	0.014	0.017	0.005	0.730	0.250	0.011	1678
2	A	0.013	0.018	0.003	0.018	< 0.005	< 0.005	1698
	B	0.010	0.017	0.003	0.740	< 0.005	< 0.005	1678
	C	0.010	0.015	0.023	0.690	0.009	< 0.005	1678
	D	0.012	0.013	0.023	0.700	0.250	0.009	1678
Starting Material (iron)		< 0.010	< 0.010	0.003	< 0.010	< 0.005	< 0.005	

[a] Also < 0.01 Cr < 0.003 S < 0.002 Sn < 0.0010 As < 0.02 Mo < 0.010 Si < 0.003 V < 0.005 Sb

[b] 0.5 h at indicated temperature and air cooling

184

3.3.2 Summary of Results

Progress in the current period is denoted by (a) 288°C irradiation and testing of the new iron alloys, (b) determinations on the character of the phosphorus mechanism, and (c) initial investigations into the mechanism of the copper contribution to radiation sensitivity and its subsequent effect on properties recovery by annealing.

The eight iron alloys were irradiated in a special reactor experiment (MID-1) in the form of SEM, FIM, IAP, Auger, and TEM samples for microscopy, and C_v, tensile, and prestrained tensile specimens for mechanical properties determinations. Postirradiation tensile tests by MEA proved highly significant (see Table 3-9); the results refute earlier reports that phosphorus does not enhance the yield strength elevation by irradiation. High phosphorus (0.025% P) material, compared to low (0.001% P) material from the same split melt, exhibited a major yield strength sensitivity to irradiation, as illustrated in Fig. 3-27. The increase in strength is about 75% of the increase in yield strength exhibited by the 0.3% copper content material (see Fig. 3-28). The fluence received by the tensile specimens was about 4.9×10^{19} n/cm^2, E > 1 MeV. Of additional interest, the alloys containing 0.4% nickel or 0.7% nickel in combination with 0.3% copper showed about the same yield strength elevation as the nickel-free, 0.3% copper material, suggesting no effect of nickel alloying on irradiation behavior. Perhaps the lower sensitivity of the 0.7% nickel alloy (code 2B2) compared to the reference iron material (code 2A2) has a bearing on this relationship. Thermal aging of the eight materials in the unirradiated condition at 288°C for 1534 h did not alter appreciably the strength properties in any one case.

One MEA subcontractor (University of Florida) obtained evidence that the phosphorus mechanism is not due to a radiation-enhanced diffusion of phosphorus to prior austenite grain boundaries in the manner of temper embrittlement. Likewise, the subcontractor determined that phosphorus did not result in a change in carbide microstructure. Together, the three findings make phosphorus precipitation in the matrix highly suspect. FIM examinations are underway to explore this possibility.

Another MEA subcontractor (GKSS at Geesthacht, FRG) performed small angle neutron scattering analyses (SANS) of selected MEA steel melts in unirradiated vs. irradiated vs. postirradiation-annealed conditions. The melts primarily feature high/low copper and high/intermediate/low phosphorus contents in A 533-B steel. A major difference in SANS signals was found between high copper (strong) and low copper (weak) materials. Defect clusters of diameters 20 Å and 10^{17} to 10^{18}/cm^3 number density were indicated for the high copper group. Postirradiation annealing at 454°C resulted in an increase in cluster size (almost double) and a reduction in number density, which would be consistent with a ripening and overaging mechanism of annealing recovery. Recovery was accompanied by a significant reduction in the measured volume fraction of clusters. With increasing phosphorus content, the high copper materials showed an increase in the number

Table 3-9 Composition Type and Ambient Temperature Tensile Strengths[a] of Laboratory-Melted Plates Before and After 288°C Irradiation

Material	Code	Yield Strength			Tensile Strength		
		Unirrad.[b] (ksi)	Irrad. (ksi)	Increase (Δksi)	Unirrad.[b] (ksi)	Irrad. (ksi)	Increase (Δksi)
Fe + 0.01 Cu	1A2	21.14	36.34	15.20	42.55	49.47	6.92
Fe + 0.3 Cu	1B2	23.05	51.33	28.32	45.09	64.09	19.00
Fe + 0.3 Cu + 0.4 Ni	1C2	24.22	53.91	29.69	46.12	66.58	20.46
Fe + 0.3 Cu + 0.7 Ni	1D2	27.68	53.74	26.06	48.03	65.48	17.45
Fe (Reference)	2A2	21.72	36.76[b]	15.04	42.66	50.28[b]	7.62
Fe + 0.7 Ni (Reference)	2B2	29.12	39.14	10.02	45.77	51.10	5.33
Fe + 0.7 Ni + 0.025 P	2C2	27.83	49.02	21.19	47.69	64.83	17.14
Fe + 0.7 Ni + 0.025 P + 0.3 Cu	2D2	29.93	53.78	23.85	47.64	67.95	20.31

[a] Average of duplicate tests unless noted [b] Single determination

186

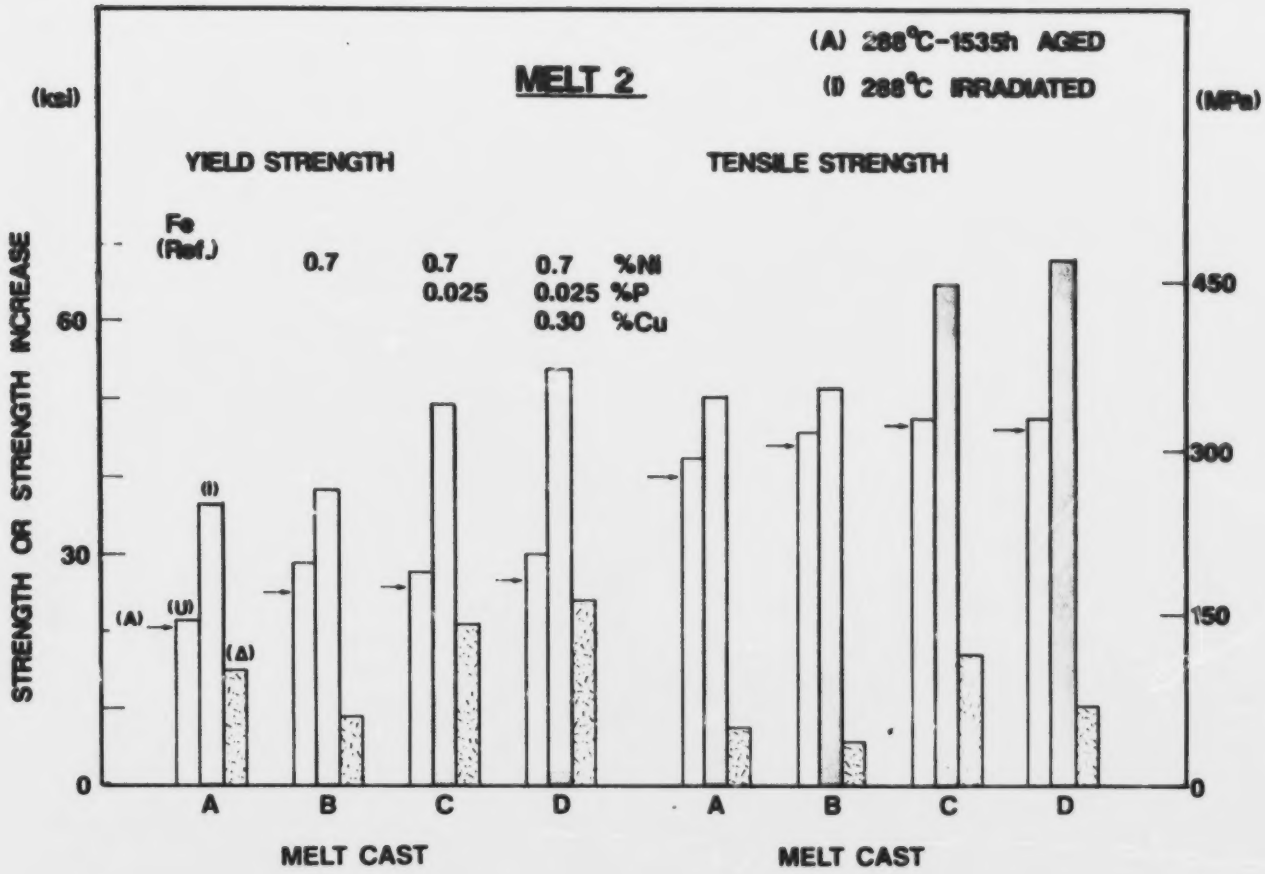

Fig. 3-27 Strength properties of plates from a 4-way split laboratory melt of iron with sequential additions of nickel, phosphorus, and copper in unirradiated (U) and irradiated (I) conditions. Properties for the thermally aged (A) condition are also indicated (see arrows).

BEST COPY AVAILABLE

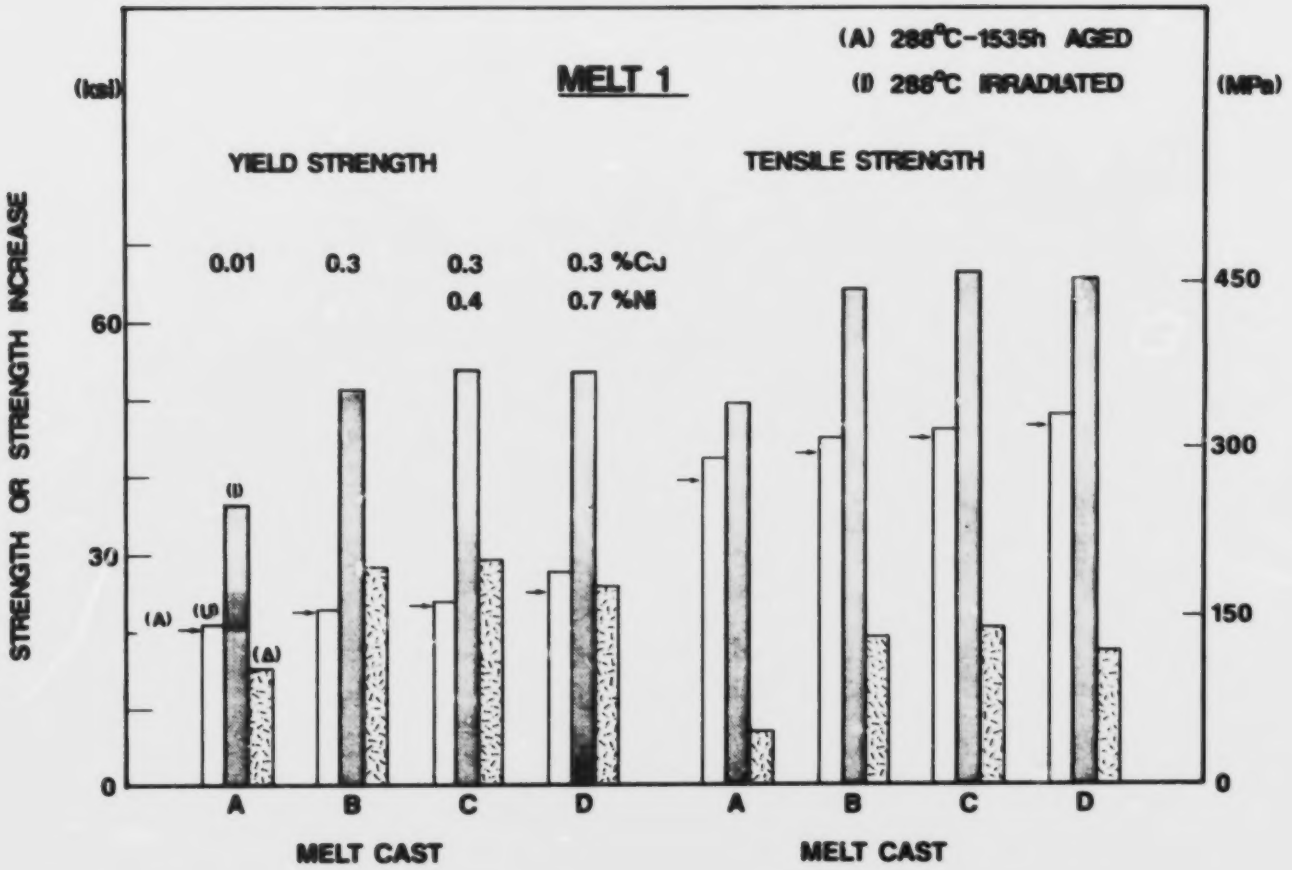

Fig. 3-28 Strength properties of plates from a 4-way split laboratory melt of iron with sequential additions of copper and nickel in unirradiated (U) and irradiated (I) conditions. Properties for the thermally aged (A) condition are also indicated (see arrows).

BEST COPY AVAILABLE

density of defects, consistent with MEA findings on tensile strength change by irradiation in high vs. low phosphorus materials.

Further examination of the cited alloys, using positron annihilation (PA) techniques, is underway at VTT as part of the cooperative VTT-MEA program. Auger studies of fracture surface chemistry are also planned here. Results are expected in mid-1987. A joint CEN-MEA program is probing suspect element-element interactions in annealing recovery, especially a suggested interaction between copper and chromium. This particular effort is expected to aid the analysis of supporting data for the recent in-situ anneal of the Belgian BR-3 power reactor vessel.

3.4 Investigation of Long-Term vs. Short-Term Irradiation Embrittlement of RPV Steels

J. R. Hawthorne

3.4.1 Background

Comparisons currently evolving from long-term (power reactor surveillance) vs. short-term (test reactor experiment) irradiation data suggest a time-at-temperature dependency of irradiation-induced embrittlement. By its nature, the dependency would add a degree of conservatism to data derived from test reactor experiments in that, for a given neutron exposure, a rapid fluence accumulation may equate to a greater embrittlement than a slow accumulation rate as experienced by steels in vessel service. A second inference from recent surveillance data is that, contrary to some projections, the embrittlement process in highly radiation-sensitive steels does not saturate at fluences that are less than end-of-life values for vessels. To verify both indications for the NRC, a set of special experiments was mounted in a test reactor by MEA in 1983.

The experiments provide the closely controlled conditions that are unobtainable in a power reactor; three neutron fluence rates (formerly termed neutron flux) are in use to span the range of power reactor-to-test reactor exposure rates. These are 7-8 x 10^{10}, 5-6 x 10^{11}, and 7-9 x 10^{12} n/cm^2-s^{-1}. Target fluences for the two highest fluence rate exposures are 0.5 x 10^{19}, 1.0 x 10^{19}, and 2.0 x 10^{19} n/cm^2 (E > 1 MeV); the target fluence for the lowest fluence rate is 0.5 x 10^{19} n/cm^2. Test materials are two reference steel plates (A 302-B and A 533-B) and two reference submerged-arc welds. Each has a high copper content and is known through test reactor experiments to have a relatively high radiation embrittlement sensitivity. Specimen types include C_v, fatigue precracked C_v (FCC_v), tensile, and 0.5T-CT specimens. Compositions of the materials are given in Table 3-10.

The irradiations are being conducted in the light-water-cooled UBR reactor, using in-core, core-edge, and reflector region (in-pool) irradiation facilities. The facility locations are shown schematically in Fig. 3-29. The exposure temperature of the specimens, 288°C (nominal), is controlled and continuously monitored by external instrumentation.

In 1985, irradiations to 5 of 8 capsules placed in the reactor in 1983 were completed. Tests of specimens from two of the units were also partially completed. Resultant data pertained to a fluence of 0.79 x 10^{19} n/cm^2 attained at a fluence rate of about 6 x 10^{11} n/cm^2-s^{-1}. Data comparisons provided an early indication of an effect of fluence rate on relative radiation sensitivity at 288°C. Moreover, data for the Linde 80 weld described an effect of power reactor vs. test reactor fluence rates which is the converse of that reported for welds irradiated to much higher fluences.

Table 3-10 Reference Plates And Submerged-Arc Weld Deposits

Material	Code	Chemical Composition (Wt-%)									
		C	Mn	Si	P	S	Ni	Cr	Mo	Cu	Sn
A 302-B Plate	23F	0.24	1.34	0.23	0.011	0.023	0.18	0.11	0.51	0.21	0.037
A 533-B Plate	23G	0.22	1.40	0.19	0.017	0.008	0.63	0.19	0.54	0.20	-----[a]
S/A Weld	W8A	0.079(min)[b]	1.27	0.71	0.010	0.012	0.55	0.10	0.42	0.37	0.002
(Linde 80 ϕ)		0.096(max)	1.36	0.79	0.017	0.019	0.68	0.13	0.50	0.42	0.004
S/A Weld	W9A	0.19 (min)	1.21	0.23	0.008	0.005	0.64	0.10	0.49	0.35	0.003
(Linde 0091 ϕ)		0.19 (max)	1.27	0.23	0.012	0.010	0.77	0.11	0.50	0.43	0.004

[a] Not analyzed

[b] Range (min/max) observed, multiple test locations in 1.83-m long weld seam

191

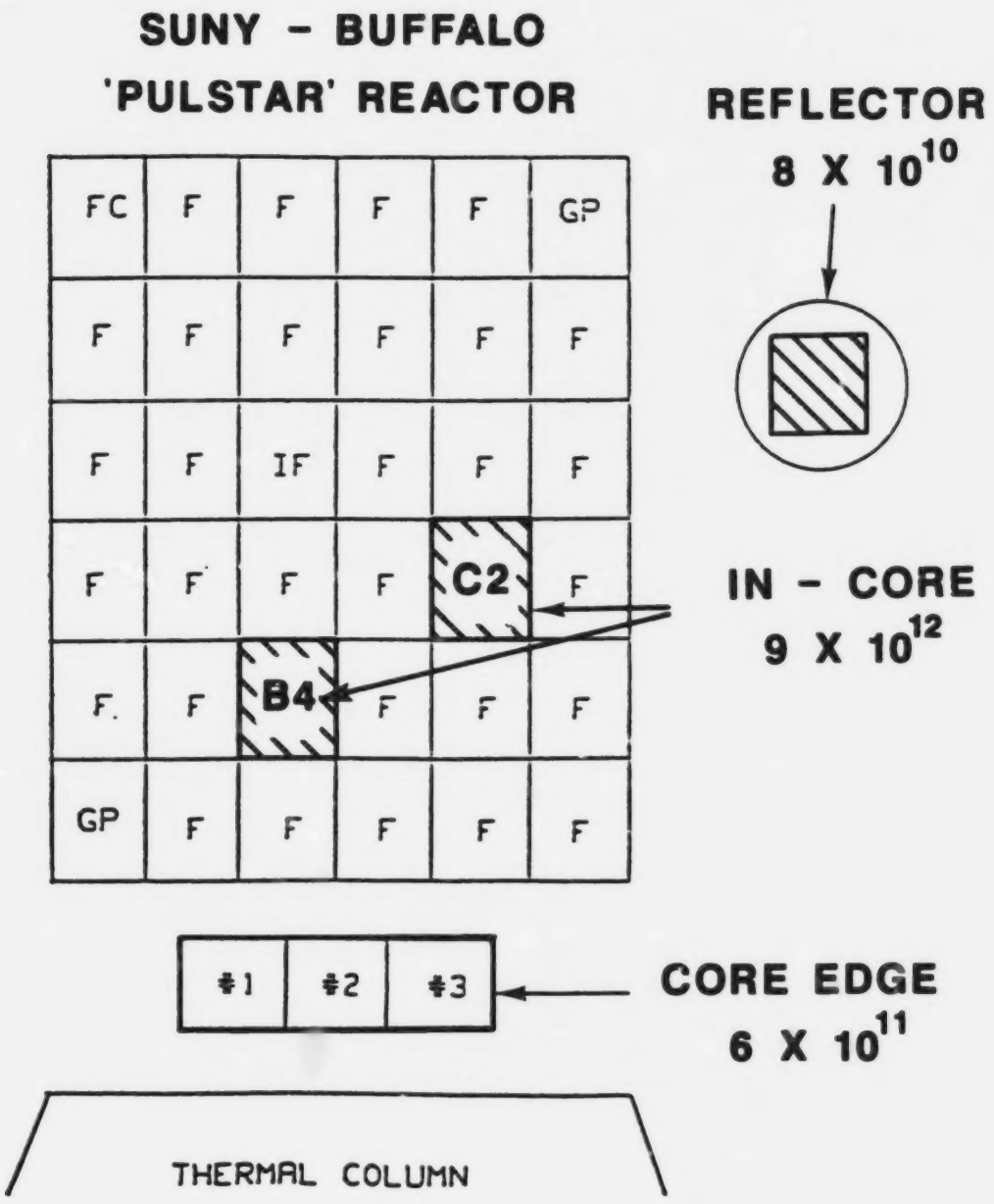

Fig. 3-29 Schematic illustration showing the locations of the irradiation facilities used for fluence rate effects qualification experiments.

BEST COPY AVAILABLE

3.4.2 Summary of Results

In 1986, reactor exposures were completed for all but 4 of the 18 capsules forming the irradiation matrix (Table 3-11). Also, postirradiation tests were completed for all units irradiated at 5-6 x 10^{11} n/cm^2-s^{-1}, that is, the intermediate fluence rate, and for two units irradiated at 8-9 x 10^{12} n/cm^2-s^{-1} corresponding to the high fluence rate.

Table 3-11 Irradiation Matrix

Material	Target Fluence[a]	Neutron Fluence Rate[b]		
		High	Intermediate	Low
	(x 10^{19})	(9 x 10^{12})	(6 x 10^{11})	(8 x 10^{10})
A 302-B	0.5	X[c]	-	X
	1.0	X	X	-
	2.0	X	X	-
S/A Weld (Linde 80 ϕ)	0.5	X	X	X
	1.0	X	X	-
	2.0	X	X	-
A 533-B	0.5	X	-	X
S/A Weld (Linde 0091 ϕ)	0.5	X	-	X
		(In-Core)	(Core-Edge)	(Reflector)

[a] n/cm^2, E > 1 MeV [b] n/cm^2-s^{-1}, E > 1 MeV [c] Irradiation scheduled

The most recent C_v test data from the intermediate fluence rate capsule series are presented in Figs. 3-30 to 3-31. The upper graph in each figure shows the earlier results from capsule CE-1 (low fluence) for judging the new results. Notice that, for both materials, the fivefold increase in neutron fluence produced only a small, additional increase in 41-J temperature. In the case of the plate, a 19°C increase was found. This plate is known worldwide as the ASTM A 302-B reference plate. An increase of about 42°C was expected based on its trend of embrittlement with fluence found with in-core irradiation exposures. For the weld, the measured difference between capsule CE-1 and capsule CE-3 was 25°C.

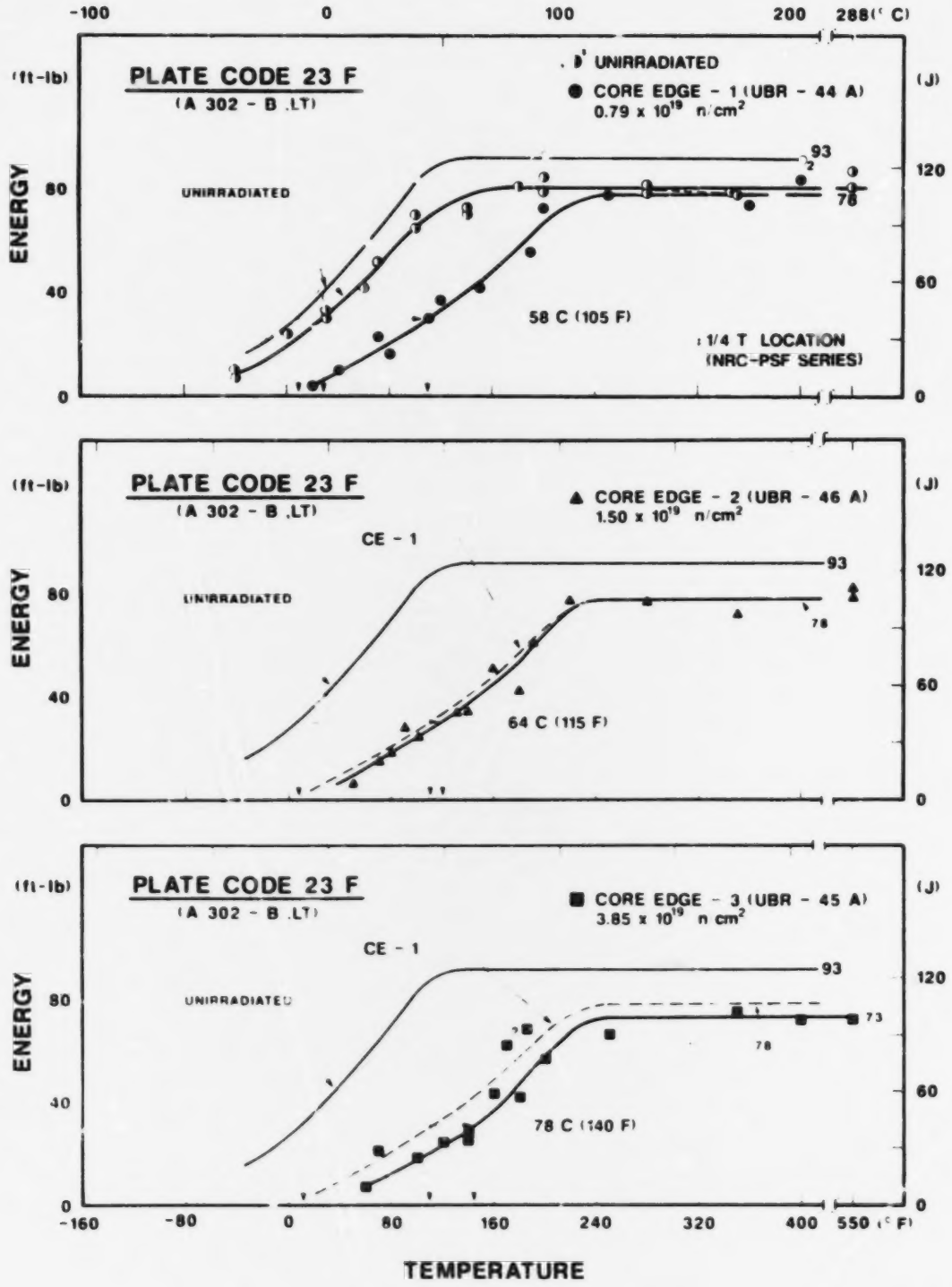

Fig. 3-30 C_v notch ductility of ASTM A 302-B reference plate after 288°C irradiation at intermediate fluence rate (Core-Edge Assemblies no. 1, 2, 3).

BEST COPY AVAILABLE

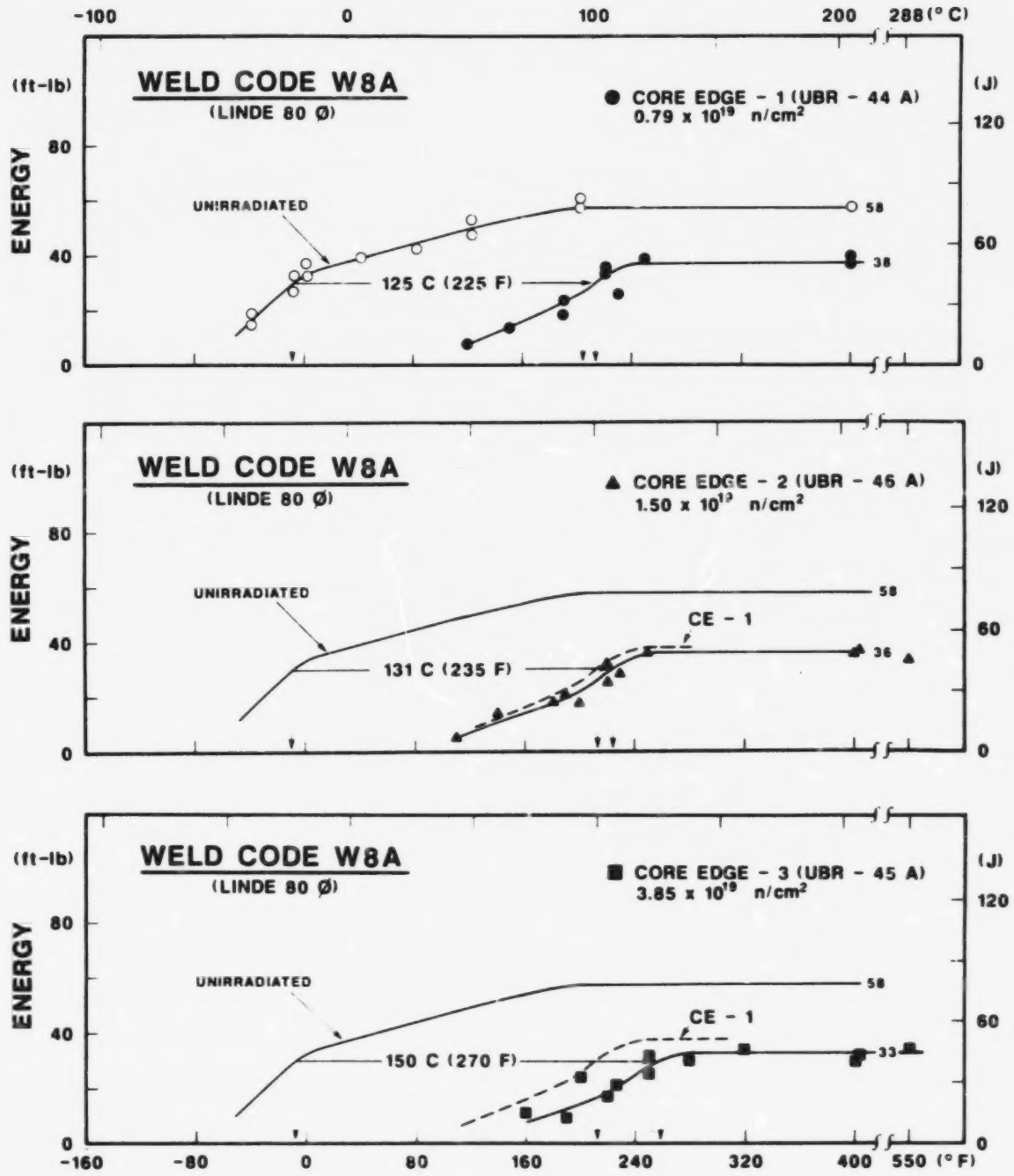

Fig. 3-31 C_v notch ductility of MEA reference weld (Linde 80 flux) after 288°C irradiation at intermediate fluence rate (Core-Edge Assemblies no. 1, 2, 3).

BEST COPY AVAILABLE

C_v test results for the low fluence, high fluence rate exposure condition (capsule IC-1) obtained in 1986 are provided in Figs. 3-32 and 3-33. Data acquired in early 1987 from capsule IC-3 are also given. Figure 3-34 summarizes the findings of intermediate and high fluence rate exposures for the plate and weld. Included in this figure are data obtained from other in-core irradiation tests of the two materials which support the indicated trend projections.

For the plate, the intermediate fluence rate appears less damaging than the high fluence rate in the high fluence regime. On the other hand, no effect of exposure rate in terms of relative 41-J temperature elevation is indicated for this material at low fluences. An opposite relationship is suggested by the trends for the Linde 80 weld. That is, a greater embrittlement with the intermediate fluence rate is found for the low fluence regime. Above a neutron exposure of 0.79×10^{19} n/cm^2, the embrittlement trends for the two fluence rate conditions tend toward convergence. While scatter in the 41-J transition temperature elevation data at fluences above 2×10^{19} n/cm^2 precludes a clear assessment of the convergence, the embrittlement condition achieved by CE-3 assembly specimens clearly was no worse than the embrittlement condition described by specimens irradiated in-core to about the same fluence level. A source of the apparent "scatter" is described below.

Fracture toughness determinations with the 0.5T-CT specimens are illustrated in Figs. 3-35 to 3-38. In general, the radiation-induced elevations in 100 MPa$\sqrt{m}$ temperature show the same effect of fluence rate as the C_v 41-J temperature elevations. The elevations in 100 MPa$\sqrt{m}$ temperature tended to be somewhat higher than the C_v 41-J temperature increase for the plate but not the weld. A similar difference between plate and weld, in terms of the C_v vs. CT correlation has been observed by MEA for other (but not all) materials (Ref. 3).

Tensile strength determinations for the intermediate fluence rate units and the one high fluence rate unit tested in 1986 likewise support the C_v data comparisons. The data are summarized in Table 3-12; supporting data from prior experiments are also given. The strength elevation shown by plate specimens from unit CE-3 (intermediate fluence rate, 3.85×10^{19}) is less than that projected by MEA for a comparable exposure in-core (by 42 MPa) (Refs. 83 and 84). In the case of the weld and the low fluence condition, the intermediate fluence rate produced a greater yield strength elevation than the high fluence rate exposure.

In Fig. 3-31 and 3-33, the data depict a very shallow ductile-to-brittle transition trend and at the higher fluences (units CE-2 and CE-3), a low C_v upper shelf energy level as well. These characteristics make identification of the 41-J temperature elevation by irradiation difficult. The cited curve characteristics are not unusual for Linde 80 welds; on the other hand, 41-J temperature identification for Linde 0091 welds generally is not hampered by either shallow slope or low upper shelf characteristics. The data scatter evident in certain regions of some of the weld transition curves may

BLANK PAGE

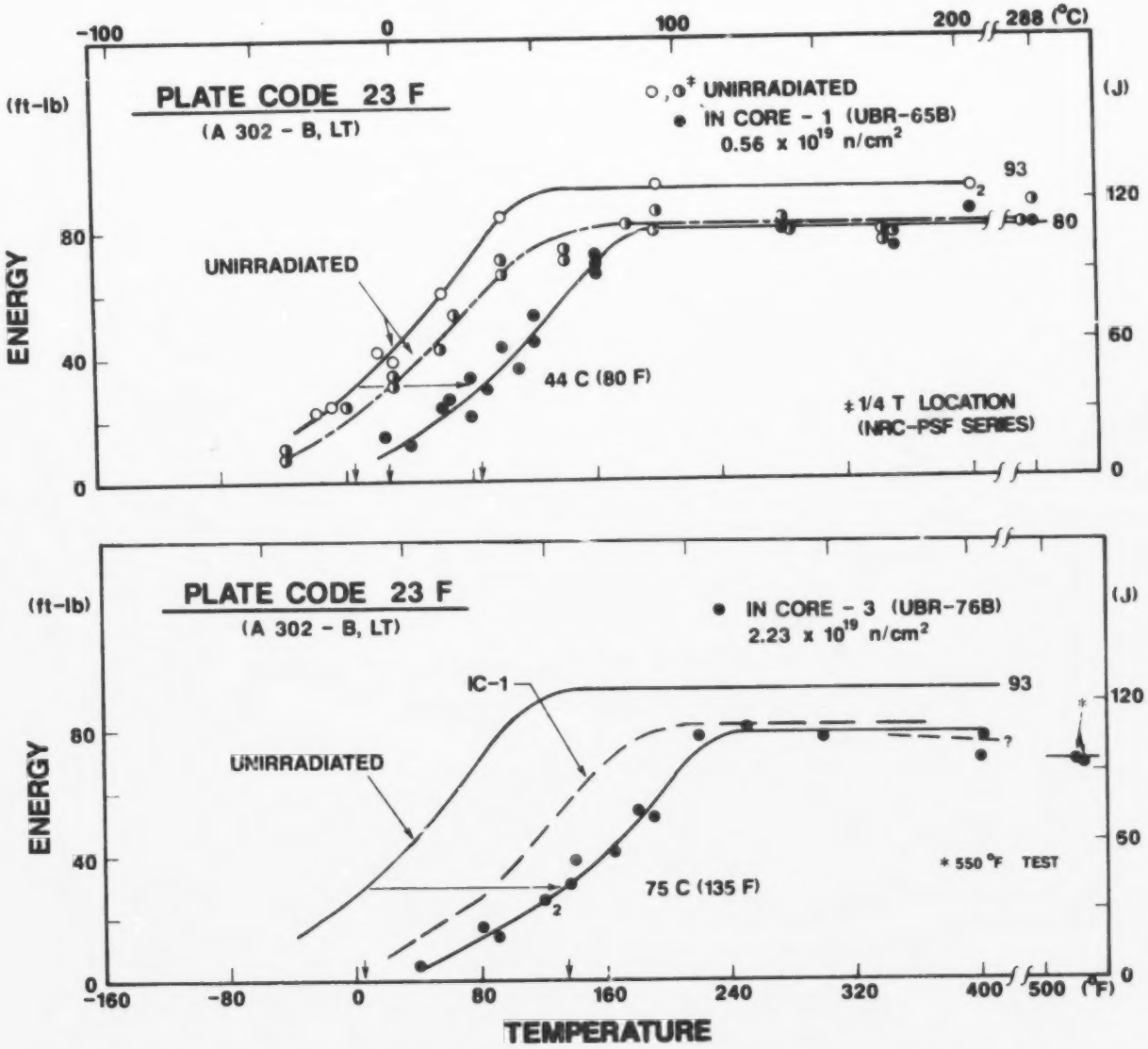

Fig. 3-32 C_v notch ductility of ASTM A 302-B reference plate after 288°C irradiation at the high fluence rate (In-Core Assemblies no. 1 and 3).

BEST COPY AVAILABLE

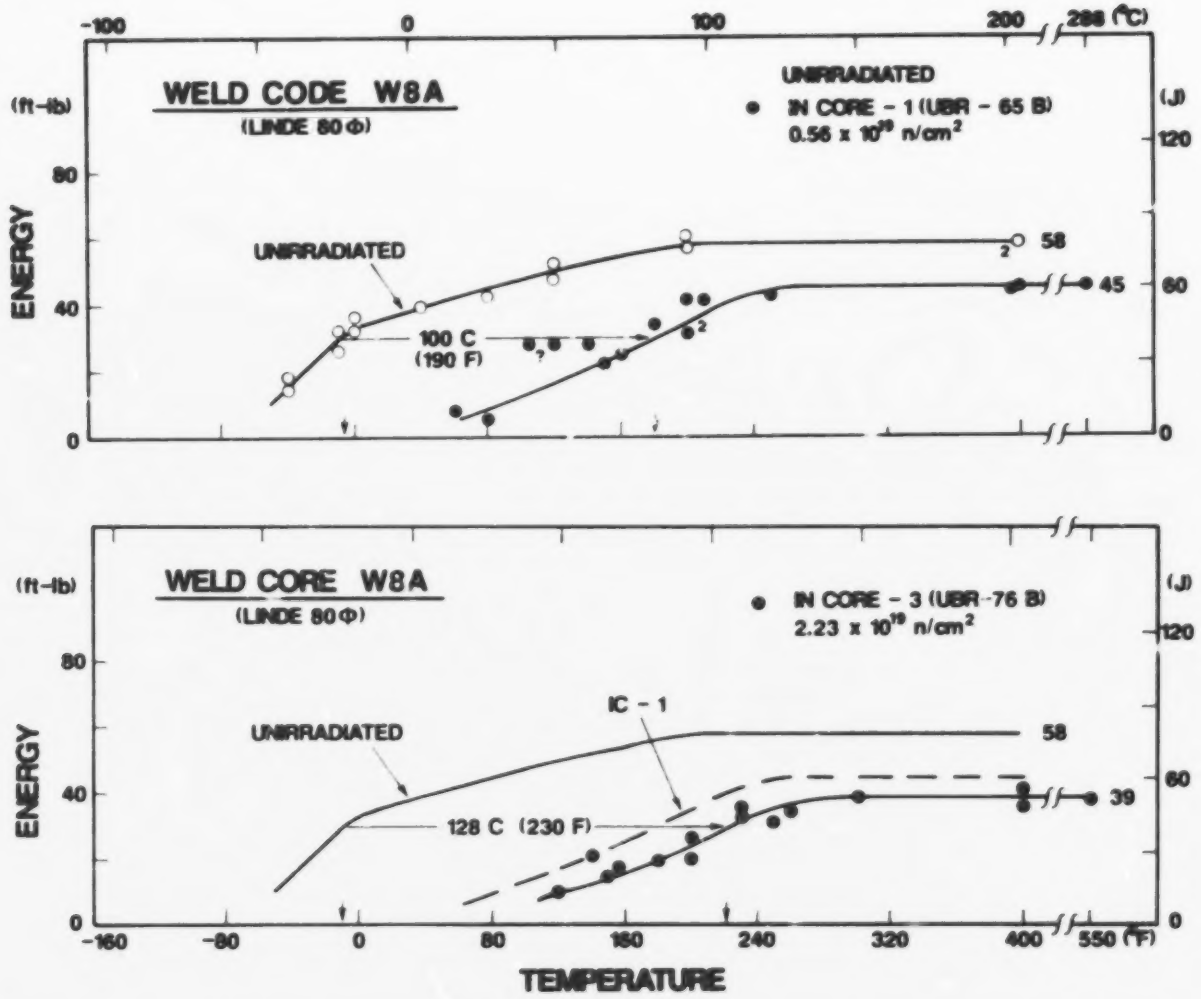

Fig. 3-33 C_v notch ductility of MEA reference weld (Linde 80 flux) after 288°C irradiation at high fluence rate (In-Core Assemblies no. 1 and 3).

BEST COPY AVAILABLE

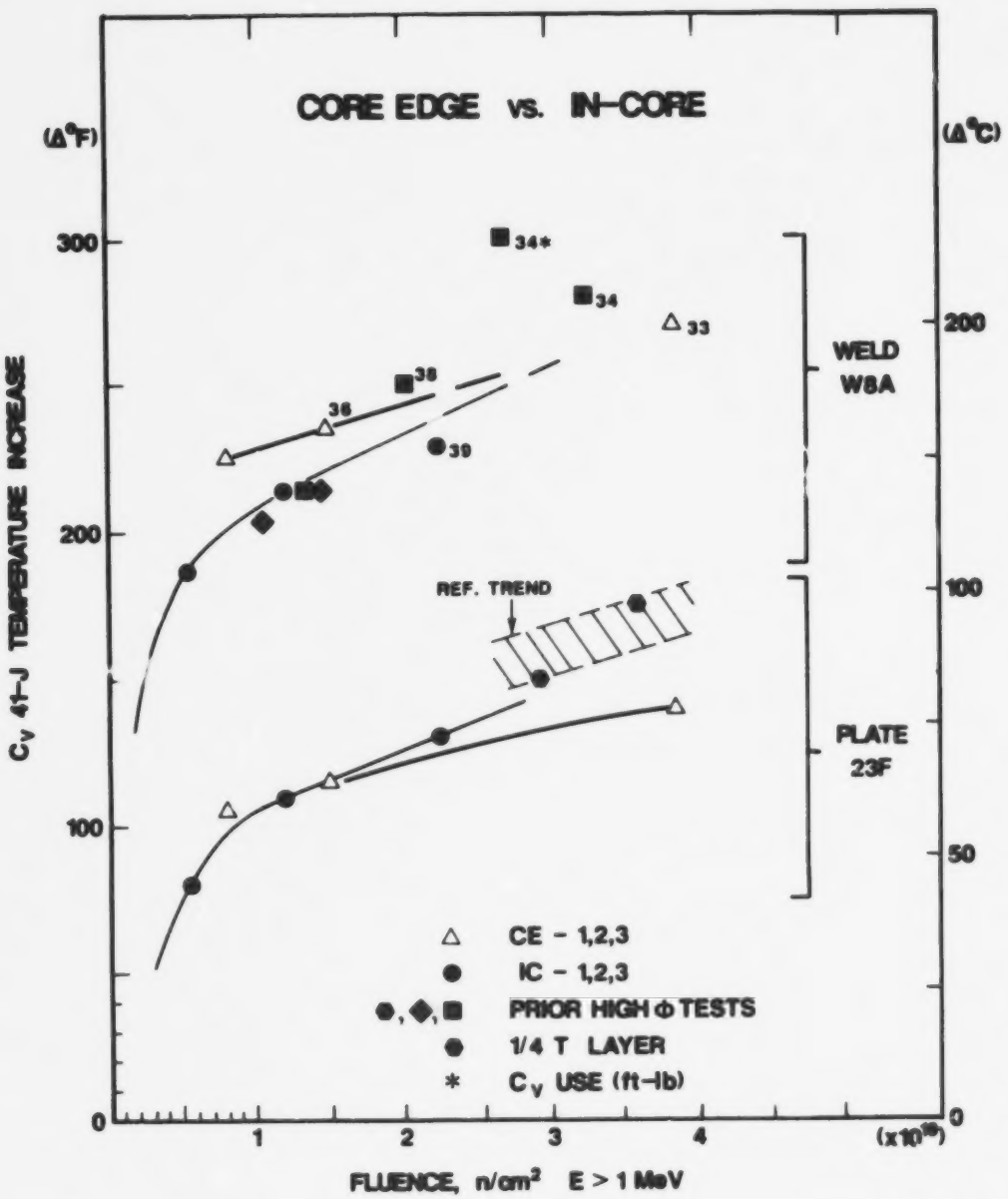

Fig. 3-34 Comparison of C_v 41-J transition temperature elevations produced by intermediate vs. high fluence rate irradiations of A 302-B plate and Linde 80 weld. The numbers adjacent to certain weld metal data points indicate the postirradiation upper shelf energy.

BEST COPY AVAILABLE

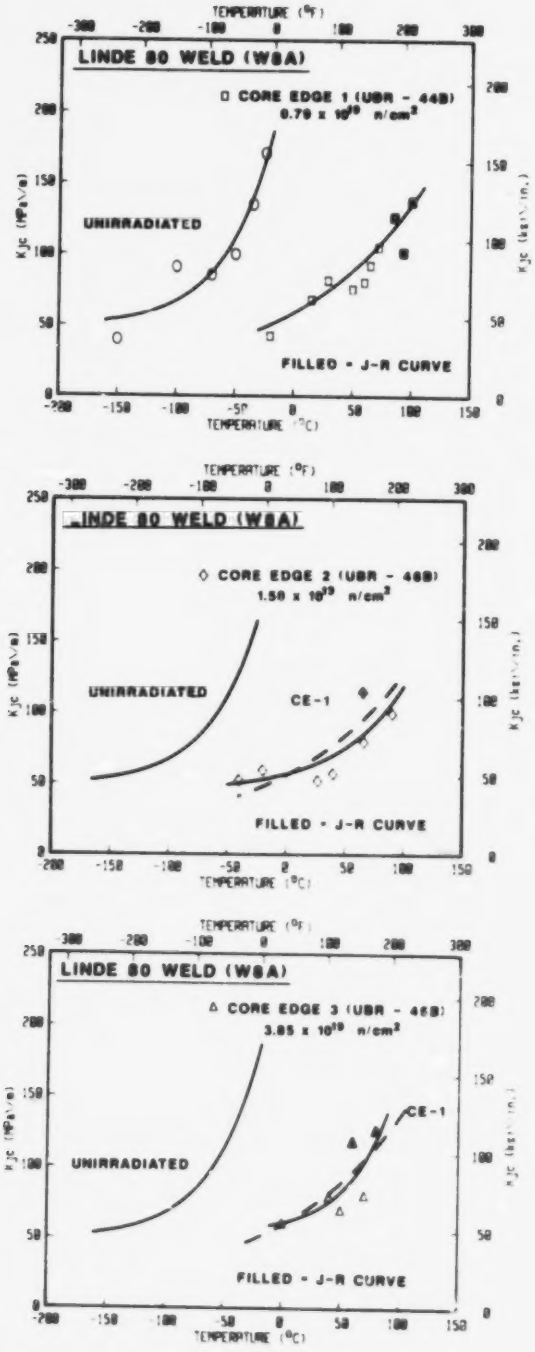

Fig. 3-35 Fracture toughness data for the Linde 80 weld code W8A after irradiation in the core-edge (intermediate fluence rate) facilities. In spite of the differences in fluence between the three irradiated capsules, the data for all three show about the same fracture toughness transition behavior.

BEST COPY AVAILABLE

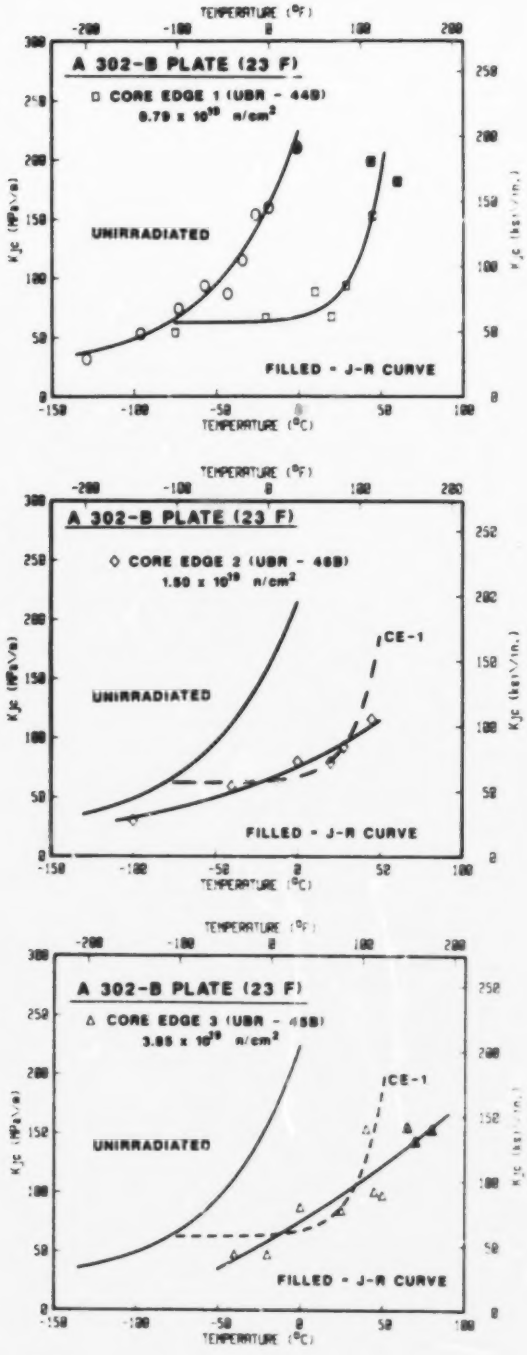

Fig. 3-36 Fracture toughness data for the A 302-B reference plate code 23F after irradiation in the core-edge (intermediate fluence rate) facilities. Paralleling observations for the Linde 80 weld (Fig. 3-35), the data for all three capsules describe common fracture toughness trend.

BEST COPY AVAILABLE

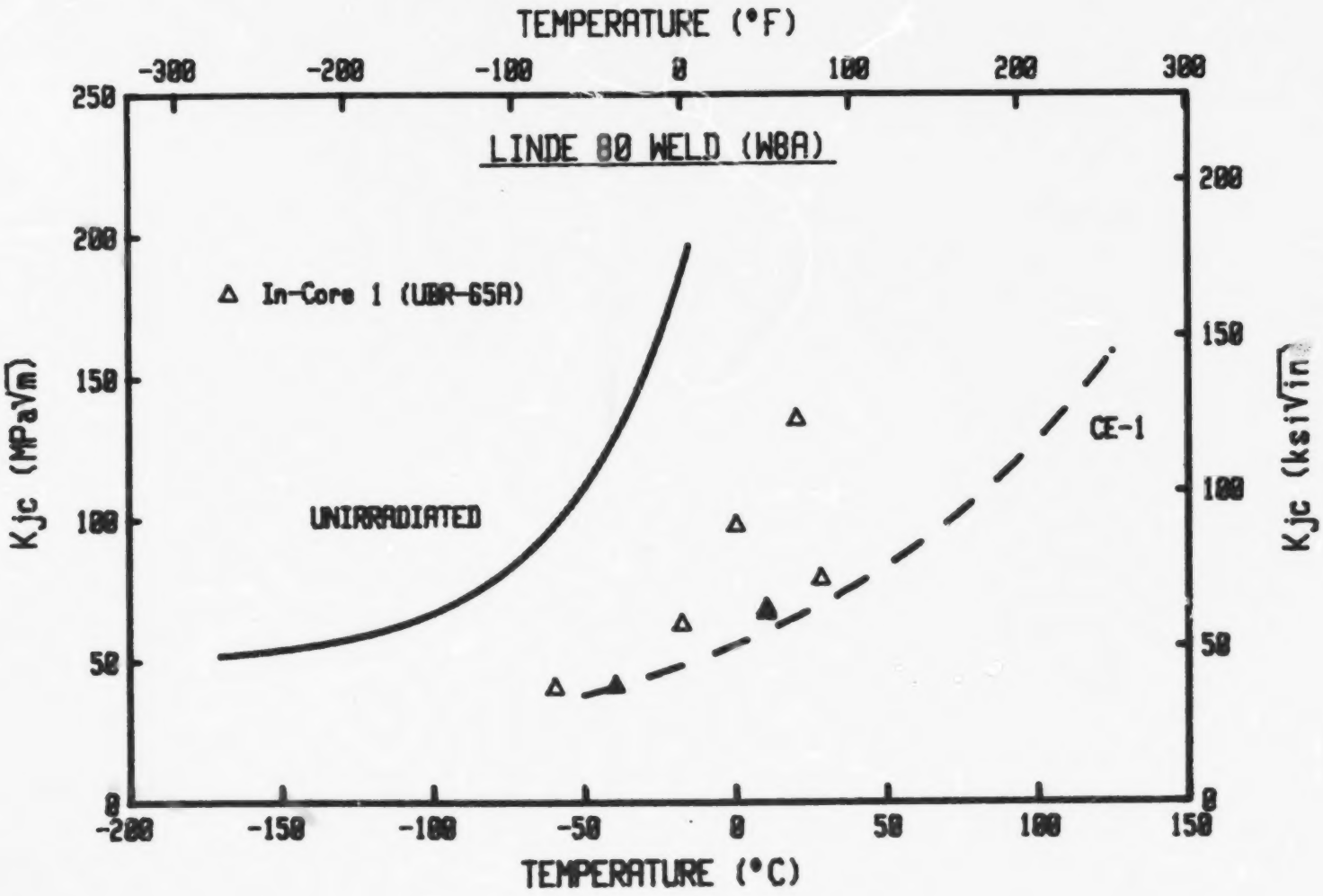

Fig. 3-37 Fracture toughness data for the Linde 80 weld code W8A irradiated in the in-core (high fluence rate) facility. The data indicate less embrittlement than data for a similar fluence exposure in the core-edge (intermediate fluence rate) facility (see dashed line).

BEST COPY AVAILABLE

202

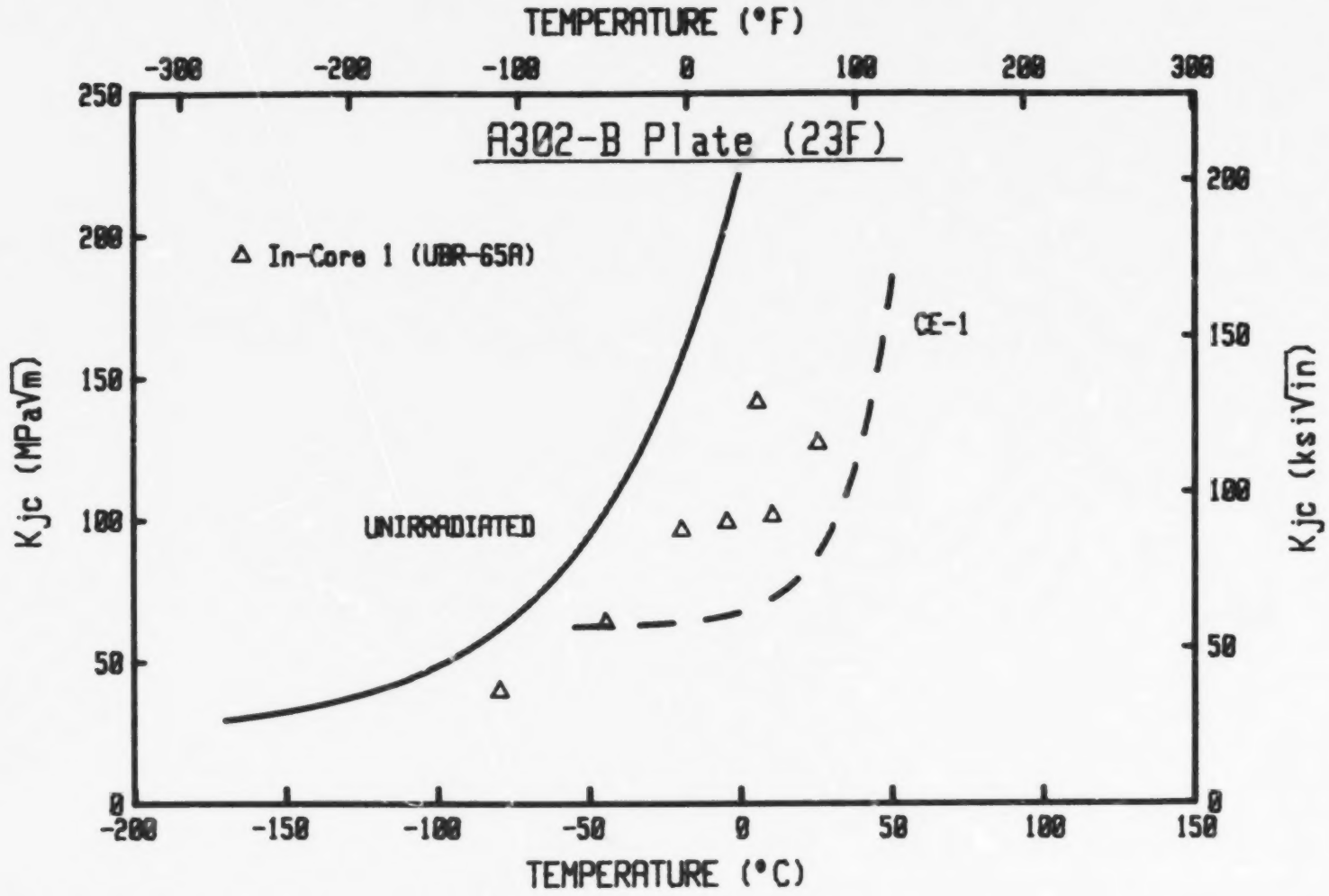

Fig. 3-38 Fracture toughness data for the A 302-B reference plate code 23F irradiated in the in-core (high fluence rate) facility. The data indicate less embrittlement than data for a similar fluence exposure in the core-edge (intermediate fluence rate) facility (see dashed line).

BEST COPY AVAILABLE

Table 3-12 Postirradiation Tensile Strengths Of A 302-B Plate And Linde 80 Submerged-Arc Weld (Ambient Temperature Tests)

Material	Irradiation Assembly	Fluence x 10^{19} n/cm^2	dpa	Yield Strength[a]			Ultimate Tensile Strength		
				MPa	ksi	ΔMPa	MPa	ksi	ΔMPa
A 302-B (Code 23F)	Unirradiated	—	—	447	64.74	—	589	85.35	—
	IC-1 (UBR-65B)	0.56	0.0091	517	74.93	70	647	93.79	58
	IC-2 (UBR-75B)	~ 1.22	~ 0.0198	538	78.06	91	668	96.85	79
	IC-3 (UBR-76B)	2.23	0.0361	564	81.73	117	691	100.22	102
	CE-1 (UBR-44A)	0.79	0.0111	550	79.81	103	680	98.68	91
	CE-2 (UBR-46A)	1.50	0.0212	554	80.32	107	683	99.08	94
	CE-3 (UBR-45A)	3.85	0.0543	566	82.14	119	696	100.91	107
S/A Weld (Code W8A)	Unirradiated	—	—	481[b]	69.76	—	604	87.59	—
				498[c]	72.18	—	617	89.50	—
	Thermal Aged[d]	—	—	483	70.06	—	604	87.56	—
	IC-1 (UBR-65B)	0.56	0.0091	592	85.86	111	699	101.44	95
	IC-2 (UBR-75B)	~ 1.22	~ 0.0198	624	90.53	143	726	105.26	122
	IC-3 (UBR-76B)	2.23	0.0361	659	95.59	178	747	108.26	143
	UBR-72[e,f]	1.06	0.0172	625	90.62	144	721	104.62	117
	UBR-55C[e,f]	3.25	0.0527	706	102.40	260	778	112.90	189
	CE-1 (UBR-44A)	0.79	0.0111	650	94.31	169	741	107.54	137
	CE-2 (UBR-46A)	1.50	0.0212	659	95.53	178	751	108.91	147
	CE-3 (UBR-45A)	3.85	0.0543	684	99.26	203	767	111.23	163

[a] Average of duplicate tests unless noted

[b] Specimen set no. 1 (reference set)

[c] Specimen set no. 2

[d] 288°C-1000 hours; corresponds to specimen set no. 1

[e] Prior MEA study

[f] Single determination

204

be due to some local weld inhomogeneities. In this regard, the test specimens were taken at random through the weld thickness.

Overall, the data denote a dose-rate effect which may extend to power reactor surveillance as well as the test reactor case. Also, the results demonstrate that a unique relationship between embrittlement and dose rate may not exist for RPV steels. The findings suggest further that earlier comparisons of high/low flux environment effects may not have placed sufficient emphasis on product form or composition differences. Fortunately, the magnitude of the fluence rate effect seen to date in the test series is not so large as to preclude the use of accelerated (test reactor) irradiations for screening metallurgical, irradiation, or postirradiation annealing variables.

REFERENCES

1. "NRC Staff Evaluation of Pressurized Thermal Shock," Enclosure A to SECY 83-79, U. S. Nuclear Regulatory Commission, Feb. 1983.

2. "Structural Integrity of Water Reactor Pressure Boundary Components, Annual Report for 1984," F. J. Loss, Ed., USNRC Report NUREG/CR-3228, Vol. 3, May 1985, pp. 44-69.

3. A. L. Hiser, "Correlation of C_v and K_{Ic}/K_{Jc} Transition Temperature Increases Due to Irradiation," USNRC Report NUREG/CR-4395, Sept. 1985.

4. J. G. Merkle, "An Examination of the Size Effects and Data Scatter Observed in Small Specimen Cleavage Fracture Toughness Testing," USNRC Report NUREG/CR-3672, ORNL/TM-9088, Oak Ridge National Laboratory, Apr. 1984.

5. G. G. Chell, J. R. Haigh, and V. Vitek, "A Theory of Warm Prestressing: Experimental Validation and the Implications for Elastic Plastic Failure Criteria," Int. J. of Fracture, Vol. 17, 1981, pp. 61-81.

6. D. A. Curry, "A Micromechanistic Approach to the Warm Prestressing of Ferritic Steels," CERL Lab Note RD/L/N103/79, Sept. 1979.

7. S. N. Atluri, "Path Independent Integrals in Finite Elasticity and Inelasticity, with Body Forces, Inertia, and Arbitrary Crack-Face Conditions," Engrg. Fracture Mech., Vol. 16(3), 1982, pp. 341-364.

8. E. F. Rybicki and R. B. Stonesifer, "Development of Models for Warm Prestressing," USNRC Report NUREG/CR-4491, Jan. 1987.

9. P. C. Paris, H. Tada, A. Zahoor, and H. Ernst, "The Theory of Instability of the Tearing Mode of Elastic-Plastic Crack Growth," in Elastic-Plastic Fracture, ASTM STP 668, American Society for Testing and Materials, Phila., PA, 1979, pp. 5-36.

10. J. W. Hutchison and P. C. Paris, "Stability of J-Controlled Crack Growth," in Elastic-Plastic Fracture, ASTM STP 668, American Society for Testing and Materials, Phila., PA, 1979, pp. 37-64.

11. A. L. Hiser, "Piping Fracture Mechanics Data Base," in Proceedings of the U. S. Nuclear Regulatory Commission Thirteenth Water Reactor Safety Information Meeting, USNRC Conference Proceeding NUREG/CP-0072, Vol. 2, Feb. 1986, pp. 321-336.

12. A. L. Hiser, "Piping Fracture Mechanics Data Base," in Proceedings of the U. S. Nuclear Regulatory Commission Fourteenth Water Reactor Safety Information Meeting, USNRC Conference Proceeding NUREG/CP-0082, Vol. 2, Feb. 1987, pp. 419-432.

13. O. K. Chopra and H. M. Chung, "Long-Term Embrittlement of Cast Duplex Stainless Steels in LWR Systems: Semiannual Report, October 1985-March 1986," USNRC Report NUREG/CR-4744, Vol. 1(1), Sept. 1986.

14. "Structural Integrity of Water Reactor Pressure Boundary Components, Annual Report for 1984," F. J. Loss, Ed., USNRC Report NUREG/CR-3228, Vol. 3, May 1985, pp. 9-20.

15. J. R. Hawthorne, "Preirradiation Qualification of Materials Identified as KRB-A Archive," MEA-2095, Aug. 1985.

16. A. L. Hiser, F. J. Loss, and B. H. Menke, "J-R Curve Characterization of Irradiated Low Upper Shelf Welds," USNRC Report NUREG/CR-3506, Apr. 1984.

17. ASME Boiler and Pressure Vessel Code, Nuclear Power Plant Components, Division 1, Subsection NB, Class 1 Components, American Society of Mechanical Engineers, New York, 1983.

18. Criteria of the ASME Boiler and Pressure Vessel Code for Design By Analysis in Sections III and VIII, Division 2, American Society of Mechanical Engineers, New York, 1969.

19. "BWR Environmental Cracking Margins for Carbon Steel Piping -- Final Report," D. Weinstein, Principal Investigator, EPRI Report NP-2406, Electric Power Research Institute, Palo Alto, CA, 1982.

20. R. E. Peterson, Stress Concentration Factors, Wiley & Sons, NY, 1974, pp. 9-11.

21. H. O. Fuchs and R. I. Stephens, Metal Fatigue in Engineering, Wiley & Sons, NY, 1980, pp. 116-117.

22. H. Neuber, "Theory of Stress Concentration for Shear-Strained Prismatical Bodies with Arbitrary Nonlinear Stress-Strain Law," J. of Applied Mechanics, Trans. of the ASME, Vol. 28(4), 1961, pp. 544-560.

23. D. F. Scoie, N. E. Dowling, and P. Karath, "Fatigue Life Estimation of Notched Members," Fracture Mechanics (15th Symposium), ASTM STP 833, American Society for Testing and Materials, Phila., PA, 1984, pp. 284-299.

24. T. A. Prater and L. F. Coffin, "Notch Fatigue Crack Initiation in High Temperature Water Environments: Experiments and Life Prediction," J. of Pressure Vessel Technology, Trans. of the ASME, Vol. 109(2), 1987, pp. 124-134.

25. G. Gabetta and W. H. Cullen, "Application of a Two-Mechanism Model for Environmentally-Assisted Crack Growth," USNRC Report NUREG/CR-4723, Oct. 1986.

26. H. Hanninen, M. Vulli, and W. H. Cullen, "Surface Spectroscopy of Pressure Vessel Steel Fatigue Fracture Surface Films Formed in PWR Environments," USNRC Report NUREG/CR-4863, 1987.

27. J. D. Landes and R. P. Wei, "The Kinetics of Subcritical Crack Growth and Deformation in a High-Strength Steel," Trans. ASME, J. Engrg. Mater. Technol., Series H, Vol. 95, 1974, pp. 2-9.

28. O. Vosikovsky, "Fatigue Crack Growth in an X-65 Line Pipe Steel at Low Cyclic Frequencies in Aqueous Environments," Trans. ASME, J. Engrg. Mater. Technol., Vol. 97, 1975, pp. 298-304.

29. I. M. Austen, "Quantitative Understanding of Corrosion Fatigue Crack Growth Behavior: Final Report," Commission of European Communities, Technical Steel Research, Brussels, EUR 8560, 1983, p. 130.

30. G. Gabetta and C. Rinaldi, "Evidence of Embrittlement and Its Prediction During Environmental Fatigue on Pressure Vessel Steels," in Proceedings of the Conference on Predictive Capability in Environmentally Assisted Cracking, ASME annual winter meeting, PVP Vol. 99, R. Rungta, Ed., Miami Beach, FL, Nov. 17-22, 1985, pp. 107-126.

31. C. Rinaldi and G. Gabetta, CISE Topical Report SMS-RT-85-001.

32. J. Gilman, "Application of a Model for Predicting Corrosion Assisted Fatigue Crack Growth in LWR Environments," in Proceedings of Second International Atomic Energy Agency Specialists' Meeting on Subcritical Crack Growth, Sendai, Japan, W. H. Cullen, Ed., USNRC Conference Proceedings NUREG/CP-0067, Vol. 2, Apr. 1986, pp. 365-384.

33. E. Eason, et al., "Development and Application of the Computer Program FATDAC for Optimal Analysis of Corrosion Fatigue Data," in Proceedings of Second International Atomic Energy Agency Specialists' Meeting on Subcritical Crack Growth, Sendai, Japan, W. H. Cullen, Ed., USNRC Conference Proceedings NUREG/CP-0067, Vol. 2, Apr. 1986, pp. 309-327.

34. H. R. Smith and D. E. Piper, "Stress Corrosion Testing with Pre-cracked Specimens," in Stress Corrosion Cracking in High Strength Steels and in Aluminum and Titanium Alloys, B. F. Brown, Ed., NRL, Washington, DC, 1972, pp. 17-77.

35. M. O. Speidel, "Stress Corrosion Cracking of Nuclear Pressure Vessel Steel," in Proceedings of Second International Atomic Energy Agency Specialists' Meeting on Subcritical Crack Growth, Sendai, Japan, W. H. Cullen, Ed., USNRC Conference Proceedings NUREG/CP-0067, Vol. 1, Apr. 1986.

36. W. H. Cullen, G. Gabetta, and H. Hanninen, "A Review of Models and Mechanisms For Environmentally-Assisted Crack Growth of Pressure Vessel and Piping Steels in PWR Environments," USNRC Report NUREG/CR-4422, Dec. 1985.

37. A. Saxena and S. Hudak, Jr., "Review and Extension of Compliance Information for Common Crack Growth Specimens," Int. Journal of Fracture, Vol. 14(5), Oct. 1978, pp. 453-468.

38. G. Gabetta and K. Torronen, "Prediction of Cyclic Crack Growth Rate in LWR Environments," in Proceedings of Second International Atomic Energy Agency Specialists' Meeting on Subcritical Crack Growth, Sendai, Japan, W. H. Cullen, Ed., USNRC Conference Proceedings NUREG/CP-0067, Vol. 2, Apr. 1986, pp. 131-152.

39. P. Maiya and W. Shack, "Stress Corrosion Cracking Susceptibility of AISI 316 NG and 316 Stainless Steel in an Impurity Environment," Corrosion, Vol. 41(11), Nov. 1985, pp. 630-634.

40. G. Slama and P. Rabbe, "French Approach and Results in Cyclic Crack Growth," Proceedings of the 5th SMIRT Post-Conference Seminar, Paris, France, Aug. 1981, pp. 311-325.

41. W. H. Bamford, L. J. Ceschini, and R. J. Jacko, "Environmentally Assisted Crack Growth Studies," in Heavy Section Steel Technology Report for July-September 1983, USNRC Report NUREG/CR-3334, Vol. 3, Mar. 1984, pp. 97-114.

42. "Corrosion Fatigue Characterization of Reactor Pressure Vessel Steel," Progress Report, October 1, 1982 to April 30, 1983, Project 1325-1, A. Van Der Sluys, Principal Investigator, Babcock & Wilcox, available from R. L. Jones, Electric Power Research Institute, Palo Alto, CA, July 1983.

43. H. Hanninen, K. Torronen, K. Kemppainen, and S. Salonen, "On the Mechanisms of Environmental Sensitive Cyclic Crack Growth of Nuclear Reactor Pressure Vessel Steels," Corrosion Science Vol. 23(6), 1983, p. 663-679.

44. W. H. Cullen, M. Kemppainen, H. Hanninen, and K. Torronen, "The Effects of Sulfur Chemistry and Flow Rate on Fatigue Crack Growth Rates in LWR Environments," USNRC Report NUREG/CR-4121, Feb. 1985.

45. K. Klemetti, H. Hanninen, K. Torronen, M. Kemppainen, and M. Pessa, "On the Role of Inclusions in Environment Sensitive Cracking of Reactor Pressure Vessel Steels," in Proceedings of the International Symposium on Environmental Degradation of Materials in Nuclear Power Systems -- Water Reactors, Myrtle Beach, SC, Aug. 22-25, 1983, National Association of Corrosion Engineers, Houston, TX, 1984, pp. 368-383.

46. F. P. Ford, "Status of Research on Environmentally-Assisted Cracking in LWR Pressure-Vessel Steels," draft of paper for ASME-PVP Meeting, June 28-July 2, 1987, San Diego, to be published.

47. K. Torronen, M. Kemppainen, and H. Hanninen, "Fractographic Evaluation of Specimens of A 533-B Pressure Vessel Steel," EPRI Report NP-3483, Final Report, Project 1325-7, Electric Power Research Institute, Palo Alto, CA, 1984.

48. W. H. Cullen, "Fatigue Crack Growth Rates in Pressure Vessel and Piping Steels in LWR Environments," USNRC Report NUREG/CR-4724, Mar. 1987.

49. K. Torronen, et al., "Final Report of Safety and Reliability Research Program on Nuclear Materials and Components," to be published, 1987.

50. G. Gabetta and G. Buzzanca, "Measurement of Corrosion Potential Inside and Outside a Growing Crack During Environmental Fatigue Tests," in Proceedings of the Second International Atomic Energy Agency Specialists' Meeting on Subcritical Crack Growth, Sendai, Japan, W. H. Cullen, Ed., USNRC Conference Proceeding NUREG/CP-2090 Vol. 2, Apr. 1986, pp. 219-230.

51. P. Combrade, M. Foucault, and G. Slama, "About the Crack Tip Environment Chemistry in Pressure Vessel Steel Exposed to Primary PWR Coolant," in Proceedings of the Second International Atomic Energy Agency Specialists' Meeting on Subcritical Crack Growth, Sendai, Japan, W. H. Cullen, Ed., USNRC Conference Proceeding NUREG/CP-2090 Vol. 2, Apr. 1986, pp. 201-218.

52. F. P. Ford and P. Combrade, "Electrochemical Reactions Rates on Bare Surfaces and Their Use in a Crack Prediction Model for the Low-Alloy Steel/Water System," in Proceedings of the Second International Atomic Energy Agency Specialists' Meeting on Subcritical Crack Growth, Sendai, Japan, W. H. Cullen, Ed., USNRC Conference Proceeding NUREG/CP-2090 Vol. 2, Apr. 1986, pp. 231-268.

53. C. H. Chen, I. Aral, and G. Theus, "Computer Calculated Potential-pH Diagrams to 300°C," EPRI Report NP-3137, Electric Power Research Institute, Palo Alto, CA, June 1983.

54. Section XI of the ASME Boiler and Pressure Vessel Code, Rules for In-Service Inspection of Nuclear Power Plant Components, ANSI/ASME-BPV-XI-1, American Society of Mechanical Engineers, New York, issued annually.

55. W. H. Cullen, "Cumulative Damage Factor for Environmentally-Assisted Fatigue Crack Growth," in "Structural Integrity of Water Reactor Pressure Boundary Components, Annual Report for 1985," F. J. Loss, Ed., USNRC Report NUREG/CR-3228, Vol. 4, June 1986, pp. 97-107.

56. R. L. Jones, "Results of ICCGR Cyclic Crack Growth Round Robin Test Programs," in Proceedings of the Second International Atomic Energy Agency Specialists' Meeting on Subcritical Crack Growth - Sessions I and II, W. H. Cullen, Ed., USNRC Conference Proceeding NUREG/CP-0067, Apr. 1986, pp. 93-114.

57. P. C. Paris and F. Erdogan, "A Critical Analysis of Crack Propagation Laws," Trans. ASME, J. Basic Engrg. Ser. D, Vol. 85(3), 1963, p. 528

58. K. Walker, "The Effect of Stress Ratio During Crack Propagation and Fatigue for 2024-T3 and 7075-T6 Aluminum, Effects of Environment and Complex Load History on Fatigue Life, ASTM STP 462, American Society for Testing and Materials, Phila., PA, 1970, pp. 1-4.

59. J. Willenborg, et al., "A Crack Growth Retardation Model Using an Effective Stress Concept," AFFDL-TM-71-1, Feb. 1971.

60. O. E. Wheeler, "Spectrum Loading and Crack Growth," Trans. ASME, J. Basic Engrg., Vol. 94D(1), 1972, pp. 181-186.

61. P. D. Bell and A. Wolfman, "Mathematical Modeling of Crack Growth Interaction Effect," in Fatigue Crack Growth Under Spectrum Loads, ASTM STP 595, American Society for Testing and Materials, Phila., PA, 1976, pp. 157-171.

62. L. F. Impellizeri, "Cumulative Damage Analysis in Structural Fatigue," in Effects of Environment and Complex Load History on Fatigue Life, ASTM STP 462, American Society for Testing and Materials, Phila., PA, 1970, pp. 40-68.

63. H. D. Hill and C. R. Saff, "Spectrum Crack Growth Prediction Method Based on Crack Surface Displacement and Contact Analysis," in Fatigue Crack Growth Under Spectrum Loads, ASTM STP 595, American Society for Testing and Materials, Phila., PA, 1976, pp. 206-217.

64. J. C. Newman, "A Crack Closure Model for Predicting Fatigue Crack Growth Under Aircraft Spectrum Loading," in Methods and Models for Predicting Crack Growth Under Random Loading, ASTM STP 748, American Society for Testing and Materials, Phila., PA, 1981, pp. 53-84.

65. H. Fuhring and T. Seeger, "Structural Memory of Cracked Components," in Fracture Mechanics (11th Conference), ASTM STP 677, American Society for Testing and Materials, Phila., PA, 1979, pp. 144-167.

66. B. T. Habibie, "Calculation Procedure to Predict Crack Growth," MMB Report UH 03-71, 1971, in German.

67. D. Broek and B. N. Leis, "Similitude and Anomalies in Fatigue Crack Growth Rates," Fatigue '81, Westbury House, 1981, pp. 129-146.

68. D. Broek, "A Similitude Criterion for Fatigue Crack Growth Modeling," in Fracture Mechanics: Sixteenth Symposium, ASTM STP 868, American Society for Testing and Materials, Phila., PA, 1985, pp. 347-360.

69. D. Broek, Elementary Engineering Fracture Mechanics, 4th Edition, Nijhoff, 1986.

70. D. Broek and S. H. Smith, "The Prediction of Fatigue Crack Growth Under Flight-By-Flight Loading," Engrg. Fract. Mech., Vol. 11, 1979, pp. 123-142.

71. W. H. Cullen, "Fatigue Crack Growth Rates of Low-Carbon and Stainless Piping Steels in PWR Environments," USNRC Report NUREG/CR-3945, Jan. 1985.

72. W. H. Cullen, et al., "The Temperature Dependence of Fatigue Crack Growth Rates of A 351-CF8A Cast Stainless Steel in LWR Environment," USNRC Report NUREG/CR-3546, Apr. 1984.

73. W. H. Cullen, "Environmentally-Assisted Crack Growth in LWR Materials--Effects of Environment and Cladding on the Growth of Surface Flaws," in Structural Integrity of Water Reactor Pressure Boundary Components, Annual Report for 1985, F. J. Loss, Ed., USNRC Report NUREG/CR-3228, Vol. 4, June 1986, pp. 108-117.

74. "Section VIII -- Division 2 of the ASME Boiler and Pressure Vessel Code Pressure Vessels -- Alternative Rules," ANSI/ASME-BPV-VIII, American Society of Mechanical Engineers, New York, NY, issued annually.

75. E. F. Rybicki, J. R. Shadley, A. S. Sandhu, "Experimental Evaluation of Residual Stresses in a Weld Clad Plate and Clad Test Specimens," USNRC Report NUREG/CR-4646, Oct. 1986.

76. L. A. James, "Fatigue-Crack Growth in Type 304 Stainless Steel Weldments at Elevated Temperature," Journal of Testing and Evaluation, Vol. 1(1), 1973, pp. 52-57.

77. W. H. Cullen, "Fatigue Crack Growth Rates in Pressure Vessel and Piping Steels in LWR Environments," USNRC Report NUREG/CR-4724, Mar. 1987.

78. W. H. Cullen, K. Torronen, and M. Kemppainen, "Effects of Temperature on Fatigue Crack Growth of A 508-2 Steel in LWR Environment," USNRC Report NUREG/CR-3230, Apr. 1983.

79. W. H. Cullen, "Fatigue Crack Growth of Irradiated Pressure Vessel Steels in LWR Environments," in Proceedings of the Second International Atomic Energy Agency Specialists' Meeting on Subcritical Crack Growth," Sendai, Japan, 1985, W. H. Cullen, Ed., USNRC Conference Proceedings NUREG/CP-0067, Vol. 1, Oct. 1985, pp. 357-378.

80. J. D. Atkinson and T. C. Lindley, "The Effect of Frequency and Temperature on Environmentally-Assisted Fatigue Crack Growth Below K_{ISCC} in Steels," in Proceedings of the Conference on the Influence of Environment on Fatigue, Institute of Mech. Engr., London, 1977, pp. 65-74.

81. J. R. Hawthorne, "Exploratory Studies of Element Interaction and Composition Dependencies in Radiation Sensitivity Development," USNRC Report NUREG/CR-4437, Nov. 1985.

82. "Structural Integrity of Water Reactor Pressure Boundary Components, Annual Report for 1985," F. J. Loss, Ed., USNRC Report NUREG/CR-3228, Vol. 4, June 1986, pp. 137-149.

83. J. R. Hawthorne, "Trends in Charpy-V Shelf Energy Degradation and Yield Strength Increase of Neutron-Embrittled Pressure Vessel Steels," in Nuclear Engineering and Design, 1970, pp. 427-446.

84. J. R. Hawthorne, et al., "Evaluation and Prediction of Neutron Embrittlement in Reactor Pressure Vessel Materials," Final Report, EPRI Report NP-2782, Electric Power Research Institute, Palo Alto, CA, Dec. 1982.

NRC FORM 335 (11-81)

U.S. NUCLEAR REGULATORY COMMISSION

BIBLIOGRAPHIC DATA SHEET

1. REPORT NUMBER (Assigned by DDC)
NUREG/CR-3228, Vol. 5
MEA-2207

4. TITLE AND SUBTITLE (Add Volume No., if appropriate)
STRUCTURAL INTEGRITY OF WATER REACTOR PRESSURE BOUNDARY COMPONENTS
ANNUAL REPORT FOR 1986

2. (Leave blank)

3. RECIPIENT'S ACCESSION NO.

7. AUTHOR(S)
Edited by F. J. Loss

5. DATE REPORT COMPLETED
MONTH: June | YEAR: 1987

9. PERFORMING ORGANIZATION NAME AND MAILING ADDRESS (Include Zip Code)
Materials Engineering Associates, Inc.
9700-B Martin Luther King, Jr. Highway
Lanham, Maryland 20706-1837

DATE REPORT ISSUED
MONTH: July | YEAR: 1987

6. (Leave blank)

8. (Leave blank)

12. SPONSORING ORGANIZATION NAME AND MAILING ADDRESS (Include Zip Code)
Division of Engineering Technology
Office of Nuclear Regulatory Research
U. S. Nuclear Regulatory Commission
Washington, D. C. 20555

10. PROJECT TASK/WORK UNIT NO

11. FIN NO.
B8900

13. TYPE OF REPORT
Technical Report

PERIOD COVERED (Inclusive dates)
1 January to 31 December 1986

15. SUPPLEMENTARY NOTES

14. (Leave blank)

16. ABSTRACT (200 words or less)

This program is being conducted for the NRC to provide analytical and experimental methods and data that are necessary to ensure the structural safety and reliability of pressure boundary components in U. S. commercial, light water reactor power systems. Emphasis is placed on characterization of material properties performance in a nuclear environment for the application to plant-life extension and mitigation of the consequences of postulated accident scenarios. Current work is organized into three major tasks: (1) fracture mechanics investigations, (2) environmentally-assisted crack growth in high temperature, primary reactor water, and (3) radiation sensitivity and postirradiation properties recovery. Research progress in these three tasks for 1986 is summarized in this report.

17. KEY WORDS AND DOCUMENT ANALYSIS

17a. DESCRIPTORS

J Integral-R Curve; Elastic-Plastic Fracture; Nuclear Pressure Vessel and Piping Steels and Weldments, Corrosion Fatigue; Load Interaction Effects; Postirradiation Heat Treatment; Radiation Embrittlement Mechanisms; Notch Ductility; Embrittlement Relief; Annealing; Fracture Mechanics Data Base; Test Methods Correlations; Stainless Steel Cladding; Three-Dimensional Cracks; Fatigue; Fatigue Crack Growth; Fatigue Life

17b. IDENTIFIERS/OPEN-ENDED TERMS

18. AVAILABILITY STATEMENT
Unlimited

19. SECURITY CLASS (This report)
Unclassified

21. NO. OF PAGES

20. SECURITY CLASS (This page)
Unclassified

22. PRICE
$

NRC FORM 335 (11-81)

*U. S. GOVERNMENT PRINTING OFFICE: 1987-181-692:60173

214

UNITED STATES
NUCLEAR REGULATORY COMMISSION
WASHINGTON, D.C. 20555

OFFICIAL BUSINESS
PENALTY FOR PRIVATE USE, $300

SPECIAL FOURTH-CLASS RATE
POSTAGE & FEES PAID
USNRC
WASH D C
PERMIT No G-67

BEST COPY AVAILABLE